

29 August 2008 | \$10

Science



 AAAS



COVER

A black-chinned hummingbird (*Archilochus alexandri*) drinks nectar from a flower of wild tobacco (*Nicotiana attenuata*). Nicotine in the nectar moderates its consumption by the hummingbird and protects against predators; the flower lip produces benzyl acetone, which attracts pollinators. Together, the repellent and attractant maximize the plant's reproductive fitness. See page 1200.

Photo: Danny Kessler

DEPARTMENTS

- 1127 Science Online
- 1129 This Week in Science
- 1134 Editors' Choice
- 1136 Contact Science
- 1139 Random Samples
- 1141 Newsmakers
- 1171 AAAS News & Notes
- 1225 New Products
- 1226 Science Careers

EDITORIAL

- 1133 Academies Active in Education
by Jorge E. Allende

NEWS OF THE WEEK

- NSF Budget Ills Send Big Chill Through Antarctic Program 1142
- Biologists Change One Cell Type Directly Into Another 1143
- Fraud Charges Cast Doubt on Claims of DNA Damage From Cell Phone Fields 1144
- Research Downturn 1144
- SCIENCESCOPE 1145
- Can Fasting Blunt Chemotherapy's Debilitating Side Effects? 1146
- First Gene for Severe Dry Macular Degeneration 1146

NEWS FOCUS

- Ancient Earthmovers of the Amazon
The Western Amazon's "Garden Cliffs"
-> Report p. 1214; Science Podcast 1148
- Physiological Society Meeting
Learning Under Anesthesia
Testing a Taste Test for Depression 1153
- Zeng Yi: A Controversial Bid to Thwart the "Cantonese Cancer"
Mortality Survey Offers Mixed Message 1154



LETTERS

- China's Energy Policy Comes at a Price Q. Wang
Response J. Pan et al. 1156
- From Darwinism to Evolutionary Biology
U. Kutschera 1158

CORRECTIONS AND CLARIFICATIONS

BOOKS ET AL.

- Canada and the United States
Differences That Count, 3rd ed. D. M. Thomas and
B. B. Torrey, Eds., reviewed by S. Randall 1159
- Guestimation Solving the World's Problems on the
Back of a Cocktail Napkin L. Weinstein and J. A. Adam,
reviewed by S. Mertens 1160

EDUCATION FORUM

- Preschool Influences on Mathematics Achievement
E. C. Melhuish et al. 1161

PERSPECTIVES

- The "Invisible Hand" of Floral Chemistry
R. A. Ragusa -> Report p. 1200 1163
- Life After Death
A. Celotti -> Report p. 1183 1164
- When Seamounts Subduct
R. van Huene -> Report p. 1194 1165
- Opening the Molecular Floodgates
C. S. Gandhi and D. C. Rees
-> Research Article p. 1179; Report p. 1210 1166
- A Catalytic Foothold for Fluorocarbon Reactions
R. N. Perutz -> Report p. 1208 1168
- Neuron Research Leaps Ahead
R. H. Brown Jr. -> Report p. 1218 1169

SCIENCE EXPRESS

www.sciencexpress.org

MEDICINE

Seeding and Propagation of Untransformed Mouse Mammary Cells in the Lung

K. Podsypanina et al.

In mice, normal mammary cells can colonize the lung, suggesting that metastases might arise from displaced normal cells acquiring genetic changes that confer malignancy.

10.1126/science.1161621

APPLIED PHYSICS

Time Reversal and Negative Refraction

J. B. Pendry

Optically active materials with nonlinear optical properties are predicted to mimic negatively refractive materials but without losses associated with true negative refraction.

10.1126/science.1162087



EVOLUTION

Natural Selection on a Major Armor Gene in Threespine Stickleback

R. D. H. Barrett, S. M. Rogers, D. Schluter

In stickleback fish transferred to fresh water, selection against the allele for the costly armor plating only partly explains the changes in allele frequencies over generations.

10.1126/science.1159978

TECHNICAL COMMENT ABSTRACTS

GEOCHEMISTRY

Comment on "Determining Chondritic Impactor Size from the Marine Osmium Isotope Record"

J. V. Morgan

full text at www.sciencemag.org/cgi/content/full/321/5893/1158p

Response to Comment on "Determining Chondritic Impactor Size from the Marine Osmium Isotope Record"

F. S. Paquay, G. E. Ravizza, T. K. Lalai, B. Peucker-Ehrenbrink

full text at www.sciencemag.org/cgi/content/full/321/5893/1158b

REVIEW

APPLIED PHYSICS

Cavity Optomechanics: Back-Action at the Mesoscale

T. J. Kippenberg and K. J. Vahala

1172

BREVIA

GEOPHYSICS

Magmatically Triggered Slow Slip at

Kilauea Volcano, Hawaii

B. A. Brooks et al.

Satellite radar and global positioning data show that intrusion of a dike into Kilauea volcano in June 2007 triggered slip but no earthquakes along a fault 15 to 20 hours later.



1164 & 1183

BREVIA CONTINUED...

GEOCHEMISTRY

Bang! Month-Scale Eruption Triggering at

Santorini Volcano

V. M. Martin et al.

Modeling the diffusion of iron in crystals shows that the 1925 eruption of Santorini was triggered by intrusion of hotter magma just a few months earlier.

1178

RESEARCH ARTICLE

STRUCTURAL BIOLOGY

The Structure of an Open Form of an *E. coli*

Mechanosensitive Channel at 3.45 Å Resolution

W. Wang et al.

Circularly arrayed transmembrane helices in the bacterial mechanosensitive ion channel, MscS, expand like the iris of a camera to open the channel and allow ion efflux.

>> Perspective p. 1166; Report p. 1219

1179

REPORTS

ASTRONOMY

Polarized Gamma-Ray Emission from the Crab

A. J. Dean et al.

Detection of polarized gamma rays from the Crab Pulsar implies that electrons must be accelerated to extreme energies to emit radiation near the rapidly rotating star.

>> Perspective p. 1164

1183

ASTRONOMY

The Metamorphosis of Supernova

SN 2008D/XRF 080109: A Link Between

Supernovae and GRBs/Hypernovae

P. A. Mazzali et al.

The spectra of a recent supernova evolved from that of a more energetic event to that of a less energetic one, providing a link between previous observations.

1185

CONTENTS continued >>>

REPORTS CONTINUED...

CHEMISTRY

- Hydrodefluorination of Perfluoroalkyl Groups Using Silylium-Carborane Catalysts** 1188
C. Douvris and O. V. Ozerov

A catalytic cycle using boron-carbon compounds efficiently converts C-F to C-H bonds and thus can destabilize environmentally persistent fluorocarbons. >> *Perspective p. 1168*

CHEMISTRY

- Inverse Velocity Dependence of Vibrationally Promoted Electron Emission from a Metal Surface** 1191
N. H. Nahler et al.

Vibrationally excited nitric oxide molecules unexpectedly ionize a surface more efficiently at slower approach velocities, apparently because there is more time for charge transfer.

GEOPHYSICS

- Weak Interplate Coupling by Seamounts and Repeating $M \sim 7$ Earthquakes** 1194
K. Mochizuki et al.

More earthquakes occur in front of a subducting seamount east of Japan than over and behind it, implying that the subducting and overriding plates are weakly coupled. >> *Perspective p. 1185*

PALEOCLIMATE

- Limits for Combustion in Low O_2 Redefine Paleoclimatic Predictions for the Mesozoic** 1197
C. M. Belcher and J. C. McElwain

Combustion experiments under realistic atmospheric conditions show that charcoal layers in Mesozoic rocks require a higher level of atmospheric oxygen than previously was thought.

PLANT SCIENCE

- Field Experiments with Transformed Plants Reveal the Sense of Floral Scent** 1200
D. Kessler, K. Gase, I. T. Baldwin

Genetic manipulation of wild tobacco plants balances the use of scent to attract pollinators and toxin to limit nectar consumption in order to optimize reproduction.

>> *Perspective p. 1163; Science Podcast*

MICROBIOLOGY

- Redox-Active Antibiotics Control Gene Expression and Community Behavior in Divergent Bacteria** 1203
L. E. P. Dietrich, T. K. Teal, A. Price-Whelan, D. K. Newman

In addition to an antiseptic function, phenazines—pigmented antibiotics made by bacteria—organize colony structure by activating a superoxidative stress regulator.

STRUCTURAL BIOLOGY

- Solution Structure of the Integral Human Membrane Protein VDAC-1 in Detergent Micelles** 1206
S. Hiller et al.

A channel that allows diffusion of metabolites across the mitochondrial outer membrane forms an unusual 19-stranded β barrel with a pore size of about 25 angstroms.

BIOCHEMISTRY

- A Structural Mechanism for MscS Gating in Lipid Bilayers** 1210
V. Váquez et al.

Electron paramagnetic resonance measurements reveal that tilting of transmembrane helices facilitates the opening of a bacterial mechanosensitive channel in a lipid bilayer.

>> *Perspective p. 1166; Research Article p. 1179*

ECOLOGY

- Pre-Columbian Urbanism, Anthropogenic Landscapes, and the Future of the Amazon** 1214
M. J. Heckenberger et al.

Archaeology and remote sensing of an Amazon basin show that its pre-Columbian inhabitants lived in distributed towns, villages, and hamlets connected by roads. >> *New story p. 1152*

DEVELOPMENTAL BIOLOGY

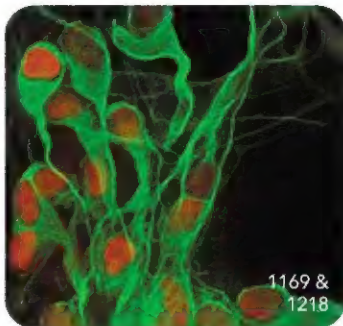
- Induced Pluripotent Stem Cells Generated from Patients with ALS Can Be Differentiated into Motor Neurons** 1218
J. T. Dimas et al.

Skin cells from elderly individuals with a mutation that causes amyotrophic lateral sclerosis (ALS) were used to derive stem cells that could then be differentiated. >> *Perspective p. 1169*

NEUROSCIENCE

- Amyloid- β Dynamics Correlate with Neurological Status in the Injured Human Brain** 1221
D. L. Brady et al.

After brain injury of normal people, the amount of an Alzheimer's disease peptide decreases in the extracellular fluid of the brain, returning to normal with recovery. >> *Science Podcast*



AAAS

ADVANCING SCIENCE, SERVING SOCIETY

Change of address: AAAS is moving, along with its new address and a digital account number. **Partners:** Send change of address to AAAS, P.O. Box 94379, Washington, DC 20090-4379. **Single-copy orders:** \$10.00 current issue, \$15.00 back issue (prepaid includes surface postage); bulk rates on request. **Authorizations to photocopy:** material for internal or personal use, or the internal or personal use of specific clients, is authorized by AAAS to libraries and other users registered with the Copyright Clearance Center (CCC) Transactional Reporting Service, provided that the base fee of \$12.00 per article is paid directly to CCC, 222 Rosewood Drive, Danvers, MA 01923. The authorization code for users is 0895-8625/2009 \$12.00. **Science:** AAAS is pleased to provide this service to its members. **Science:** AAAS is pleased to provide this service to its members.



Printed on
30% post-consumer
recycled paper.

CONTENTS continued >>



Foul wind.

SCIENCENOW

www.sciencenow.org

HIGHLIGHTS FROM OUR DAILY NEWS COVERAGE

Bats: Gone With the Wind

How are wind turbines killing thousands of bats? It's not the blades.

How to Disown a Body Part

Rubber-hand illusion makes people forget about a real appendage.

Did Rumbling Give Rise to Rome?

Ancient civilizations preferred to settle along the edges of earthquake-prone regions.



The SDB Meeting, Philadelphia.

SCIENCE SIGNALING

www.sciencesignaling.org

THE SIGNAL TRANSDUCTION KNOWLEDGE ENVIRONMENT

FORUM: Open Forum on Cell Signaling

A. M. VanHook

Read highlights from the 67th Annual Meeting of the Society for Developmental Biology (SDB).

ST NETWORK: Kinase.com

Kinase.com explores the functions, evolution, and diversity of protein kinases; in Protein Databases.

PRIMARY RESEARCH

Watch out for the publication of the first primary research articles in the next issue of *Science Signaling*.



Veterans studying combat-related brain injuries.

SCIENCE CAREERS

www.sciencereers.org/career_development

FREE CAREER RESOURCES FOR SCIENTISTS

Making a Scientific Impact

S. Gaidos

A team of military veterans at Harvard is investigating mechanical forces involved in traumatic brain injury.

University of California Postdoc Union Wins Official Recognition

B. Benderly

California's employment board officially confirms unionizing the nation's largest group of postdocs.

After Success Abroad, a Polish Scientist Returns Home

C. Wold

Agnieszka Dobrzyń has reaped the rewards of efforts to keep top young scientists in Poland.

From the Archives: The Postbac—One or Two Years That Make Careers

S. Webb

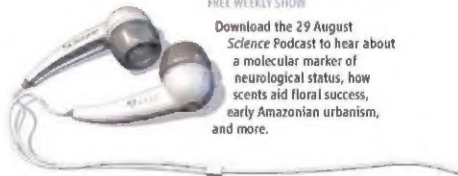
A break from education after the bachelor's degree allows students to gain perspective and learn new skills before starting grad school.

SCIENCE PODCAST

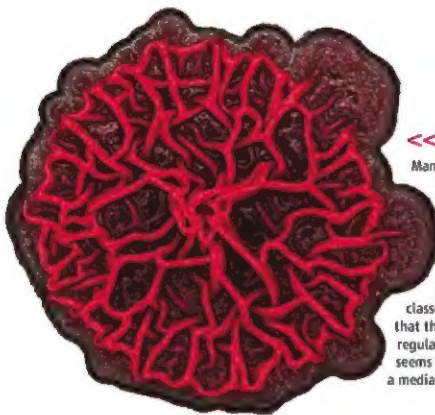
www.sciencemag.org/multimedia/podcast

FREE WEEKLY SHOW

Download the 29 August *Science* Podcast to hear about a molecular marker of neurological status, how scents aid floral success, early Amazonian urbanism, and more.



Separate individual or institutional subscriptions to these products may be required for full-text access.



<< Rainbow Signals

Many microorganisms produce antibiotics that kill other microbes. Indeed, human beings and other organisms have become adept at exploiting these natural products to guard themselves from infection. But it seems these substances are not just disinfectant waste products; there are hints that some have quite specific functions, for example, in facilitating the uptake of metals. Dietrich *et al.* (p. 1203) analyzed the production of antibiotic pigments called phenazines from two classes of bacteria, *Pseudomonas* and actinomycetes, and found that the pigments play important roles as signaling molecules in regulating the structure of the microbial community. This activity seems to be mediated via the SoxR regulon, classically thought to be a mediator of oxidative stress responses.

Polarized Crab Nebula

Pulsar systems containing neutron stars accelerate particles to immense energies, typically one hundred times more than the most powerful accelerators on Earth. It is uncertain exactly how these systems work and where the particles are accelerated. Dean *et al.* (p. 1183; see the Perspective by Celotti) detected polarized gamma-ray emission from the vicinity of the Crab Nebula—one of the most dramatic sights in deep space. The results show polarization with an electric vector aligned with the spin axis of the neutron star, demonstrating that a significant fraction of the high-energy electrons responsible for the polarized photons are produced in a highly ordered jet structure close to the pulsar. These findings provide a powerful diagnostic tool to expose the inner structure of this class of powerful cosmic machines.

Wildfire Past and Present

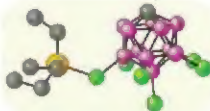
How much oxygen must there be in the air for wildfires to burn? Charcoal, the most ubiquitous proxy for wildfires, is found throughout the geological record, and other direct evidence of the abundance of O_2 is rare. Most of what is understood about the evolution of atmospheric O_2 comes from models, some of which have concluded that the concentration of atmospheric O_2 was as low as 10% during some intervals of the Mesozoic (251 to 65 million years ago). In comparison, the present-day atmosphere contains about 21% O_2 . Belcher *et al.* (p. 1197) present results from laboratory combustion experiments over a range of O_2 concentrations to show that fire is not sustainable in an atmosphere with an O_2 content below 15%.

By combining their findings with a record of paleowildfires in the Mesozoic, they conclude that prolonged intervals of atmospheric oxygen levels between 10% and 12% could not have occurred in the Mesozoic.

A Clean H/F Swap

Many applications of synthetic fluorocarbons rely on their inertness, which stems partly from the high strength of C-F bonds. The flip side, however, is a tenacious resistance to environmental degradation once the compounds join the waste stream—a problem of growing concern in light of their strong atmospheric greenhouse absorptions. Douvris and Ozerov (p. 1188; see the Perspective by Perutz) present an efficient catalytic scheme for hydrotellururation (C-F to C-H bond conversion) based on chlorinated or brominated carborane anions that can robustly stabilize Si- and C-centered cations in solution.

By mixing trialkylsilanes with fluorocarbons in the presence of carborane, they exchange F substituents on C with H substituents on Si, presumably via successive abstractions by silyl and carboranyl cations. Unlike metal-catalyzed defluorinations, this process selectively converts aliphatic sites over aromatic ones.



Electrons Sprung Slowly

In the same way bullets do more damage than arrows, surface chemistry induced by incoming molecules has tended to scale in efficiency with

those molecules' incident velocity. Nahler *et al.* (p. 1191) document a surprising exception to this dictum, in which highly vibrationally excited NO molecules liberate electrons from a sparsely cesium-coated gold surface more effectively when they approach more slowly. A model in which the electron affinity of the NO varies depending on the N-O bond length, with electrons attracted at the outer limit of the stretching cycle and then expelled upon compression can account for the observations. A low translational velocity affords more time for the charge transfer to occur at the requisite separation distance from the surface.

Seamounts and Earthquakes

To what extent does topography across subducting plates control the extent and distribution of

great subduction zone earthquakes, for example, where the earthquakes start and stop, and whether uneven topography increases earthquake size? The largest features likely to influence such earthquakes are typically underwater seamounts, but whether these enhance or suppress large quakes has been uncertain.

Mochizuki *et al.* (p. 1194; see the Perspective by von Huene) examine the Japan Trench, where a series of seamounts have been subducted and there is a long earthquake record. Seismicity is enhanced in front of the seamount but reduced in its wake, implying only weak coupling between the two plates.

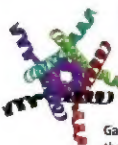
Continued on page 1131

Sweet Scent of Outcrossing

Floral compounds that affect scent and nectar have long been assumed to increase a plant's outcrossing rates by attracting insect pollinators, but experimental evidence for this idea is scarce, and the function of repellents is unknown. **Kessler et al.** (p. 1200, cover; see the Perspective by **Raguso**) studied the genetic basis and evolutionary consequences of pollinator choice in wild tobacco, using a combination of manipulations of secondary products from chemistry, genetics, transgenesis, natural history, and field experiments affecting attractants and repellents. The attractive scent was found to be necessary to bring pollinators to the flower. The plants also used toxins (nicotine) in their nectar in order to enforce modest drinking behavior in their pollinators, allowing for more pollinator visits. Thus, floral compounds play a dual role both to attract and to repel pollinators, and both roles are necessary to optimize a plant's reproductive output.

Ancient Urban Wisdom

Amazonia was more densely populated with indigenous peoples before the arrival of European colonists. Using a combination of remote sensing and archaeological techniques, **Heckenberger et al.** (p. 1214) now show that the pre-Columbian societies of the Upper Xingu river basin in Brazilian Amazonia lived in an urban landscape of distributed towns, villages, and hamlets organized by a road network that connected settlements arranged in a gridlike pattern. The inhabitants created a highly productive and heterogeneous cultural landscape through careful, multigenerational resource creation and management. These arrangements may provide lessons for current attempts at sustainable development in the region.



Channel Opening

The *Escherichia coli* mechanosensitive channel, MscS, opens in response to membrane tension to allow ion efflux, so that bacteria can survive hypo-osmotic shock. Now two papers provide insight into the molecular basis of channel gating (see the Perspective by **Gandhi and Rees**). **Wang et al.** (p. 1179) determined the crystal structure of the MscS channel in an open



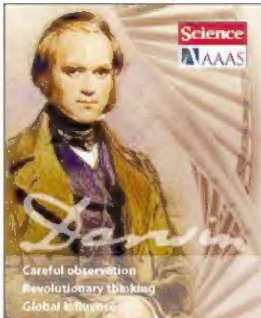
conformation and **Vásquez et al.** (p. 1210) obtained electron paramagnetic resonance measurements on the open conformation in a lipid bilayer. Comparison with a previously determined closed-state structure, combined with functional data or computational analysis, allowed modeling of the movements of the transmembrane helices that cause channel opening.

Stem Cells from ALS Patients

Stem cells hold promise both for replacing damaged cells and for opening up avenues for research into disease processes. These avenues would benefit from cells derived to match a specific patient or to reflect a specific disease. **Dimos et al.** (p. 1218, published online 31 July; see the Perspective by **Brown**) have now derived induced pluripotent cells from skin samples taken from two elderly patients who carry a genetic mutation associated with a familial form of ALS, amyotrophic lateral sclerosis. The induced pluripotent cells, which resemble stem cells in their flexibility, were then enticed in culture to develop into differentiated cells. Of particular interest was derivation of cells that resemble motor neurons, the cell type that is much afflicted as the disease ALS takes its course.

Amyloid- β in Living Human Brain

A great deal of interest has been directed at Alzheimer's disease, and the amyloid- β peptide (A β) has been at the center of much of this attention. Yet, despite over 20 years of study since the discovery that A β is the principal constituent of the hallmark senile plaques, virtually nothing is known about the concentration or regulation of A β in the extracellular space of the human brain, where these plaques form and neurotoxic effects are likely to occur. Now **Brody et al.** (p. 1221) present measurements of the concentrations of A β in the living human brain, and show that A β is dynamically regulated in concert with neurological status. The findings were obtained using intracerebral microdialysis in brain-injured patients and will contribute to future pathophysiological and pharmacodynamic studies of brain injury and Alzheimer's disease.



The Festival

5-10 July

2009

Celebrating the 200th anniversary of Darwin's birth and the 150th anniversary of the publication of *The Origin of Species*

Scientific, arts & humanities programmes
Satellite and fringe programmes
Local, European and global outreach
Tailored sponsorship packages

Speakers and discussants include:

Gillian Beer, Richard Dawkins, Randolph Nesse, Sarah Hrdy, Paul Nurse, Dan Dennett, John Hedley Brooke, Janet Brown, Robert May, Martin Rees, Niles Eldridge, Cynthia Kenyon, Matt Ridley, Steve Jones, Herb Gintis, John Krebs, Ian McEwan and Antonia Byatt.

Visit www.Darwin2009festival.com or contact Programme Director Miranda Gomperts phone: +44 1223 852437 email: mg129@cam.ac.uk



UNIVERSITY OF CAMBRIDGE

Darwin

2009 Anniversary Festival



Jorge E. Allende is vice president for research at the University of Chile, coordinator of the IAP Science Education Program, and a former president of the Chilean Academy of Sciences.

Academies Active in Education

SUSTAINABLE SOCIOECONOMIC AND CULTURAL DEVELOPMENT REQUIRES NATIONS WITH A citizenry that understands science, shares its values, and uses scientific critical thinking. This can best be attained through science education that is based on inquiry, an approach that reproduces in the classroom the learning process of scientists: formulating questions, doing experiments, collecting and comparing data, reaching conclusions, and extrapolating these findings to more general situations. The Program for International Student Assessment, an international organization of industrialized nations, measures the extent to which 15-year-olds can identify scientific issues, explain phenomena scientifically, and use scientific evidence to draw conclusions. The results, made public earlier this year (<http://nces.ed.gov/surveys/ipeds>), reveal that all developing countries and many industrial ones, including the United States, are failing to prepare their children adequately for life in the modern world. Leading scientists of each nation, acting through their national science academies, are working together to change this state of affairs.

In 1985, the U.S. National Academy of Sciences and the Smithsonian Institution established the National Science Resources Center, an organization that has helped to spread inquiry-based science education to nearly 20% of U.S. school districts. About 10 years later, across the Atlantic, the French Academy of Sciences engaged France's Ministry of Education with its "La Main à la Pâte" program, which today extends to most primary schools in France. The Swedish and Australian Academies similarly began major programs in their nations. Then in 2000, the InterAcademy Panel on International Issues (IAP), an organization of science academies from 98 nations, committed itself to mobilizing similar actions by academies on a global scale.

In Chile, supported by the U.S. and French Academies, the Chilean Academy of Sciences and the University of Chile proposed in 2002 to establish a national inquiry-based program called Educación en Ciencias Basada en la Investigación (ECBI). Two years later, the Chilean Academy was asked to lead the IAP's international effort, channeling it through networks of academies, each covering a major geographical region. Thus, in 2005, the IAP helped the Network of African Science Academies launch an African science education program that organized activities in Senegal, Uganda, Kenya, South Africa, Nigeria, and Cameroon. Eighteen science academies of the Asia-Pacific region met in Bangkok in 2007 and approved a regional program with IAP sponsorship. And this October, science academies in Europe will explore establishing an IAP European Regional Program during a European Union conference on science education.

These regional efforts began in the Americas in 2004, where the IAP program was established in partnership with the 16 Academies of the Inter-American Network of Academies of Sciences. This program was recognized as a Hemispheric Initiative by the Americas Science Ministers and currently supports teacher training courses, scientist-educator workshops, and short-term fellowships in 15 countries. Notably, in the past 2 years, it has generated inquiry-based science education projects in Bolivia, Panama, Peru, and Venezuela, with plans to start programs in Costa Rica, Guatemala, and the Dominican Republic.

Our ECBI program in Chile began with six schools and 1000 children in Cerro Navia, a poor municipality near Santiago. The school communities responded beyond all expectations. Attendance went up on the days when there was science class, and parents visited schools to see the children's experiments. The program has now grown to 260 schools with 90,000 children throughout the country, through collaboration among the Ministry of Education, a consortium of 12 universities, and the Chilean Academy. An evaluation supervised by a team of IAP international experts reported enthusiastic results from teachers and students: In the participating schools, children overwhelmingly chose science as their favorite subject. The Chilean Congress has now recommended that ECBI be expanded to all the schools in the country.

The efforts of the world's science academies in promoting inquiry-based science education are relatively new. But these efforts are necessary if we want to instill in future generations a fascination with scientific discovery and a firm understanding and appreciation of scientific endeavors.

—Jorge E. Allende



CELL BIOLOGY

Nuclear Membrane Mechanics

In the fission yeast *Schizosaccharomyces pombe*, the nucleus is tethered to the cytoskeleton by KASH domain-containing proteins in the outer nuclear membrane and SUN domain-containing proteins in the inner nuclear membrane. By exerting force on these SUN-KASH complexes, the cytoskeleton controls the position of the nucleus within the cell. Centromeric DNA inside the nucleus has been observed to cluster near SUN-KASH complexes during interphase, raising the possibility that this association mediates a functional connection to the cytoskeleton. King *et al.* have identified an inner nuclear membrane protein (Ima1) in *S. pombe* that links DNA to SUN-KASH complexes. They show that Ima1 binds to centromeric DNA in vitro and colocalizes with the SUN domain-containing protein Sad1 at the inner nuclear membrane; in Ima1-deficient yeast, colocalization between centromeric DNA and Sad1 was disrupted, and nuclei were frequently deformed and asymmetric. The authors propose that these protein-protein interactions may therefore be required to maintain nuclear shape and integrity in the face of cytoplasmic tensioners and provide a means by which cytoskeletal forces contribute to organizing DNA within the nucleus. —NM*

Cell 134, 427 (2008).

GENETICS

Making a Meristem

Plant development is regulated by meristems, which give rise to all plant organs, including the root, shoot, and flowers. In *Arabidopsis*, the meristem is controlled primarily by a signaling cascade initiated by CLAVATA (CLA) receptors that are activated by CL peptides. Suzuki *et al.* have examined homologs of the *Arabidopsis* CLAVATA3 protein (a CL peptide), which controls meristem development, in rice. They found that two closely related rice genes together appear to reflect



the general function of the single peptide in *Arabidopsis*, suggesting that development of the meristem is evolutionarily conserved despite the approximately 180 million years separating *Arabidopsis* and rice. However, they also find that within rice, the function of the two peptides has diverged, so that they appear to have undergone sub-functionalization. —LMZ

Plant Cell 20, 10.1105/pc.107.057257 (2008).

*Nilah Monnier is a summer intern in Science's editorial department.



CHEMISTRY

Gold for the Shortest Bond?

As the Olympic Games come to a close, it's worth pointing out that chemists, like athletes, enjoy keeping records. What's the shortest bond? The longest? The weakest? The strongest? In the realm of metals, it turns out that chromium (Cr) has a special distinction. It has just enough electrons that when two Cr atoms come together in the gas phase, they can join in a sextuple bond. Unfortunately, making a compound you can handle in solution requires adding ligands, which bring with them extra electrons that lower the bond order to quintuple at most. After realization of a stable quintuply bonded Cr compound, the question shifted to how short the bond could be, and how equitably the five pairs of electrons were really being shared. Tsai *et al.* have now succeeded in pushing the Cr centers a little closer together, creating a Cr₂ anion protected by three bidentate amidinate ligands that x-ray crystallography revealed to have a central bond length of just under 1.74 Å. At nearly the same time, Noor *et al.* prepared a neutral Cr₂ complex, similarly flanked by bidentate nitrogen ligands (in this case, two amidopyridines), with a bond length of just below 1.75 Å. For comparison, the gas-phase sextuple comes in at 1.68 Å. —JSY

Angew. Chem. Int. Ed. 47, 10.1002/anie.200801286; 10.1002/anie.200801160 (2008).

evolutionary radiations. Often, net diversification is rapid early in the history of a clade and declines later on. This "explosive-early" pattern could be produced either by a fall in speciation rates over time or by a rise in extinction rates—alternatives that support distinct ecological explanations for diversification.

Rabolsky and Lovette present an analytical model, based on the birth-death process, in which speciation and extinction rates vary continuously over time. They apply their framework to three published phylogenies (Australian agamid lizards, Australo-Papuan pythons, and North American wood warblers), and they use simulations to fit features of lineage accumulation curves to different modes of declining net diversification. They find

Calibrating robust molecular phylogenies of clades of extant species against time offers a means of characterizing the tempo and mode of

EVOLUTION

Adding Less or Substrating More?

Calibrating robust molecular phylogenies of clades of extant species against time offers a means of characterizing the tempo and mode of

CREATING: (TOP LEFT) BEHNS/ISTOCK; (MIDDLE LEFT) CORBIS; (TOP RIGHT) J. TSU; (BOTTOM RIGHT) J. TSU. BOTTOM: © THE NATIONAL HISTORY MUSEUM, LONDON.

that the explosive-early pattern can be explained only by declining speciation rates and is not observed in scenarios with high ratios of extinction rates to speciation rates. Their results also show that an apparent excess of recently diverged lineages in lineage-through-time plots (typically seen as the result of increasing diversification or high relative extinction rates) can be produced when declining net diversification is driven by increasing speciation rates. —ShJS

Evolution 62, 1866 (2008).

CHEMISTRY

Less Strain, More Force

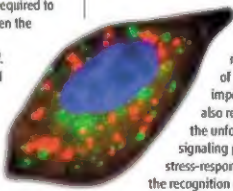
Many studies have probed the force required to pull apart double-stranded DNA. Given the interest in using pore structures to sequence nucleic acids, Ashcroft *et al.* have now measured the force needed to separate hairpins in a self-attracted single strand of DNA as it is pulled through such a pore, in this case a β -cyclodextrin ring. The ring was attached to an atomic force microscope tip and threaded onto a surface-immobilized polyethylene glycol molecule, to which a single strand of DNA that could form a hairpin was then linked at the free end. The force needed to pull the β -cyclodextrin ring through the hairpin was about 40 times greater than that typically needed to pull double-stranded DNA apart directly. The authors note that the transition state for destabilizing the hairpin occurs over a much smaller distance, and so more force must be applied. —PDS

Small 4, 10.1002/smll.200800233 (2008).

VIROLOGY

Hitchhiking in Membrane Traffic

Autophagy is a process whereby cells rid themselves of defunct organelles and proteins by enclosing them in a double-membraned vesicle that then fuses with and is degraded by a lysosome. Autophagy is important in general cellular homeostasis, in development, and in certain aspects of pathology. In complementary papers, Sir *et al.* found that cells infected with the hepatitis C virus (HCV) accumulate autophagosomes but fail to increase autophagic degradation, probably because of a failure in autophagosome-lysosome fusion. The increase in morphologically distinguishable autophagosomes required the expression of genes known to be important in autophagy, but also required the activity of the unfolded protein response signaling pathway, which is a stress-response pathway involved in the recognition of aberrant proteins in



HCV-infected cell: autophagosomes, green; HCV protein, red; nucleus, blue.

the endoplasmic reticulum. Blocking HCV-dependent autophagosome accumulation by blocking autophagy or by blocking the unfolded protein response pathway suppressed virus replication. Thus, it seems that HCV exploits degradation-defective autophagosomes during its replication cycle. —SNH

Hepatology 48, 10.1002/hep.22464 (2008);

Autophagy 4, 830 (2008).

Find.
Decide.
Buy.
Better.
Try the new
Invitrogen.com



Science Signaling



<< Restricted Redundancy

The serine-threonine protein phosphatase PP2A, which participates in signaling cascades induced by TGF- β family ligands, is a heterotrimer composed of catalytic,

structural, and regulatory subunits. The B family of regulatory subunits comprises four members that differ in tissue specificity and subcellular localization but otherwise appear similar enough to be functionally redundant. Batist *et al.* report that B α and B δ have distinct functions in mediating signaling elicited by the ligands TGF- β , Activin, and Nodal. B δ knockdown expanded anterior structures in *Xenopus* embryos, whereas B α knockdown caused loss of anterior structures, suggesting that B α potentiated and B δ inhibited Nodal signaling. In *Xenopus* animal cap assays, B α knockdown blocked Activin-induced axial elongation reduced phosphorylation of the TGF- β family effector Smad2 (pSmad2), and prevented nuclear accumulation of pSmad2. In contrast, B δ knockdown enhanced elongation and increased the amount and nuclear accumulation of pSmad2, suggesting that B α and B δ affected Activin signaling oppositely. Knockdown analyses in keratinocytes and in *Xenopus* animal caps indicated that B α inhibits lysosomal degradation of ALK4 and ALK5—type I receptors that transduce signaling from TGF- β ligands—and that B δ inhibits ALK4 receptor clustering. Thus, both subunits appear to influence the threshold ligand concentration that can elicit signaling, but act on distinct processes to exert their opposing effects. —AMV

Development 135, 2927 (2008).

invitrogen™

www.invitrogen.com

©2008 Invitrogen Corporation. All rights reserved.



What the Iceman Wore

Seventeen years after emerging from an Alpine glacier, the 5300-year-old frozen mummy known as Ötzi the Iceman continues to reveal new secrets. Scientists reported last week that analyses of single hairs show that his clothes were made from the hides of domesticated animals. His coat and leggings were probably sheepskin, and his moccasins were cowhide.

In the past, the garments were thought to have been from goat or deer skins. Geochemist Wolfgang Müller of the Royal Holloway University of London, who has studied the Iceman for years but did not take part in the work, says the new data support the theory that Ötzi took livestock on seasonal migrations to grazing grounds.

Chemist Klaus Hollenmeyer of Saarland University in Saarbrücken, Germany, and colleagues applied a newly developed method called MALDI-TOF mass spectrometry to take peptides from hair proteins and sort them by molecular weight to form a species-specific pattern. The scientists matched the patterns with those in a database of reference species, they report in the journal *Rapid Communications in Mass Spectrometry*.

Ancient-DNA researcher Eske Willerslev of the University of Copenhagen in Denmark says the method "may be important for future work on ancient hair" because it requires far less material than is needed for DNA sequencing, there is less risk of contamination, and proteins are more stable than DNA molecules. DNA, he notes, still offers higher resolution in species identification—such as the geographic origin or sex of the animal.

Scientists on the Job

A new Web exhibit called Evidence, from the Exploratorium in San Francisco, California, aims to give students a realistic look at how science works.

The site provides a case study of how researchers from the Max Planck Institute for Evolutionary Anthropology in Leipzig, Germany, are piecing together human evolution. In more than a dozen video clips, scientists discuss matters such as chimp tool technology and the use of CT scans and computer models to reconstruct incomplete fossils. Interactive features let users follow the procedure for extracting DNA from Neandertal fossils or zoom in on a tooth cross section (above) to learn what scientists can deduce from its microscopic growth lines. Age, disease, and nutrition all leave their marks on teeth.

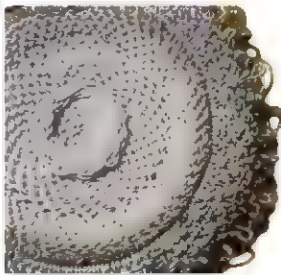
www.exploratorium.edu/evidence



Designing Cell Death

"Suicidal Textiles" is designer Carole Collet's name for her creations inspired by John

Sulston's Nobel Prize-winning research on cell development in the worm *Caenorhabditis elegans*. Collet took apoptosis—cell death that enables development to take place—as the key theme for her furniture that combines natural and synthetic materials. Like *C. elegans*, this knitted ottoman will organically change over time, as natural materials degrade to reveal the final, synthetic form. It's part of the Nobel Textiles project, a collaboration among five Nobel laureates and five professional designers on display from 14 to 22 September at the Institute of Contemporary Arts in London.

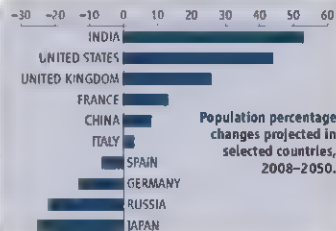


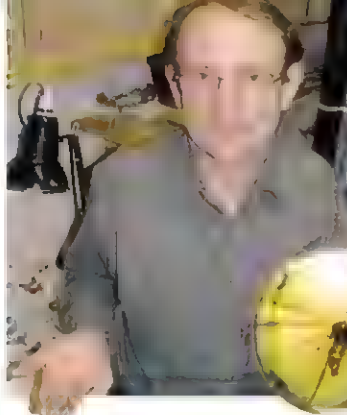
Close-up of Collet's pouf.

THE POPULATION GAP

While all other developed nations have sharply reduced population growth, patterns in the United States appear to be taking after those of the world's poor countries, according to the Population Reference Bureau (PRB). At its annual briefing last week in Washington, D.C., officials reported that the U.S. Census Bureau this month revised its population projection from 420 million to 439 million in 2050. A record 4.3 million births were registered in 2007.

PRB says efforts to reduce birthrates have stalled in many of the world's poorest countries, including most of sub-Saharan Africa. But there's a lag in public perception of the problem, which is still shaped by lowered population projections in the 1980s, said demographer Carl Haub of PRB. "Now you will absolutely see raised projections," he said.





In the Field

A BARGAIN. Instead of digging in the dirt, British entomologist Richard Harrington has found a new species of aphid for \$37 on eBay. The amber-encased specimen, estimated to be between 35 million and 50 million years old, is believed to be from the amber-rich region around Kaliningrad, a Russian city on the Baltic Sea.

Harrington, who studies the agricultural pests at Rothamsted Research Institute in Hertfordshire outside London, wanted to name it *Mindarus ebayi*. But Danish paleo aphid expert Ole Heie, who identified it as a new species, decided to name it after Harrington.

The aphid is now at the Natural History Museum in London, and Harrington says "I'll certainly keep my eyes open" for other opportunities on eBay.

MOVERS

TO INNOVATE. Psychiatrist Hussein Manji, an expert on bipolar disorder, is quitting the U.S.



National Institute of Mental Health (NIMH) for a high-flying position at Johnson & Johnson. He'll be based in New Brunswick, New Jersey, overseeing drug development for both neurological and psychiatric disorders as global

vice president for central nervous system and pain disorders.

Manji, 49, has been at NIMH for the past 15 years, leading the Mood and Anxiety Disorders Research Program, the largest program of its kind in the world. The decision to leave was "very, very difficult," he says. "I still think that the NIH [National Institutes of Health] is the best place in the world to do 'pure research.'"

But, says Manji, "I really believe that the time is right to develop truly innovative treatments" for devastating diseases such as schizophrenia, and he thinks a company is the best setting for that. Johnson & Johnson, he says, "assured me about their commitment to innovative treatments and not 'me too' drugs."

Basically, they share my views that focusing on signs and symptoms isn't good enough."

IN THE COURTS

STAY MUM. Three undergraduates at the Massachusetts Institute of Technology (MIT) in Cambridge have learned firsthand about the potential legal pitfalls of doing computer security research.

As part of a class project, Zack Anderson, Alessandro Chiesa, and R. J. Ryan discovered

flaws in the fare-collection system of the Massachusetts Bay Transportation Authority (MBTA). The students had to cancel a planned presentation this month at the DefCon hackers conference in Las Vegas, Nevada, after a federal district judge granted the MBTA's request for a temporary restraining order. Last week, another judge in the same court ended the restraint, in effect allowing the students to discuss the work.

But the students no longer plan to present the paper anywhere. Both sides say they hope to meet to discuss the security flaws. "So much time and effort has been spent on this whole legal battle... when really the MBTA should have been focusing its effort on fixing the system," Anderson says.

IN PRINT

AN UNLIKELY COLLABORATION. In 2006, Finnish science journalist Jani Kaaro was following a story about an established link between migraines and holes in the heart. A clinical trial in which doctors closed the holes to try to ease migraines had just failed. Even after he was done covering the work for a Helsinki newspaper, Kaaro remained obsessed with the topic.

Switching from journalist to researcher mode, he scoured the literature and developed a theory: The migraines were driven not

by the heart defect but by a brain abnormality sharing the same embryonic origin as the hole in the heart. For help testing it, Kaaro, who never completed high school, reached out to migraine researcher Nouchine Hadjikhani of Harvard Medical School and the Swiss Federal Institute of Technology. At first, she says, "I was very skeptical. Who is this person, and what are they talking about?"

But Hadjikhani was impressed by Kaaro's meticulously documented references and rationale.

Examining brain scans from 39 migraine patients and 26 controls, she found that the pineal gland, a structure that normally sits along the midline of the brain, tended to be skewed to one side or the other in those with migraines—as Kaaro had predicted. The finding, which could provide a new handle on migraines, was published this week in *NeuroReport*, with Kaaro as first author. "It's as good an idea as any," says neurologist Stewart Tepper of the Cleveland Clinic in Ohio, who thinks the theory is worth exploring.



Get a tip for this page? E-mail jeff.e@aaas.org

Two Cultures >>

This cartoon, by California-based animator Brian Narelle, is one of 12 cartoons on the politicization of science that grace a new calendar from the Union of Concerned Scientists (UCS). The works were chosen from among hundreds submitted for UCS's annual scientific integrity cartoon contest. To see all the cartoons, visit www.ucsusa.org.



POLAR SCIENCE

NSF Budget Ills Send Big Chill Through Antarctic Program

Terrie Williams was prepared for the -40°C temperatures, 16-hour workdays, and treacherous crevasses that come with studying how seals forage at night during the unforgiving Antarctic winter. But the University of California, Santa Cruz, physiologist and her eight-member team are helpless against two other impediments to science—soaring fuel prices and flat budgets—that are forcing the U.S. National Science Foundation (NSF) to cut by half their planned 6-week stint on the ice. The reduction will drastically reduce the number of seals they can tag this fall and the amount of information collected before the Antarctic spring brings longer days.

The seal project is one of dozens of research studies, along with several construction projects, that NSF program managers have been forced to shorten or defer because of a 1-year, 67% jump in the cost of fuel needed to operate on the frozen continent. That \$19 million bite out of the program's \$228 million logistics budget follows on the heels of a 44% increase in fuel costs last year that NSF had to eat despite a \$5 million budget cut. Making matters worse, NSF's request for double-digit increases for logistics and for its \$60 million Antarctic science programs is bogged down in Congress as part of an impasse on the entire 2009 federal budget that likely won't be resolved until after the next president takes office in January.

That's too late for a cycle of science that begins in October and runs until the end of the austral summer in March. "Everybody who's doing science in Antarctica has been on a roller-coaster ride," says Robin Bell, a geophysicist at Lamont-Doherty Earth

Observatory in Palisades, New York, and chair of the U.S. National Academies' Polar Research Board. NSF's fiscal problems are compounded by the agency's commitment to dozens of multinational projects taking place during the current International Polar Year (IPY) that runs from 2007 to 2009 (*Science*, 16 March 2007, p. 1513). Bell is also lead scientist on one of these projects, imaging an ice-covered mountain range in



Net loss. Budget cuts have delayed a planned expansion this year of a geophysics monitoring network being installed in West Antarctica.

central Antarctica, for which NSF has reluctantly scaled back support. "If ever there would have been a time you want to invest in [Antarctica], this would be the time," says Williams.

NSF's Office of Polar Programs equips and supports a small army of ships, planes, and scientists that from October to February comprises the world's largest research program on the southern continent. To prepare for the next year, a tanker delivers roughly 150,000 barrels of fuel for planes and ground operations each January to storage facilities at McMurdo Station, the largest of the three U.S. stations and the main staging

area for Antarctic researchers. NSF's current woes began in June, when the Pentagon told NSF that the next shipment would cost \$30 million—a \$12 million increase for 13% less fuel. (In addition, fuel costs for NSF-funded Antarctic cruises are expected to rise by \$7 million.)

To cope with the hit, NSF decided to cut by 20% the number of flights of the gargantuan C-17 cargo jets, which haul personnel and equipment between Christchurch, New Zealand, and McMurdo. That reduction will limit service to the beginning and end of the season. Medium-sized LC-130s, which usually provide scientists trips beyond McMurdo, will try to fill in. But NSF has also had to shrink the size of the fleet serving

Antarctica, from eight to five planes. Together, the changes translate into a reduction from 411 to 305 in the number of planned missions on the continent this season.

Of the roughly 150 research projects scheduled for the 2008–09 season, NSF expects about 25 to be affected by the reductions. For example, last year scientists with PoleNet, an international geophysics collaboration, installed 19 remote stations featuring GPS sensors and seismometers throughout the interior of the continent and around McMurdo. But they'll have to wait another year to add 11 more stations along the coast of the West Antarctic Ice Sheet. PoleNet head and geologist Terry Wilson of Ohio State University in Columbus worries about what might happen if NSF's funding picture doesn't brighten next year. "We don't want to miss the signal of the change [in ice]," she says, noting that satellite data suggest that ice sheet is shrinking along the coast of the Southern Ocean.

NSF and its international partners have tried to protect IPY projects as best they can, including an eight-nation effort to image the Gamburtsev Mountains, whose more than 3000-meter-high peaks are frozen beneath eastern Antarctica. Even so, the reduced number of LC-130 flights, which deliver

fuel and other supplies, will mean 25% fewer passes over the region with lasers, radars, and other instruments. And that's the best-case scenario. As part of its belittling, NSF has also removed so-called buffer days to account for bad weather, sickness, or mechanical delays. That step puts every project's scientific payoff in jeopardy.

"A couple big blizzards" is all it would take to foil her seal study, notes Williams.

Still, that's better than the fate dealt dozens of other projects. Lamont geochemist Taro Takahashi, for example, was slated to measure profiles of CO₂ concentrations through the Drake Passage next month on NSF's Nathaniel B. Palmer research vessel,

but NSF deferred the cruise for 1 year. It will mean a break in a 4-year trend line, but Takahashi is trying to put a good face on the news. "[In] tough times," he says, "we have to be flexible." Scientists with good ideas are also out in the cold, with proposal success rates plunging this year from 27% to 19%.

—ELI KINTISCH

CELL BIOLOGY

Biologists Change One Cell Type Directly Into Another

Researchers at Harvard University report that they have found a way to reprogram pancreatic cells in live mice, turning them into the insulin-producing cells that are damaged or destroyed in diabetes. They say their procedure opens the door to "direct reprogramming", inducing adult cells to jump from one lineage to another.

The feat brings scientists closer to the goal of cell therapy for diabetes, say Douglas Melton and colleagues at the Harvard Stem Cell Institute and Children's Hospital Boston. It shows that, with the right recipe, scientists can turn one kind of cell into another without first reverse engineering the cells to turn them into pluripotent stemlike cells. The team reported the development in a paper published online by *Nature* this week.

Finding a way to generate pancreatic beta cells to treat diabetes has been an urgent goal since research with embryonic stem cells began to explode a decade ago. Melton says researchers have been pursuing two different approaches. One is to grow existing beta cells in the lab; a second is to coax populations of pluripotent cells—such as embryonic stem cells or the newly developed induced pluripotent cells (iPS)—to differentiate into beta cells. No one has yet come up with an efficient way to make either approach work, Melton says.

So Melton and his colleagues have been trying a third way: direct reprogramming. For the past 2 years, they've been sifting through more than 1000 transcription factors—proteins that tell cells which genes to turn on or off—to find which ones are needed to turn pancreatic exocrine cells, the most common cell type in the pancreas, into insulin-producing beta cells. The team, led by postdoctoral fellow Qiao Zhou, eventually narrowed the search to nine candidate genes, which they

tried injecting into mice in various combinations, using an adenovirus to ferry the genes into the pancreas. In the end, they found that just three genes, known as *Ngn3*, *Pdx1*, and *Mafk*, were needed to turn exocrine cells in the pancreases of living mice into beta cells. These three factors are also involved in the embryonic development of both exocrine and endocrine pancreatic cells.

Within 10 days after being injected into mice, about 20% of the cells that had taken up the gene combination were looking like beta cells, although they were outside the islets that normally contain beta cells. The new cells also behaved like beta cells, producing insulin and synthesizing a factor that promotes blood vessel growth. When injected into mice whose pancreatic islets had been chemically destroyed, the new cells led to "significant" lowering of blood sugar levels, although not enough cells were transformed to cure diabetes. The new beta cells are "fully differenti-

ated ... and very stable for many months," says Melton. Once the transcription factors had turned on the necessary genes, they stayed on. What's more, Melton says that his group used a safe, "nonintegrating" adenovirus to introduce the genes into the pancreatic cells; in contrast, reprogramming adult cells into iPS cells requires a retrovirus, which raises potential problems.

The work has implications for diseases beyond diabetes, says geneticist Kenneth Zaret of the Fox Chase Cancer Center in Philadelphia, Pennsylvania, who notes that "one of the most interesting aspects of the study" is that it casts light on factors "that not only activate a new cellular program but also repress an existing one." The scientists say the technique may point the way to a "general strategy" for reprogramming one adult cell type into another, which might be used in diseases in which a single cell type is affected.

Stem cell researcher Ronald McKay of the National Institute of Neurological Disorders and Stroke in Bethesda, Maryland, says that although the new work offers an alternative to directed differentiation of pluripotent cells, "it seems likely that both approaches will have scientific and clinical value." Scientists at Harvard were exuberant about the Melton work. It will "revolutionize what is already a revolutionary field," said stem cell researcher George Daley in a press release.

Now that they have shown that mouse cells can be reprogrammed in vivo, Melton's team is trying to reprogram human pancreatic and liver cells in vitro. Liver cells, Melton explains, may be the best target for human diabetes therapy. They are easier to obtain for research than pancreas cells, and liver injections are safer than those in the pancreas, which may cause pancreatitis.

—CONSTANCE HOLDEN





SCIENTIFIC MISCONDUCT

Fraud Charges Cast Doubt on Claims of DNA Damage From Cell Phone Fields

The only two peer-reviewed scientific papers showing that electromagnetic fields (EMFs) from cell phones can cause DNA breakage are at the center of a misconduct controversy at the Medical University of Vienna (MUV). Critics had argued that the data looked too good to be real, and in May a university investigation agreed, concluding that data in both studies had been fabricated and that the papers should be retracted.

The technician who worked on the studies has resigned, and the senior author on

both papers initially agreed with the rector of the university to retract them. But since then, the case has become murkier as the senior author has changed his mind, saying that the technician denies wrongdoing. He will now agree to retract only one paper, and he also says his critics have been funded by the cell phone industry, which has an obvious interest in discrediting any evidence of harm from its products.

The contested studies, which exposed cells to EMFs equivalent to those from the most common American and European cell

Broken connection. A university investigation found that data in two papers reporting DNA breakage in cells exposed to electromagnetic fields were fabricated.

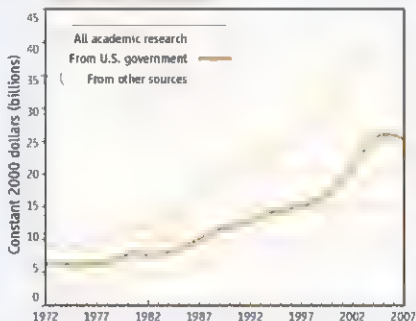
phones, have been widely cited by advocates of tighter regulations on cell phones. Both studies are from the lab of Hugo Rüdiger, who retired this past October after serving as director of the department of occupational medicine at MUV. Other teams have reported only cellular effects of EMFs that are more subtle than DNA breakage, such as changes in gene activation or expression. "If this work isn't solid, then one really has to give up the hypothesis that these fields cause genotoxic effects," says Anna Wobus, a developmental biologist at the Leibniz Institute of Plant Genetics and Crop Plant Research in Gatersleben, Germany, who has studied the effects of EMFs on stem cells.

The first paper, published in 2005 in *Mutation Research*, was part of a €3.2 million European Union-funded project called REFLEX, designed to investigate the cellular effects of various EMF sources. The paper soon came under strong outside criticism. Leading the way has been Alexander Lerchl, a professor of biology at Jacobs University Bremen in Germany and a member of Germany's national Radiation Protection Board. Lerchl, who has received funding from an umbrella organization that investigates EMFs, which is funded in part by multiple cell phone operators and manufacturers, says he originally noticed something strange about the numbers in a table from the 2005 report. The variation is too low, he says. "They could not be data from biological experiments." ▶

RESEARCH DOWNTURN

Sometimes there is a wolf. Federal support for academic research, in real terms, has dropped for 2 years running, according to the U.S. National Science Foundation (NSF). It's the first time that has happened in NSF's 35-year record-keeping history, according to a new report from its Science Resources Statistics division (NSF 08-320). The 1.6% decline (after inflation) in 2007, which followed a 0.2% drop in 2006, reinforces the message repeated in a flood of recent reports that the U.S. government should invest more in basic research.

The National Institutes of Health provided 56% of the \$30.4 billion that the U.S. government spent in 2007, with NSF a distant second at 11%. Johns Hopkins University remains atop the pack of recipients, with its \$1.5 billion nearly double the amount going to second-ranked University of California, San Francisco. Duke University has made the fastest ascent up the ladder, from 14th in 2004 to seventh in 2007, and biomedical engineering is the fastest growing discipline, with an average annual increase of 15% since 2000. Spending by nonfederal sources rose by 5% last year, to \$19 billion, with institutional funds making up half the total.



CREDITS: TOP TO BOTTOM: MICROBIOLOGICAL; NSF/NSF, 2008

Last year, Lerchl conveyed his concerns to editors at *Mutation Research* and to MUV officials. In November, the editors responded saying that their experts on the technique and biostatisticians found Lerchl's calculations "suggestive" but that they "do not prove anything as serious as data falsification." Given that the experimental setup was blinded, they said, it would have



Lab chief. Hugo Rüdiger is retracting one paper because the blinding may have been compromised, but he says data in the other were not tainted.

been impossible to make up data that produced a desired result.

At MUV, a newly established ethics commission eventually decided to look into the matter in early 2008. Their full report has not been made public, but on 23 May, the university issued a press release saying that an independent review body "suggests that the suspicions were justified: The data were not measured experimentally but fabricated." In the press release, the university rector, Wolfgang Schütz, called for the 2005 paper and a 2008 paper by Rüdiger's group to be retracted.

Meanwhile, in April, unaware of the university's investigations, Christian Wolf, the interim head of Rüdiger's former department, was taking an independent look at the data after hearing they were under dispute. Wolf told *Science* that he and a colleague examined the lab notebook of technician Elisabeth Kratochvil, first author of the 2005 paper and a co-author of the 2008 study. Wolf says that they noticed a column of numbers corresponding to a code from the instrument designed to

expose cell lines to EMFs. The code revealed which chamber was exposed to EMFs and which was the control. Rüdiger's team was supposed to receive the key only after sending their observational data to the device's manufacturer in Zürich, but Wolf found that the code could be observed by the turn of a knob to an "unused" channel. After being confronted with the notebook, Wolf says, Kratochvil resigned. Later, Wolf says, they found code entries in laboratory notebooks going back to the fall of 2005.

Rüdiger says he initially agreed to withdraw both papers based on the ethics committee's findings. But several days later, he discovered that the chair of the ethics committee was a lawyer who had worked for a telecom company. He also says that Kratochvil denies any wrongdoing. She quit, he told *Science*, to focus on finishing an MBA. (Kratochvil did not respond to requests from *Science* for comment.)

In June, the university established a second commission, this time with a substitute chairperson. After discussion with that body, Rüdiger says, he agreed to retract the 2008 paper, published in the *International Archives of Occupational and Environmental Health*, because he could no longer guarantee that the blinding had been airtight. In return, he says, the committee members agreed that the case would be closed. The 2005 paper is not tainted, he says. That work was done in 2003, before his lab had its own exposure device. Kratochvil spent several weeks in a laboratory in Berlin collecting data for that study, and he says there is no evidence that she knew that device's code.

Franz Adlkofer, director of the Foundation for Behaviour and Environment in Munich and a co-author of both papers, has not agreed to the retraction, however. He says that the university declined to send him the ethics commission report, asking him instead to travel to Vienna to see it. Until he does, he says, he sees no reason to doubt Kratochvil, whom he calls an "uncommonly talented and intelligent" technician. Also not satisfied, Lerchl continues to push his case, saying he has additional evidence that data were fabricated, which he has sent to MUV. He has called on the MUV University Council, the university's highest governing body, to undertake a new investigation into all eight papers on which Kratochvil was an author. Lerchl says the chair has promised to bring up the matter when the council meets on 8 September. And an editor at *Mutation Research* told *Science* that there is an ongoing investigation into the 2005 paper.

—GRETCHEN VOGEL

Anti-Extremist Bill Progresses

California state legislators are aiming to complete work next week on a bill to protect researchers and their families from animal-rights extremists. The legislation would make it a misdemeanor to publish personal information about academic researchers and their immediate family members that is likely to incite acts or threats of violence against them or to trespass on a researcher's property in order to interfere with his or her work. "This legislation is an important step toward preventing increasingly threatening and destructive tactics employed by extreme animal-rights activists," said University of California (UC) President Mark Yudof in a 6 August letter to the head of the Senate Public Safety Committee.

This month, the home of one UC Santa Cruz researcher and the car of another were firebombed, the latest in a recent string of incidents (*Science*, 8 August, p. 755). The American Civil Liberties Union dropped its opposition to the bill after lawmakers narrowed the definition of actions subject to prosecution. If the bill does not pass this week, when the legislature's term ends, lawmakers will try to pass the bill in December, when the new term opens.

—GREG MILLER

Whales to Receive Protection

The U.S. government has taken a step toward protecting North Atlantic right whales from ship collisions, a major cause of death for the endangered species. In 2006, the National Oceanic and Atmospheric Administration's (NOAA's) National Marine Fisheries Service proposed reducing ship speeds in important whale habitat over the objections of shipping trade groups. Last week, NOAA released its final Environmental Impact Statement on the regulations.

NOAA favors a 10-knot speed limit for ships plying feeding grounds off the northeastern United States and in calving areas farther south. But the traffic-calming zone would now begin 37 kilometers from major ports rather than 56 kilometers as under the earlier draft rule. NOAA plans to issue the rule "expeditiously" after the public comment period closes on 29 September. Although environmentalists wanted tougher rules, whale researcher William McLellan of the University of North Carolina, Wilmington, calls moving forward with regulation "a hugely positive step."

—ERIK STOKSTAD



CANCER RESEARCH

Can Fasting Blunt Chemotherapy's Debilitating Side Effects?

Asking a cancer patient to fast while undergoing chemotherapy may seem like adding insult to injury. But a dramatic experiment in mice has led some researchers to suggest that fasting may blunt the side effects of cancer treatment and perhaps even allow patients to tolerate higher drug doses. The idea is considered radical, even worrying, to some oncologists—especially because patients have already begun trying it on their own. Now, a clinical trial, in which patients undergoing chemotherapy for bladder and lung cancer will fast for as long as 3 days with only water to drink, is slated to begin in the next 2 months.

The strategy is the brainchild of Valter Longo, a gerontology researcher at the University of Southern California (USC) in Los Angeles who has long studied how calorie restriction extends life span in various species. Although the precise mechanism isn't clear,

it's widely believed that cutting calories slows the growth rate of cells and makes them more stress-resistant, protecting them from the cumulative damage of aging.

Longo wondered whether this effect might help protect healthy cells from chemotherapy, which kills rapidly dividing cells, whether normal or cancerous. In yeast, he found, most cells, as expected, became more stress-resistant when nutrients were dialed down. But yeast cells expressing genes similar to the oncogenes that help drive cancer did not react to calorie restriction; they kept on growing and dividing. Longo reasoned that in cancer cells "it's the oncogenes that regulate the stress resistance," and "those are always on," causing the cells to produce growth factors unaffected by calorie restriction.

Longo, along with cancer biologist Lazzara Raffaghello of the Gaslini Children's Hospital

in Genoa, Italy, USC graduate student Changan Lee, and their colleagues, tested this strategy in mice. Recognizing that cancer patients could not endure long-term calorie restriction, they tried a briefer but more extreme version, total fasting. Mice starved for 48 to 60 hours and then given high doses of a chemotherapy drug showed no visible signs of toxicity, yet many control animals died from the treatment. When the animals were injected with a neuroblastoma cell line, which mimics an aggressive pediatric cancer, the fasting combined with chemotherapy didn't

appear to blunt the treatment's effects on the cancer, suggesting that healthy cells were protected from chemotherapy by fasting but cancer cells were not.

To Rafael de Cabo, a researcher who studies aging at the National Institute on Aging branch in Baltimore, Maryland, the findings make sense. It's a hallmark of calorie restriction that animals "are much more resistant to any type of toxin," he says.

Longo's only publication so far on the subject appeared in late March in the *Proceedings of the National Academy of Sciences*, but "a lot of people are already doing it" on their own, he says. "Even though we were very clear, 'Don't try this at home,' I get an e-mail every day" from individuals interested in doing so.

One enthusiast is Thomas Cravy, a 66-year-old retired ophthalmologist in Santa Maria, California, who is battling metastatic prostate

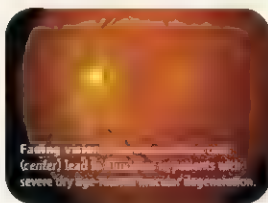
GENETICS

First Gene for Severe Dry Macular Degeneration

The past few years have been a bonanza for researchers hunting for genes that cause age-related macular degeneration (AMD), the disease that robs tens of millions of elderly people of their vision. Now comes the first report of a genetic variant linked to slightly higher risk for severe "dry" AMD, one of the two advanced forms of the disease. The results could eventually lead to a new treatment for macular degeneration. But the authors also have a second message. They say that their findings suggest a safety risk from using a therapy recently introduced to treat the other, so-called wet, form of AMD.

Some outside researchers, however, are skeptical of the new gene discovery, reported online this week in the *New Eng-*

land Journal of Medicine (NEJM). "It's an amazing result, but the excitement is tempered by the absence of an effect in other cohorts," or patient groups, says ophthalmologist and geneticist Albert Edwards of



Fasting vision (center) led to improved patients with severe dry age-related macular degeneration.

the Mayo Clinic in Rochester, Minnesota.

Advanced AMD involves loss of fine vision after age 60 in the center of the retina, or the macula. Patients with the wet type lose vision because blood vessel growth damages the macula; in the "dry" type, also known as geographic atrophy, light-sensing cells in the retina slowly die. At least three genes that steeply raise the risk of both types have been found by scanning the entire genome for disease markers (*Science*, 20 October 2006, p. 405).

The *NEJM* study, however, used an older approach. The researchers hunted in specifically on genes for Toll-like receptors, proteins that recognize pathogens and signal the immune system to respond.

Probing the DNA of 825 Utah patients with AMD and about 360 healthy controls, a multi-institution team led by ophthalmologist and geneticist Kang Zhang of the University

cancer Cravy just finished his third round of chemotherapy in 2 months, each combined with fasting. After the first round left him suffering some side effects, Cravy extended the time he fasts after treatment from about 8 hours to 24 hours, to go beyond the half-life of the most toxic drug, he also fasts for about 64 hours before treatment. Cravy now reports

virtually no ill effects from chemotherapy. "On day five [after treatment] was the first time I played golf and walked the whole golf course," he says. He admits that his mental sharpness fades during the 3½ days he fasts. But the approach has made him much more willing to try chemotherapy, which he had long resisted because he so feared its side effects.

The possibility that patients will try fasting before the approach has been properly tested "is exactly my fear," says Leonard Saltz, an oncologist who specializes in colon cancer at Memorial Sloan Kettering Cancer Center in New York City. "I still do fast on Yom Kippur," he says, and those 24 hours without sustenance are a challenge. "Would I be enthusiastic about enrolling my patients in a trial where they're asked not to eat for 2½ days? No."

That, however, is exactly what Longo and

clinical colleagues at USC are gearing up to do. David Quinn, a genitourinary oncologist at USC, is preparing with Longo and others to recruit 12 to 18 bladder and lung cancer patients who will fast for 24, 48, or 72 hours before and just after chemotherapy. They will begin gradually, with 24 hours of fasting, before ramping up. If the fasting appears

safe and potentially effective, the group will recruit another 42 patients, 14 of whom will not fast. Everyone will receive the same chemotherapy regimen. The work is funded by USC and the V Foundation for Cancer Research, an advocacy group that funds many mainstream cancer studies.

Quinn hopes fasting will not only minimize chemotherapy's toxicity but also make cancer cells more susceptible to chemotherapy. Hints of such increased effectiveness appeared in the mouse data, but the clinical trial will be too small to test this hypothesis.

"It's reasonable enough to at least look at it in a small number of patients," says Alan Sandler, an oncologist who treats lung cancer at Vanderbilt University in Nashville, Tennessee. "But it really goes against a lot of the thoughts that people have, that you need to eat to feel better."

—JENNIFER COUZIN

of California, San Diego, identified a single-base glitch in the gene for Toll-like receptor 3 (TLR3) that modestly raises the risk of advanced AMD. They also found this association in two other groups of patients of European descent.

TLR3 recognizes double-stranded RNA from viruses and tells infected cells to die. To explore how this might cause macular degeneration, Zhang's team injected the eyes of mice carrying two copies of the protective variant with double-stranded RNA. Fewer retinal cells died than did cells in mice that lacked the variant. In patients without any protective copies, a viral infection in the eye might push TLR3 into overdrive so that it keeps killing retinal cells, they suggest.

A small molecule that blocks TLR3 might slow the disease in patients with dry AMD, says Zhang. But the news could be bad for an experimental therapy for wet AMD: adding

double-stranded RNA to cells to block a specific gene to prevent the formation of blood vessels. Although this RNA interference therapy may slow wet AMD, it could also spur some patients to develop the dry form. "It's a cautionary note," says Zhang.

That's assuming that the results hold up. Edwards and others published a paper last April that did not find a significant association with the same TLR3 variant in two cohorts with AMD. Geneticist Rando Allikmets of Columbia University also hasn't seen the link in five cohorts he's studying. But geneticist Nicholas Katsanis of Johns Hopkins University in Baltimore, Maryland, a co-author of the *NEJM* study, says one key difference is that their controls had "squeaky-clean retinas" without even a trace of macular degeneration. He hopes other investigators will reanalyze their data using the same strict criteria.

—JOCELYN KAISER

EPA Is Going Down the Drain

The U.S. Environmental Protection Agency (EPA) is taking a closer look at the health or environmental impact of pharmaceuticals and personal care products that get flushed down the toilet. Earlier this month, the agency asked for public comment on its plans to collect data from hospitals and nursing homes. The agency has also asked the U.S. National Academies to run a 2-day workshop in December about possible ways to assess the risk to human health when the drugs get into drinking water. Meanwhile, EPA is revising its procedures to account for the effects of disposed drugs on aquatic life. The potential impact on health of these chemicals "is definitely a big deal," says environmental scientist G. Allen Burton of Wright State University in Dayton, Ohio. "It's gratifying to see EPA moving ahead with this."

—ERIK STOKSTAD

National Medals Awarded

Three physicists, two biologists, a chemist, a computer scientist, and an electrical engineer have received the 2007 National Medal of Science, the U.S. government's highest scientific honor. Most already have a bagful of laurels, including Andrew Viterbi, the father of wireless communications, and molecular biologist Robert Lefkowitz, who in recent years has won the \$1 million Shaw Prize for his work on cell receptors. In previous years, men predominate. Nuclear physicist Fay Ajzenberg-Selove is the only woman, joining Mustafa El-Sayed, Leonard Kleinrock, Bert O'Malley, Charles Slichter, and David Vineland as the other laureates.

The White House last week also named the winners of the 2007 National Medal of Technology and Innovation, including two California-based companies—eBay and Lockheed Martin's Skunk Works—and six individuals.

—YUDHJIT BHATTACHARJEE

Climate Call

A coalition of U.S. organizations that study climate and weather want presidential candidates John McCain and Barack Obama to bolster U.S. climate science efforts once in office. In a 12-page document released last week, the groups advocate more research funding and computing resources for climate change studies, including a strengthened emphasis on the societal impacts of "severe weather and climate change." They back a report issued last year by the National Research Council that called on the government to commit a total of roughly \$7 billion through 2020 for Earth-observing systems.

—ELI KINTISCH

Ancient Earthmovers Of the Amazon

The forested western Amazon was once thought barren of complex human culture. But researchers are now uncovering enigmatic earthworks left by large, organized societies that once lived and farmed here

Alceu Ranzi was a geography student in 1977 when he helped discover half a dozen huge, prehistoric rings carved into the landscape in his home state of Acre in western

Brazil. At the time, he was helping to conduct the first-ever full archaeological survey of Amazonia, which was being opened up for cattle ranches at a speed that was causing

worldwide protests. The earthworks came to light on newly logged land.

The find attracted little attention. The Smithsonian-sponsored National Program of Archaeological Research in the Amazon Basin did not formally announce the rings for 11 years, and even then only in a little-read report. And Ranzi, who went on to become a respected paleontologist, most recently at the Federal University of Acre in Rio Branco, didn't get back to studying the ditches until more than a decade after that. On a flight to Rio Branco in 1999, he spotted

the earthworks again from the air and soon began looking for more. Within a year, he says, "we had found dozens more" of what he calls geoglyphs.

Shaped like circles, diamonds, hexagons, and interlocking rectangles, the geoglyphs are 100 to 350 meters in diameter and outlined by trenches 1 to 7 meters deep. Many are approached by broad earthen avenues, some of them 50 meters wide and up to a kilometer long. The geoglyphs "are as important as the Nazca lines," Ranzi says, referring to the famed, mysterious figures outlined in stone on the Peruvian coast. But even though the Acre geoglyphs had been observed 20 years before, "nobody still knew anything about them."

Today, Ranzi co-leads a research team with Martin Pärssinen of the University of Helsinki and Denise Schaan of the Universidade Federal do Pará in Belém. More than 150 geoglyphs have been identified in Acre and the adjoining states of Amazonas and Rondônia—a figure, Pärssinen believes, that represents "less than 10%" of the total; indeed, on a recent overflight with a *Science* reporter,

Schaan and Ranzi spotted three more. So far, the sole published carbon date suggests that the Acre geoglyphs were constructed relatively recently, in about 1250 C.E. And their purpose remains unclear. Nonetheless, Schaan says, enough is known to be sure that they are "very difficult to fit in with what we thought in the past."

For most of the last century, researchers believed that the western Amazon's harsh conditions, poor soils, and relative lack of protein (in the form of land mammals)

precluded the development of large, sophisticated societies. According to the conventional view, the small native groups that eked out a living in the region were concentrated around the seasonally flooded river valleys, which had better soil, the few exceptions were short-lived extensions of Andean societies. Meanwhile, the upland and headwaters areas—which include nearly all of western Amazonia—had been almost empty of humankind and its works.

Yet during the past 2 decades, archaeologists, geographers, soil scientists, geneticists, and ecologists have accumulated evidence that, as the geoglyphs team puts it, the western Amazon was inhabited "for hundreds of years" by "sizable, regionally organized populations"—in both the valleys and the uplands. The geoglyphs, the most recent and dramatic discovery, seem to extend across an area of about 1000 kilometers (km) from the Brazilian states of Acre and Rondônia in the north to the Bolivian departments of Pando and the Beni in the south (see map, p.1150). Much of this area is also covered by other, older forms of earthworks that seemingly date as far back as 2500 B.C.E.—raised fields, channel-like

Online sciencemag.org

S Hear author Charles C. Mann discuss the earthworks left by the early Amazonians.



Farsighted. Brazilian researchers Denise Schaan and Alceu Ranzi believe fewer than 10% of the region's geoglyphs have been found.





Geoglyphs in the Amazon
Aerial view of a geoglyph in Acre,
Brazil, showing a 250-meter-long structure.

canals, tall settlement mounds, fish weirs, circular pools, and long, raised causeways (Science, 4 February 2000, p. 786), suggesting the presence of several cultures over a long period. And on page 1214 of this issue of Science, a U.S.-Brazilian team proposes that indigenous people in the south-central Amazon, 1400 km from Acre, lived in dense settlements in a form of early urbanism and created ditches and earthen walls that some say resemble the geoglyphs (see sidebar).

Researchers are still puzzling over whether and how these earthworks fit together and what they reveal about the people who created them. But already the implications of these enormous endeavors are clear, says Clark Erickson, a University of Pennsylvania researcher who has been working in the area with Bolivian colleagues since 1995. Far from being trapped by the Amazon's ecological obstacles, he says, these large populations systematically transformed the landscapes around them. One example: Because geoglyphs cannot readily be constructed or even seen in wooded areas, the researchers argue that people must have made them at a time when the region had little tree cover—meaning that in the not-too-distant

past the great forests of the western Amazon may have been considerably smaller.

Not only did the peoples of western Amazon alter their environments, but they also transformed the biota in them. Emerging evidence suggests that this little-known region may have been a place where long-ago farmers first bred some of the world's most important crops. In Erickson's view, western Amazonia serves as a model of how human beings create and maintain productive landscapes from even the most apparently limited environments.

The new findings show that the region was "a cosmopolitan crossroads" between the societies of the eastern Amazon and the Andes, of whom the most famous were the Inka, says Susanna Hecht, a geographer at the University of California, Los Angeles. "You have every language group in lowland South America represented there," she adds. "It was a major cultural center—and it's incredible that this is just coming out."

Counterfeit paradise, or a real one?

Archaeologists once regarded Amazonia as unpromising terrain. Clearing the forests for agriculture risks destroying fragile tropical

soils by exposing them to the tropics' punishing heat and rain, a contention that lay at the heart of Smithsonian archaeologist Betty Meggers's *Amazonia: Man and Culture in a Counterfeit Paradise* (2nd ed., 1996), probably the most influential book written about the area. Meggers reasoned that in consequence, settlements could not long survive with conventional farming; she once suggested that the river basin's ecological constraints limited maximum village size to about 1000 people. In addition, those people would have left little behind, because Amazonia has little stone or metal. As a result, "99% of material culture was perishable," Erickson says. "Cane, chontia [palm wood], bones, baskets, wood—none of it survives these conditions." Except for pottery, "the whole culture, even if it was there for thousands of years, seems to be gone."

"In the Andes, the societies are easy to see," says Sergio Calla, a student at the Universidad Mayor de San Andrés in La Paz who works with Erickson. "There is no forest covering up their traces. Also, they could build in stone, which is rare here. But this region is just as rich culturally. We just have to look harder and smarter."

Looking smarter, in Erickson's view, means going beyond archaeology's traditional focus on the individual site to entire landscapes. "What Amazonian peoples did in constructing/building environments was more visible and permanent at a regional scale than at the site scale," he argues. To study at this scale, archaeologists are adopt-

grassland. These low, interconnected berms change direction, zigzag-style, every 10 to 30 meters. At the angles are funnel-like openings for nets or traps. Built as early as the 13th century, they fell into disuse only in the 18th century. "Think of it as aquaculture," Erickson says. "The weirs allowed people to manage and harvest the catch."

Because the mounds, weirs, and fields required enormous labor to construct and maintain, Erickson believes these societies must have had large populations—"tens or even hundreds of thousands of people." Some early Jesuit accounts back this view.

To move people and goods around, Indians built networks of ruler-straight causeways and canals, some of them as long as 7 km. Puzzlingly, the causeways and canals are common near raised fields but not around settlement mounds. To make sense of the pattern, Erickson and Patrick Brett—a Wall Streeteer taking time off to pursue his academic dreams—are trying to apply the techniques of network analysis to search for key nodes in the networks of connected causeways, canals, mounds, and fields. The hope, he says, is "to stop us from flailing around, trying to figure out which of the thousands of *islas* we should put a trench into." Early analysis, Erickson says, "shows a few key forest islands in control of a vast network of communication and interaction covering 550 square kilometers, as large as many early states."

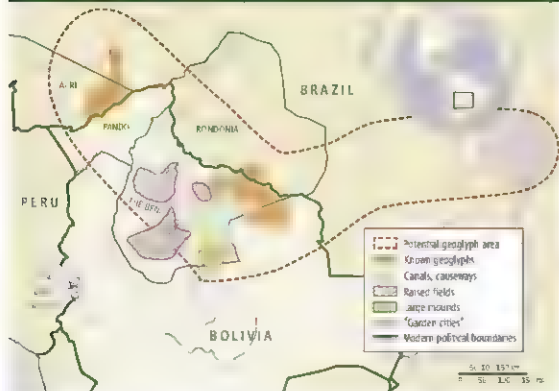
Birthplace of crops

Even as archaeologists try to work out how the area's early inhabitants reshaped their physical environment, botanists are beginning to trace out their impacts in its genetic heritage. "The Amazon is world-famous as a center for biodiversity," says botanist Charles R. Clement of Brazil's National Institute for Amazonian Research in Manaus. "But its role in agricultural biodiversity remains still too little known." In his view, the western Amazon was a center for plant domestication—a "Vavilov center," as botanists call them, after pioneering Soviet botanist Nikolai Vavilov, who invented the concept.

Agricultural geneticists have long accepted that the western Amazon was the development ground for peanuts, Brazilian broad beans (*Canavalia plagiasperma*), and two species of chili pepper (*Capsicum baccatum* and *C. pubescens*; see *Science*, 29 June 2007, p. 1830). But the list is much longer, Hecht says. For example, she would add rubber, made from the sap of *Hevea brasiliensis*. Used for countless purposes by pre-Columbian populations, "it is at least a semi-domesticated, and it was clearly distributed by humans." Also on her list are tobacco, cacao, the tuber *Xanthosoma sagittifolium*, peach palm (*Bactris gasipar*, a major Amazonian crop), and, most important, the worldwide staple *Manihot esculenta*, better known as manioc, cassava, or yuca.

Because the domestications of manioc and peach palm apparently occurred before

CULTIVATED LANDSCAPES OF THE SOUTHWEST AMAZON



Ancient crossroads? Researchers suspect that prehistoric earthworks across the western Amazon may be related

ing new methods, from soil chemistry to network theory.

The Beni in Bolivia, where Erickson's team focuses its efforts, is an example. Exceptionally low and flat, much of the department is covered for up to 4 months of the year by a slowly moving wash of water—snowmelt from the Andes and heavy local rainfall—that is typically 30 to 100 centimeters deep. During the dry season, the water evaporates and the Beni becomes a hot, and savanna, kept open by annual burning. In the low areas, early inhabitants avoided the flood by using natural knolls known as *islas* and by constructing thousands of *lomas* (mounds typically 1 to 5 hectares) as dwelling places. Most *lomas* were small—artificial hummocks barely above the water—but a small percentage were up to 18 meters in height. Some are still inhabited by native groups.

Living on this artificial island archipelago, Amazonian peoples ate a diet heavy in fish, which migrate and spawn in the flooded savannas. Today, as Erickson discovered in 2000, networks of earthen fish weirs still crisscross a 500-square-kilometer area in the

When the waters receded, the area's early inhabitants ensured that they drained into hundreds of artificial fish ponds. Typically about 30 meters across, they are often full of fish today.

Agriculture was just as intensive. In a broad, 50,000-square-kilometer swath of savanna around the mounds, the Beni's indigenous peoples built raised fields—artificial platforms of soil that lift crops above the floodwaters, according to research by geographer William Denevan, a professor emeritus at the University of Wisconsin, Madison, who in 1963 was one of the first to call attention to them. Like raised beds in temperate-zone gardens, the mounds promote drainage and increase the amount of topsoil. From the few carbon dates available, Erickson says, "we see raised fields coming in and out of production from 3000 B.P. to 500 B.P."—or until roughly the time the conquistadors arrived, bringing diseases that wiped out much of the native population. "Like any agricultural fields, these were not used forever. They go in and out of production, which suggests to me a long-term but dynamic system."

the earthworks were built, agriculture may have, as in other cultures, created the surplus necessary for complex societies to emerge. But a "note of caution" is appropriate in such speculations, says anthropologist Peter Stahl of Binghamton University in New York. Although "tending to agree" that the region was a center for domestication, he notes that it's possible that ancestral species still survive in southwestern Amazonia "because it's

out of the way" rather than because domestication happened there.

Strikingly, one of the Amazon's most important agricultural innovations may have originated soon after the breeding of modern manioc and peach palm. Known as *terra preta*, it consists of patches of soil ranging from less than 1 hectare to several hectares that have been modified by adding huge quantities of crumbled charcoal (*Science*, 9 August 2002, p. 920).

An informal Brazil-Germany-US collaboration has been investigating this artificial soil, which maintains its fertility for long periods despite the harsh tropical conditions. Earlier this year, five researchers led by Christoph Steiner of the University of Bayreuth in Germany reported that adding charcoal and soot to weathered Amazonian soils caused a "sharp increase" in microbial activity: Soils damaged by exposure became, so to speak, more alive

The Western Amazon's "Garden Cities"

IN 1902, BRITISH PLANNER EBENEZER HOWARD PUBLISHED *GARDEN CITIES OF TO-MORROW*, which argued that the coming century's cities—metropolises ringed by bedroom communities—should be replaced by more livable, medium-sized "garden cities," linked by railroads and gridded by agricultural green belts. Howard inspired planners in the United Kingdom and Germany, but by the 1970s his views had been forgotten. Now, on page 1234, a U.S.-Brazilian research team led by archaeologist Michael Heckenberger of the University of Florida, Gainesville, reports finding a set of urban settlements startlingly similar to Howard's garden cities—built in the forests of the south-central Amazon as early as 1250 C.E.

The paper identifies dozens of densely packed "towns, villages, and hamlets" covering perhaps 30,000 square kilometers—an area the size of Belgium—in the headwaters of the Xingu River. The settlements, built by indigenous peoples, were tied together by "well-planned road networks" and embedded in a matrix of agricultural land. (By coincidence, the Xingu complexes are also where famed British adventurer Percy Fawcett disappeared in 1925 while searching for a mythical lost city known as "Z.")

The new claims are sure to stir controversy. "Some urbanists may say, 'In your dreams,'" Heckenberger says, laughing. But he argues that the key comparison is not to big centralized cities such as Ur or Athens, "but the other thousand poleis [in ancient Greece] that were not Athens." Like them, he says, the Xingu polities "have sophisticated systems of regional planning, a strongly hierarchical spatial organization, and a basic core-hinterland division within clearly marked territories."

The new work "raises huge and important questions," says Susanna Hecht, an Amazon specialist at the University of California, Los Angeles. It further contradicts the once-dominant view that the Amazonian uplands and headwaters regions were nearly empty. Indeed, the earthworks are similar enough to the geoglyphs to the west in the Beni (see main text), says geographer William Denevan of the University of Wisconsin, Madison, that "they must be related, though we don't know how." Hecht also notes that the Xingu settlements challenge the implicit belief that "current urbanism with its hyperconcentration is a kind of historical norm," when "smaller agglomerations interacting with forest and agriculture" may have been widespread, too.

Since the early 1990s, Heckenberger has focused on the upper Xingu River, much of which is a 2.6-million-hectare reserve set aside for 14 indigenous groups, including

the Kuikuro, who number about 500. Two weeks after Heckenberger arrived, community leader (and co-author of the *Science* paper) Afakaka Kuikuro showed him the ruins of an earthen wall more than a kilometer long. Heckenberger realized that the wall, which was associated with a moatlike ditch 10 or more meters wide, was from before the time of Columbus. Then, he says, "I found out the Kuikuro knew about a lot of these walled settlements, and they weren't small."

Patently converting indigenous knowledge into GPS-verified mapping and archaeological excavation, Heckenberger's team discovered that the present-day Kuikuro forest concealed what had been two regional polities, each about 250 square kilometers, comprised of small villages and towns centered on plazas 120 to 150 meters across. Each polity had a kind of capital with roads radiating out to other villages and towns. "The settlements are packed in the region along the Xingu," Heckenberger says, "one after another, always in this highly regular pattern." Each center has equidistant towns to its north and south, for example, as well as smaller towns east and west, with the two axes being of constant lengths. Similarly, the prehistoric plazas in the towns are regularly patterned, with the primary and secondary leaders' houses facing each other at opposite ends. "All their roads are amazingly straight, too," Heckenberger says. "If there was a wetland, they just built causeways and bridges over it." In his view, this careful layout suggests that the capitals had a ritualistic function.

To Heckenberger, the settlements represent a novel kind of urbanism. As he readily agrees, "No single Xingu settlement merits the term 'city.' But what do you do with a core of five settlements a few kilometers away from each other? A fast walk from one to another would take you 15 minutes, maximum."



Radiocarbon dating suggests that these communities were at their height from the 13th to the 16th centuries, with a regional population greater than 50,000, based on extrapolation from current settlements. Soon after Europeans reached Brazil in 1500, diseases killed two-thirds or more of the native population, and forest quickly grew into cleared areas, colonists later tended to believe that the forest was of great antiquity.

These pre-Columbian urban concentrations may have lessons for today's planners. "Given the complexity of Amazonian biotic and water regimes, a decentralized model may have been more adapted to address very large volumes of water that hang around for a long time," Hecht says. Because tropical areas today are dominated by huge centralized cities, she says, it is striking to note that their original inhabitants chose a different path.

—C.C.M.

Terra preta is believed to have been an essential part of a distinctive agricultural system. According to the *terra preta* team, Indians slowly cleared off the forest to create farm plots and planted annual crops such as manioc and peanut. In the past, researchers argued that as the exposed soil lost its fertility, farmers shifted to other areas in a pattern called "slash and burn." But researchers now suggest that Indians instead took steps to retain soil fertility by creating *terra preta*. According to studies by Wisconsin's Denevan, removing trees with stone axes was so difficult that the logical path for native peoples would not have been to clear additional forest every few years but to replant the enriched fallow earth with tree species useful to humankind—rotating annual and tree crops over time.

The oldest *terra preta* patches yet known, carbon-dated to about 2500 B.C.E., are in

Digging deep

Around and atop many of the Beni forest islands are deep ditches, commonly oval or ring-shaped. Analogs of the geoglyphs found by Ranzi in Acre, they are typically 100 to 200 meters across, though some are as much as 1 km in diameter. Many are surprisingly deep; Erickson and his Bolivian co-investigator, Patricia Alvarez of the Universidad Mayor de San Simón in Cochabamba, discovered one ring originally dug to 10 meters. The region is now overgrown, so the team measures geoglyphs by slowly chopping through trees and vines, during *Science*'s visit, Erickson spent most of an afternoon hacking with a machete through thick forest to identify the track of a single big ditch on a Global Positioning System.

Partly because of the recent tree cover, nobody knows how many of these geoglyphs

cultural landscape of the region probably reflects "a patchwork of different ethnic groups working in different areas" with constant, intense "interethnic communication"—a crowded, jumbled social landscape that Alvarez believes extended for hundreds of kilometers in every direction. The sphere of intense interaction, she believes, may have lasted for centuries.

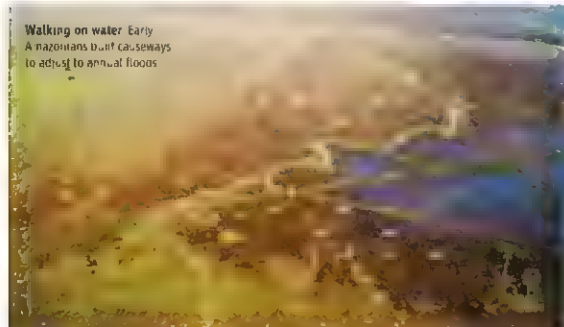
Researchers think it likely that the geoglyphs extend continuously between Acre and the Beni. Pärssinen notes the recent discovery of large geoglyphs near the city of Riberalta, on the northernmost tip of the Beni. But they cannot be sure, because between Riberalta and Rio Branco, in Acre, is about 150 km of the mostly forested department of Pando. "It seems unlikely there is no connection, but any connection is not yet proven," Schaun says.

Nor is it known whether the geoglyphs served any practical function. Most of the Acre geoglyphs are on higher ground, making them of little use for drainage. Many have outer walls that look down on the central area, suggesting that they were not used for defense. To be sure, one of Walker's earthworks was connected to a river "by a deep channel and had a connection to a swamp on the other side," he says. "It could have been used to control water flow off the savanna in the dry season. So at least some of these earthworks could have had a hydraulic function." Many, though, are almost entirely without other traces of human presence, such as ceramics. "The immediate response is that they were symbolic places," says Stahl. "But that's the old archaeological canard: If you can't figure out the function of something, you say it was for ritual."

The late arrival and ubiquity of the geoglyphs may indicate that some type of cultural movement swept over earlier social arrangements. "But whatever was there, these societies have been completely forgotten," says anthropologist Guillermo Rios, director of sustainable development and indigenous peoples for the Pando. "It's only been 400 years since they vanished. Why does nobody here know anything about them? They were living here for such a long time, and nobody knows who they were."

One reason for the lack of attention, in his view, is archaeology's long focus on Andean societies of Peru and Bolivia, with their grand stone ruins. "The idea is that the tribes in the lowlands were living like animals in the wild," Rios says. "When you tell them that there were great, important civilizations here in the western Amazon, they don't believe it. But it's true."

—CHARLES C. MANN



Walking on water Early Acreans built earthenways to adjust to annual floods

Rondônia, not far from the Brazil-Bolivia border, suggesting to Eduardo Goes Neves of the University of São Paulo that these techniques may have been invented there. In surveys this year and last, Neves discovered "*terra preta* almost everywhere we looked." Pärssinen, though, says that the geoglyphs team has not yet found big patches of *terra preta* in Acre. "How these large groups supported themselves there without it is a mystery," he says.

If the rest of the Rondônia *terra preta* is as old as the dated patches, Neves says, "we're looking at a huge jigsaw puzzle" of an ancient culture—or cultures. As he sees it, "in the west and southwest, there's the mounds and canals, there's the development of manioc and peach palm, there's the fish weirs that Clark [Erickson] found—and we don't know how any of it fits together. On top of that, there's the geoglyphs all over the place."

exist. Erickson, for his part, says he "wouldn't be surprised if almost every one of the artificial lomas had them." Perhaps backing this view, anthropologist John Walker of the University of Central Florida in Orlando reports, in a forthcoming paper, the discovery of ditches on savannas and river-edge forests in north-central Bolivia, in an area where they had not previously been reported. "We found ceramics on four forest islands that we examined," he told *Science* in an e-mail from Bolivia, "and each of them also had earthworks that I am willing to call ring ditches"—circular geoglyphs.

The relation of the geoglyphs to the other, often older, earthworks is unclear. "We have one set of people constructing the *canyas* [ring ditches] and another set of people constructing the causeways and canals," Alvarez says. "The question is whether they are the same people." In her view, the variegated

MEETINGBRIEFS>>

PHYSIOLOGICAL SOCIETY MEETING | 14-16 JULY 2008 | CAMBRIDGE, U K



Learning Under Anesthesia

Marcel Proust knew the powerful association between smells and memories. So do exterminators—and researchers studying social learning among rodents. When a rodent gets a whiff of a friend's recent meal, its olfactory bulb—the section of the brain that processes smell—quickly commits the odor to memory as a preferred food using a process known as olfactory learning. “People in the rat-poison industry have known about this for years,” says neuroscientist Alister Nicol of the Babraham Institute in Cambridge, U.K., noting that a poisoned rat will live for a few days and pass along the odor to its comrades, fooling them into eating the poison as well.

At the meeting, Nicol reported that this scent-based social learning occurs even when mice are knocked out by anesthesia. After Nicol fed a mouse coriander-scented food and had it breathe onto the nose of an anesthetized comrade, the unconscious mouse preferred coriander-scented food when it woke up. Nicol then repeated the experiment with the coriander scent paired with carbon disulfide, a compound found naturally in rodent breath. This combination was enough to make the anesthetized mice prefer food with that odor. Without the carbon disulfide, the mice were indifferent to the scented food.

Bennett Galef, a psychologist who studies animal behavior at McMaster University in Hamilton, Canada, finds it interesting that the social learning of food preferences in rodents is not the result of higher level processing. And Nicol says his research could enable closer studies of the neurons that process smells, because anesthetized

mice should experience fewer stimuli that distract from the specific act of olfactory learning. Peter Brennan, a behavioral neuropsychologist at Cambridge University in the U.K., who studies olfaction, agrees. But he cautions that this technique may have drawbacks. “We do have to remember that the anesthetized brain isn't the same as a normal brain,” he says.

Testing a Taste Test For Depression

Jan Melichar believes he has a simple test that could help doctors to better diagnose and treat patients with depression: a taste test. With a simple dab of a flavor on your tongue, the psychiatrist told a Cambridge audience, a physician could determine whether you're clinically depressed and tell you what to take for it if you are. Now, Melichar and physiologist Lucy Donaldson, his University of Bristol colleague, are about to put their taste test to the test.

In 2006, Melichar and Donaldson gave healthy volunteers a tiny dab of faint flavor on the tongue and asked if they could taste it. The sample was so diluted that they couldn't. The researchers then gave the volunteers pills that boosted brain levels of one of two neurotransmitters, serotonin or noradrenaline. To boost serotonin, for example, patients took a Prozac-like drug known as a selective serotonin-reuptake inhibitor. When volunteers got a serotonin jump, they were suddenly able to taste the feeble flavor if it

was bitter or sweet. With noradrenaline boosted, the volunteers were able to taste the dab if it was bitter or sour. Donaldson and Melichar suspected that depressed people had blunted taste buds—the illness is often tied to a lack of either neurotransmitter—and that the right antidepressant would allow depressed people to experience the true vibrancy of flavors.

To test this idea, Melichar and Donaldson had wanted to run a carefully controlled trial with depressed people who were willing to have their flavor sensitivity analyzed—which meant abstaining from antidepressants for a short while. If there was a consistent difference between healthy and depressed people, Melichar says, it could be used as a benchmark in the clinic. Due to difficulty in getting funding for the unusual project, the pair now plan to piggyback onto a clinical trial run by John Potokar, a psychiatrist also at Bristol University. The trial will examine hepatitis C patients as they start a type of drug known as pegylated interferon—a treatment for hepatitis with an unpleasant tendency to induce depression in about 20% to 30% of patients. Thus, Melichar and Donaldson will be able to test these patients' taste levels before, during, and after depression. “I'm hoping we can get some really robust results,” Melichar says.

If those results validate the flavor test, it could become the equivalent of the cholesterol test that persuades someone to take action against heart disease. “The patient has no objective marker” that tells them they're depressed, says Melichar. As a result, he notes, a lot of people end up not taking their medication.

Moreover, given that the researchers have found that serotonin is linked to sweet and noradrenaline is linked to sour, the taste test could be a useful way to determine which drug to use, a big plus because antidepressants can take several weeks or more to have an effect. And with this disease, time is of the essence—if treated within 3 months of becoming depressed, a person has a very good chance of getting better.

Stephen Roper, a physiologist who studies taste mechanisms at the Miller School of Medicine at the University of Miami in Florida, believes Melichar and Donaldson's work is important. “They are among a select few studying taste sensitivity in humans vis-à-vis its relationship to moods,” he says.

—LAUREN CAHOON



PROFILE: ZENG YI

A Controversial Bid to Thwart the 'Cantonese Cancer'

Zeng Yi has spent 3 decades probing a connection between Epstein-Barr virus and nasopharyngeal cancer. A new vaccine should show whether he is on the right track

NANNING, CHINA—In the coming weeks, scientists here plan to launch the first clinical trial of a vaccine that aims to mobilize the immune system to prevent nasopharyngeal cancer (NPC). It is the climax of one researcher's quest to decipher a disease that kills as many as 13,000 Chinese each year—more than 10 times the fatalities in the rest of the world combined.

Zeng Yi, a 78-year-old virologist at the Institute for Viral Disease Control and Prevention of the Chinese Center for Disease Control and Prevention in Beijing, earned fame for revealing a link between Epstein-Barr virus (EBV) infection and NPC. Based on this insight, Zeng initiated screening programs to detect NPC at an early stage. Along the way, he crossed swords with skeptics—and prevailed. Colleagues admire his indefatigable character. "Without Zeng's work, we would not have today's achievements in NPC control and treatment," says Tang Bujian, chair of the Guangxi Society of Cancer Research in Nanning.

Cancer became the number one killer in China in 2005 (see sidebar), and the government has begun paying more attention to prevention, says Qi Guoming, vice-chair of the Chinese Medical Association and a former top health official in charge of epidemic control. That's why, Qi says, the government is ready to back a \$1.2 million trial of a preventative vaccine that builds on Zeng's work. Some experts laud the attempt. "Targeting the one risk factor shared by virtually all patients with NPC—that is, EBV—seems like a reasonable approach," says Ellen

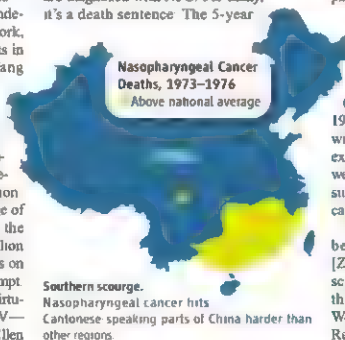
Chang, an epidemiologist at Northern California Cancer Center in Fremont.

Not everyone is convinced. The link between EBV and NPC is too shaky to focus on a vaccine, argues Yao Kaitai, an oncologist at Southern Medical University in Guangzhou. EBV's carcinogenic role, he says, "is not as decisive as the links between hepatitis viruses and liver cancer and between human papilloma virus and cervical cancer."

Zeng disagrees. "Our experiments prove the EBV can induce cancer and that our vaccine is effective."

Early clues

Every year in China, as many as 40,000 people are diagnosed with NPC. For many, it's a death sentence. The 5-year



Indefatigable. Zeng Yi hopes a vaccine trial will validate his theory about how people contract nasopharyngeal cancer.

survival rate is less than 50%. In much of the world, NPC is rare, with less than one case per 100,000 people, on average. But in southern China's Cantonese-speaking Guangdong Province and Guangxi Zhuang Autonomous Region, the incidence is 15 to 25 cases per 100,000. NPC is called the "Cantonese cancer."

Although Zeng is a Guangdong native, he paid scant attention to NPC until 1973, when he came across a report about high levels of immunoglobulin G (IgG) in the serum of an NPC patient. Zeng knew that IgG can be a marker of EBV infection. "My instinct told me that there would be a relationship between EBV infection and NPC," he says.

Zeng started probing which antigens are elevated in NPC patients. He zeroed in on EBV-specific IgA/virus capsid antigen (IgA/VCA), another marker of EBV infection. Levels of IgA/VCA are high in nasopharyngeal epithelial cells of NPC patients, he found, suggesting that antigen levels rise with NPC onset. Although early-stage NPC can be treated effectively with radiation therapy, at the time only 20% to 30% of cases were caught at that stage. Screening for EBV biomarkers, Zeng reasoned, could increase the success rate. But there was a hitch. More than 90% of people worldwide are infected with EBV sometime in their lives. Which ones would develop NPC?

The answer occurred to Zeng after a serendipitous field trip. In 1977, Zeng was invited to Nanning, the capital of Guangxi, to lecture on cancer. Afterward, health officials coaxed Zeng to visit an NPC hot spot: Wuzhou in Guangxi's mountainous southeast. "Cancer patients were sleeping in the streets, waiting for beds in the hospital," says Deng Hong, former director of Wuzhou Oncology Institute. A few months later, Zeng persuaded health practitioners to screen for IgA/VCA levels in the serum of people in Cangwu County, near Wuzhou. In 1977 and 1978, screening 23,711 people turned up 1308 with high biomarker levels, of whom 15, after examination of their nasopharyngeal tissue, were diagnosed with NPC. "The facts strongly suggested that EBV infection is at least one cause of NPC," Zeng says.

But direct proof—and a mechanism—has been elusive. "We highly appreciated [Zeng's] NPC screening, but at the time the scientific community was not fully convinced that EBV really caused NPC," says Hans Wolf, a microbiologist at the University of Regensburg in Germany who thinks EBV is

involved—but not the whole story. Labs failed to infect cultured human nasopharyngeal epithelial cells with EBV.

"The ubiquitous presence of EBV antibodies worldwide was not seen to be specific enough to prove a causal relationship," Wolf says.

Faced with skepticism about his proposed EBV infection-NPC link, Zeng searched for potential environmental triggers of the disease. Intriguingly, he and his colleagues found that 52 herbs in traditional Chinese medicine contain compounds that activate EBV in cell culture. Of these herbs, 45 are planted and used in Guangdong and Guangxi, including *Liugewang* (*Radix Wikstroemiae*), which is widely prescribed for inflammation. Although EBV may be relatively benign in most people, its effects might be altered by such herbs, Zeng argues. Genetic factors could also play a role, as southern Chinese are much more likely to contract NPC than other population groups, even after they move elsewhere.

In 1996, Zeng proposed that EBV infection, abetted by environmental factors, causes NPC in people with genetic susceptibility and frail immune systems. That year, Zeng's lab performed a critical experiment. His group infected human fetal nasopharyngeal tissue, which is vulnerable to viral infection, with EBV. Next, they transplanted the infected tissue into mice and fed them tumor promoters extracted from Guangdong herbs. Three months later, tumors appeared in transplanted fetal tissue that expressed EBV genes and antigens but not in fetal tissue without the tumor promoters.

Despite successes in the lab, NPC screening has faltered. "Doctors were reluctant to spend their time" on a venture from which they couldn't turn a profit, says Deng. In 2006, he moved to a Guangzhou hospital to promote voluntary EBV antibody screening, which costs less than \$1 thanks to an immunoenzyme test Zeng developed. Still, health workers have found it difficult to persuade people to spend a small sum to look for a disease they are unlikely to contract. "We would not give up," Zeng says. "Without identifying antibody-positive people, our tremendous efforts would be in vain."

Taking their best shot

Zeng's new tack is a vaccine. The idea is to prevent the cancer by blocking an EBV gene called *latent membrane protein 2* (*LMP2*) that integrates itself into human DNA and can trigger NPC in susceptible people. Says Zhou Ling, chief scientist of the NPC vaccine project at the Chinese Centers for Disease Control and Prevention. A plasmid encoding the

MORTALITY SURVEY OFFERS MIXED MESSAGE

Determining the mortality rate and causes of death in a vast population is a costly, arduous task that China has undertaken only three times in 60 years. Findings from the latest survey, released last April, show that cancer has become the number one killer in urban China, causing one in four deaths, and it is number two in the countryside after cerebrovascular disease.

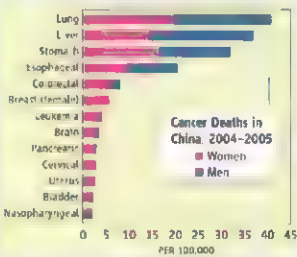
The retrospective study analyzed 1.29 million deaths in 2004–05. Surveys were carried out in 63 urban districts, 97 rural counties, and at 40 cancer registries and 13 locations—dubbed "cancer villages" by Chinese media—with reportedly high cancer rates, says Chen Wanqing of the Cancer Institute and Hospital of the Chinese Academy of Medical Sciences in Beijing.

There is some good news. After a comprehensive survey in the mid-1970s flagged high-incidence areas for cervical, liver, and other cancers attributed largely to infectious agents, screening and prevention programs have reduced mortality rates. For example, age-adjusted deaths from cervical cancer declined from 5.7 per 100,000 in the mid-1970s to 0.94 per 100,000 in the recent survey, an 84% reduction. And nasopharyngeal cancer (see main text) fell 50% to one per 100,000.

On a darker note, lung cancer is the fastest rising killer, with 41.34 deaths per 100,000 men and 19.84 per 100,000 women reported in the latest survey. Overall, age-adjusted lung cancer deaths shot up 261% in 30 years. Alarming, the increase in lung cancer "may even accelerate," as the gap between the peak of smoking prevalence and peak of lung cancer deaths can take a few decades, says epidemiologist Tai Hing Lam of the University of Hong Kong. In mainland China, which has some 350 million smokers, tobacco-control efforts have been halfhearted at best, says Lam. "I am quite disappointed by the low emphasis on tobacco control relative to other measures such as screening," he says.

To fulfill its promise of a "smoke-free Olympics," Beijing from May banned smoking in government offices, sports venues, schools, and hospitals and required restaurants to set up smoking-free sections. But a fine of less than \$150 is a feeble deterrent, and one city alone can't turn the tide. If authorities fail to rein in smoking, warns the World Health Organization, China should brace for a horrific 900,000 lung cancer deaths a year by 2025.

—HAO XIN



Top killers. Cancer deaths per 100,000 for women (pink) and men (blue) in China.

LMP2 gene should elicit a cellular and humoral immune response, which in turn should damp down *LMP2* expression.

The plan is to launch a safety trial in 30 cancer patients by the end of 2008, pending approval from China's State Food and Drug Administration. If the 1-year trial is a success, and if funds are available, the vaccine will be given to 300 volunteers who test positive for the IgA/VCA antibody but don't have cancer at Shantou University Medical School in Guangdong and Guangxi People's Hospital in Nanning.

Some argue that large-scale vaccination against NPC is economically unjustified. "The cost is too high to immunize 100,000 people just to prevent 10 to 20 cancers," says Zhao Ping, director of the Cancer Institute and Hospital of the Chinese Academy of Medical Sciences in Beijing. Others contend that the

science itself is too weak. "Much more work is needed to repeatedly prove the causal link between EBV and NPC," says Yao.

Zeng Yixin, director of the State Key Laboratory of Oncology at Sun Yat-sen University in Guangzhou, says, "A vaccine, no matter for EBV infection or for blocking NPC initiation, has been a dream for many labs in the field, but the evidence for using *LMP2* to induce a strong immune response specific to NPC is not sufficient."

Wolf, for one, is in Zeng's corner. His team planned to test a similar preparation in the late 1990s, but the project was abandoned after funds failed to materialize. A vaccine, Zeng hopes, might someday make NPC just as rare among Cantonese speakers as it is in most other regions of the world.

—JIA HEPENG

Jia Hepeng is a science writer in Beijing. With reporting by Hao Xin.

1160



1163



LETTERS | BOOKS | POLICY FORUM | EDUCATION FORUM | PERSPECTIVES

LETTERS

edited by Jennifer Sills

China's Energy Policy Comes at a Price

IN THE POLICY FORUM "CLIMATE CHANGE—THE CHINESE CHALLENGE" (8 FEBRUARY, P. 730), N. Zeng *et al.* describe the challenges and opportunities inherent in China's efforts to address climate change. However, they do not mention government-set energy prices.

China's energy prices are mainly decided and controlled by the government. Because the government emphasizes social stability (1) over scarcity of resources or environmental cost (2), it sets the energy prices very low. For example, Chinese gasoline and diesel prices rose by less than 10% (3) in 2007, when global oil price nearly doubled. Moreover, in January 2008, the Chinese government decided to freeze energy prices in the near term, even as international crude oil futures have continued to surge (4).

Energy conservation and efficiency are hard to achieve because government-set prices encourage excessive energy consumption and waste (4). The low energy prices send a distorted market signal to consumers that there is no shortage of natural resources, indicating that enhancing energy efficiency is unnecessary and waste is justified. In 2007, sales of cars with large engines (3 to 4 liters) increased by a factor of 4.5 compared to sales in 2006, and SUV sales increased by 50.09%. Meanwhile, sales of more energy-efficient cars with smaller engines (1 liter) dropped by 30.90%, also compared to 2006 sales (5). If China's 1.3 billion citizens each took small measures to conserve energy, they could reduce annual CO₂ emissions by 200 million tons (6). Unfortunately, the government is not helping to motivate people when energy prices are set so low.

The energy prices set by the Chinese government have increased the competitiveness of China's high-energy-consuming and resource-based products, enlarged export surpluses, and exaggerated the pressure on CO₂ emission.

For example, low energy prices have fueled China's shift from a net importer to the largest exporter of steel in a span of only 2 or 3 years (7). Now about 23% of Chinese CO₂ emission is attributed to producing goods exported to other countries (8). The awful truth is that China has not been effective at cutting CO₂ emissions despite the substantial investment in China of the Clean Development Mechanism (9).

A market-oriented energy-pricing mechanism is an inevitable requirement for China to address climate change, although the reform of the energy pricing mechanism means increased energy prices, which will bring public dissatisfaction and possibly social instability.

QIANG WANG

Guangzhou Institute of Geochemistry, Chinese Academy of Sciences, Guangzhou, 510640, China, and Graduate University of Chinese Academy of Sciences, Beijing 100049, China

References

1. J. Vardley, "Fighting inflation, China freezes energy prices," *New York Times*, 9 January 2008. www.nytimes.com/2008/01/09/business/09china.html.
2. Information Office of the State Council of the People's Republic of China, "China's energy conditions and policies," 26 December 2007. Beijing, www.china.org.cn/english/whoreport/energy/237089.htm.
3. Wees report, "Domestic oil products prices increase" (in Chinese), <http://finance.sina.com.cn/focus/yajia/2007/>.
4. J. Liu, J. Diamond, *Nature* **451**, 435 (2005).
5. Y. Feng, "The data of China Association of Automobile Manufacturers show auto production and sales increase by more than 20% in 2007," *Chinese Motor Vehicle News*, 25 January 2008 (in Chinese), available at <http://www.sohu.com/2008/01/25/25n254866778.shtml>.
6. The Ministry of Science and Technology of the People's Republic of China, "Energy saving and emission reduction manual" (in Chinese), www.most.gov.cn/ztzl/gjgonglunwen/gonglunwen/gonglunwen.htm.
7. U. C. V. Haley, "Shedding light on energy subsidies in China: An analysis of China's steel industry from 2000–2007," *Industry seminar: United States International Trade Commission*, 8 January 2008. www.americanmanufacturing.org/wordpress/wp-content/uploads/2008/01/energy-subsidies-in-china-jan-8-08.pdf.
8. T. Wang, J. Watson, "Yndall Centre Briefing Note no. 23" (October 2007), http://myndallwebapp1.usa.ac.uk/publications/briefing_note/2007/23.pdf.
9. H. Wain, *Nature* **445**, 595 (2007).

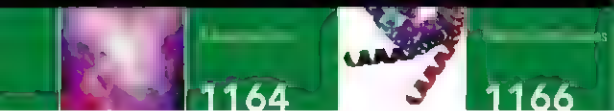
Response

WANG RAISES AN IMPORTANT POINT ABOUT the effect of energy prices on emission reduction efforts, but there are many other important factors that must be considered.

In China, fuel and electricity prices are under strict government control, and both are lower than market levels. This does not mean that the government is unaware of the problem. On 20 June 2008, China's National Development and Reform Commission announced an increase of petroleum product prices by 20% (1) and electricity price by 5% (2). Considering that the world oil price has



Traffic in Beijing. Low energy prices in China have contributed to an increase in sales of less efficient cars.



increased by 100% and the domestic coal price by 70% in the past 6 months (3), the price is likely to be raised again, probably after the 2008 Olympics. An energy tax is also under consideration (4). The Chinese government has to weigh both normative considerations and political practicality in the decision-making process. For reasons of inflation control and social stability, the political and transaction cost might be considered too high for the government to allow a volatile energy price (5). Indeed, the government cautiously exempted the regions affected by the recent Sichuan earthquake from the price hike and allocated 19.8 billion yuan (2.8 billion U.S. dollars) to offset impact on sectors such as public transportation and agriculture (7).

For mature market economies, the transportation sector represents a considerable proportion of energy consumption and carbon emissions. For example, in the United States and the European Union, 31 and 25% of total carbon emissions, respectively, came from this sector in 2005, compared with only 6.6% in China (6). In the developed world, high fuel prices do not prevent people from driving. Gasoline prices in China are around \$1 per liter, comparable to the U.S. level in absolute terms, yet per capita automobile ownership is 1/40 of that in the United States (7). Low oil prices play a role in stimulating the high share of large-engine cars in the Chinese market, but to a lower extent than other institutional factors such as the large government automobile fleets and income inequality. Focusing on the consumption patterns of China's richest citizens deflects attention from the fact that the vast majority of Chinese still have a modest to

poor living standard. The general public in China are highly sensitive to price changes, as they have to bear much of the cost of energy price increases.

China is at the stage of capital-intensive industrialization, with heavy investment in physical infrastructure. Most energy-intensive products such as cement and steel are produced and consumed domestically. For instance, only 10% of the steel that China produces is exported (8). Trade competitiveness is attributable to many other factors besides subsidized energy, such as low labor cost and currency exchange rates. As the world's workshop, China has a large trade surplus but huge deficit in the balance of embodied emissions in trade, as a large fraction of emissions are used to produce goods consumed in other parts of the world (9).

Wang makes an important point when he notes that artificially low energy prices potentially thwart efforts to reduce greenhouse gas emissions. However, price is only one of many institutional factors and is constrained by many other considerations, such as income distribution, trade, and tax policies. These issues should also be examined at both national and international levels, as climate change mitigation requires concerted global efforts (10).

JIAHUA PAN,¹ NING ZENG,² YIHUI DING,³
HUIJUN WANG,⁴ JAY GREGG⁵

¹Research Center for Sustainable Development, Chinese Academy of Social Sciences, Beijing, China. ²Department of Atmospheric and Oceanic Science, University of Maryland, College Park, MD 20742, USA. ³National Climate Center, Chinese Meteorological Administration, Beijing, China. ⁴Institute of Atmospheric Physics, Chinese Academy of Sciences, Beijing, China. ⁵Department of Geography, University of Maryland, College Park, MD 20742, USA.

*To whom correspondence should be addressed. E-mail: zeng@atmos.umd.edu

References

- National Development and Reform Commission. Directive on Increase in Oil Price, NDRC 205, 19 June 2008. www.ndrc.gov.cn/czfb/czfb/t20080619/t20080620_219171.htm
- National Development and Reform Commission. Directive on Increase in Electricity Price, NDRC 207, 19 June 2008. www.ndrc.gov.cn/czfb/czfb/t20080619/t20080619_218923.htm
- Xu, Y. "Coal price is pushed up further by state price control." *Shanghai Securities News*, 26 June 2008. www.cnss.com.cn/fin/chinese/
- J. Xiong. "Energy tax is under consideration by the treasury." *First Finance and Economy Daily*, 18 June 2008.

www.china.cn.com/fin/chinese/

- J. Wu. Government Work Report presented at People's Congress, 5 March 2008. www.china.com.cn/2008/03/05/content_13046560_5.htm (in Chinese)
- IEA. CO₂ Emissions from Fossil Fuel Combustion, 1971–2005 (International Energy Agency Statistics, Paris, 2007)
- Intergovernmental Panel on Climate Change. *Mitigation of Climate Change. Contribution of Working Group III to the IPCC 4th Assessment Report* (Cambridge Univ. Press, Cambridge, 2007), chap. 5.
- International Steel Association. "Global Steel Production and Import/Export of Steel by China." 1 February 2008. www.iiscs.com/News_View.asp?ID=7402 (in Chinese)
- J. Pan, Y. Chen, J. Xu, in *WRF Key Issues in Climate Change Mitigation in China* (China Environment Press, Beijing, 2007), pp. 25–42.
- P. Bao, T. Athanasiou, S. Karla. *The Right to Development in a Climate Constrained World* (Heinrich Böll Foundation Publication, Berlin, 2008).

From Darwinism to Evolutionary Biology

IN THE NEWS FOCUS STORY "MODERNIZING the modern synthesis" (11 July, p. 196), E. Pennisi reports that, seven decades after the publication of Julian Huxley's seminal book (1), we need another update of our concepts about the mechanisms of evolution (2). Such a major revision and expansion of Darwin's classical theory of descent with modification has already been attempted by several evolutionary biologists.

Twenty years ago, Endler and McLellan (3) suggested an approach toward a new synthesis. However, Carroll (4) was the first to explicitly point out that data from molecular and developmental biology, geology, and the fossil record should be integrated into an "expanded evolutionary synthesis." In more recent publications, an expansion of the synthetic theory by integration of 10 additional disciplines from the biological, geological, and computer sciences was proposed (5, 6). In addition, these authors incorporated the neglected concept of symbiogenesis (i.e., the subtheories of primary and secondary endosymbiosis) into this version of the expanded synthetic theory. These key macro-evolutionary processes in the history of aquatic unicellular life on Earth led to the emergence of the first eukaryotic cells, which later gave rise to animals and plants. Moreover, ancient secondary endosymbiotic events led to the majority of extant photosynthetic phytoplankton taxa of the oceans (such as dinoflagellates).

On the last page of his monograph, Huxley (1) introduced the term "evolutionary biology." This interdisciplinary branch of the life sciences has evolved into a system of theories that explain different aspects of organismic evolu-



tion (5). I recommend that we replace old-fashioned terms such as "Darwinism" and "synthetic theory" by Huxley's "evolutionary biology."

U. KUTSCHERA

Institute of Biology, University of Kassel, Heinrich-Plett Str. 40, D 34109 Kassel, Germany. E-mail: kurtung@kassel.de

References

1. J. Huxley, *Evolution, The Modern Synthesis* (Allen & Unwin, London, 1942).
2. M. Pigliucci, *Evolution* 62, 2743 (2007).
3. J. A. Endler, T. McElan, *Am. Nat.* 159, 335 (1988).
4. R. L. Carroll, *Trends Ecol. Evol.* 15, 27 (2000).
5. U. Kutschera, K. J. Niklas, *Naturwissenschaften* 91, 259 (2004).
6. F. P. Ryan, *Biol. J. Linn. Soc.* 88, 855 (2006).

TECHNICAL COMMENT ABSTRACTS

COMMENT ON "Determining Chondritic Impactor Size from the Marine Osmium Isotope Record"

Joanna V. Morgan

Paquay *et al.* (Reports, 11 April 2008, p. 214) reported that osmium isotope ratios in marine sediments can be used to determine the size of a chondritic impactor. Their assumptions on the late of an impacting projectile may need to be reassessed, however, because only a

small, unpredictable fraction of the impactor ends up dissolved in seawater.

Full text at www.sciencemag.org/cgi/content/full/321/5893/1158a

RESPONSE TO COMMENT ON "Determining Chondritic Impactor Size from the Marine Osmium Isotope Record"

François S. Paquay, Gregory E. Ravizza, Tarun K. Datta, Bernhard Peucker-Ehrenbrink

Morgan argues that excursions in the marine Os record are of little value for estimating impactor size. This claim is based on computer simulations of the formation of the Chicxulub crater and distribution of the ejecta, which are difficult to validate. More important, by narrowly focusing on the Cretaceous-Tertiary event Morgan's comment misses the broader implications of our study.

Full text at www.sciencemag.org/cgi/content/full/321/5893/1158b

CORRECTIONS AND CLARIFICATIONS

Perspectives: "How now brown fat?" by M. A. Lazar (22 August, p. 1048). The cell identified as "Precursor for white adipocyte" should not have been labeled with "Myf5." The corrected illustration of the cell is shown here.

Precursor for white adipocyte

News Focus: "Deciphering the genetics of evolution" by E. Pennis (8 August, p. 760). A statement attributed to Sean Carroll, "But for morphological changes, it's a shutout" in favor of cis elements, was incorrectly reported. Carroll was referring only to studies of genes' underlying morphological changes published in the past 18 months, not to all morphological changes. Carroll argues that cis-regulatory mutations are the predominant but not exclusive genetic path of morphological evolution.

News Focus: "Building a scientific legacy on a controversial foundation" by J. Merlis (25 July, p. 480). The name of the vice president for university relations at Tufts University was spelled incorrectly. She is Mary Ijka. Also, the *Chronicle of Higher Education* has resumed its tally of academic ear marks. A story on the projects in the 2008 federal budget appeared in its 28 March issue.

Special Section on HIV/AIDS: Follow the Money: "Where have all the dollars gone?" by J. Cohen (25 July, p. 520). In the caption for the top cited paper on page 521, the author's name was misspelled. It should be Patella.

NewsMakers: "Celestial symphony" (11 July, p. 183). The date for the performance of the work *Cosmic Reflection* has yet to be set; it will be played by the Boston University Symphony Orchestra.

News Focus: "Modernizing the modern synthesis" by E. Pennis (11 July, p. 196). The photo caption misidentified Massimo Pigliucci and Gerd Müller. Pigliucci is on the left, and Müller is on the right. The opening paragraph implied that journalist Susan Mazur wrote that Pigliucci would be a "headliner" at the Allenberg conference; she is referred to him only as a "principal architect" and participant.

Linus Pauling Institute Prize for Health Research Call for Nominations

The Linus Pauling Institute Prize for Health Research is sponsored by the Linus Pauling Institute (LPI) at Oregon State University (<http://lpi.oregonstate.edu>). The Prize consists of \$50,000 and a medal, and is awarded biennially. The LPI functions from the basic premise that an optimum diet and a healthy lifestyle are the keys to optimum health. The purpose of the Prize is to recognize innovation and excellence in research relating to the roles of micronutrients, vitamins, and phytochemicals in promoting health and preventing or treating disease and the roles of oxidative/nitrosative stress and antioxidants in human health and disease. The aim is to stimulate innovative research that enhances our knowledge of the role of diet and lifestyle in the primary and secondary prevention of disease, and the role of oxidative/nitrosative stress in the causation of disease.

Procedure: The nominator should submit a nomination letter, two supporting letters solicited from his/her colleagues, and the candidate's up-to-date curriculum vitae. The candidate's research accomplishments in light of the purpose of the Prize should be amply described in the letters. The awardee must be present to accept the Prize and present a talk at the "Diet and Optimum Health" conference organized by LPI in Portland, Oregon, May 13-18, 2008. Nominations should be sent to: Linus Pauling Institute, Attn: Barbara McVicar, Oregon State University, 571 Wanger Hall, Corvallis, OR 97331. Complete nomination materials must be received by November 1, 2008.



Alzheimer's
Drug Discovery
Foundation

élan

CALL FOR PROPOSALS

Novel Approaches to Drug Discovery
for Alzheimer's Disease

The Alzheimer's Drug Discovery Foundation (ADDF) invites scientists from biotechnology companies and academia worldwide to apply for research funds to advance the discovery and development of novel therapies for Alzheimer's disease. This program is made possible by a donation from Elan Corporation, plc and funds from ADDF.

Submission deadline

October 1, 2008

Funding awarded in January 2009

Grant applications and program description are available at www.alzdiscovery.org.

For more information

James Keller

212 901 8005

jkeller@alzdiscovery.org

POLITICAL SCIENCE

Contrasts Across the 49th Parallel

Stephen Randall

It has become a minor academic industry to seek contrasts and similarities between Canada and the United States as well as to identify those factors that account for those resemblances and differences. The fact that *Canada and the United States: Differences That Count* is now in its third, substantially revised, edition [the first appeared in 1993 (2, 3)] is one reflection of the continuing scholarly and public interest in the issues. That level of interest escalated in the aftermath of the tragic events of 9/11 and the deterioration of Canadian-American relations that followed the U.S. invasion of Iraq.

Scholarship in this field ranges from the highly quantitative work of Neil Nevitte and Ronald Inglehart, who apply data from the

what they have identified as a shift in values from materialist to postmaterialist culture. Whereas Lipset and Adams found differences, Nevitte and Inglehart have tended to identify commonalities of values among Canadians and Americans.

The volume's provocative collection of analytical essays makes it evident where editors David Thomas and Barbara Boyle Torrey and their authors stand on this persistent debate. As the subtitle reflects, the differences do count. Or, as Michael Adams discusses in his chapter, it is valuable to address what might be considered small differences.

Canada and the United States
Differences That Count, 3rd ed.

David M. Thomas and Barbara Boyle Torrey, Eds.
Burlington, VT: Ashgate, 2006.
288 pp., \$49.95 (hbk), \$24.95 (pbk).
ISBN 9781851171726

nence is not valuable. It is, but the findings from the World Values Survey need to be supplemented by more specific analyses. By contrast, the authors in the Thomas and Torrey volume hone in on such important areas as health care, welfare systems, taxation and debt,

legal systems, crime, immigration patterns and policies, aboriginal policies (a topic unfortunately absent from the first edition), political institutions, and the nature of federalism.

It is curious that the volume does not address defense and foreign policies or cultural policies. The editors contend that given the vast disparity between the Canadian and U.S. defense establishments, a comparison is not justified. But that argument misses a critical point. The nature and roles, both historical and contemporaneous, of the military in the two countries is in fact a critical difference. Canada's continued focus on soft power and human security, on peacekeeping and peace building, provides a substantial distinction between it and its neighbor. Nor does the volume do justice to Quebec and French Canada, although several of the authors rightly stress the importance of regional differences in both countries.

In a short introductory chapter, Torrey describes the research challenges of engaging in comparative social science research on Canada and the United States. One of the many is the difference between the sources of official statistical data in the two countries: the Canadian data being centralized under Statistics Canada, the American scattered among some 30 different agencies. Any scholar beginning comparative work would be well advised to read her brief essay.

In spite of the subtitle *Differences That Count*, the overall impression one has in reading the excellent essays contained in the volume is that some differences are considerably more important than others. In contrast to the very substantial variations that Robert Evans, John Harles, David Perry, and Roger Kerans identify in health care, welfare policies, taxation, and the legal systems, respectively, does it really matter that the U.S. Senate is elected whereas the Canadian Senate is appointed? Far more convincing, and I believe the most valuable comment in *Canada and the United States*, is Harles's suggestion that the underly-



Border crossing (Quebec/Maine).

World Values Survey that is based at the University of Michigan (4), and that of Michael Adams in his popular and prize-winning volume *Fire and Ice* (5) to the earlier, more conceptual analysis by Seymour Martin Lipset. Although by no means the first scholar to seek to explain differences between Canada and the United States, Lipset nonetheless set the stage with his analysis in *Continental Divide* (6) that Canada lacked a revolutionary past comparable to that of the United States. Lipset's focus was of course on political orientation and institutions, and that is the primary focus of the essays in *Canada and the United States*. On the other hand, the work of Nevitte and Inglehart has been on a much broader spectrum, dealing with

The first edition of *Canada and the United States* was almost exclusively written by Canadian academics. The original editor, Thomas, has made the new edition richer and more comprehensive by adding co-editor Torrey (previously at the National Research Council of the U.S. National Academy of Sciences) along with several authors from U.S. institutions. Together they address a broad range of political, cultural, economic, and social questions. The volume is divided into four thematic areas: perceptions, values, and democracy; social policies and safety nets; laws, crimes, and courts; and political institutions and politics. Each section also contains a valuable appendix on data sources for further research.

The specificity of these sections is refreshing when compared with the very broad categories that characterize the World Values

The reviewer is at the Institute for United States Policy Research, University of Calgary, Calgary, Alberta T2N 1N4, Canada. E-mail: sranda@ucalgary.ca

ing values that communities hold are what determine public policy

References and Notes

1. The volume was included in the Broadview Press publishing list's purchased in May by the University of Toronto Press.
2. D. M. Thomas, Ed., *Canada and the United States: Differences That Count* (Broadview, Peterborough, Ontario, 1993).
3. I contributed a chapter to the 1993 volume but have not been involved in either of the subsequent editions.
4. See, for example, R. Inglehart, N. Nevitte, M. Barak, *The North American Region: Culture, Economic, and Political Ties Among the United States, Canada, and Mexico* (Albino de Gruyter, New York, 1996).
5. M. Adams, *Fire and Ice: The United States, Canada, and the Myth of Converging Values* (Penguin Canada, Toronto, 2003).
6. S. M. Uppel, *Continental Divide: The Values and Institutions of the United States and Canada* (Canadian American Committee, Washington, DC, 1990).

10.1.26/science.1163097

GENERAL SCIENCE

On the Back of an Envelope

Stephan Mertens

An important skill of great use in science is the ability to derive an approximate result from insufficient data. That ability allows one to determine

whether or not an answer is reasonable by a quick calculation. The physicist Enrico Fermi (1901–1954) was a master of this art, and he used to practice his skills by working out “impossible” problems such as “How many piano tuners are there in the city of Chicago?” or “How many alien civilizations are there in our Galaxy?” Questions of this type are now known as Fermi problems (1), and they are frequently used in job interviews to test applicants’ ability to think on their feet and to make inspired guesses from very little data. What matters there is not the accuracy of the answer but the way of reasoning.

Guesstimation is a collection of 73 Fermi problems that physicist Lawrence Weinstein and mathematician John A. Adam (professors at Old Dominion University, Virginia) gathered from everyday life and various fields of science. Even the science questions require

little more than common sense to be answered Fermi style. Take, as an example, the question of how many years of life the average smoker loses. Well, smoking kills primarily through lung cancer and heart disease. These are late-onset diseases whose victims typically die after reaching the age of 50. On average, smoking cannot cost one more than 30 years because life expectancy is less than 80. It will cost more than one year, as otherwise it wouldn’t be a major health issue, so the number of lost years is between 1 and 30. Here we apply one of the few rules of guesstimation: if you have reasonable upper and lower bounds, take the geometric mean of the bound, i.e., the square root of the product of the bounds. In this case we take the square root of 30, which is a little more than 5. On average, smokers die 5 years earlier than nonsmokers. This guess is close to the actual number of 6.5 years (2). It also tells us that the main factor that determines the number of lost years is not the nicotine but the fact that smoking generally starts killing at age 50.

The rule of taking the geometric mean of the bounds instead of their average reflects the fact that guessed bounds are usually orders of magnitude apart, so taking the average would give too much weight to the upper bound. How many people could we cram into a car? Certainly more than one and less than 100. The average (50) seems to be too high, but the geometric mean (10) is reasonable.

“Use the geometric mean” is the most important precept of guesstimation. Another rule says, dare to be inaccurate. For quick calculations on the back of an envelope or in your head, simplify the numbers and focus on the order of magnitude. Days have 25 hours, π is 3, and every adult weighs 100 kg. It also helps if you know the order of magnitude of a few quantities like the population of the United States or the density of water. One needs to know only very few numbers to estimate a lot of other numbers. Suppose you want to know the number of cells in your body. An individual cell cannot be seen by the unaided eye. Among the smallest things we can see are the lines of a ruler, which are a small fraction of 1 mm wide. Hence we can assume that cells are

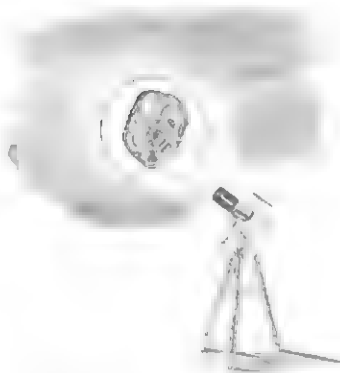
smaller than 0.1 mm or 10^{-4} m. On the other hand we remember that cells were discovered by viewing through the early microscopes, which had a magnification less than 100. This means that cells can’t be smaller than 10^{-6} m. The geometric mean of both bounds yields 10^{-5} m for the size of a cell and 10^{15} m³ for its volume. The volume of your body is easily derived from the density of water and the observation that we float. You do the math.

Guesstimation presents its collection of Fermi problems with an invitation to work them out yourself. After the authors work through a trio of examples, each problem is posed at the top of a right-hand page. Printed upside down below the question (and a sketch, usually humorous, by Patty Edwards) are hints to get you started if you are completely clueless. If you give up, you can turn the page for a full Fermi-style reasoning to the answer. Working out questions like “How many people are airborne over the US at any given moment?” or “How long a hot dog can be made from a typical cow?” is both entertaining and enlightening—especially if you do so along with friends or your children. It may also foster your career. Not just because you may encounter Fermi questions in job interviews, but because making correct guesses quickly establishes your reputation as an expert.

References

1. P. Morrison, *Am. J. Phys.* **31**, 626 (1963).
2. M. Shure, R. Mitchell, D. Doring, *Br. Med. J.* **320**, 53 (2000).

The reviewer is at the Santa Fe Institute and the Institut für Theoretische Physik, Otto von Guericke University, 39106 Magdeburg, Germany. E-mail: mertens@congol.de



How many cells are there in the human body?



10.1.26/science.1161440

THE EARLY YEARS

Preschool Influences on Mathematics Achievement

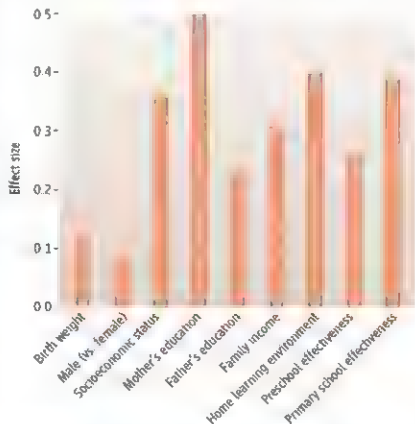
Edward C. Melhuish,^{1*} Kathy Sylva,² Pam Sammons,³ Iram Siraj-Blatchford,⁴ Brenda Taggart,⁴ Mai B. Phan,⁵ Antero Malm¹

Universal preschool is being considered as a policy option in many parts of the world, but the most influential evidence relates to disadvantaged groups. Preschool improves disadvantaged children's school readiness, educational achievements, and social adjustment (1). It is not the only influence—parental support also benefits children's development, particularly if combined with center-based programs (2). Additionally, the longer-term effects of preschool for disadvantaged children are mediated by the schools subsequently attended (3, 4).

Studies with disadvantaged children may have little relevance for the general population. Nonetheless, such evidence has fueled an increasing interest in the universal provision of preschool education (pre-kindergarten) as a means of advancing children's school readiness and later attainment (5). Some argue that preschool experience is critical for children's future competence, coping skills, health, and later employment (6). Furthermore, it is argued that the benefits outweigh the costs (7).

England has high levels of preschool use from age 3 onward, which produces benefits over no preschool in the early school years (8). Our study concerns longer-term effects in the general population in England. This study considered the influence of home environment on children's development [often a stronger factor than socio-demographic characteristics (9)], and preschool and school effectiveness (10).

Preschool centers (141) were randomly chosen in six areas demographically similar to England overall. The preschool stage of the study involved children from nursery classes, playgroups, private day nurseries,



Highest effects for predictors of mathematics attainment at age 10. The effect sizes are in standard deviation units to facilitate comparison between predictors.

centers run by a local authority, nursery schools, and integrated children's centers and, thus, included all types of preschool centers in England at the time of the study. Children's cognitive ability at ages 3 to 4 and 5 and mathematical attainment at age 10 were assessed and family data obtained by interview (11). The parental interview when children were age 3 to 4 covered learning activities enabling the creation of a home learning environment (HLE) index (11). The typical child attended preschool for 18 months part-time, and primary school for more than 5 years full-time by age 10.

Children's numeracy at the start of primary school (age 5) was analyzed, with controls for background influences and prior attainment at age 3 to 4 years (start of pre-

The advantages of home learning environment and preschool are apparent years later in children's math achievement

school). Multilevel models are a standard form of regression analysis, particularly suited to data exhibiting a hierarchical structure (12), and they provide a method of analyzing mathematics achievement at age 5, with 30 child, family, area, and preschool variables as covariates (11). Residual effects associated with individual preschools after these variables were accounted for provided a measure of a preschool's effectiveness in promoting numeracy. Preschools where children performed better than expected on the basis of prior attainment and background were deemed more effective, preschools where children performed worse than expected were deemed less effective (11).

Children in English state primary schools take national assessments at 7 and 11 years. Analyses of data from 540,000 pupils attending 15,000 schools produced school effectiveness measures standardized for all English state primary schools. We controlled for prior ability, eligibility for free school meals (poverty marker), gender, age, ethnicity, English as second language, school composition, and area characteristics.

School-level residuals from multilevel models of age 11 mathematics attainment provided measures of school effectiveness in promoting mathematics. Schools' effectiveness varied by child ability (fig. S1). Therefore, school effectiveness was derived separately for children of below-average, average, and above-average ability. Effectiveness measures for three successive years were averaged and then matched to children by ability in this longitudinal study (11).

Children ($n = 2558$) were clustered by preschool ($n = 141$) and school ($n = 960$). Statistically significant variables were kept in the model. Then, measures of the home learning environment, preschool effectiveness, and primary school effectiveness were added.

¹Institute for the Study of Children, Families and Social Issues, Birkbeck, University of London, 7 Bedford Square, London, WC1B 3RA, UK. ²University of Oxford, Oxford OX2 6PY, UK. ³University of Nottingham, Nottingham, NG8 1BB, UK. ⁴Institute of Education, University of London, WC1H 0AL, London, UK. ⁵University of Kent, Canterbury, Kent, CT2 7NZ, UK.

*Author for correspondence. E-mail: emelhuish@birk.ac.uk

Findings

Variables in the data set typically had less than 5% missing data. Multiple imputation was used to produce estimates for missing data and to avoid any possible bias. Results for complete and imputed data were equivalent, and imputed data results are reported. The HLE, preschool effectiveness, and primary school effectiveness all showed significant effects on children's mathematics achievement at age 10 ($P < 0.001$). Total variance accounted for was 22%. Effect sizes (ESs) are from the final model, after we allowed for all other variables (supporting online material text).

Low birth weight, girls (versus boys), and lower parental occupational, educational, or income status were significantly and independently linked with lower mathematics scores (table S2). Ethnic group differences were regarded as unreliable owing to small group size. Cognitive ability of the average preschool child and the percent of children in the primary school with special educational needs (SEN) had weak, significant relations with mathematics achievement at age 10. Other factors were not statistically significant after allowing for the above. After controlling for other child, parental, preschool, and school variables, the HLE, preschool effectiveness, and primary school effectiveness all showed separate significant effects on mathematics achievement at age 10 ($P < 0.001$).

We examined the effects on mathematical attainment at age 10 of having high (1 SD or more above mean), low (1 SD or more below mean), and medium (within 1 SD of the mean) scores in HLE and preschool and school effectiveness. The HLE had significant, positive effects at both high and medium levels, compared with low ($ES = 0.40$ and 0.21 , respectively). Preschool effectiveness was significant only for high compared with low ($ES = 0.26$), whereas primary school effectiveness had significant effects for both high and medium levels ($ES = 0.32$, and 0.39 , respectively) compared with low levels.

The sample was divided into families with low annual incomes ($<£17,000$ (or \sim US \$32,000), 52.5%) or higher incomes ($>£17,000$, 47.5%). The final multilevel model was run separately for each income group. Results were similar for the two groups, which indicated that the effects apply across the income spectrum with minor differences (table S2).

Discussion

The effects observed for background variables were similar to other studies (13, 14). However, HLE effects were substantial and occurred across the whole population. The HLE had low correlations with parents'

socioeconomic status or education ($r = 0.28$ to 0.32) and showed independent effects slightly less than mother's education but greater than father's education and family income. This indicates that what parents do is as important as who parents are.

Previous work with this sample had shown that the effect of 1 year of part-time preschool was equivalent to increasing family income by more than £10,000 (US \$19,000) a year (8). We show that the effect of primary school was even more important than preschool (0.39 versus 0.26 SD), but both were sufficiently large to be important for any government wishing to maximize educational achievement. They are greater than the effect for father's education and similar to that for family income but less than that for mother's education (see figure, page 1161). Analyses for low and higher income groups reveal that the effects for the HLE and preschool and school effectiveness are remarkably similar for both income groups, which indicates their importance across the income spectrum. These effects are predictive, but we cannot assume causality. Observational studies, such as this study, do not have random assignment, so it is always possible that results may reflect selection bias and/or the operation of unmeasured variables (11).

Countries vary in preschool provision. Some deliver preschool services universally (United Kingdom, Scandinavia, and France), whereas other countries provide services to some children only (United States) and some are moving rapidly to increase provision (China) (15). However, there is international support for our findings. The PISA project indicates that enhanced mathematics achievement is associated with preschool experience internationally (16). In the United States, prekindergarten improved mathematics and reading at kindergarten (17), with greatest gains if preschool started between 2 and 3 years as found in England (18). Preschool boosted primary school achievement in Bangladesh (19), with similar results reported for 10 countries (20). During preschool expansion in Uruguay, comparisons of (i) siblings with and without preschool and (ii) regional variations revealed clear preschool benefits in secondary school (21). Similar Argentine data revealed that 1 year of preschool was associated with primary school attainment increases of 0.23 SD (22), analogous to the effect of high versus low effective preschools reported here.

Our study demonstrates the relative magnitude of home, preschool, and school effects likely to occur with universal preschool education, which is common in many advanced

societies and is increasingly sought by others. The HLE before school exerted a powerful effect. Although any preschool has benefits (18), effective or higher-quality preschools have the greatest effect. Preschool learning environments can be improved through programs that target cognitive functioning (23) and staff training (24).

References and Notes

1. A. Karoly, M. R. Kilburn, J. S. Cannon, *Early Childhood Interventions: Proven Results, Future Promises* (RAND Santa Monica, CA, 2005).
2. J. M. Joffe et al., *Dev. Psychol.* **41**, 885 (2005).
3. J. Currie, D. Thomas, *J. Hum. Resour.* **35**, 755 (2000).
4. A. J. Reynolds, S. Ou, J. D. Topitzes, *Child Dev.* **75**, 1299 (2004).
5. E. Zigler, W. Gilliam, S. James, *A Vision for Universal Preschool Education* (Cambridge Univ. Press, New York, 2006).
6. M. McCaig, J. F. Mustard, *Early Years Study: Reversing the Real Brain Drain* (Publications Ontario, Toronto, 1999).
7. J. J. Heckman, *Science* **312**, 1500 (2006).
8. K. Sylva, E. Melhuish, P. Sammons, S. Siraj Blatchford, B. Taggart, "The Effective Provision of Pre-School Education (EPPE) Project: The final report" (Tech. Paper 12, Department for Education and Skills (DfES), London, 2004).
9. E. C. Melhuish et al., *J. Soc. Issues* **64**, 95 (2008).
10. P. Sammons, *School Effectiveness: Coming of Age in the 21st Century* (Sage & Ziff Verlag, Los Angeles, Netherlands, 1993).
11. Materials and methods and additional discussion are available as supporting material on Science Online.
12. H. Goldstein, *Multilevel Statistical Models* (Unwin, London, ed. 3, 2003).
13. I. Feinstein, *Economica* **70**, 73 (2003).
14. A. Sacker, I. Schwan, M. Bartley, *Soc. Sci. Med.* **55**, 863 (2002).
15. E. C. Melhuish, K. Petrucci, Eds., *Early Childhood Care and Education: International Perspectives on Policy and Research* (Routledge, London, 2006).
16. *Learning for Tomorrow's World: First Results from PISA 2003* (Organisation for Economic Cooperation and Development, Paris, 2004).
17. S. Lueke, M. Bringer, D. Baskin, B. Fuller, R. W. Rumberger, *Econ. Educ. Rev.* **26**, 52 (2007).
18. P. Sammons et al., "Measuring the impact of pre-school on children's cognitive progress over the pre-school period" (Tech. Paper 8, Institute of Education, University of London, London, 2002).
19. F. E. Aboud, *Early Child. Res. Q.* **23**, 46 (2004).
20. J. E. Morris, Z. Xiang, J. Schwanhart, *Early Child. Res. Q.* **23**, 113 (2006).
21. S. Berlinsky, S. Gal, M. M. Manacorda, *Giving Children a Better Start: Pre-School Attendance and School Age Profiles* (Institute for Fiscal Studies, London, 2007). www.ifs.org.uk/wp060606.pdf.
22. S. Berlinsky, S. Gal, A. Gertler, *The Effect of Pre-Primary Education on Primary School Performance* (Institute for Fiscal Studies, London, 2006). www.ifs.org.uk/wp060606.pdf.
23. A. Diamond, W. S. Barnett, J. Thomas, S. Muon, *Science* **318**, 1387 (2007).
24. K. Sylva et al., *Int. J. Early Years Educ.* **15**, 49 (2007).
25. We thank A. Leyland for technical advice. Supported by the U.K. Department for Children, Schools and Families. Our data will be publicly available as an anonymized data set subject to government approval. Further information is available from the authors on request.

Supporting Online Material
www.sciencemag.org/cgi/content/full/322/5893/1161/DC1

10.1126/science.1158808

PLANT SCIENCE

The "Invisible Hand" of Floral Chemistry

Robert A. Raguso

Flowering plants that compete successfully for pollinator services often advertise their commodities—nectar, pollen, and other nutritious rewards—with dazzling color displays and alluring perfumes. Pollinator abundance and preference may limit a plant's reproductive success, especially if its reproductive window is brief (1). Such circumstances predict a "buyer's market" for pollinators, which should engender fierce competition among neighboring plant species for attracting pollinators through quality rewards and truthful, enticing advertisements. Flowers that abuse the good will of their consumers with meager or distasteful rewards should fare poorly in such an arena. Enter *Nicotiana attenuata*, a tobacco from North America's Mojave Desert that laces its floral nectar with nicotine (see the figure). Why would a plant adopt such a strategy when its hawkmoth and hummingbird pollinators are demonstrably repelled by the taste and odor of nicotine (2)? On page 1200 of this issue, Kessler *et al.* address this conundrum (3) by combining gene silencing, paternity analysis, and field experiments. Surprisingly, the combination of nicotine and benzyl acetone (the most attractive scent component) best serves the reproductive interests of the tobacco plant. Those with this floral blend sire more seeds on other plants and produce larger seed capsules themselves.

One novel aspect of this study is its selective manipulation of specific scent and nectar components. The amount of scent and nectar can be augmented (4, 5), but their experimental deletion is more difficult. Kessler *et al.* silenced genes associated with nicotine and benzyl acetone biosynthesis in *N. attenuata* and then presented pollinators with arrays of such plants whose flowers emitted different nicotine-benzyl acetone combinations. The presence of nicotine decreased the time hummingbirds and hawkmoths spent drinking from individual flowers but increased the number of flowers visited, presumably to satisfy the caloric demands of hovering flight. Conversely, birds and moths visited fewer flowers for longer periods when nectar lacked



Better pollination through chemistry. The desert tobacco *N. attenuata* lures hummingbirds (*Archilochus alexandri*) with sweet nectar flavors but sends them away with nicotine. This strategy allows them to both attract pollinators and effectively move their pollen between plants.

nicotine, which suggests that the pollinators' interests are best served by extended visits to a few nectar-rich flowers (6). Responses to plants lacking benzyl acetone were more ambiguous. The taste and/or scent of this compound are preferred by hummingbirds and hawkmoths (2), and plants lacking both nicotine and benzyl acetone were ignored by hawkmoths, possibly because of reduced odor (7). Flowers with nicotine absolutely deterred florivory by caterpillars and nectar-robbing by carpenter bees, both of which could directly reduce reproductive fitness. These results, combined with seed and seed capsule production data, suggest that chemically mediated "pull" and "push" strategies optimize reproductive fitness in *N. attenuata* by attracting pollinators, preventing them from loitering, and deterring floral enemies.

The study of Kessler *et al.* highlights a paradox in floral behavior: Flowers must compete vigorously for pollinators without being so attractive that they never leave. A plant must encourage a pollinator to visit other flowers of its own species without forsaking it for flowers

Volatile compounds help flowering plants balance attracting pollinators and maximizing overall reproductive success.

of a competitor. In *N. attenuata*, nicotine functions as a floral filter (8) for antagonistic visitors (caterpillars and nectar-robbers) but manipulates pollinators by altering their movement patterns (and pollen export) through a population. For this to work, nicotine must be somewhat tolerable—if deterrent—to hummingbirds, or the local nectar market must be poor. In either case, nicotine would function more as an economic hurdle (9) than as a filter, which suggests that pollinators supplement additional reproductive options at the tobacco's disposal. Such a scenario is amenable to a game theory approach. Indeed, *N. attenuata* flowers are self-compatible, capable of maturing seed capsules without pollinators.

In this light, testing a pollinator's tolerance for nicotine-spiked nectar appears less risky. Yet, how might outcrossing—when a flower is fertilized by pollen from a different plant—benefit a plant that can pollinate itself, such as *N. attenuata*? Perhaps the

answer lies in the plant's life history. It is a fire-adapted desert annual that can spend decades as a dormant seed, awaiting a smoke signal that will trigger germination. This life-style is notoriously unpredictable, and bet-hedging strategies are commonly invoked (10) in studies of germination success. Even a low percentage of outcrossing might improve seedling survivorship, especially if seeds germinate under variable climatic conditions.

This study adds to a growing list of ruses by which plants manipulate pollinator movement to optimize gene flow. Nearly a third of all orchids have no floral nectar (11). When sugar solutions are added to such flowers, pollinators remain longer at individual plants, resulting in increased inbreeding or pollen wastage (12). Similarly, the reduction of nectar by extrinsic factors (such as mites) may benefit plants by altering pollinator movement or floral contact (13). Another floral scheme is to turn up the heat. Dramatic increases in temperature and odor concentration compel cycad pollinators to leave male cones (where they feed on pollen) for female cones on different plants, thereby

effecting cross-pollination (14).

The results of Kessler *et al.* present a cautionary tale. The subtle interactions between *N. attenuata* and its floral visitors could not have been revealed through mainstream pollination studies, in which nonvisual floral traits and nonsugar nectar components are often ignored (15). Through the "invisible hand" of floral volatiles, the self-interests of tobacco plants and their pollinators are mediated with

an apparent net outcome of mutual benefit.

References

1. T. M. Knight *et al.*, *Annu. Rev. Ecol. Syst.* **36**, 467 (2005).
2. D. Kessler, T. Baldwin, *Plant J.* **49**, 845 (2007).
3. D. Kessler, K. Gase, I. T. Baldwin, *Science* **323**, 1205 (2008).
4. T. I. Ashman *et al.*, *Ecology* **84**, 2099 (2005).
5. L. S. Adler, R. L. Irwin, *Ecology* **88**, 2948 (2005).
6. J. A. Bittell *et al.*, *Proc. Natl. Acad. Sci. U.S.A.* **105**, 3404 (2008).
7. R. A. Raguso, M. A. Willis, *Anim. Behav.* **69**, 407 (2005).
8. S. D. Johnson, A. J. Hargreaves, M. Brown, *Ecology* **87**, 2709 (2006).
9. R. H. Frank, *The Economic Naturalist* (Basic Books, New York, 2007).
10. M. J. C. Davies, D. L. Venable, *Am. Nat.* **155**, 148 (2000).
11. S. Cazzulani, A. Widmer, *Trends Ecol. Evol.* **20**, 447 (2005).
12. S. D. Johnson *et al.*, *Proc. R. Soc. London Ser. B* **273**, 803 (2006).
13. C. Lara, J. F. Ometas, *Oikos* **96**, 470 (2002).
14. L. Terry, G. H. Walther, C. Moore, R. Roemer, *C. Mull. Science* **318**, 10 (2007).
15. R. A. Raguso, *Entomol. Exp. Appl.* **128**, 196 (2008).

10.1126/science.1163570

ASTRONOMY

Life After Death

Annalisa Celotti

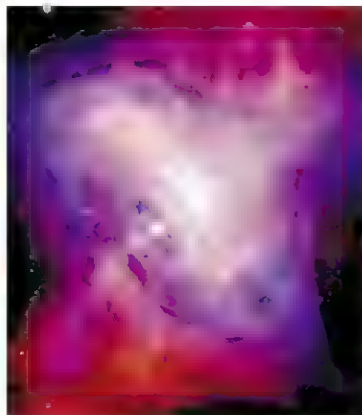
In 1054 C.E., Chinese and Arab (1-3) astronomers recorded the observation of a bright explosion in the sky. Now known to have been a supernova explosion, the remnant—the Crab nebula—still emits particles energized to extremely relativistic energies and radiates light at x-ray and gamma-ray wavelengths. On page 1183 of this issue, Dean *et al.* (4) report the discovery that the high-energy radiation (hard x-rays) from the Crab is polarized, yielding insights into the processes and mechanisms involved in making a dead star so active.

When a massive star exhausts its fuel for nuclear fusion, it collapses under its own gravity into a neutron star or black hole, releasing energy that heats and expels the outer star layers. The material expands at a speed as high as 1% that of light, sweeping through the interstellar medium and giving rise to a supernova remnant. The Crab nebula is such a remnant, resulting from the explosion of a star thought to have been 10 times as massive as the Sun. It is located in our galaxy, in the constellation Taurus, about 6500 light-years from Earth, and is about 10 light-years in size.

Inside the Crab, a relatively young neutron star (5, 6) of 1.4 to 2 solar masses is active as a pulsar. The neutron star rotates at about 30 times per second. As it slows down, at a rate of 38 ns per day, its rotational energy is converted in part to radiation collimated along the axis determined by the pulsar magnetic field. Because this magnetic axis is misaligned with the rotation axis, like the beam from a lighthouse, such emission is observed from Earth as pulses of light from radio- to gamma-ray wavelengths. But most of the neutron star spin energy goes into powering a wind of relativistic

particles and electromagnetic fields. Highly energetic particles moving in such a field will emit radiation. The x-ray image (see the figure) reveals morphological features over a scale of about 5 light-years, comprising a narrow collimated "jet" and a doughnut-shaped "torus," as well as ripples, wisps, and arcs.

Even 40 years after the discovery of the Crab pulsar and more than 20 years after the basis of the currently accepted interpretation was formulated (7, 8), key questions remain: How is the rotation power converted into the electromagnetic and the kinetic power of the wind? How are particles accelerated to emit high-energy radiation?



The Crab nebula. A composite of optical data (red) from the Hubble Space Telescope and x-ray imaging (blue) from the Chandra X-ray Observatory.

How is a dead massive star still able to energize extremely relativistic particles?

Understanding how the Crab system works will elucidate the late stages of stellar evolution, the physics of magnetized relativistic plasma, the conditions of matter at nuclear densities, and the mechanisms by which extremely relativistic particles are efficiently accelerated in the universe. Indeed, observations of radiation from the Crab at extremely high energies (9), up to ~100 TeV (1 TeV = 10^{12} eV), requires electrons (and positrons) to have been energized to 100 million times the energy associated with their own mass.

The spectrum of the Crab, from radio to gamma-ray frequencies, is well known. Its brightness in x-rays promoted it to the role of a flux (and time) calibrator for x-ray detectors. The high degree and direction of polarization at high energies reported by Dean *et al.* provide valuable information on the site of acceleration of the particles and on the structure of the magnetic field associated with the pulsar. Such information cannot be provided by the spectrum alone.

Electromagnetic waves oscillate in a plane perpendicular to their direction of travel. They are linearly polarized if the electric and magnetic field vectors oscillate along the same direction in such a plane. For that to occur, the emitting system has to be characterized by some order, or degree of symmetry. For synchrotron radiation, an elevated level of polarization thus indicates that the magnetic field (and possibly the radiating particles) is

International School for Advanced Studies (SIS), via Beirut 2, 4, 34014 Trieste, Italy. E-mail: celotti@sissa.it

not randomly oriented but has a preferential direction. As reported by Dean *et al.*, the electric field appears to be very closely aligned with the pulsar's jet axis, suggesting that the highly energetic particles are produced close to the pulsar, where the magnetic field has a predominantly toroidal or donut-shaped configuration. Such a field geometry is also likely to be responsible for the collimation of the detected light and particle beams.

Polarimetry (the analysis and interpretation of polarized light) from radio to optical frequencies has been a powerful diagnostic tool in astronomy. However, its use at higher (x-ray and gamma-ray) energies has been hampered by the difficulty not only in reconstructing the polarization direction for the photons, but also in achieving a high enough sensitivity to apply it to astronomically distant sources. The next generation of polarimeters,

which are now under development (10, 11), will be able to measure polarization levels of a few percent even in extragalactic sources. The potential for astrophysical studies is fascinating, not only for understanding pulsars. The new polarimeters will help elucidate processes within active galactic nuclei, where collimated flows, moving at 99% the speed of light, are formed, and thought to be powered by black holes with masses millions to billions of times that of the Sun.

Polarimetric information, as demonstrated by Dean *et al.*, is expected to provide a diagnostic for the origin of their powerful emission in the x-ray and gamma-ray bands. Perhaps an even more intriguing prospect is the possibility of shedding light on the nature of the high-energy emission in gamma-ray bursts. These cosmological sources are the most luminous events known, and are

believed to be the aftermath of the explosion of stars even more massive than those leading to Crab-like remnants, and ending their lives as black holes. But here, too, there is life after death.

References:

1. J. J. Dwyer, *Pub. Astron. Soc. Pacific* **54**, 91 (1942).
2. N. J. Mayall, *J. H. Dorr, PASP* **54**, 95 (1942).
3. K. Brecher *et al.*, *Observatory* **109**, 106 (1983).
4. A. J. Dean *et al.*, *Science* **321**, 1183 (2008).
5. W. Baade, *Astrophys. J.* **96**, 188 (1942).
6. R. Nisikawa, *Astrophys. J.* **96**, 199 (1942).
7. C. F. Kennel, V. C. Corbelli, *Astrophys. J.* **283**, 694 (1984).
8. C. F. Kennel, V. C. Corbelli, *Astrophys. J.* **283**, 710 (1984).
9. A. M. Hillas *et al.*, *Astrophys. J.* **503**, 744 (1998).
10. E. Costa *et al.*, *Nature* **411**, 662 (2001).
11. J. Knudsen *et al.*, *Proc. SPIE* **6668**, 5 (2007).

10.1126/science.1163887

GEOPHYSICS

When Seamounts Subduct

Roland von Huene

Volcanoes on the sea floor of ocean basins—called seamounts—migrate with the ocean plates as they subduct beneath continental plates. This process creates shear interfaces called subduction zones, where most of the world's earthquakes nucleate. It has been proposed that scraping a subducted seamount from the oceanic plate nucleates great subduction-zone earthquakes (magnitude 8 or above) (1). However, at crustal depths below 10 km, where great earthquakes nucleate, ship-based seismic techniques cannot image subducted seamounts. On page 1194 of this issue, Mochizuki *et al.* (2) use an array of seismometers on the sea floor to investigate these issues. They show that seamounts provide an opportunity to investigate causes for a transition from stable to the unstable slip that nucleates earthquakes and find a clear beginning limit of seismogenic behavior.

Numerous seamounts with heights of 2 to 3 km and basal widths of 20 to 50 km exist on oceanic plates that migrate toward continents. The converging plates meet at deep ocean trenches, where the ocean plate carrying the seamounts bends downward into trenches to subduct beneath the continental plate. When high seamounts collide with the wedge-

shaped continental margin, they first plow open the thin apex of weak material, creating an embayment in the landward slope of the trench (see the figure). As the colliding seamount plows into an increasingly thick part of the continental wedge, the entire seamount tunnels beneath the continental framework. Insertion of the seamount produces a broad bulge in the overlying sea floor; collapse of the trailing flank layers sends debris slides toward the trench (see the figure). Removal of collapse debris produces a furrow in the sea floor for distances proportional to the seamount's height.

Seamounts off the central Costa Rica continental margin Seamounts in the Pacific Basin (five of which can be seen in the lower part of the image) typically have diameters of ~20 km and heights of 2 to 2.5 km. At this location, the oceanic and continental plates converge at a rate of 90 km per million years. As the ocean crust flexes into the 4.5-km deep Middle America trench (middle), bend faults form the stepped topography of the trench axis. On the trench slope are two circular bulges above subducted seamounts. Across the seaward slopes of the bulges and down slope are furrows from slides as the sea floor steepens seaward.

Data from an array of seismometers on the sea floor show the complex pattern of earthquakes around subducted seamounts.



pore fluid pressured by the overburden weight that reduces subduction zone friction. Therefore, subduction produces few recordable earthquakes until fluid drains to 10 to 15% and the continental wedge is thick enough to accumulate the elastic strain released in earthquakes (3). Earthquakes of magnitude ~ 3 or above can be recorded at stations on land. But with only distant land station records, the precise location of these offshore earthquakes cannot be determined.

Sea-floor seismic records indicate deep anomalous features along subduction zones that are associated with aftershock clusters beneath the shelf (4–6). However, it will be difficult to prove that seamounts nucleate these earthquakes without understanding the mechanism through which they do so. Mochizuki *et al.* now show that with two-dimensional data from an array of sea-floor seismometers, a subducted seamount at 10 km depth along the subduction zone can be outlined as a diffuse bump on the subducting plate. Leaving the array above the seamount for extended periods to record local earthquakes provides sufficient precision to resolve the relation between seismicity and the seamount. Surprisingly, seismicity around the studied seamount is concentrated in front of its leading flank, rather than over its crest. These data imply that friction over the seamount is less than in adjacent deeper areas. They also indicate a steady or stable sliding over the seamount, whereas the sub-

duction zone in front of the seamount slides intermittently during earthquakes (referred to as unstable sliding).

Recent observations are consistent with the inferred low friction. In a study of a subducted Costa Rican seamount (see the figure), Sahling *et al.* found large volumes of fluid vent from sediment layers exposed by trailing flank collapse (7). The strata ramped upward over the subducting seamount will create a hydraulic gradient up its flanks, which will concentrate fluid above its crest and thus reduce friction. This can help explain the distribution of friction off Japan found by Mochizuki *et al.*

Whether scraping seamounts from the subducting plate produces great earthquakes is still speculative (1). Mochizuki *et al.* examined a seamount subducted to a depth where earthquakes first nucleate, so their experiment does not answer this question. Subducted seamounts at depths of 20 km are proposed to uplift the coast of Costa Rica (8), so they remain attached at least to these depths. Some detached fossil seamounts are exposed in outcrops on land, although a graveyard of many detached fossil seamounts is not commonly recognized in outcrops on land. The low friction indicated by Mochizuki *et al.* is consistent with seamounts remaining attached in shallow regions of the seismogenic zone. Perhaps lower friction at the beginning of seismogenesis

increases deeper in the subduction zone to detach subducting relief. Although detachment must sometimes occur, its relation to great earthquakes remains unresolved.

Recording a grid of signals from a surface ship (commonly two or more intersecting lines of shots are recorded) could provide the required three-dimensional seismic coverage. Three-dimensional data can also be acquired from an array of seismometers in a drill hole, yielding vertical seismic profiles. From such data, physical properties in subduction zones can be derived (9). Such data will help to elucidate whether frictional behavior changes are a result of physical relief or changes in the physical properties of fault materials.

References

- M. Cloos, *Geology* **20**, 601 (1992).
- K. Mochizuki, T. Yamada, M. Shinohara, Y. Yamakawa, *T. Kanazawa Science* **321**, 1194 (2008).
- C. R. Ranero *et al.*, *Geochim. Geophys. Geosyst.* **9**, Q03504 (2007).
- S. Husen, R. Quintero, E. Kisting, *Geophys. Res. Lett.* **29**, 1029/2001GL014045 (2002).
- S. L. Bilek, S. V. Schwartz, H. R. DeShon, *Geology* **31**, 455 (2003).
- H. R. DeShon *et al.*, *J. Geophys. Res.* **108**, 1029/2002JG002794 (2003).
- M. Sahling *et al.*, *Geochim. Geophys. Geosyst.* **9**, Q03505 (2008).
- M. Fisher *et al.*, *Geology* **26**, 467 (1998).
- R. von Huene, D. Claret, C. Papenberg, *Geochim. Geophys. Geosyst.* **9**, Q03507 (2008).

10.1126/science.1162868

BIOCHEMISTRY

Opening the Molecular Floodgates

Chris S. Gandhi¹ and Douglas C. Rees^{1,2}

The uncontrolled flow of water can be devastating. Engineers have tamed water by creating structures ranging from dams, levees, and aqueducts to faucets, drains, and microfluidic devices. Biological systems face comparable challenges. One of the most fundamental involves the permeability of cell membranes to water. For example, osmotic downshock, which occurs when a bacterium is suddenly exposed to fresh water, leads to an influx of water across the membrane. Without safety valves to release their cellular contents, such cells cannot withstand the high internal pressures resulting from this

influx. Two reports in this issue, by Wang *et al.* on page 1179 (1) and Vázquez *et al.* on page 1210 (2), shed light on how bacteria address this challenge.

About 20 years ago, Kung and co-workers identified stretch-activated (mechanosensitive) proteins in bacterial membranes that sense the increase in membrane tension during osmotic downshock (3). Two major families of prokaryotic mechanosensitive channels were subsequently cloned: the mechanosensitive channel of large conductance (MscL) (4), and the mechanosensitive channel of small conductance (MscS) (5), the focus of the current studies. These proteins form channels in the inner membrane that open and close in direct response to tension applied to the bilayer, allowing the efflux of cytoplasmic contents to restore

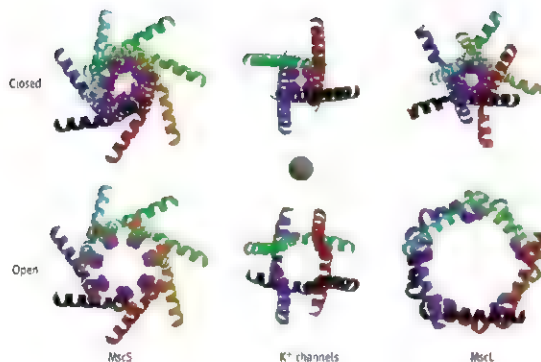
Structural studies reveal how mechanosensitive channels respond to membrane tension

the osmotic balance to a sustainable level.

How can such channels sense and couple membrane tension to reversible opening (6)? Some of the first clues came from crystal structures of putatively closed states of *Escherichia coli* MscS and *Mycobacterium tuberculosis* MscL (7–9), which indicated that packing of symmetry-related transmembrane (TM) helices—TM3 in MscS, and TM1 in MscL—creates the permeation pathway in these channels. The helix-helix interfaces in both structures contain conserved Gly and Ala residues, and are expected to rearrange to form a large pore in the open state. The structural studies of the open state of the *E. coli* MscS by Wang *et al.* and Vázquez *et al.* substantially advance our understanding of this process.

The challenge in structurally characterizing the open state of MscS is that the closed state is

¹Division of Chemistry and Chemical Engineering, California Institute of Technology, Pasadena, CA 91125, USA. ²Howard Hughes Medical Institute, California Institute of Technology, Pasadena, CA 91125, USA. E-mail: drees@caltech.edu



Permeation pathways of gated channels. The arrangements of α helices lining the permeation pathways in the closed (top) and open (bottom) states of MscS (left), potassium (K^+) channels (middle), and MscL (right) are shown, viewed from the outside of a cell, in the direction perpendicular to the membrane plane. Coordinate sets for the closed (9) and open (11) forms of MscS, the closed (27) and open (28) forms of potassium channels, and the closed state of MscL (9) were taken from Protein Data Bank (29) sets 20AU, 2VV5, 1K4C, 2R9R, and 2OAR, respectively. The coordinates of an open state model of the *E. coli* MscL were derived by Sucharev and Guy from cross-linking and computational studies (24). The hydrophobic residues constricting the pore in the closed state are shown as magenta space-filling models. The side chains of MscS residue 106, the site of the Ala-to Val substitution in the open state, are shown as orange space filling models. The sphere of 4.5 Å radius in the center of the figure approximates the threshold between a closed and open hydrophobic pore for water conduction (15). Figure prepared with MOLSCRIPT and RASTER3D.

strongly favored in the absence of applied tension, but tension cannot be conventionally applied to solutions or crystals. The authors overcame this obstacle through the inspired application of two complementary approaches.

Wang *et al.* crystallized a mutant channel, in which the wild-type Ala at position 106—which is conserved in the TM3-TM3 interface—was replaced with Val (a mutation referred to as A106V). Electrophysiological characterization indicated that this substitution requires greater tension to open, but once open forms a stable subconducting state (10). Vázquez *et al.* first reconstituted wild-type MscS into membranes and then trapped it in the open state by adding lysophosphatidylcholine (a cone-shaped lipid) to the outer leaflet of the bilayer. This lipid perturbs the lateral pressure profile of the membrane and stabilizes the open conformation of MscS, as originally demonstrated for MscL (11). Through the use of site-directed spin-labeling (SDSL)-based spectroscopy methodologies, the environments of the residues in the TM helices of MscS were characterized and converted into a three-dimensional structure through computational approaches.

Both studies show a wider separation between TM3 helices leading to an increased pore radius through the membrane, in addition to a repositioning of the first two TM helices surrounding the permeation pathway. However, there are clear differences between the structures. The A106V crystal structure shows that the TM3 helices are aligned nearly parallel to the pore axis, whereas the SDSL study indicates that these helices are more tilted. An understanding of the origin of these distinctions will undoubtedly be informative.

MscS thus joins the small but increasing list of channels for which structural and biophysical information is available in multiple states. The helices lining the permeation pathway in the closed and open states are compared in the figure for three of these systems: MscS (1, 2, 8), potassium (K^+) channels (12, 13), and MscL (8, 11, 14). Of these three systems, *E. coli* MscS is the only gated channel where the crystal structure of a single protein (that is, not homologs) has been solved in multiple states.

Each system has unique elements, but several general points can be made. First, the gating transition is associated with changes in helix-helix packing around the pore. Second, the closed channels are characterized by a plug of hydrophobic residues that seal the pore. Computational studies (15) indicate that hydrophobic pores of radii smaller than 4.5 or 6.5 Å are closed to conduction of water and ions, respectively; these results imply that nonconducting pores need not be geometrically closed.

Third, there is no structurally conserved conformational change associated with gating. The transition between closed and open states is often described in terms of an ratchet motion of helices; however, the details differ between the three channels. The transitions may involve changes in helix tilt (13, 14), as well as in helix kinking (13, 16).

Fourth, establishing the relationship between structurally characterized forms and functionally assigned states remains challenging. Solubilization, crystallization, probe introduction, and mutagenesis perturb channels in ways that are poorly understood, and our ability to predict function from structure is still primitive.

Given these many challenges, the studies of Wang *et al.* and Vázquez *et al.* represent important advances in our understanding of channel gating. Progress in membrane protein structural biology may appear glacial but is speeding up, and the focus is increasingly shifting to the structural definition of multiple conformational states. The goal of deciphering the mechanisms of channel gating in structural detail (that is, understanding the molecular plumbing), while still daunting, is no longer a pipe dream.

References and Notes

- W. Wang *et al.*, *Science* **321**, 1219 (2008).
- V. Vázquez, M. Sotomayor, J. Cardozo-Morales, K. Schulten, E. Perozo, *Science* **321**, 1230 (2008).
- B. Marrero, M. Burchard, A. H. Delgado, J. Adler, C. Kung, *Proc. Natl. Acad. Sci. U.S.A.* **84**, 2297 (1987).
- S. Sucharev *et al.*, *Nature* **368**, 255 (1994).
- N. Veenstra *et al.*, *EMBO J.* **18**, 1730 (1999).
- C. P. Harrell, Ed., *Mechanotransduction Channels*, Part A (Academic Press, San Diego, 2007), vol. 58.
- G. Chang, R. H. Spensky, A. T. Lee, M. T. Barclay, D. C. Rees, *Science* **282**, 2220 (1998).
- R. B. Bass, P. Strup, M. Barclay, D. C. Rees, *Science* **298**, 1587 (2002).
- S. Stroobant, R. B. Bass, P. Strup, D. C. Rees, *Curr. Top. Membr.* **58**, 1 (2007).
- M. D. Edwards *et al.*, *Nat. Struct. Mol. Biol.* **12**, 113 (2005).
- F. Perozo, D. M. Cortez, P. Sompomporn, A. Kloda, B. Marrero, *Nature* **408**, 947 (2005).
- A. Doyle *et al.*, *Science* **280**, 69 (1998).
- V. Jiang *et al.*, *Nature* **417**, 523 (2002).
- S. Sucharev, M. Burchard, C. S. Chiang, H. R. Guy, *Nature* **409**, 120 (2001).
- O. Beckstein, M. S. P. Sansom, *Phys. Biol.* **1**, 42 (2004).
- B. Ahsan-Ul-Haque, N. Lu, S. Sucharev, *Nature Struct. Mol. Biol.* **14**, 1141 (2007).
- Y. Zhou, J. H. Moras, C. A. Kuhlmann, R. MacKinnon, *Nature* **414**, 43 (2001).
- S. B. Ong, X. Tao, E. B. Campbell, R. MacKinnon, *Nature* **450**, 316 (2007).
- M. S. Sansom *et al.*, *Nucleic Acids Res.* **28**, 235 (2000). (<http://www.rcsb.org/pdb>).
- C. S. Chiang, supported by postdoctoral fellowships from the NIH and the Beckman Foundation.

10.126/science.1162963

CHEMISTRY

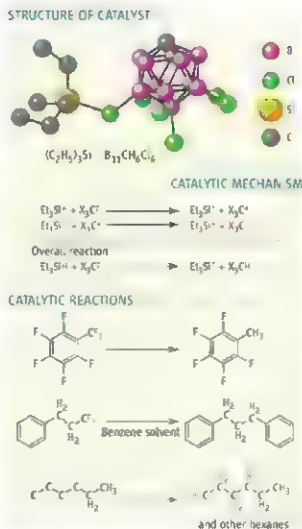
A Catalytic Foothold for Fluorocarbon Reactions

Robin N. Perutz

Molecules containing several carbon-fluorine bonds, or fluorocarbons, find innumerable uses that depend on the lack of reactivity of C-F bonds. Fluorocarbon polymers can be found in clothing, lubricants, and nonstick cookware (1). Smaller fluorocarbon molecules are used as refrigerants or solvents, ligands for catalysis, anesthetics, imaging agents in medicine, etchants for semiconductors, and even blood substitutes (1, 2). However, the inertness of C-F bonds can be too much of a good thing. Once formed, they can prove difficult to dispose or recycle into other useful products. The Montreal protocol banned the use of chlorofluorocarbons as refrigerants because of their ability to destroy the ozone layer. Other fluorocarbons cause concerns because of their global warming potential or their toxicity in soil or water (3, 4). On page 1188 of this issue, Douvris and Ozerov report on catalysts they have developed that can activate the C-F bonds of saturated fluorocarbons and remain active for many reaction cycles (5).

What makes the C-F bonds of fluorocarbons so unreactive? High bond strength is one factor but is by no means sufficient. For example, the Si-F bonds in tetrafluorosilane (SiF_4) are stronger than the C-F bonds in tetrafluoromethane (CF_4) (6), but SiF_4 is far more reactive than CF_4 . The reason is that silicon can increase its coordination number (the number of atoms to which it bonds) from four to five or six.

Acidity and basicity are also essential aids to understanding reactivity. Neither SiF_4 nor CF_4 are donors or acceptors of protons (Brønsted acids and bases), but SiF_4 is a good acceptor of electron pairs (a Lewis acid), whereas CF_4 is neither a good electron pair donor nor a good electron pair acceptor. Because CF_4 combines all these properties—strong bonds, an absence of acidity or basicity,



Pulling fluorine off, putting hydrogen on. (Top) Structure of triethylsilylium hexachloromonocarborene catalyst, adapted from the crystal structure of the triisopropyl analog (14). Hydrogen atoms are omitted for clarity (Middle). Catalytic mechanism of hydrodefluorination; X represents any substituent group on carbon, and all three X groups may be different. (Bottom) Reactions catalyzed by the Douvris-Ozerov catalyst.

and an inability to increase the coordination number of carbon—it is one of the least reactive molecules known.

So where is the Achilles' heel of saturated fluorocarbons? There has been some progress with reactions of saturated compounds containing tertiary C-F bonds (in which C-F is connected to three other carbon atoms), because abstraction of fluoride, F^- , results in a somewhat more stable carbocation than for CF_2 or CF_3 groups (7). It is also possible to react fluorocarbons with sodium metal to

A reagent-catalyst combination reveals how to make hitherto inert fluorocarbons react at room temperature, which will help to solve the problem of their disposal.

form sodium fluoride, but this reaction is hazardous and not practical for larger-scale use. None of these reactions is catalytic. In contrast to the saturated fluorocarbons, reactions of the more activated C-F bond of aromatic fluorocarbons have been more successful, especially when mediated by transition metal complexes (8). There are now several examples of catalytic replacement of C-F bonds by C-H bonds (9) and of catalytic cross-coupling of aromatic C-F bonds (10). A catalytic reaction is desirable because it may allow a transformation at lower temperature than without catalyst, so energy costs are reduced. Moreover, a compound may be too expensive as a reagent that is consumed but may be cost-effective as a catalyst that is reused.

A few years ago, Ozerov and co-workers showed that saturated fluorocarbons can react catalytically with extremely powerful Lewis acids, but the catalysts did not survive for many reaction cycles (11). Douvris and Ozerov have now developed a much more stable catalyst. The keys to their success are an exceptionally powerful Lewis acid and an energetically favorable reaction. The acid consists of a triethylsilylium ion, a positively charged silicon center with a coordination number of 3. Such an ion can only be stable if it is accompanied by a counterion that is extremely reluctant to coordinate or bond to the positive ion. Thus, activation of strong bonds proceeds with the help of a counterion that is extremely poor at bond formation.

The search for the least coordinating negative ion has been a long-standing theme of inorganic chemists. Douvris and Ozerov chose a state-of-the-art, weakly coordinating ion, $[\text{HCB}_6\text{H}_5\text{Cl}_6]^-$, a derivative of the icosahedral "carborane" ion $[\text{HCB}_6\text{H}_5\text{Cl}_6]^-$ (12). The catalyst is the cationic triethylsilylium hexachlorocarborane (see the figure, top panel). This molecule represents one of the closest approaches to a true silylium salt and was first described by Reed *et al.* (13).

As a reagent that can act as a hydrogen source, Douvris and Ozerov used the silicon-hydrogen bond of the neutral form of their silylium cation, $\text{H-Si}(\text{C}_2\text{H}_5)_3$. The reaction replaces a fluorine atom in the fluorocarbon by hydrogen (hydrodefluorination) and so generates a C-H bond and a Si-F bond. The

overall reaction is energetically very favorable because C-H bonds are stronger than Si-H bonds, whereas Si-F bonds are stronger than C-F bonds. The silylium cation abstracts fluoride from the fluorocarbon, whereas the resulting carbenium abstracts hydride from the trimethylsilane and regenerates the catalyst (see the figure, middle panel).

Douvis and Ozerov have used this reagent and catalyst on three different fluorocarbons. The first substrate, $C_6F_5CF_3$, contains both aromatic and aliphatic C-F bonds. The unprecedented result was complete disappearance of the substrate at 25°C after 6 hours and an 86% yield of $C_6H_5CH_2CH_2CH_2CH_3$ (see the figure, bottom panel). The reaction is thus completely selective for the saturated C-F bonds and leaves the aromatic C-F bonds untouched, even though the aromatic bonds are more reactive toward conventional reagents.

In the second substrate, $C_6H_5CH_2CH_2CF_3$, the CF_3 group is located far from the benzene ring, and it was thus possible to exclude any effect of the ring. When the authors dissolved this substrate in benzene and applied the catalyst-reagent mixture, they again observed complete disappearance of the substrate. This time, the product, $C_6H_5CH_2CH_2CH_2CH_2CH_3$,

resulted from hydrodefluorination and reaction with the solvent.

The final substrate, $CF_3(CH_2)_4CF_3$, contains saturated C-F and saturated C-H bonds. It demanded higher temperature, more catalyst, and longer reaction times (50°C and 120 hours), but strikingly, the authors observed complete conversion to linear, branched, and cyclic hexanes in various isomeric forms (see the figure, bottom panel).

Three parameters indicate that all of these reactions are highly effective: Conversion of the starting material exceeds 97%, small amounts of catalyst are needed, and turnover numbers (the number of times the catalyst runs the reaction) are high (14). These results open up the possibility of catalytic conversion of fluorocarbons to hydrocarbon products that could be reused or incinerated without special equipment. In addition to prospects for more satisfactory disposal of fluorocarbons, there are exciting possibilities for applying these principles in synthesis. However, in either case we will need ready access to hexachlorocarbon salts, and the system must be optimized to achieve even higher turnovers. The principle has yet to be extended to perfluoroalkanes—that is, fully

saturated molecules without C-H, such as $F_3CCF_2CF_3$. This remains a major challenge because it is likely that the initial reaction of perfluoroalkanes with Douvis and Ozerov's catalyst is energetically unfavorable.

References and Notes

- G. Sandford, *Philos. Trans. R. Soc. London Ser. A* **358**, 455 (2000).
- N. Morimoto et al., *Angew. Chem., Int. Ed.* **42**, 1255 (2003).
- V. C. Hoang, H. S. Jhu, *Phys. Plasmas* **10**, 3410 (2003).
- M. K. So et al., *Env. Sci. Tech.* **38**, 4056 (2004).
- C. Douvis, D. V. Ozerov, *Science* **321**, 1108 (2008).
- J. E. Huheey, E. A. Keiter, R. L. Keiter, *Inorganic Chemistry* (DisserCollins, New York, ed. 4, 1993).
- G. Sandford, *Tetrahedron* **59**, 437 (2003).
- T. Braun, R. N. Pezzit, in *Comprehensive Organometallic Chemistry*, H. H. G. Cottrell, D. M. P. Higgins, Eds. (Elsevier, Oxford, 2006), chapter 1.26.
- J. Vela et al., *J. Am. Chem. Soc.* **127**, 7857 (2005).
- W. Wang, B. J. Allama, *J. Am. Chem. Soc.* **129**, 5629 (2007).
- V. J. Scott, R. Celenligil, G. D. V. Ozerov, *J. Am. Chem. Soc.* **127**, 2852 (2005).
- C. A. Reed, *Chem. Commun.* **2005**, 1669 (2005).
- C. A. Reed, Z. Xie, R. Bau, A. Benveniste, *Science* **262**, 402 (1993).
- The catalyst loading, defined as the mole ratio of catalyst per reactive C-F bond in the substrate, is between 0.036% and 0.5%. The turnover number, defined as the number of C-F bonds in the substrate reacted per mole of catalyst, is between 200 and 2700.

10.1126/science.1161182

DEVELOPMENTAL BIOLOGY

Neuron Research Leaps Ahead

Robert H. Brown Jr.

There has been substantial progress in defining the primary molecular defects causing inherited forms of major neurodegenerative diseases such as Alzheimer's disease, amyotrophic lateral sclerosis (ALS), and Parkinson's disease. However, developing therapies for these diseases has been hindered by several experimental limitations, including the absence of in vitro models that accurately reproduce the genetic milieu of the disease and inadequate systems to dissect the roles of diverse cell types in the pathogenesis of these diseases. On page 1218 in this issue, Dimos et al. (1) demonstrate that new technologies in stem cell biology may overcome these barriers by reprogramming adult fibroblasts into embryonic stem cells that can subsequently yield patient-specific neural cells (neurons and astroglial cells) (2). The study focuses on ALS, but the findings are applicable to

diverse neurological diseases.

The Dimos et al. study follows a series of pioneering investigations on the production of embryonic stem cells. In 2006, Takahashi and Yamanaka showed that forced expression of four transcription factors (Oct4, Sox2, Klf4, and Myc) reprogrammed adult mouse fibroblasts into mouse embryonic stem cells, designated induced pluripotent stem cells (3). Over the past 18 months, the same strategy, with some modifications, has been used to reprogram human cells to become the equivalent of embryonic stem cells (3-6).

Dimos et al. obtained fibroblasts from two elderly sisters (in their 80s) with ALS-associated mutations in the gene encoding superoxide dismutase (*SOD1*). One of the sisters had developed the neurodegenerative disorder. Fibroblasts from a skin biopsy of this patient were transduced with retroviruses that expressed the four key transcription factors, thus producing induced pluripotent stem cells (see the figure). Analysis of several parameters (e.g., mor-

Technologies that reprogram adult dermal cells into motor neurons should advance our understanding of neurodegenerative diseases.

phology, cell cycle status, cell surface markers, and gene expression patterns) verified that the derived cells were similar to embryonic stem cells. When propagated in culture, these induced pluripotent stem cells formed embryoid bodies, a hallmark of embryonic stem cells. Using a protocol from Wichterle and colleagues (7), Dimos et al. triggered the differentiation of motor neurons from embryoid bodies by treatment with sonic hedgehog and retinoic acid, agents that modify transcription and differentiation. Moreover, the *SOD1* mutation of the original donor was present in the patient-derived motor neurons. Within the same cultures, glial cells were also identified.

Dimos et al. not only demonstrate that human neural cells—in particular, disease-related neural cells—can be generated from induced pluripotent stem cells, but also that the method can be successfully applied to fibroblasts derived from elderly patients, a key issue for age-dependent disorders (like most of the neurodegenerative diseases)

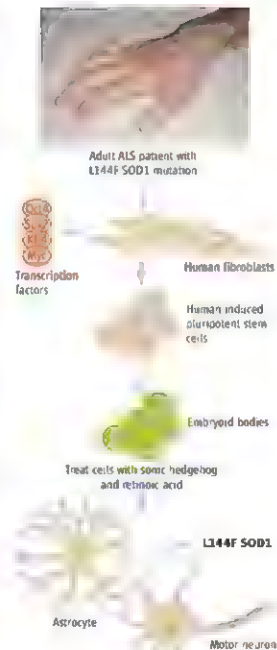
Massachusetts General Hospital, 14th Street, Navy Yard, Charlestown, MA 02129, USA. E-mail: rbrown@partners.org

Moreover, the study shows the feasibility of producing large numbers of induced pluripotent stem cells from a small skin biopsy.

One anticipates that this approach will be immediately useful in the analysis of motor neuron diseases. It should soon be possible to investigate disease-related characteristics of each type of patient-derived cells. In ALS, studies of rodents that are genetically engineered to express extremely high amounts of mutant SOD1 protein document multiple types of neuronal pathology, including perturbations of mitochondrial function, excessive excitation, and altered transport of molecules through axons (8, 9). In the same rodent models, data suggest that transport of glutamate into astroglia is defective (8, 9). It should now be possible to reexamine these phenomena by using neurons and glia that express physiological amounts of the mutant SOD1 protein, and establish a hierarchy of importance of the multiple findings from rodent models. It should also be possible to reanalyze the non-cell autonomous aspects of this disease. A study by Di Giorgio *et al.* recently showed that astrocytes from the transgenic amyotrophic lateral sclerosis animals secrete substances *in vitro* that adversely affect motor neurons (10); it should now be possible to determine whether this finding is reproducible in nontransgenic cells.

Our current understanding of the molecular basis for the neurodegenerative diseases is predicated largely on studies of gene defects transmitted as Mendelian traits. Still unknown is the degree to which the overall genetic makeup of patients with sporadic neurodegenerative diseases alters disease susceptibility or characteristics. A plausible hypothesis is that combinations of gene variants in sporadic ALS may increase sensitivity to harmful environmental influences. The use of genome analyses to address this challenging problem has thus far produced inconsistent results, although the field of complex genetics of sporadic neurodegeneration is still in its infancy (11, 12). The use of induced pluripotent stem cells should make it possible to study human embryonic motor neurons from sporadic patients *in vitro*, permitting analysis both of factors in the patients' genetic makeup that enhance disease susceptibility and of external factors that promote disease in the context of a patient-specific genotype.

The ability to generate induced pluripotent stem cells also has implications for developing therapies to treat neurological diseases. To the extent that disease phenotypes can be defined *in vitro*, these are now amenable to high-throughput approaches to drug screening, because large amounts of the implicated



Skin cells generate human neural cells Fibroblasts from a patient's skin biopsy are transduced with four transcription factors to form pluripotential cells and then embryoid bodies which, after exposure to sonic hedgehog and retinoic acid, generate both motor neurons and astrocytes.

cell types can be generated from human fibroblasts. The availability of large numbers of neural cells that accurately reproduce the genotype of patients may also facilitate strategies of cell transplantation therapy. It has been proposed, for example, that transplantation of neural precursor cells into the spinal cord of patients with amyotrophic lateral sclerosis may be beneficial as a platform for delivering neurotrophic factors that promote neuron differentiation and growth (13).

For many years, a holy grail in neurodegenerative disorders has been the repopulation of the affected neural tissue with new neurons. In the most optimistic view, the Dimos *et al.* study can be cautiously viewed as a step

in that direction. It raises the prospect of using induced pluripotent stem cell technology to generate new motor neurons *ex vivo* that are genetically identical to those of a given patient and potentially useful for transplantation without rejection by the patient's immune system. Noteworthy is the observation that dopaminergic neurons derived by induced pluripotent stem cell technology can confer functional improvement when transplanted into a rat model of Parkinson's disease (14). Yet another option arising from this technology is the possibility that transcription factors could be delivered directly to the spinal cord to reprogram endogenous cells to generate new motor neurons.

Several cautionary questions arise. Given that the studies to date have relied on retroviruses to transduce the cells targeted for reprogramming, does the induced pluripotent stem cell method entail a risk for tumorigenesis? It hoped that alternative induction methods (transient delivery of the transcription proteins or the use of small molecules mimicking the proteins) will address this issue. Will the embryonic neurons generated via induced pluripotent stem cells *in vitro* differentiate into mature motor neurons capable of extending axonal processes to allow functional innervation of muscle? If the biology of the disease *in vivo* is recapitulated in the induced pluripotent stem cell-derived neurons *in vitro*, will this prohibit effective use of patient-derived cells as donors in novel transplantation strategies? These concerns notwithstanding, the study by Dmos *et al.* is a seminal achievement. The authors have created a new platform for studying the biology of normal and diseased human neural cells that is likely to enhance studies of disease pathophysiology and accelerate the development of therapies for many categories of human nervous system disorders.

References

1. J. T. Dinno et al., *Science* **321**, 1219 (2008), published online 31 July 2008 (DOI:10.1126/science.1158799).
2. K. Takahashi and S. Yamakawa, *Cell* **126**, 663 (2006).
3. K. Takahashi et al., *Cell* **131**, 861 (2007).
4. J. Yu et al., *Proc. Natl. Acad. Sci.* **104**, 1917 (2007).
5. M. Nakagawa, *Nat. Biotechnol.* **26**, 101 (2008).
6. L. H. Park et al., *Nature* **451**, 143 (2003).
7. H. Wichterle, *J. Neurosci.* **24**, 10972 (2004).
8. P. Pasnelli, R. H. Brown Jr., *Nat. Rev. Neurosci.* **7**, 710 (2006).
9. S. Söhlte, C. Vande Velde, D. W. Cleveland, *Neuron* **52**, 399 (2006).
10. J. De Giorgio et al., *Hum. Mol. Genet.* **10**, 408 (2001).
11. M. W. van Es et al., *Cancer Res.* **6**, 669 (2007).
12. T. Dumbelly, *M. Engl. J. Med.* **357**, 715 (2007).
13. S. M. Klein et al., *Hum. Gene. Ther.* **16**, 509 (2005).
14. M. Wernig et al., *Proc. Natl. Acad. Sci. U.S.A.* **105**, 5856 (2008).



AAAS INTERNATIONAL

S&T Leaders See a Renewed Role for Science Diplomacy

The headlines have been dominated in recent months by conflict and the grinding efforts to find a peaceful resolution in Iran, North Korea, the Middle East, and other hotspots. But quietly, and with little fanfare, U.S. science and engineering organizations are mounting an increasingly ambitious campaign to build global understanding and trust through science diplomacy.

Now, with Congress, the executive branch, and S&T organizations showing resurgent interest in such engagement, AAAS has opened a new Center for Science Diplomacy in hopes of using it to build both science and improved international relations. Science diplomacy was constructive in working with Russia and China during the Cold War, and AAAS officials and their partners believe it can be similarly effective in dealing with today's most difficult conflicts and pressing challenges.

The new center "is to be guided by the overarching goal of using science and scientific cooperation to promote international peace, understanding, and prosperity," AAAS Chief Executive Officer Alan I. Leshner testified before the U.S. House Subcommittee on Research and Science Education. "We are particularly interested in identifying opportunities for science diplomacy to serve as a catalyst between societies where official relations might be limited, and to strengthen existing partnerships in science and technology."

The House subcommittee—headed by Chairmen Brian Baird (D-Wash.) and Rep. Vernon J. Ehlers (R-Mich.)—used the 15 July hearing to explore the role of nongovernmental organizations and universities in international S&T cooperation. Baird welcomed Leshner's announcement about the new AAAS center, saying, "I can't think of a better organization to do that."

Vaughan Turekian, the AAAS chief international officer, will direct the new center. Norman P. Neureiter, who heads the AAAS Center for Science, Technology and Security Policy, will serve as senior adviser.

Turekian has guided a number of recent AAAS diplomacy initiatives, laying the foundation for promising relationships with China,

Vietnam, and Rwanda. In early 2007, he worked with the U.S. State Department to organize a landmark meeting in Kuwait that brought 200 women scientists and engineers from the Arab world together with about two dozen women holding leadership positions in U.S. science, business, education, and government.



(Left to right) Alan I. Leshner, AAAS; Michael T. Clegg, National Academy of Sciences; Wm. A. Wull, Civilian Research and Development Foundation; and James Cahyn, Texas A&M University, testify before the U.S. House Subcommittee on Research and Science Education.

Neureiter is a veteran of science diplomacy. A chemist by training, he was the first U.S. science attaché in Eastern Europe in the 1960s. He served in President Richard Nixon's Office of Science and Technology, helping craft scientific elements of historic agreements with the Soviet Union and China. From 2000 to 2003, he served as the first science adviser to the U.S. Secretary of State. He traveled to Iran last October with a National Academies delegation that received an enthusiastic welcome.

The scientist-to-scientist relationships developed during the Cold War "made real contributions toward creating the very different world we live in today," Neureiter said. "Today the challenges are different, the threats are different, but the potential of science to address these problems is as powerful now as it was then."

The renewed focus on science diplomacy comes as overseas views about the U.S. have reached a nadir. But while surveys in many foreign nations register strong disapproval of U.S. government policies, they also have shown very positive views of U.S. science and technology.

That has helped drive the renewed interest in science diplomacy at AAAS and other S&T organizations. The nonprofit Civilian Research & Development Foundation (CRDF), for exam-

ple, has undertaken a range of science and technology missions involving Iraq, the former states of the Soviet Union, and other countries.

There is increasing "recognition that a lot of the issues we face today globally—the issues we face and that the next administration will face—have science and technology components," said Cathleen A. Campbell, CRDF's president and CEO. Solutions require the engagement of many nations, Campbell added, because "no one country has all the answers."

Turekian envisions the center as a forum where scientists and engineers can engage with the foreign policy community, and where they can work together to identify projects that could strengthen civil society relationships between nations. Climate change, energy, sustainability, innovation, and health could be prime fields for such collaboration, he said.

But, he added, the spirit of the engagement will be critically important. Science diplomacy is not an end program, there is no quid pro quo. Rather, it is a way to improve global science and build capacity—and a way to build mutual trust.

"At the heart, this is a matter of respect," Turekian said. "We're saying 'You regard this as important, and we regard this as important, so let's find ways that we can engage.' And in doing that, we can try to build a reputation that the United States is a good country to engage with."

—Benjamin Samers contributed to this report

INTERNATIONAL

Meetings Strengthen AAAS Ties in Europe

On a whirlwind July trip, AAAS President James I. McCarthy renewed cooperative ties with science partners in Ireland and the United Kingdom, including Johnny Devins, the Irish minister of Science, Technology and Innovation. The visit by McCarthy and AAAS Director for International Cooperation Tom Wang "was very much welcomed," said Patrick Cunningham, chief science adviser to the Irish government, as Dublin bids for the title of European City of Science in 2012.

From 18 to 22 July, AAAS staff traveled to Barcelona, Spain, for the EuroScience Open Forum. Experts at the Forum predicted that science R&D would continue to be a powerful economic driver on both sides of the Atlantic. But they warned that the benefits of R&D could be undermined if scientists fail to engage in a respectful dialogue with the public about their findings.

—Becky Ham and Edward W. Lempinen

Cavity Optomechanics: Back-Action at the Mesoscale

T. J. Klippenberg^{1,2†} and K. J. Vahala^{2*}

The coupling of optical and mechanical degrees of freedom is the underlying principle of many techniques to measure mechanical displacement, from macroscale gravitational wave detectors to microscale cantilevers used in scanning probe microscopy. Recent experiments have reached a regime where the back-action of photons caused by radiation pressure can influence the optomechanical dynamics, giving rise to a host of long-anticipated phenomena. Here we review these developments and discuss the opportunities for innovative technology as well as for fundamental science.

The reflection of a photon entails momentum transfer, generally referred to as "radiation pressure," with the resulting force called the scattering force. Besides this scattering force, the spatial variation of an intensity distribution can give rise to a gradient or dipole force. Interest in radiation pressure was first generated by the trapping of dielectric particles using laser radiation (1). This technique is widely adapted today in the biological and biophysical sciences and is known as the "optical tweezer." In atomic physics, the ability to cool atoms with the use of radiation pressure (2, 3) has enabled many advances (4), including the realization of exotic quantum states such as Bose-Einstein condensates.

Radiation pressure can also have an effect on macroscopic mechanical masses (such as on an optical interferometer's mirror) and has been considered theoretically for decades (5, 6). The mutual coupling of optical and mechanical degrees of freedom in an optical resonator (or optical cavity) has been explored in laser-based gravitational wave interferometers, in which radiation pressure imposes limits on continuous position detection. Beyond setting detection limits, radiation pressure can also influence the dynamics of a harmonically bound mirror. A discernible effect on mirror motion was first demonstrated in the optical bistability resulting from the static elongation of cavity length caused by radiation pressure (7), and later, in work demonstrating the optical spring effect (a radiation pressure-induced change in stiffness of the "mirror spring") (8). These phenomena, however, do not rely on the cavity delay, rather, each results from an adiabatic response of the cavity field to mechanical motion. Phenomena of a purely dynamical nature were predicted (5, 9) to arise when the decay time of the photons inside the cavity is comparable to or longer than the me-

chanical oscillator period. Creating such delays through an electro-optic hybrid system was later proposed and demonstrated to induce radiation pressure "feedback cooling" of a cavity mirror (10, 11), also known as cold damping. Whereas in subsequent attempts dynamic radiation-pressure phenomena were masked by thermal effects (12), recent advances in micro and nanofabrication

made it possible to access the regime where the effects of cavity-enhanced radiation pressure alone dominate the mechanical dynamics. Demonstrations of mechanical amplification (13, 14) and cooling (14–16) via dynamical back-action signal that a paradigm shift (17) in the ability to manipulate mechanical degrees of freedom is now under way, which has long been anticipated (18, 19). Central to all current work is the role of back-action in setting dynamical control and performance limits. This review is intended to provide context for these recent accomplishments and also to present an overview of possible and anticipated future research directions.

Dynamical Back-Action Versus Quantum Back-Action

Photons at optical frequencies are uniquely suited to measure mechanical displacement for several reasons. First, because of the high energy of optical photons (~1 eV), thermal occupation is negligible at room temperature. Moreover, present-day laser sources are available that offer noise performance that is limited only by quantum noise. To measure displacement, a commonly used experimental apparatus is a Fabry-Pérot interferometer,

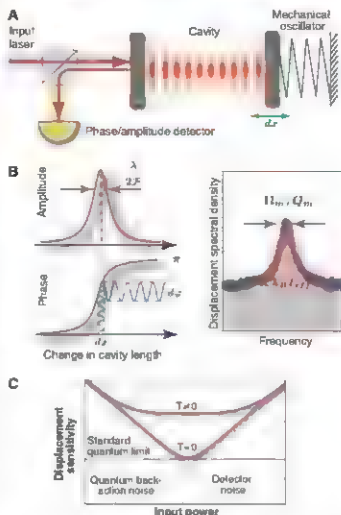


Fig. 1. (A) Schematic of the cavity optomechanical interaction of a cavity field (red) and a moveable mirror. (B) Transduction mechanism for the laser resonantly probing the cavity. The mechanical motion (green) causes the reflected field to be phase-modulated around its steady-state value. This occurs because the mirror motion changes the total cavity length and thereby changes the resonance frequency of the cavity by $\Delta\omega = \frac{2\pi}{\lambda} \Delta L$, where ΔL is the separation between the two mirrors and Δx is the mirror displacement. The change in the phase of the reflected laser field and λ is the incident wavelength of the laser, allowing minute mirror displacements to be detected. The reflected amplitude is left unchanged. (Right) Fourier analysis of the reflected phase reveals the mechanical spectrum of the mirror motion. Mechanical resonance frequency (Ω_m), quality factor (Q_m), and temperature (T_m) can be determined using this spectrum. (C) Sensitivity of the

*Max Planck Institute für Quantenoptik, 85748 Garching, Germany. [†]Department of Applied Physics, California Institute of Technology, Pasadena, CA 91125, USA.

To whom correspondence should be addressed. E-mail: klippen@mpq.mpg.de (T.J.K.); vahala@caltech.edu (K.J.V.)
[†]Present address: Swiss Federal Institute of Technology (EPFL), Lausanne, Switzerland.

interferometer measurement process for the case of a zero-temperature mechanical oscillator mirror and for finite temperature T . For low-input laser power, detector noise due to the quantum shot noise of the laser field dominates, whereas at higher laser power the quantum fluctuations of the light field cause the mirror to undergo random fluctuations (quantum back-action). At the optimum power, the two sources of fluctuation contribute equally to the measurement imprecision, constituting the SQL. At finite temperature, the mechanical zero-point motion is masked by the presence of thermal noise.

whose purpose is to determine differential changes in distance between the two end mirrors (Fig. 1A). To account for the mirror suspension or the internal mechanical modes of a mirror, it is assumed that the end mirror is free to oscillate. This harmonic confinement can be either intentional or intrinsic, as we will discuss later. The high reflectivity end mirrors enhance the number of roundtrips photons undergo (by a factor F/π , where F is the cavity Finesse) and enable very sensitive measurement of the end mirror position (Fig. 1B). For a laser resonant with the cavity, small changes in cavity length shift the cavity resonance frequency and, enhanced by the cavity Finesse, imprint large changes in the reflected phase of the laser field. To date, the best displacement sensitivities attained with optical interferometers [such as those at the Laser Interferometer Gravitational-Wave Observatory (LIGO) or Fabry-Pérot cavities (20)] are already exceeding 10^{-19} m/ $\sqrt{\text{Hz}}$, which implies that a displacement equivalent to 1/1000 of the radius of a proton can be measured in 1 s.

This extremely high sensitivity, however, also requires that the disturbances of the measurement process itself must be taken into account. The ultimate sensitivity of an interferometer depends on the back-action that photons exert onto the mechanically compliant mirror, caused by radiation pressure. In terms of mirror displacement measurement, two fundamental sources of imprecision exist (Fig. 1C). First, there is the detector noise that, for an ideal laser source (emitting a coherent state) and an ideal detector, is given by the random arrival of photons at the detector; i.e., shot noise. The detector signal-to-noise ratio increases with laser power, thereby improving the measurement precision. Increasing power, however, comes at the expense of increased intracavity optical power, causing a back-action onto the mirror. This leads to a second source of imprecision. The resulting random momentum kicks of reflected photons create a mirror-displacement noise. This random force causes the mechanical oscillator to be driven and thus effectively heated. Although this noise can also contain a contribution due to classical sources of noise (excess phase or amplitude noise), it is ultimately, under ideal circumstances, bound by the quantum nature of light and is termed quantum back-action (21, 22). Taking into account

mirror sensitivity of an interferometer is achieved at the standard quantum limit (SQL). At the SQL, detector noise and quantum back-action noise contribute each a position uncertainty equal to half of the zero point motion of the mirror, where the latter is given by $x_0 = \sqrt{\hbar/2m\Omega_m}$ (\hbar is Planck's constant divided by 2π , m is the effective mass (23) of the mirror, and Ω_m is the mirror's har-

monic frequency). Much research in the past decade has also focused on ways of circumventing this limit. For example, the use of squeezed light (24) can enable surpassing this limit. So far, however, experiments with mechanical mirrors have not observed the radiation pressure quantum back-action because it is masked by the random, thermal motion of the mirror (Fig. 1C). Fluctua-

tions of the radiation pressure force have been observed in the field of atomic laser cooling (25), where they are responsible for a temperature limit (the Doppler limit).

The optical cavity mode not only measures the position of the mechanical mode, but the dynamics of these two modes can also be mutually coupled. This coupling arises when the mechanical motion changes the intracavity field amplitude, which thereby changes the radiation-pressure force experienced by the mirror. For small displacements, this occurs when the laser is detuned with respect to the cavity resonance (Fig. 2A). This mutual coupling of optical and mechanical degrees of freedom can produce an effect called dynamic back-action that arises from the finite cavity delay. This delay leads to a component of the radiation pressure force that is in quadrature (out of phase) with respect to the mechanical motion. The component is substantial when the cavity photon lifetime is comparable to, or larger than, the mechanical oscillator period and creates an effective mechanical damping of electromagnetic origin. This is the essence of dynamic back-action (5), which, like quantum back-action, modifies the motion of the object being measured (the mirror). Unlike quantum back-action, which effectively sets a measurement precision (by causing the mirror to be subjected to a stochastic force resulting from quantum fluctuations of the field), the effect of dynamic back-action is to modify the dynamical behavior of the mirror in a predictable manner. Two consequences of this form of back-action in the context of gravitational wave detection have been identified. With a laser field blue-detuned relative to the optical cavity mode, the mirror motion can be destabilized (5) as a result of mechanical amplification (13). Similar to the operation of a laser, the onset of this instability occurs when the mechanical gain equals the mechanical loss rate and could thus create an effective limit to boosting detection sen-

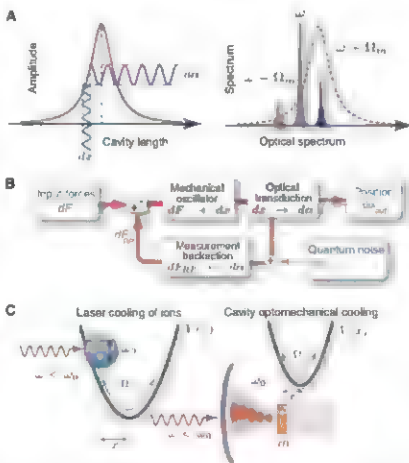


Fig. 2. (A) Dynamic back-action results from the coupling of the mechanical motion to the fluctuations of the intracavity field amplitude (dx), which occurs when the cavity is excited in a detuned manner. In the frequency domain, the amplitude modulation at Ω_m can be interpreted as sidebands around the optical laser frequency (shown at right). The sideband amplitudes are asymmetric because of the density of states of the cavity. This photon imbalance results in work on the mechanical oscillator (either amplification or cooling), as is further detailed in Fig. 4. (B) Basic elements of a feedback loop describing the measurement process and its back-action on the mirror. The mechanical oscillator is subject to a force dF (e.g., because of the thermal force or an externally applied signal force) that induces a mechanical response (dx). The latter causes a change in the optical field (either in amplitude dx or in phase, depending on the detuning), allowing measurement of mechanical position. This transduction is not instantaneous on account of the finite cavity lifetime. For a detuned laser, the amplitude change caused by this measurement process feeds back to the mechanical oscillator through the radiation-pressure force, closing the feedback loop. The sign of the feedback depends on the cavity detuning and can produce either damping (red-detuned pump) or amplification (blue-detuned pump). In a quantum description, this feedback branch is not noiseless but is subjected to quantum noise of the optical field ($d\alpha_{\text{in}}$), which yields a random force due to the quantum fluctuations of the field (i.e., the quantum back-action). Although dynamic back-action can be prevented by probing the cavity on resonance (causing $dx = 0$ and thereby preventing feedback), the quantum back-action nevertheless feeds into the mechanical oscillators' input (and thereby reinforces the SQL $d\alpha_{\text{in}}$ are the amplitude fluctuations of the reflected laser field; dF_{opt} are the fluctuations in the radiation pressure force). (C) Analogy of dynamical back-action cooling to the laser cooling of harmonically bound ions. In both the case of a harmonically trapped ion and a harmonically oscillating end mirror of a cavity, a dissipative force arises because of the Doppler effect. $V(x)$ denotes the trapping potential of the mirror and ion.

sitivity by increasing optical power in interferometers. On the other hand, a red-detuned pump wave can create a radiation component of mechanical damping that leads to cooling of the mechanical mode, i.e., a reduction of the mechanical mode's Brownian motion (9, 26).

One description of this process is given in Fig. 2B, where a feedback loop that is inherent to the cavity optomechanical system is described. The elements of this loop include the mechanical and optical oscillators coupled through two distinct paths. Along the upper path, a force acting on the mechanical oscillator (for instance, the thermal Langevin force or a signal force) causes a mechanical displacement, which (for a detuned laser) changes the cavity field due to the optomechanical coupling (the interferometric measurement process). However, the amplitude fluctuations, which contain information on the mirror position, are also coupled back to the mechanical oscillator via radiation pressure (lower path), resulting in a back-action. A blue-detuned pump wave sets up positive feedback (the instability), whereas red detuning introduces negative feedback. Resonant optical probing (where the excitation frequency equals the cavity resonance frequency, $\omega = \omega_0$) interrupts the feedback loop because changes in position only change the phase, not the amplitude, of the field. As described below, this feedback circuit also clarifies the relation between "feedback cooling" and cooling by dynamic back action.

Experimental Systems

Systems that exhibit radiation pressure dynamic back action must address a range of design considerations, including physical size as well as dissipation. Dynamic back-action relies on optical retardation, i.e., is most prominent for photon lifetimes comparable to or exceeding the mechanical oscillation period. Very low optical dissipation also means that photons are recycled many times, thereby enhancing the weak photon pressure on the mirror. On the other hand, the mechanical dissipation rate governs the rate of heating of the mechanical mirror mode by the environment, limiting the effectiveness of optomechanical cooling. It also sets the required amplification level necessary to induce regenerative oscillations. These considerations illustrate the importance of high optical Finesse and mechanical Q in system design.

It is only in the past 3 years that a series of innovative geometries (shown in Fig. 3) has reached a regime where the observation of radiation pressure dynamic back action could be observed. These advances have relied on the availability and improvements in high-Finesse mirror coatings (as used in gravity wave detectors) and also on micro- and nanofabrication techniques [which are the underlying enabling technology for nano- and micro-electromechanical systems (27)]. A commonly used hybrid system consists of a conventional input mirror made with a high reflectivity coating and an end mirror whose dimensions are meso-

scopic and which is harmonically suspended. This end mirror has been realized in multiple ways, such as from an etched, high reflectivity mirror substrate (14, 15), a miniaturized and harmonically suspended gram-scale mirror (28), or an atomic force cantilever on which a high reflectivity and micron-sized mirror coating has been transferred (29). A natural optomechanical coupling can occur in optical microcavities, such as microtoroidal cavities (13) or microspheres, which contain coexisting high Q , optical whispering gallery modes, and radio-frequency mechanical modes. This coupling can also be optimized for high optical and mechanical Q (30). In the case of hybrid systems,

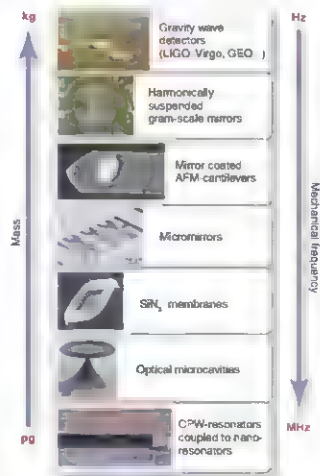


Fig. 3. Experimental cavity optomechanical systems. (Top to Bottom) Gravitational wave detectors [photo credit LIGO Laboratory], harmonically suspended gram-scale mirrors (28), coated atomic force microscopy cantilevers (29), coated micromirrors (14, 15), SiN₂ membranes dispersively coupled to an optical cavity (31), optical microcavities (13, 16), and superconducting microwave resonators coupled to a nanomechanical beam (33). The masses range from kilograms to picograms, whereas frequencies range from tens of megahertz down to the hertz level CPW, coplanar waveguide.

yet another approach has separated optical and mechanical degrees of freedom by using a miniature high Finesse optical cavity and a separate nanomechanical membrane (17). Whereas the aforementioned embodiments have been in the optical domain, devices in the micro- and radio-wave domain have also been fabricated (22, 32), such as a nanomechanical resonator coupled to a superconducting microwave resonator (33).

Many more structures exist that should also realize an optomechanical interaction in an efficient manner. In particular, nanophotonic devices such as photonic crystal membrane cavities or silicon ring resonators might be ideal candidates owing to their small mode volume, high Finesse, and finite rigidity. Owing to their small length scale, these devices exhibit fundamental flexural frequencies well into the gigahertz regime, but their mechanical quality factors have so far not been studied, nor has optomechanical coupling been observed. As described in the next section, such high frequencies are interesting in the context of regenerative oscillation and ground state cooling.

Cooling and Amplification Using Dynamical Back-Action

The cooling of atoms or ions using radiation pressure has received substantial attention and has been a successful tool in atomic and molecular physics. Dynamical back-action allows laser cooling of mechanical oscillators in a similar manner. The resemblance between atomic laser cooling and the cooling of a mechanical oscillator coupled to an optical (or electronic) resonator is a rigorous one (34). In both cases, the motion (of the ion, atom, or mirror) induces a change in the resonance frequency, thereby coupling the motion to the optical (or cavity) resonance (Fig. 2C). Indeed, early work has exploited this coupling to sense the atomic trajectories of single atoms in Fabry-Pérot cavities (35, 36) and, more recently, in the context of collective atomic motion (37, 38). This coupling is not only restricted to atoms or cavities but also has been predicted for a variety of other systems. For example, the cooling of a mechanical oscillator can be achieved using coupling to a quantum dot (39), a trapped ion (40), a Cooper pair box (41), an LC circuit (5, 32), or a microwave stripline cavity (33). Although the feedback loop of Fig. 2B explains how damping and instability can be introduced into the cavity optomechanical system, the origins of cooling and mechanical amplification are better understood with the use of a motional sideband approach, as described in Fig. 4 (13).

Cooling has been first demonstrated for microelectromechanical oscillators coupled to optical cavities (14–16) and, using an electromechanical analog, for a Cooper pair box coupled to a nanomechanical beam (41). Because the mechanical modes in experiments are high Q (and are thus very well isolated from the reservoir), they are easily resolved in the spectra of detected probe light reflected from the optical cavity (Fig. 1B). Furthermore, their effective temperature can be inferred from the thermal energy $k_B T$ (where k_B is

the Boltzmann constant), which is directly proportional to the area of detected mechanical spectral peak (Fig. 1B). In the first back-action cooling experiments, a temperature of ~ 10 K was achieved for a single mechanical mode. The bath and all other modes in these experiments were at room temperature, owing to the highly targeted nature of cooling (Fig. 4). Since the completion of this work, cooling of a wide variety of experimental embodiments ranging from nanomembranes (31) and gram-scale mirrors (28) to the modes of kilogram-scale gravitational bar detectors (such as AUREG) has been demonstrated. At this stage, temperatures are rapidly approaching a regime of low phonon number, where quantum effects of the mechanical oscillator become important. To this end, cooling with the use of a combination of conventional cryogenic technology with dynamical back action cooling is being investigated. Technical hurdles include collateral reheating of the mechanical mode, exacerbated by the very high mechanical Q , which leads to relatively long equilibration times.

Quantum back action sets a fundamental limit of radiation-pressure cooling (34, 42) that is equivalent to the Doppler temperature in atomic laser cooling (25). It may also be viewed as a consequence of the Heisenberg uncertainty relation in that a photon decaying from the resonator has an uncertainty in energy given by $\Delta E = \hbar\kappa$ (where κ is the cavity decay rate), implying that the mechanical oscillator cannot be cooled to a temperature lower than this limit. It has been theoretically shown (34, 42) that ground state cooling is nevertheless possible in the resolved sideband regime (also called the good cavity limit), in analogy to atomic laser cooling, where this technique has led to ground state cooling of ions (43). This regime is characterized by mechanical sidebands that fall well outside the cavity bandwidth and has recently been demonstrated experimentally (44). Detection of the ground state could probably prove to be as challenging as its preparation. Proposals to measure the occupancy are diverse, but one method is to measure the weights of the motional sidebands generated by the mechanical motion (34).

It is important to note that cooling of mechanical oscillators is also possible using electronic (active) feedback (10, 11, 29, 45). This scheme is similar to "stochastic cooling" (46) of ions in storage rings and uses a "pick-up" (in the form of

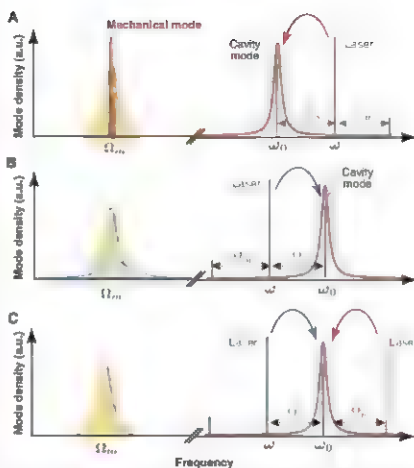


Fig. 4. Frequency domain interpretation of optomechanical interactions in terms of motional sidebands. These sidebands are created on the optical probe wave as photons are Doppler shifted from the mirror surface (which undergoes harmonic motion driven by its thermal energy). Doppler scattering rates into the red (Stokes) and blue (anti-Stokes) sidebands are imbalanced when the probe wave resides to one side of the optical resonance, which can be viewed as a consequence of the asymmetric density of electromagnetic states (Fig. 2A). This imbalance favors the Stokes sideband for a blue-detuned pump and the anti-Stokes sideband for the red-detuned pump, thereby creating a net imbalance in electromagnetic power upon scattering. This imbalance is the origin of mechanical amplification (blue detuning) and cooling (red detuning). (Cooling in this fashion is similar to cavity cooling of atoms.) Only mechanical modes that produce appreciable sideband asymmetry will experience significant gain or cooling. Moreover, the degree of asymmetry can be controlled in an experiment so that a particular mechanical mode can be selected for amplification or cooling. (A) Dynamic back-action amplification of mechanical motion via a blue-detuned laser field. The laser scatters pump photons into the cavity, thus creating phonons and leading to amplification. (B) Dynamic back-action cooling via a red-detuned laser. Pump photons are scattered into the cavity resonance, thereby removing thermal mechanical quanta from the mechanical oscillator. (C) Two-transducer scheme. By symmetrically pumping the cavity on both upper and lower sideband, only one of the quadratures of the mechanical motion is measured with a precision that can exceed the standard limit, thus providing a route to preparing a mechanical oscillator in a squeezed state of mechanical motion via measurement-induced squeezing. a.u., arbitrary units.

an optical cavity interferometer) to measure the mechanical motion and a "locker" (a radiation pressure force exerted by a laser on the mirror) to provide a viscous (feedback) force. The idea can also be understood in terms of the feedback loop in Fig. 2B, wherein the lower right optical feedback branch is replaced by an electrical path driving a second pump laser, which acts as a force actuator on the mirror.

Finally, although originally conceived as a potential limitation in gravitational wave detection, the parametric instability (blue detuned operation of the pump wave) can also be understood as

the result of amplification (negative damping) of the mechanical motion (13, 17, 47). In this sense, the instability is simply the threshold condition in which intrinsic mechanical loss is compensated by amplification. This threshold phenomenon and the subsequent regenerative mechanical oscillation have been studied as a new type of optomechanical oscillator (48). Above threshold, the oscillator is regenerative, and oscillation at microwave rates (49) has been demonstrated. Additionally, the phase noise of the oscillator has been characterized and observed to obey an inverse power dependence, characteristic of fundamental, Brownian noise (48). Quantum back action is also predicted to set a fundamental low-temperature limit to this linewidth (50). The ability to amplify mechanical motion is potentially useful as a means to boost displacements and forces sensitivity (51). Finally, returning to the analogy with atomic physics, it is interesting to note that regenerative oscillation (i.e., amplification of mechanical motion) would be expected to occur for trapped ions under blue detuned excitation.

Cavity Quantum Optomechanics

A mechanical oscillator has a set of quantum states with energies $E_N = (N + \frac{1}{2})\hbar\Omega_m$, where N is the number of mechanical quanta, and $N = 0$ denotes the quantum ground state. For a mechanical oscillator in the ground state, the ground state energy, $E_0 = \hbar\Omega_m/2$, gives rise to the zero-point motion, characterized by the length scale $x_0 = \sqrt{\hbar/2m\Omega_m}$. As noted earlier, this length scale sets the SQL of mirror position uncertainty in an interferometer such as in Fig. 1. The zero-point motion for structures shown in Fig. 3 ranges from $\sim 10^{-17}$ m for a macroscopic mirror to $\sim 10^{-12}$ m for the nanomechanical beam. Such small motions

are masked by the thermal motion of the mechanical oscillator, and to enter the regime where quantum fluctuations become dominant and observable requires that the mechanical mode's temperature satisfy $k_B T \ll \hbar\Omega_m$, equivalently a thermal occupation less than unity. Over the past decade, cryogenically cooled nanomechanical oscillators coupled to an electronic readout have been steadily approaching the quantum regime (19, 52, 53). Cavity optomechanical systems exhibit high readout sensitivity, in principle already sufficient to detect the minute zero-point motion of a microscopic system. The main challenge toward

observing quantum phenomena in cavity optomechanical systems lies in reducing the mechanical mode thermal occupation. Using conventional cryogenic cooling, the latter is challenging (1 MHz, corresponding to a temperature of only 50 μ K). However, in principle, cooling to these temperatures and even lower is possible with the use of optomechanical back action cooling.

If a sufficiently low occupancy of the mechanical oscillator is reached (using, for instance, a combination of cryogenic precooling and back action laser cooling), quantum phenomena of a mesoscopic mechanical object may arise. For example, the quantum back action by photons could become observable (54) or signatures of the quantum ground state. Moreover, the interaction of cold mechanics and a light field can give rise to squeezing of the optical field (55). This can be understood by noting that the mechanical oscillator couples the amplitude and phase quadrature of the photons. Moreover, the optomechanical coupling Hamiltonian has been predicted to allow quantum non-demolition measurement of the intracavity photon number (56, 57). The coupling afforded by radiation pressure might even allow the production of squeezed states of mechanical motion. These highly noninvasive quantum states have been produced for electromagnetic fields over the past decades, and producing them in the mechanical realm would be a notable achievement. Such highly nonclassical states may be possible to generate using measurement induced squeezing. In this method (22), one quadrature component of the mechanical oscillator motion is measured (and no information of the complementary variable is gained) so as to project the mechanical oscillator into a squeezed state of motion. This method (Fig. 4C) involves two incident waves and moreover requires that the mechanical frequency exceeds the cavity decay rate (the resolved sideband regime). A great deal of theoretical work has also been devoted to the question of entangling mechanical motion with an electromagnetic field, or even entangling two mechanical modes. Examples include proposals to achieve quantum superpositions of a single photon and a mirror via a "which path" experiment (58) or entangling two mirrors via radiation pressure (59).

Emerging Cavity Optomechanical Technologies

Cavity optomechanics may also enable advances in several other areas. First, the ability to provide targeted cooling of nano- and micromechanical oscillators (which are otherwise part of devices at room temperature) bodes well for practical applications because, in principle, conventional cryogenics are unnecessary. Beyond providing a better understanding of fluctuation and dissipative mechanisms, the fact that high displacement sensing is an important element of cavity optomechanics will have collateral benefits in other areas of physics and technology, ranging from scanning probe techniques (60) to gravitational-wave detection. Moreover, the ability to create all-optical photonic oscillators on a chip with

narrow linewidth and at microwave oscillation frequencies may have applications in radio frequency-photonics. Equally important, cavity optomechanical systems already exhibit strong nonlinearity at small driving amplitudes, which offer new functions related to optical mixing (61). Finally, although all current interest is focused on radiation-pressure coupling, cavity optomechanical systems based on gradient forces are also possible. Although aimed at a separate set of applications, there has been substantial progress directed toward gradient-force control of mechanical structures using cavity optomechanical effects (62–64).

Summary

The interaction of mechanical and optical degrees of freedom by radiation pressure is experiencing a paradigm shift in control and measurement of mechanical motion. Radiation pressure coupling has opened an extremely broad scope of possibilities, both applied and fundamental in nature. With the continued trends toward miniaturization and dissipation reduction, radiation pressure can become an increasingly important phenomenon that will probably allow advances, both in terms of technology as well as in fundamental science. It may well provide a way to probe the quantum regime of mechanical systems and give rise to entirely new ways of controlling mechanics, light, or both. It also seems likely that beyond precision measurement, there will be new technologies that leverage cooling and amplification.

References and Notes

- A. Ashkin, *Proc. Natl. Acad. Sci. U.S.A.* **94**, 4853 (1997).
- T. W. Hänsch, A. L. Schawlow, *Opt. Commun.* **33**, 68 (1975).
- D. Wineland, D. Dehmelt, *Bull. Am. Phys. Soc.* **20**, 637 (1975).
- A. Ashkin, *Proc. Natl. Acad. Sci. U.S.A.* **94**, 4853 (1997).
- V. B. Braginsky, *Measurement of Weak Forces in Physics Experiments* (University of Chicago Press, Chicago, 1977).
- M. C. Cox, *Phys. Rev. D Part. Fields* **23**, 1693 (1981).
- A. Dorel, J. D. McCullen, P. Mestiz, E. Vignes, H. Walther, *Phys. Rev. Lett.* **51**, 1550 (1983).
- B. S. Shrivastava, M. B. Gray, C. M. Moore, *Phys. Rev. D* **49**, 057101 (2004).
- D. E. McClelland, S. E. Whitcomb, *Phys. Rev. A* **69**, 057101 (2004).
- M. L. Dykman, *Sov. Phys. Solid State* **20**, 1306 (1978).
- S. Mancini, D. Vitali, P. Tombesi, *Phys. Rev. Lett.* **90**, 608 (1998).
- P. F. Cohodan, A. Heidmann, M. Pinard, *Phys. Rev. Lett.* **83**, 3174 (1999).
- C. H. Metzger, C. Knap, *Nature* **432**, 1002 (2004).
- T. J. Kippenberg, H. Rabl, A. C. Schreyer, K. J. Vahala, *Phys. Rev. Lett.* **95**, 033901 (2005).
- O. Arcut, P. F. Cohodan, T. Brunt, M. Pinard, A. Heidmann, *Nature* **444**, 71 (2006).
- S. Gigan, *et al.*, *Nature* **440**, 67 (2006).
- A. Schreyer, P. Del'Haye, M. Nooshi, K. J. Vahala, *Phys. Rev. Lett.* **97**, 243905 (2006).
- T. J. Kippenberg, K. J. Vahala, *Opt. Express* **15**, 17172 (2007).
- K. Jacobs, J. T. Hosten, H. M. Wiseman, S. Schreyer, *Phys. Rev. D* **60**, 538 (1999).
- K. C. Schwab, M. L. Roukes, *Phys. Today* **58**, 36 (2005).
- O. Arcut, *et al.*, *Phys. Rev. Lett.* **97**, 133601 (2006).
- C. M. Cox, K. S. Thorne, R. W. P. Dreier, V. D. Sandberg, M. Zehnermann, *Rev. Mod. Phys.* **52**, 341 (1980).
- V. B. Braginsky, F. Y. Khalili, *Quantum Measurement* (Cambridge Univ. Press, Cambridge, 1992).

- M. Pinard, Y. Hadjar, A. Heidmann, *Eur. Phys. J. D* **7**, 107 (1999).
- H. J. Kimble, Y. Levin, A. B. Matsko, K. S. Thorne, S. P. Vyatchanin, *Phys. Rev. D Part. Fields* **65**, 022002 (2002).
- S. Steinhilber, *Rev. Mod. Phys.* **58**, 699 (1986).
- V. B. Braginsky, S. P. Vyatchanin, *Phys. Lett. A* **293**, 228 (2002).
- H. G. Craighead, *Science* **290**, 1332 (2000).
- C. Ockel et al., *Phys. Rev. Lett.* **98**, 150802 (2007).
- D. Kleckner, D. Boumeester, *Nature* **444**, 75 (2006).
- G. Anetsberger, R. Riviere, A. Schreyer, O. Arcut, T. J. Kippenberg, *Nat. Photonics*, in press, preprint available at <http://arxiv.org/abs/0802.4384> (2008).
- J. D. Thompson, *et al.*, *Nature* **452**, 72 (2008).
- K. R. Brown, *et al.*, *Phys. Rev. Lett.* **99**, 137205 (2007).
- C. A. Regal, J. D. Teufel, K. W. Lehnert, preprint available at <http://arxiv.org/abs/0801.1827> (2008).
- L. Wilson-Rae, M. Nooshi, W. Zwerger, T. J. Kippenberg, *Phys. Rev. Lett.* **99**, 093902 (2007).
- C. J. Hood, T. W. Lynn, A. C. Doherty, A. S. Parkins, H. J. Kimble, *Science* **287**, 1447 (2000).
- P. Naimi, *et al.*, *Nature* **428**, 50 (2004).
- K. W. Murch, K. L. Moore, S. Gupta, D. M. Stamper-Kurn, *Nature* **461**, 561 (2008).
- F. Brennecke, S. Ritter, T. Donner, T. Esslinger, preprint available at <http://arxiv.org/abs/0807.2347> (2008).
- L. Wilson-Rae, P. Zoller, A. Imamoglu, *Phys. Rev. Lett.* **92**, 075707 (2004).
- L. Tian, P. Zoller, *Phys. Rev. Lett.* **93**, 266403 (2004).
- A. Naik, *et al.*, *Nature* **443**, 193 (2006).
- F. Marquardt, J. P. Chen, A. A. Clerk, S. M. Grvin, *Phys. Rev. Lett.* **99**, 093902 (2007).
- D. Leibfried, A. Wall, C. Monroe, D. Wineland, *Rev. Mod. Phys.* **75**, 281 (2003).
- A. Schreyer, R. Riviere, G. Anetsberger, O. Arcut, T. J. Kippenberg, *Mod. Phys.* **4**, 415 (2008).
- M. Poggio, C. A. Deghe, J. J. Mamin, D. Ruger, *Phys. Rev. Lett.* **99**, 072101 (2007).
- S. Vaidman, *Rev. Mod. Phys.* **57**, 689 (1985).
- H. Rabl, T. J. Kippenberg, T. Carmon, K. J. Vahala, *Opt. Express* **13**, 5293 (2005).
- M. Hossein-Zadeh, H. Roldan, A. Hajmami, K. J. Vahala, *Phys. Rev. A* **74**, 023813 (2006).
- T. Carmon, K. J. Vahala, *Phys. Rev. Lett.* **98**, 123901 (2007).
- K. J. Vahala, *Phys. Rev. A* **78**, 2 (2008).
- O. Arcut, T. Brunt, A. Heidmann, M. Pinard, *Phys. Rev. A* **73**, 033819 (2006).
- G. K. Knobel, A. C. Cleland, *Nature* **424**, 291 (2003).
- M. O. Lohmeyer, Q. Bou, B. Camarota, K. C. Schwab, *Science* **304**, 74 (2004).
- J. T. Hosten, *et al.*, *Phys. Rev. A* **59**, 1038 (1999).
- C. Fabre, *et al.*, *Phys. Rev. A* **49**, 1337 (1994).
- P. Allong, G. J. Milburn, D. F. Walls, *Phys. Rev. A* **37**, 2970 (1988).
- A. Heidmann, Y. Hadjar, M. Pinard, *Appl. Phys. B* **64**, 173 (1997).
- M. Marshall, C. Simon, R. Perce, D. Boumeester, *Phys. Rev. Lett.* **91**, 133901 (2003).
- S. Mancini, V. Giovannetti, D. Vitali, P. Tombesi, *Phys. Rev. Lett.* **98**, 120401 (2007).
- D. Ruger, R. Roldan, H. J. Mamin, B. W. Chu, *Nature* **430**, 329 (2004).
- M. Hossein-Zadeh, K. J. Vahala, *Photonics Technol. Lett.* **20**, 4 (2007).
- M. L. Povinelli, *et al.*, *Opt. Express* **13**, 8286 (2005).
- P. T. Rakich, M. A. Popovich, M. Soljacic, E. P. Ippen, *Nat. Photonics* **1**, 658 (2007).
- M. Eichenfield, C. P. Michael, R. Perata, O. Painter, *Nat. Photonics* **1**, 416 (2007).
- K. J. Acknowledgments support from the Alexander von Humboldt Foundation, T.J.K. gratefully acknowledges support via a Max Planck independent Junior Research Group, a Marie Curie Excellence Grant, the Deutsche Forschungsgemeinschaft (DFG) project "Ground State Cooling", and Nanosystems Initiative Munich. The authors thank T. W. Hänsch for discussions.

10.1126/science.1156392

Magmatically Triggered Slow Slip at Kilauea Volcano, Hawaii

Benjamin A. Brooks,¹ James Foster,¹ David Sandwell,² Cecily J. Wolfe,¹ Paul Okubo,³ Michael Poland,³ David Myer²

The discovery, primarily at subduction zones, of spontaneous aseismic slip events (slow slip events, SSEs) has led to the recognition that SSEs represent behavior between steady sliding and dynamic earthquake rupture. Furthermore, slow slip, down dip of plate boundary seismity (30- to 45-km depth), may delineate the lower boundary of the locked plate interface and constrain the fault geometry of great magnitude (M 8 to 9 earthquakes) (*1*). SSEs have also been found recently at depths shallower than ~10 km on the decollement (or related faults) underlying the mobile south flank of Hawaii's Kilauea volcano (*2, 3*). The Kilauea SSEs occur in a

different tectonic setting and rheological context, up dip of the region of decollement seismity, although potentially within the locked portion that can rupture in earthquakes greater than M 7 (*4, 5*). Within a rate-state-dependent friction theoretical context, SSEs are believed to occur at the transition between unstable and stable sliding. A general understanding, however, of SSE initiation is still unresolved. We show that a dike intrusion in June 2007 triggered an SSE at Kilauea.

During 17 to 19 June 2007, Kilauea was intruded by a dike that originated from the volcano's summit and extended its east rift zone (ERZ) by as much as ~1 m (*6*). We created an interferogram from two Ad-

vanced Land Observing Satellite synthetic aperture radar images to produce a high resolution map of the intrusion (Fig. 1A). The interferogram indicates subsidence at Kilauea's summit and two uplift lobes (separated by a narrow subsidence zone) related to the dike intrusion. Continuous Global Positioning System (GPS) data further revealed anomalous, southeast directed, centimeter-scale horizontal motions at sites far from the dike (stations PGF1, 5, and 6 in Fig. 1 and Fig. S1, A to D) that cannot be explained by models of the dike intrusion and are best explained as arising from an SSE. Horizontal motions from the four previous SSEs are nearly identical, although the 17 June event has a larger magnitude (Fig. 1A) (*2, 3*). Additionally, south flank coastal sites exhibit subsidence not predicted by the dike model, although similar to the vertical motion during prior SSEs (Fig. S1E). Lastly, ~24 hours after dike-related seismity started, seismity increased sharply in the north-south trending region that previously displayed SSE triggered seismity (*2, 3*) (Fig. 1A). Although this region has experienced past elevated seismity unassociated with SSEs, it was quiescent during previous ERZ dike intrusions in 1997 and 1999, thus, elevated activity during the 2007 event is consistent with SSE occurrence.

Hourly GPS positions show that SSE-related motions likely began ~15 to 20 hours after the intrusion, suggesting that the intrusion triggered the SSE (Fig. 1B). We further test this hypothesis by modeling stress changes in the south flank due to secular deformation and the intrusion (Fig. 1C). The models imply that the intrusion increased the Coulomb failure stress on shallowly landward-dipping fault planes (the presumed geometry of the SSE slip surfaces) by roughly the same amount as secular deformation since the last SSE [deep rift opening combined with decollement creep (*4*)]. These results, in concert with the observation that no previous SSEs were directly preceded by intrusions but rather occurred during times of normal background deformation, suggest that both extrinsic (intrusion triggering) and intrinsic (secular fault creep) fault processes produce SSEs at Kilauea.

References and Notes

1. S. V. Schwartz, *J. Geophys. Res.* **102**, 10,129 (1997).
2. B. A. Brooks, J. H. Foster, M. F. Bevis, C. J. Wolfe, M. J. Bevis, *Earth Planet. Sci. Lett.* **246**, 207 (2006).
3. P. Segall, L. K. Desmarais, D. Shelly, A. Miklius, P. Cervelli, *Nature* **442**, 71 (2006).
4. V. Cayol, J. H. Dieterich, A. T. Okamura, A. Miklius, *Science* **288**, 1243 (2000).
5. S. Okuma, R. Burgmann, *J. Volcanol. Geotherm. Res.* **150**, 163 (2006).
6. M. Poland et al., *EOS Trans. Am. Geophys. Union* **89**, 37 (2008).
7. We thank A. Miklius, K. Kamibayashi, M. Salo, and P. Segall for their collaboration on operation of the Kilauea GPS network. This work was supported by NSF's Geophysics program.

Supporting Online Material

www.sciencemag.org/cgi/content/full/321/5893/1177/DC1

Materials and Methods

Fig. S1

References

12 April 2008; accepted 10 June 2008

10.1126/science.1155907

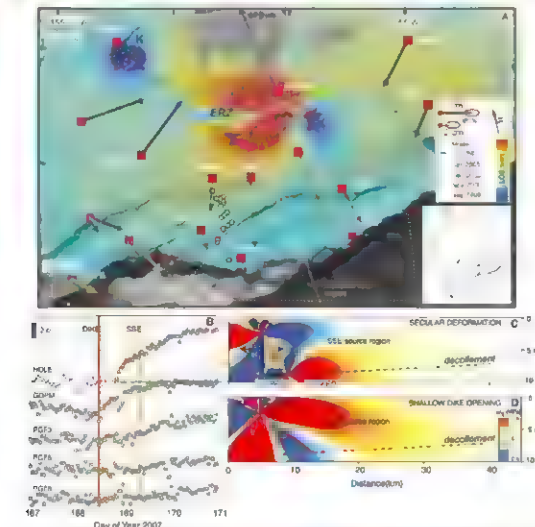


Fig. 1. (A) Line-of-sight interferometric displacement map from ALOS PALSAR (Phased Array Type L-Band Synthetic Aperture Radar) ascending acquisitions in fine beam dual-polarization mode (FBD-HH, 14 MHz) on 5 May and 20 June 2007. K, Kilauea summit caldera; ERZ, east rift zone. Black vectors with arrows show static GPS horizontal displacements estimated from times around the dike intrusion event. Because of large dike-related displacements, sites are plotted with two different scales. Other colored vectors at sites PGF1, 5, and 6 show horizontal displacements from previous SSEs; gray vectors show expected displacements due to the dike intrusion (see also Fig. S1). White circles show earthquake epicenters (from U.S. Geological Survey Hawaii Volcano Observatory catalog) > 5 days from 17 June for all events between depths of 5 to 10 km. White circles with thicker outline indicate north-south band of events that occurred 24 hours after the dike intrusion started. (B) GPS position (projected onto average motion direction) time series for selected sites. Approximate timing of dike initiation and SSE initiation indicated with vertical colored bars. Coulomb failure stress models for (C) secular deformation and (D) shallow dike opening scenarios.

Bang! Month-Scale Eruption Triggering at Santorini Volcano

Victoria M. Martin,¹ Daniel J. Morgan,^{2*} Dougal A. Jerram,¹ Mark J. Caddick,³ David J. Prior,⁴ Jon P. Davidson¹

Many large silicic volcanic eruptions are thought to be triggered by intrusion of hotter, more mafic melt into an existing magma chamber at depth, but the timing between trigger and eruption has been difficult to determine. We used diffusion profiles of olivine crystals from biotite of andesite magma to show that the 1925–28 eruption of Nea Kameni Volcano, Santorini (Greece) was triggered by a mafic magma intrusion about 1 month earlier.

The 1925–28 eruptive cycle of the Nea Kameni volcanic center produced a silicic magma (dacite) with entrained fragments (enclaves) of a more mafic magma (basaltic andesite). These enclaves represent a pre-eruptive recharge event, where hot, basaltic andesite intruded into the base of the cooler, dacitic magma chamber (1). As the basaltic andesite chilled, volatile saturation occurred, and the andesite overturned, rapidly distributing enclaves and heat into the overlying dacite, triggering eruption in a manner analogous to that

proposed for eruptions at Thera and elsewhere (2, 3).

Enclaves within the 1925–28 lava flow contain zoned olivine crystals that record a complex and intriguing history. Magnesian-rich crystal cores imply derivation from a basaltic parent melt but are hosted in andesitic enclaves, suggesting remobilization of basaltic crystallization products by a later, andesitic melt. This hybrid basaltic andesite was then intruded into the cooler dacitic magma chamber, where it quenched and solidified while transferring its heat to the overlying material (1). During this process, iron-rich rims formed on olivine crystals, and an adjacent crystal framework of plagioclase feldspar grew. Diffusive exchange between the Mg-rich crystal cores and their Fe-rich rims occurred during the period between input of the volcanic trigger and subsequent eruption of the volcano.

Fe-Mg diffusion rates within olivine are relatively well constrained (4) and both strongly temperature

dependent and anisotropic. Plagioclase-melt thermometry (5) constrains the maximum intrusion temperature of the Santorini basaltic andesite hybrid at $1080 \pm 30^\circ\text{C}$ (2σ). Olivine fugacity (f_{O_2}) was constrained between 10^{-16} and 10^{-13} bars, following (6).

Our method is similar to that used previously by (7), but we determined the Fe-Mg diffusion distance through back-scattered electron (BSE) compositional (z) contrast images (Fig. 1A), calibrating with electron microprobe point analyses. Crystallographic axis orientations were determined by electron back-scatter diffraction and U-stage (three-dimensional) petrography. We modeled diffusion profiles by using a two-dimensional, finite-difference method with composition, orientation, and activity dependent diffusion parameters (Fig. 1, A to C). Further details can be found in the supporting online material.

The best fit of the forward model results to observed diffusion profiles for five crystals (Fig. 1D) implies that the basaltic andesite intruded into the magma chamber 15 to 75 days before eruption, with a >95% confidence interval of between 20 and 60 days. Understanding this recharge-to-eruption duration for previous eruptive cycles at Santorini, and potentially other volcanoes, is particularly valuable because the input of batches of recharging magma is detectable seismically. Thus, the use of previously erupted materials can, via this approach, obtain characteristic time scales that may ultimately lead to improved hazard forecasts.

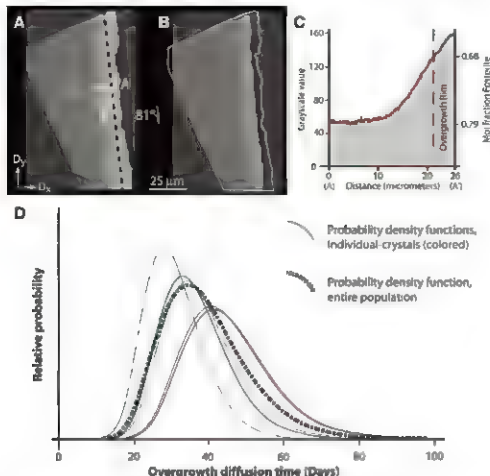


Fig. 1. Results from enclave sample K2-01. (A) Image of crystal OL_08 showing diffused rim zone (D), overgrowth to right of dashed line, tick mark displaying dip of crystal face, and modeled components of diffusion (D_{Fe} , D_{Mg}). Fe-rich compositions appear as paler gray shades. (B) Result of best fit forward model, at 33 days equilibration. (C) Traverse A-A' showing model (red line) and raw data (gray lines) with gray scales and calibrated compositions. (D) Fine lines show intrusion-to-eruption time probability distributions for five crystals (calculated by using the combined temperature and f_{O_2} uncertainties); bold dash-dotted line shows the integrated probability for the entire population.

References and Notes

1. V. M. Martin, M. S. Holness, D. A. Jerram, J. Volcanol. Geotherm. Res. 154, 89 (2006).
2. T. H. Druitt et al., *Geol. Soc. London Mem.* 19, 1 (1999).
3. M. L. Coombs, J. C. Elchertberger, M. J. Rutherford, *Contrib. Mineral. Petrol.* 140, 99 (2000).
4. R. Dohren, S. Chakraborty, *Phys. Chem. Miner.* 34, 409 (2007).
5. K. Petráš, *Am. Mineral.* 90, 336 (2005).
6. G. F. Zellmer et al., *J. Volcanol. Geotherm. Res.* 140, 171 (2005).
7. F. Costa, *M. Dungan, Geology* 33, 837 (2005).
8. This work was funded by grant NE/C510316/1 of the Natural Environment Research Council of the UK, and by ETH Research Funds (to M.J.C.). SEM imaging was assisted by E. Camilleri (Leeds). The authors thank two anonymous reviewers for input, which encouraged f_{O_2} variations to be considered and improved the manuscript. Editorial assistance from R. B. Hanson is warmly appreciated.

Supporting Online Material

www.sciencemag.org/cgi/content/full/321/5839/1178/DC1

Materials and Methods

References

24 April 2008; accepted 10 June 2008

DOI: 10.1126/science.1159584

¹University of Durham, Department of Earth Sciences, South Road, Durham DH1 1TA, UK. ²University of Leeds, School of Earth and Environment, Leeds LS2 9JT, UK. ³Institute for Mineralogy and Petrology, Eidgenössische Technische Hochschule (ETH) Zürich, Clausstrasse 25, Zürich 8092, Switzerland. ⁴Earth and Oceanic Sciences, University of Liverpool, 4 Brownlow Street, Liverpool L69 3GP, UK.

*To whom correspondence should be addressed. E-mail: d.j.morgan@leeds.ac.uk

The Structure of an Open Form of an *E. coli* Mechanosensitive Channel at 3.45 Å Resolution

Wenjian Wang,^{1*} Susan S. Black,^{2*} Michelle D. Edwards,^{2*} Samantha Miller,² Emma L. Morrison,² Wendy Bartlett,² Changliang Dong,² James H. Walsmith,^{1,†} Ian R. Booth^{2,†}

How ion channels are gated to regulate ion flux in and out of cells is the subject of intense interest. The *Escherichia coli* mechanosensitive channel, MscS, opens to allow rapid ion efflux, relieving the turgor pressure that would otherwise destroy the cell. We present a 3.45 angstrom-resolution structure for the MscS channel in an open conformation. This structure has a pore diameter of ~13 angstroms created by substantial rotational rearrangement of the three transmembrane helices. The structure suggests a molecular mechanism that underlies MscS gating and its decay of conductivity during prolonged activation. Support for this mechanism is provided by single-channel analysis of mutants with altered gating characteristics.

Ion channels display two intrinsic properties: selectivity and gating in response to specific stimuli. Despite extensive study, the structural changes that accompany the gating transition from closed (nonconducting) to open (conducting) states are poorly understood for many channels. Bacterial channels have proved to be excellent experimental systems for analysis and have provided invaluable insights into all facets of channel biology (1–6). The bacterial mechanosensitive channels, MscS and MscL, open in response to membrane tension so that small osmotically active ions and molecules can exit the cell (6, 7), allowing bacteria to survive hypo-osmotic shocks equivalent to transmembrane pressures > 14 atm (8). The free energy required to open these channels is relatively small, ~28 kJ/mol and ~46 kJ/mol for MscS and MscL, respectively (9, 10).

MscS and MscL have been characterized in detail, including characterization by three-dimensional crystallographic analysis (7, 11, 12). The crystal structure of MscL has been determined in a nonconducting state (7, 11). The first crystal structure for MscS revealed the protein was a heptamer with a sevenfold rotational axis parallel to the normal axis of the membrane (11). Each monomer has three N-terminal transmembrane helices, these are named TM1 (residues 30 to 50), TM2 (residues 60 to 90), and TM3 (residues 95 to 126) (11, 13). A pronounced kink centered at G113 (14) separates TM3 into the pore-lining TM3a helix (S95 to L111) and the TM3b helix (G113 to M126), which connects to the C-terminal domain. Seven TM3a helices are arranged in a helical barrel, the central axis of

which marks out the presumed route of ions across the membrane. The seven TM3b helices point outwards from the central barrel tangential to the pore axis. The cytoplasmic C-terminal domains from each monomer are assembled by the sevenfold symmetry into an oval-shaped compartment with a large central cavity that is contiguous with the TM3a helical barrel (11). Entrance to the central cavity is through seven 10-by-8 Å portals arranged around the side of the oval. The original crystal structure was assigned as an open form (11). However, subsequent analysis and modeling established that the structure represents a nonconducting state (15). In the closed form, the side chains of L105 and L109 are inserted into the pore lumen. These two rings of bulky hydrophobic side chains and the hydrophobic nature of TM3a have been proposed to prevent wetting of the channel pore, thus blocking the passage of ions, including the hydronium ion, this has been termed a “vapor lock” (15, 16).

A conserved pattern of glycine and alanine residues in TM3a of MscS (termed “knobs and holes”) is important in gating and also in forming the tightly packed, symmetrical TM3a arrangement seen in the nonconducting form (17). As part of this investigation, we identified A106V as one of a series of mutants with unique electrophysiological properties *in vitro* that are sufficiently distinct from the wild type to allow us to generate new crystallographic insights. Crucially, the mutant is fully functional *in vivo* (17). Here we report the crystal structure of an open/conducting form of MscS and propose a structural model for the transition from the closed to the open state. Crystal structures are necessarily static structures, and there may be additional open and/or closed states *in vivo*. We have therefore supported our model by testing its predictions with an analysis of mutants created by site-directed mutagenesis.

A106V structure. The A106V protein assembles in the membrane, proteins in hypo-osmotic

shock assays, and gates at pressures intermediate between wild type (WT) MscS and MscL (Fig. S1) (17, 18). The principal distinctions of the mutant are its increased resistance to pressure and ability to adopt a reduced conducting state at high pressures. Overall, therefore, the mutation by itself does not grossly change protein activity *in vivo*. MscS A106V was crystallized following the same protocol developed for WT MscS (11), and the structure was solved using molecular replacement to 3.45 Å resolution. The transmembrane helices were removed from the molecular-replacement model and fitted to unbiased difference electron density (19). A106V MscS is a heptamer and, like the WT structure, is composed of three cytoplasmic domains and a transmembrane region of three helices (Fig. 1, A and B). The cytoplasmic portion is essentially unchanged from the wild type (7, 11), but there are major changes in the transmembrane domain (Fig. 1B). On the basis of these differences, we identify the A106V structure as an open/conducting state of MscS, in contrast to a closed/nonconducting form seen in the WT protein crystal structure. In the wild type, nonconducting structure, A106 is packed against G108 from the neighboring subunit so that structural rearrangement would be required to accommodate a valine side chain (Fig. S2A). We suggest that it is the additional bulk of 106V that hinders formation of the state previously observed in the WT crystals (11).

Pronounced changes in transmembrane region. Relative to the closed structure, TM1 and TM2 rotate as a rigid unit by ~45° clockwise (Fig. 1B and Fig. S3) (20) in addition to the rotation, TM1 and TM2 helices increase their tilt by 15° with respect to the sevenfold axis. This motion results in their burying more volume in the membrane. The loop between TM1 and TM2 now interacts with the surface of TM3b within the same monomer and with TM3a of the neighboring monomer (Fig. S2B). We suggest that it is these specific interactions that stabilize the state we observe. Importantly, these interactions are all remote from the A106V mutation, and 106V occupies a large open pocket (Fig. S2B). Thus, although the A106V mutation has enabled an open form to be trapped, we do not believe that the side chain has created an artefactual open state.

Accompanying the changes in TM1 and TM2, TM3a pivots around the Co of G113 (Fig. 1C). TM3b, which is attached to the cytoplasmic domain, remains essentially unchanged. In the mutant, the TM3a helices have moved outwards from the central axis and have rotated around their axis by ~15° clockwise (Figs. 1C and 2A). At the N-terminal end of TM3a, the Co of S95 shifts by over 9 Å and at the C-terminal end, the Co of L109 moves by ~4 Å. In permitting this movement of TM3a, G113 does not adopt Ramachandran angles forbidden to other amino acids, consistent with both its lack of conservation in other MscS proteins and its insensitivity to mutation in *Escherichia coli* (21, 22). It has been proposed that during the

¹Centre for Biomolecular Sciences, The North Haugh, University of St. Andrews, KY16 9ST, Scotland, UK. ²School of Med. and Sci., Institute of Medical Sciences, University of Aberdeen, Foresterhill, Aberdeen, AB25 2ZD, Scotland, UK.

*These authors contributed equally to this work.

†To whom correspondence should be addressed. E-mail: walsmith@st-and.ac.uk (J.H.W.); i.r.booth@abdn.ac.uk (I.R.B.).

opening of the channel, TM3a lengthens and TM3b shortens, such that the junction between TM3a and TM3b moves from G113 to G121 (27). The struc-

tural conservation of the TM3a to TM3b junction in the mutant and WT crystal structures does not support this hypothesis.

An open structure for MscS. In the open structure, the helical axes of the seven TM3a helices are parallel to the sevenfold axis, and

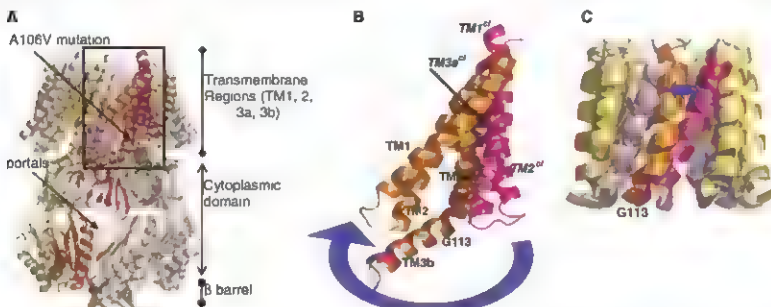


Fig. 1. Conformation changes between the A106V and WT structures. (A) Structures are oriented such that the sevenfold axis is parallel to the membrane normal. For the A106V structure, one monomer (subunit A) is colored orange; the remaining six subunits are shown in gold. The site of the A106V mutation is highlighted. For the WT structure, the A subunit is colored purple, and the remaining six subunits B to G are shown in lilac. One of the seven portals through which ions are presumed to enter from the cytoplasm is marked. The cytoplasmic domain is essentially unchanged from the WT structure; however, there are profound changes in the transmembrane helices, which are boxed. An orthogonal view is shown in Fig. S3. The environments of A106 and 106V in their respective structures are shown in more detail in Fig. S2. (B) Expanded view of the boxed transmembrane helices of

the A subunit. The helices are colored and oriented as above. The blue arrow represents the motion from the closed to the open state. The helices are labeled TM1, 2, 3a, and 3b in accordance with the text. In the A106V structure, TM1 and TM2 have undergone a rigid-body clockwise rotation relative to their position in the closed structure (labeled TM1^{cl} and TM2^{cl}). TM3a also adjusts its position relative to the closed form (TM3a^{cl}). There is only a small change in TM3b. G113, the pivot point, is labeled. (C) Central pore showing only TM3a colored and oriented as in (A). Comparing the WT and A106V channel structures, TM3a has pivoted around G113. The blue arrow denotes the movement from closed to open states. As a result of this motion, the helical axis of TM3a in the A106V structure is parallel to the membrane normal, rather than at an angle as in the WT structure.

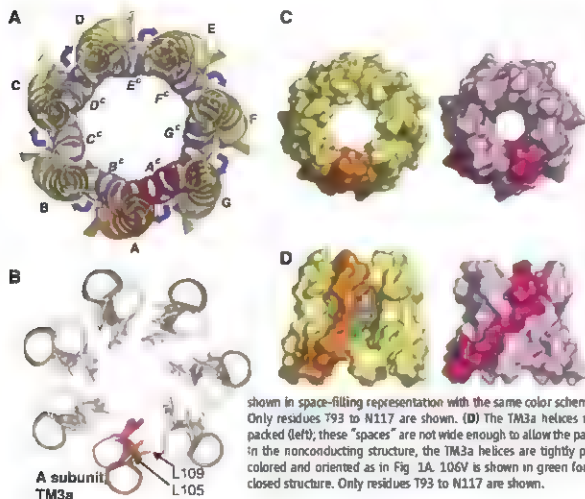


Fig. 2. A106V represents an open structure. (A) Superposition of the helical pore (helix TM3a) in MscS. The color scheme is the same as in Fig. 1A. The subunits are labeled; the labels for those in the closed structure are on the inside. The TM3a helices in the A106V MscS structure move out from the center and align parallel to the sevenfold axis. The blue arrows denote motion from the closed to the open state. The helical pore is oriented such that one is looking from the periplasm into the cytoplasm. (B) The L105 and L109 side chains, which fill the central pore in closed structure, have moved out of the pore in the A106V structure, creating the open channel by breaking the vapor lock. This motion is akin to the opening of camera iris. The color scheme is the same as in Fig. 1A and the orientation as in (A). (C) The pore formed by the seven TM3a helices in the A106V MscS (left) has a diameter of ~13 Å and is assigned as an open (conducting) state of MscS. The WT channel has a diameter of 4.8 Å (right) and is thought to represent a closed (nonconducting) channel. The TM3a helices are

shown in space-filling representation with the same color scheme as in Fig. 1A and the same orientation as in (A). Only residues 793 to N117 are shown. (D) The TM3a helices in the conducting A106V structure are not tightly packed (left); these "spaces" are not wide enough to allow the passage of molecules but may interact with the lipids. In the nonconducting structure, the TM3a helices are tightly packed (right). The open and closed structures are colored and oriented as in Fig. 1A. 106V is shown in green for the open structure, and A106 is in green for the closed structure. Only residues 793 to N117 are shown.

to the membrane normal (Fig. 1C). This is quite distinct from the arrangement seen in the closed structure, where TM3a helices are diagonal to the sevenfold axis. The interior of the pore remains predominantly hydrophobic, as the main-chain atoms are all involved in helical interactions and do not present a polar surface. However, we cannot experimentally determine the extent of TM3a solvation. As a result of these changes in TM3a, the

side chains of L105 and L109 have moved out from the center of the pore in the A106V mutant structure, in a manner reminiscent of the plates of a mechanical camera iris (Fig. 2B). This breaks the vapor lock by expansion of the pore, a mechanism suggested from the modeling of nanotubes (16). We expect that this represents an open channel rather than a subconducting state, because the A106V mutant channel only forms subconduct

ing states when subjected to high tension close to that required to open MacS. Such conditions are unlikely to prevail in protein crystals.

The program HOLE (23) estimates that the pore in the open structure has a diameter of just under 13 Å, as compared with 4.8 Å for the closed structure (7, 11) (Fig. 2C). At 13 Å, this is very clearly conducting and would allow the passage of solvated ions and small solutes. The outer membrane protein Wza, which allows the passage of complex oligosaccharides, has a helical barrel with a comparable internal diameter of 17 Å (24). The increase in diameter of 8 Å is similar to that previously predicted (9). The central pore in the A106V structure is now wider than the lateral cytoplasmic portals and suggests that it is the flow into the cytoplasmic central cavity through the portals, not out through the TM3a pore, that limits the observed conductivity to 1200 pS (where $1 \text{ S} = 1 \text{ A/V}$) (9, 10). This is consistent with the increased conductivity observed for a deletion mutant lacking the base of MacS, consequently creating a larger opening into the central cytoplasmic cavity (Fig. 1A) (22).

The A110-115 "switch." The change in position of TM3a with respect to TM3b is accompanied by a shift of A110 (TM3a) from one side of the L115 side chain (TM3b) of a neighboring monomer to the other side (Fig. 3A). Analogous to a switch, we believe this interaction defines an open and closed state of the channel. Because the open state is higher in energy, this switch will stabilize the open form by creating a kinetic barrier. To test this hypothesis, mutations were introduced: A110 to G and V and L115 to G, I, and V. All of the mutant proteins were inserted into the membrane at levels comparable to the wild type (Fig. S4). An A110V mutant is extremely difficult to open ($P_L P_H$ (18) $\sim 1.08 \pm 0.04$, $\sim 42 \text{ kJ/mol}$) (25) as compared with $P_L P_H \sim 1.59$; 28.4 kJ/mol for WT MacS, exhibits reduced conductance (17), and does not protect against osmotic downshock (Fig. S1). The A110G mutant protects against downshock but opens at lower pressures than does the wild type ($P_L P_H \sim 2.2$; $\sim 20 \text{ kJ/mol}$) and is unstable in the open state (Fig. 4 and Fig. S1). L115V also protects against downshock and opens at lower pressures than does the wild type ($P_L P_H \sim 2.1$; $\sim 22 \text{ kJ/mol}$), though its behavior was complex (Fig. 4B and Fig. S1). These observations are consistent with our model, which suggests that the bulkier A110V would require more structural distortion to go past L115. In contrast, the A110G and L115V mutants having smaller side chains at these positions, would allow easier interconversion between closed and open states, and thus open at a lower pressure and create flickery channel behavior (Fig. 4).

Functional analysis of the gating transitions. In the gating transition, the methyl group of A102 has to slide across the protein surface of TM3a from the neighboring subunit (Fig. 3B). This would represent an obstacle to closure that could stabilize the open form. We created single mutants at A102 to test this and extend our analysis of TM3a (17) (Fig. S1). An A102G mutant opened at a similar pressure to that of the wild type ($P_L P_H$

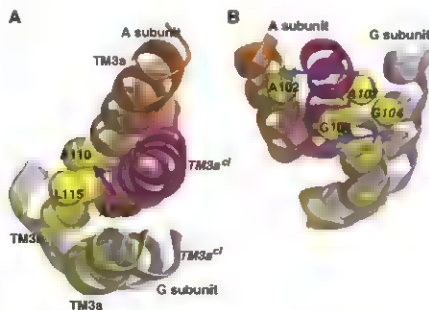
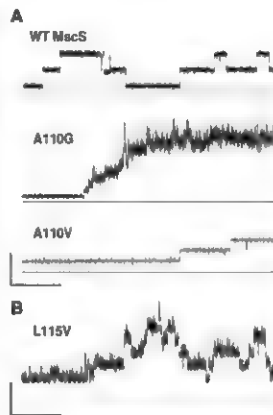


Fig. 3. Structural features of the channel transition. (A) In the closed structure, the side chain of A110 (shown as a red sphere) sits in a pocket on one side of the L115 side chain in TM3b from the neighboring G subunit. In the open A106V structure, A110 (shown as a yellow sphere) sits in another pocket on the opposite side of the L115 side chain. These different positions of A110, akin to a switch, define the closed and open states. The remainder of the molecule is colored as in Fig. 1A. The blue arrow defines the motion from closed to open. (B) The methyl group of A102 from the A subunit must cross the face of TM3a from the G subunit, creating a guide to the opening and closing. The A102G mutant opens and closes more easily than the WT channel, consistent with the removal of this guide. The double mutant A102G/L104A reintroduces a methyl group, re-creating the guide, and is indeed essentially WT. The molecules are colored the same as in Fig. 1A.

Fig. 4. Mutations at A110 and L115 affect MacS channel opening. Patch clamp analysis of excised protoplast membrane patches expressing WT or mutant MacS protein. (A) WT channels show step-like opening and closing events. Substitution of A110 to glycine produces channels that are unstable in the open state; thus openings are rapidly followed by closures giving channel activity of a flickery appearance. Substitution to valine leads to a channel that does not open fully; its open state is stable but exhibits a decreased conductance. (B) Exchange of L115 for a smaller valine residue disrupts the ability of the channel to open fully and/or remain open. Vertical scale bar, 50 pA; horizontal scale bar, 200 ms.



-1.54 ± 0.11 , -29 kJ/mol) but was unable to sustain the fully open state (Fig. 5A). The A102G mutant exhibited a flickery channel phenotype that undergoes rapid adaptation (Fig. 5B). This is consistent with a model in which the loss of the methyl group reduces the barrier between the states and allows very rapid cycling between them once sufficient pressure is applied to gate the channel. An A102V mutation significantly increased the pressure to gate the channel ($P_{1/2}$, -1.26 ± 0.04 , -36 kJ/mol) (Fig. 5C), presumably because the bulkier valine side chain cannot easily slide across the surface.

Single-mutant analysis can prove misleading, as changing one residue may modify a number of interactions, and this may have the consequence of potentiating kinetic pathways that are cryptic in the WT protein (26). To further test our model, we sought to identify residues that couple with A102G using mutant cycle analysis, which has proved invaluable in both enzymology and the study of ion channels (26–30). A second mutation was introduced either at G104, a position the model suggests should be coupled, or at G101, which the model predicts is not coupled. The A102G/G104A double mutant exhibited both a WT gating pressure ($P_{1/2}$, -1.50 ± 0.02 , -30 kJ/mol) and a stable open state (Fig. 5C and Fig. S1). Pressure difference calculations for this mutant cycle were greater than zero (0.38), indicating coupling between the two residues (Fig. 5D) (26, 29–31).

The double mutant A102G/G104A reintroduces a methyl group (in TM3a from the neighboring subunit) opposite A102G (Fig. 3B). Our model had suggested that this reintroduction of the methyl group would re-create the kinetic barrier of a methyl group moving across a protein surface (Fig. 5), and this appears to be the case. In contrast, the G101A/A102G double mutant exhibited stable channel openings, but the pressure required for opening was the same as that for the G101A single mutant alone ($P_{1/2}$, -1.37 ± 0.05 , -33 kJ/mol) (Fig. 5C and Fig. S1). The calculated pressure difference for the mutant cycle was close to zero (0.02, Fig. 5D), supporting our structural model, which suggests the independence of these two residues (30, 31).

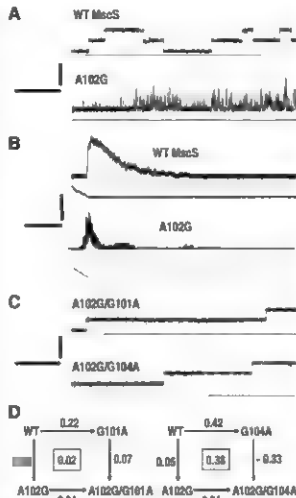
A molecular model for adaptation. During sustained application of subunitizing pressures to membrane patches, *E. coli* MscS channels will decay to a nonconducting state; this is termed “adaptation” (1, 8, 21, 22, 32). Adaptation has two contributory processes: inactivation and desensitization. Inactivated channels can be reactivated after resting in the absence of pressure (21), whereas desensitized channels can be reactivated by increasing the pressure. These processes are common in many channels and receptors (33), yet structural understanding is sparse. In this open form of MscS, the seven TM3a helices are no longer close-packed but are physically separated (Fig. 2D). In returning to the closed form, the very specific pattern of knobs and holes of TM3a must

be re-established. There is the possibility that during this “repacking” the protein molecule could become conformationally trapped by mismatching the knobs and holes. The rate of adaptation would then be proportional to the rate of cycling between open and closed states. This is indeed the case: At pressures high above the gating threshold, where the channel is open with no cycling between states, no decay is observed. The mutant A102G, which rapidly flickers between open and closed states, exhibits very rapid adaptation (Fig. 5B). Changes that increase the separation between TM3a helices are predicted by our model to lead to more rapid adaptation. In both structures Q112 points into the pore and in the closed form makes contacts with several other residues. The Q112G mutant that would remove this “guiding hand,” shows an extremely rapid decay of conductivity (21). Because MscK (an *E. coli* homolog of MscS) has much bulkier side chains in TM3a, one might predict a more constrained pathway to the closed state. Indeed, MscK does not exhibit any decay of conductivity (8). Rapidly adapting MscS mutants have been described with changes that are located in TM3b and in the loop between TM1 and TM2 (21, 34). Our model suggests that these mutations perturb protein/protein interactions, as TM1 TM2 crosses the face of TM3b (Fig. 1B) during the transition between states.

Model for channel gating. The rearrangement of the three transmembrane helices between the closed and open conformations of MscS presents a structural basis on which we can now propose a molecular model for channel gating. Under excessive outwardly directed osmotic pressure, the density of lipids in the cytoplasmic membrane is decreased. TM1 and TM2 respond to this decrease in density by adjusting their conformation to increase their buried volume. We suggest that the rotation and tilting movement of TM1 and TM2 act as a lever on TM3a. This rigid-body movement of TM1 TM2 is conceptually similar to the movement of the “voltage sensing paddle” in the voltage-dependent potassium channel KvAP (35–38). TM3a then pivots around Q112 to G113 while the rest of the structure remains essentially unchanged. This movement of TM3a withdraws the side chains of L105 and L109 from the central pore, breaking the vapor lock and allowing solvated ion transport (Fig. 2). Leucine rings are a central motif in many channels, and mutational analysis has shown similar roles to those proposed for MscS (39–41). The tight packing of these leucine residues in the closed form is important for protein stability and function. Single mutants of L105 or L109 to smaller amino acids affect the assembly of the channel in the membrane (42). Notably, the channels that do form still gate but at lower pressures, suggesting that one leucine ring alone can block conduction. This is analogous to mutants affecting the leucine rings in the acetylcholine receptor that lower the concentration of agonist required to gate the channel (40, 41).

The opening and closing of channels is central to biology, yet is still poorly understood at a mo-

Fig. 5. Alanine at position 102 is important to maintain the open state of MscS. (A) to (C) Patch clamp recordings of WT and A102G mutant MscS channels. (A) A102G mutation renders the channels unstable in the open state. Vertical scale bar, 50 pA; horizontal scale bar, 200 ms. (B) Prolonged application of pressure (shown in lower panel of both traces) causes open WT channels to adapt and become nonconducting. Thus, the current trace (upper panel in each recording) returns to baseline in the presence of applied pressure. A102G mutant channels rapidly adapt to sustained pressure. Vertical scale bar, 200 pA and 340 mV; horizontal scale bar, 10 s. (C) Reciprocal double mutations at positions 102/101 or 102/104 return the stable, fully open conformation. Vertical scale bar, 50 pA; horizontal scale bar, 200 ms. (D) Mutant cycle analysis (26) of the gating pressures (derived from patch clamp analysis) for each single and double mutant. The $P_{1/2}$ ratio for each single and double mutant was measured as described in the SOM (18). The $P_{1/2}$ ratio difference between the single mutants and the wild type, and between double mutants and single mutants, was calculated to measure the change associated with the introduction of the indicated mutation. Summation across the diagram (i.e., comparing the effect of introducing a specific mutation into either the WT or mutant channel) indicates that, whereas residue G101 does not couple to A102 (difference value of 0.02 is close to zero), G104 and A102 appear to energetically interact (difference value of 0.38 is greater than zero) (26–31).



lular level. The use of mutants with modified gating kinetics may prove a widely applicable approach to crystallize different channel conformations. By combining functional data with an open structure of the MacS channel, we have described the transitions between closed and open forms that involve tilting and separation of the transmembrane helices reminiscent of a camera iris.

References and Notes

1. B. Aktulga, A. Anishkin, S. Sukharev, *J. Gen. Physiol.* **125**, 143 (2005).
2. J. R. Booth, M. D. Edwards, S. Miller, *Biochemistry* **42**, 10045 (2003).
3. R. Dutzler, E. B. Campbell, M. Cadene, B. Y. Chait, R. MacKinnon, *Nature* **415**, 287 (2002).
4. Y. Jiang et al., *Nature* **417**, 515 (2002).
5. Y. Jiang et al., *Nature* **417**, 523 (2002).
6. C. Klug, *Nature* **436**, 647 (2005).
7. S. Steinbacher, R. Bass, P. Stopp, D. C. Rees, *Curr. Top. Membr.* **58**, 1 (2007).
8. M. Jernina et al., *EMBO J.* **28**, 1730 (1999).
9. S. Sukharev, *Biophys. J.* **83**, 290 (2002).
10. S. Sukharev, V. J. Sigurdson, C. Kung, F. Sachs, *J. Gen. Physiol.* **113**, 525 (1999).
11. R. B. Bass, P. Stopp, M. Barclay, D. C. Rees, *Science* **298**, 1582 (2002).
12. G. Chang, R. H. Spencer, A. T. Lee, M. T. Barclay, D. C. Rees, *Science* **282**, 222 (1998).
13. S. Miller, M. D. Edwards, C. Ockrent, R. Booth, *J. Biol. Chem.* **278**, 32246 (2003).
14. Single letter abbreviations for the amino acid residues are as follows: A: Ala; C: Cys; D: Asp; E: Glu; F: Phe; G: Gly; H: His; I: Ile; K: Lys; L: Leu; M: Met; N: Asn; P: Pro; Q: Gln; R: Arg; S: Ser; T: Thr; V: Val; W: Trp; and Y: Tyr.
15. A. Anishkin, S. Sukharev, *Biophys. J.* **86**, 2883 (2004).
16. O. Beckstein, M. S. P. Sansom, *Proc. Natl. Acad. Sci. U.S.A.* **100**, 7063 (2003).
17. M. D. Edwards et al., *Nat. Struct. Mol. Biol.* **12**, 113 (2005).
18. Pressure ratios were measured using the patch clamp technique, and experimental details are reported in the supporting online material (SOM) and in fig. S1.
19. Extensive details of the crystallography are given in the SOM and in fig. S5.
20. Clockwise is defined when looking along the sevenfold axis from the periplasm into the cytoplasm.
21. A. Aktulga, A. Anishkin, N. Liu, S. Sukharev, *Nat. Struct. Mol. Biol.* **14**, 1141 (2007).
22. M. D. Edwards, W. Bartlett, L. R. Booth, *Biophys. J.* **94**, 1000 (2008).
23. O. S. Smart, J. G. Medvedev, X. Wang, B. A. Wallace, M. S. P. Sansom, *J. Mol. Graphics* **24**, 354 (1996).
24. C. Dong et al., *Nature* **446**, 224 (2006).
25. The value for the free energy change reported for the mutants is calculated by proportionation, assuming a linear relation between the free energies of the closed to open transitions of MacS and of Mac1. Our interpretation does not depend on this linearity.
26. L. Serrano, A. Morozov, B. Avram, M. Bycroft, A. R. Forsht, *Biochemistry* **29**, 9343 (1990).
27. J. Ayaz, J. P. Rizz, G. A. Gutman, K. G. Chandy, *J. Biol. Chem.* **271**, 31013 (1996).
28. R. Rangaswamy, J. H. Lewis, R. MacKinnon, *Neuron* **16**, 131 (1996).
29. P. J. Carter, G. Winter, A. J. Wilkinson, A. R. Forsht, *Cell* **38**, 835 (1984).
30. A. Morozov, A. R. Forsht, *J. Mol. Biol.* **234**, 613 (1990).
31. A. Morozov, L. Serrano, B. Avram, M. Bycroft, A. R. Forsht, *J. Mol. Biol.* **216**, 1031 (1990).
32. P. Koprancic, A. Kubalicki, *J. Membr. Biol.* **164**, 253 (1998).
33. H. T. Kunita, D. Fedida, *Prog. Biophys. Mol. Biol.* **92**, 185 (2006).
34. T. Nomura, M. Sokabe, K. Yoshimura, *Biophys. J.* **94**, 1638 (2008).
35. S. B. Long, E. B. Campbell, R. MacKinnon, *Science* **309**, 903 (2005); published online 7 July 2005, 10.1126/science.1116270.
36. S. B. Long, E. B. Campbell, R. MacKinnon, *Science* **309**, 897 (2005); published online 7 July 2005, 10.1126/science.1116269.
37. S. B. Long, X. Tan, E. B. Campbell, R. MacKinnon, *Nature* **430**, 316 (2007).
38. Y. Jiang et al., *Nature* **423**, 33 (2003).
39. O. Beckstein, M. S. P. Sansom, *Phys. Biol.* **3**, 147 (2006).
40. G. N. Filatov, M. White, *Mol. Pharmacol.* **48**, 379 (1995).
41. A. Miyazawa, Y. Fujiyoshi, H. Ushio, *Nature* **423**, 949 (2003).
42. S. Miller et al., *EMBO J.* **22**, 36 (2003).
43. Our research was supported by the Wellcome Trust (Grants GR077646A and 040714), Medical Research Council (G0700277), Jntewer (UG) and Biotechnology Biological Sciences Research Council (BBSRC) GR073457/01. Structural biology used the facilities of the Scottish Synchrotron Proteomics Facility funded by the Scottish Funding Council and BBSRC. We thank K. Johnson, T. Rasmussen, and F. Flett for their contributions to this work. D. Rees and R. Bass for advice on crystallization and for pre-release of x-ray intensities, and A. Leslie for a critical reading of the manuscript. Coordinates and data have been deposited in the Protein Data Bank (www.rcsb.org) with accession number 2w5.

Supporting Online Material

www.sciencemag.org/cgi/content/full/321/5893/1175/DC1
Materials and Methods
Figs. S1 to S5
Table S1
References

17 April 2008; accepted 10 May 2008
10.1126/science.1159262

Polarized Gamma-Ray Emission from the Crab

A. J. Dean,¹ D. J. Clark,¹ J. B. Stephen,² V. A. McBride,¹ L. Bassani,² A. Bazzano,³ A. J. Bird,¹ A. B. Hill,⁴ S. E. Shaw,⁴ P. Ubertini³

Pulsar systems accelerate particles to immense energies. The detailed functioning of these engines is still poorly understood, but polarization measurements of high-energy radiation may allow us to locate where the particles are accelerated. We have detected polarized gamma rays from the vicinity of the Crab pulsar using data from the spectrometer on the International Gamma-Ray Astrophysics Laboratory satellite. Our results show polarization with an electric vector aligned with the spin axis of the neutron star, demonstrating that a substantial fraction of the high-energy electrons responsible for the polarized photons are produced in a highly ordered structure close to the pulsar.

The origin of the high-energy emission from rotation-powered pulsars and their associated pulsar wind nebulae (PWNs) is an unresolved problem. The observed pulsating radiation constitutes only a small fraction of the pulsar's spin-down energy losses, most of the energy is carried off in the form of a magnetized

relativistic pulsar wind. In a number of cases, including the Crab nebula, a highly collimated jet, thought to be aligned with the spin axis of the pulsar, and a circumstellar torus are also seen (1–11). The Crab is known to accelerate electrons and possibly other particles to extremely high energies, where observations in the gamma ray domain can be used to trace them. Using imaging and polarization measurements of the unpulsed emission in the gamma ray band, we showed that these energetic photons originate close to the pulsar

The x-ray spectrum of the Crab varies on an angular scale of arc seconds throughout the (arc minute-sized) nebula (12,13), showing a gradual spectral softening from the inner pulsar region to the outer nebula, with a variation in photon index Γ from ~ 1.9 to ~ 3.0 (Γ is defined from the spectral relationship $F = KE^{-\Gamma}$ photons/cm²/keV, where K is a constant and E is the energy). This is consistent with particle injection from the pulsar in two different directions: the equatorial plane containing the torus and the axis of symmetry along the jet. Both these regions have spectral indices around 2.0, suggesting that the spectra of the electrons injected from the pulsar are similar in these two directions. The pulsed component is unambiguously attached to the rotating neutron star, although we have only scant ideas as to the detailed radiation processes. The origin of the unpulsed emission, which constitutes $\sim 75\%$ of the emitted 0.1–1 MeV flux (14), is even less clear. Energetic electrons are capable of generating gamma rays through either the synchrotron or curvature radiation processes as they are accelerated within the magnetic field structure that permeates the PWN. However, because their radiative lifetimes are very short, they will necessarily radiate close to their acceleration zone and hence identify the source of injection.

¹School of Physics and Astronomy, University of Southampton, Southampton SO17 3BJ, UK. ²Istituto Nazionale di Astrofisica-Istituto di Astrofisica Spaziale e Fisica Cosmica (INAF-ASF), Via Piero Gobetti 101, 40129 Bologna, Italy. ³INAF-ASF, Via Fosso del Cavaliere 100, 00133 Roma, Italy.

The European Space Agency (ESA) observatory INTEGRAL [International Gamma-Ray Astrophysics Laboratory (15)] comprises a spectrometer [spectrometer on INTEGRAL (SPI)] with a resolution of 2.5 keV at 1 MeV and an imager [imager on board the INTEGRAL satellite (IBIS)] with high angular resolution (12 arc min), in combination covering the energy range from 15 keV to 8 MeV. IBIS was able to locate the centroid of the Crab flux with an accuracy of 20 arc sec between 18 and 60 keV (16) to a zone encompassing the pulsar and the surrounding jet/torus structure. The unpulsed gamma-ray emission is well described by a power-law spectrum of $\Gamma = 2.23 \pm 0.02$ (17). The spectral index of the gamma-ray flux as measured by IBIS provides an excellent match to that observed in x-rays from the central zone, including the jet, possible counterjet, and torus, thus indicating that most of the gamma rays are derived directly from the jet and/or the torus structure.

Another way to pinpoint the site of the high energy emission is by means of polarization studies, for which SPI is the most sensitive instrument on INTEGRAL. Data from over 600 individual observations of the Crab from February 2003 to April 2006 have been combined. We selected events that occur during the off-pulse fraction of the pulsar cycle (Fig. 1) in the energy range most suited for Compton scattering, 0.1 to 1 MeV. The polarization of the detected radiation was evaluated by looking for asymmetry in the azimuthal distribution of the gamma-ray photons that Compton-scatter from one detector element to another within the detection plane of SPI. To measure this asymmetry, we created simulated data sets to compare with the measurements. We have developed a computer model that exploits the GEANT4 (18) Monte Carlo simulation code and contains the physics necessary to track all particle interactions in SPI. This computer model was extensively used and verified throughout the preflight calibration phase of the INTEGRAL project. The ability of the GEANT4 software package to provide an accurate representation of the response to polarized photons has also been confirmed by comparison with calibration tests on a custom-built polarimeter (19).

For each individual pointing, simulated photons from the same direction and spectrum as that of the Crab were fired into the modeled geometry. Nineteen sets of 50 million test photons were processed for each pointing: 18 were polarized beams for each 10° azimuthal step between 0° and 170° , and one was of an unpolarized flux. Only the polarization angles between 0° and 170° need be modeled because of the 180° symmetry of the Compton scattering process. The total number of double events in the simulated data was $\sim 6.6 \times 10^6$, more than three orders of magnitude greater than the $\sim 5 \times 10^3$ double events detected from the Crab. The scattered events from each pointing were binned into the scatter directions defined by the detection plane and then converted into coordinates on the sky. All the pointings were summed to produce a percentage of counts scattered into each direction on the sky. The real data,

background-subtracted using SPI flat-field observations normalized to the same exposure time, were then compared to the simulated data for each polarization angle and percentage using a χ^2 test.

By minimizing the χ^2 fit between the real and simulated observations, we find that the data are consistent with a linearly polarized beam with the electric vector at an angle of $123^\circ \pm 11^\circ$ (measured from north, anticlockwise on the sky), closely aligned with the pulsar spin orientation angle, which has been estimated to be $124.0^\circ \pm 0.1^\circ$ (20). The polarization is $46 \pm 10\%$. The errors are dominated by nonstatistical effects (see supporting online text). A major advantage of the mass model simulation technique is that the process automatically compensates for a great many of the systematic errors. In order to confirm this, we have taken all of the scattered events and randomly assigned a new detection element as the site of the second interaction. When the same analysis was performed, we found no evidence of significant polarization.

Polarization measurements of unpulsed emission taken from approximately the same phase interval have been reported from the Crab in both x-ray (21) and optical (22) wavelengths. In the former, linear polarization at 2.6 and 5.2 keV was found at a level of 19.2 and 19.5%, respectively, with corresponding angles of 156.4° and 152.6° , whereas in the latter case the polarization found was 33%, with an angle of around 123° . The optical results come from an area of several arc seconds around the pulsar, but the x-ray measurements integrate over a 3° field of view. Because x-rays are emitted from all of the morphological features associated with the Crab PWN (2, 3), we might expect to find a lower degree of linear polarization in this case. Although the optical polarization angle is well aligned with the gamma-ray angle, the x-ray vector is rotated further, thus implying that there is no continuous rotation with photon energy.

If the gamma-ray photons are created through the synchrotron process, the parent electrons will have a power-law distribution of index $p = 2\Gamma - 1 \approx$

Fig. 1. The light curve of the Crab emission as seen by SPI nonscattered events. The 0.1 to 1 MeV gamma-ray events used for the polarization analysis were selected from within the phase interval from 0.5 to 0.8 of the pulsar period (shaded area).

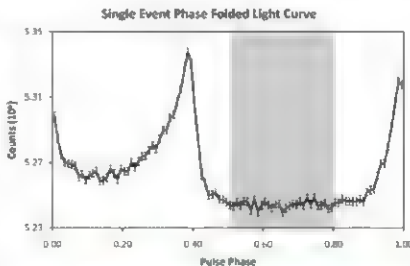


Fig. 2. The gamma-ray polarization vector superimposed on a composite image of the Crab from Chandra (x-ray/blue) and the Hubble Space Telescope (optical/red). The vector is drawn so as to pass through the position of the pulsar. The limits on the direction of the vector are indicated by the shading. The direction of the polarization vector shows a remarkable alignment with the inner jet structure. [Image credits: NASA/CXO/ASU/J. Hester et al., *Astrophys. J.* 577, L49 (2002) (x-ray image) and NASA/HST/ASU/J. Hester et al., *Astrophys. J.* 577, L49 (2002) (optical image)]



3.5 For such a power-law distribution of electrons, the maximum degree of linear polarization that is physically possible is defined by the expression $(23) \Pi = (p + 1)/(p + 7/3)$ giving $\sim 77\%$. Any inhomogeneities in the structure of the magnetic field will result in the degree of linear polarization being reduced. The high linear polarization measured at gamma wavelengths, roughly 60% of the maximum physical limit, implies a high degree of uniformity in the magnetic field configuration associated with the unpulsed emission and makes substantial polarized gamma-ray emission from the rather tangled magnetic field associated with the PWN unlikely.

The argument of the polarization vector along the jet axis implies an orthogonal magnetic field configuration if the synchrotron process operates. Analyses of radio and optical polarization studies of jets in radio galaxies (24, 25) indicate that the apparent magnetic field vector is parallel to the jet axis in the inner reaches of the jet, becoming perpendicular closer to the termination point. Taking the value for the magnetic field within the Crab jet close to the termination point derived from Chandra observations to be 9.1×10^{-6} G, the synchrotron process would require electrons with energies of $\sim 2 \times 10^6$ eV to create polarized gamma-ray photons at 400 keV and $\sim 2 \times 10^{13}$ eV for the kilo-electron volt x-rays detected by Weisskopf et al. (21).

Chandra images of the Crab (1) (Fig. 2) indicate that the jet is curved, so energetic electrons streaming along the jet also could radiate by curvature radiation, for which the electric vector is parallel to the jet, as observed by SPI. In the relativistic limit, the emission frequency is given by $\omega_c = (3c/4\pi R)\gamma^3$, where γ is the Lorentz factor of the radiating electrons and R is the radius of curvature of the field lines. Taking an estimate of $R \sim 2.5 \times 10^8$ cm for the Crab jet, in order to generate the few hundred kilo-electron volt photons detected by INTEGRAL, we would require electrons with energies of typically 10^{15} eV, which is entirely plausible in the context of the Crab pulsar.

The remarkable alignment of the electric vector with the rotational axis of the pulsar, together with its similarity to the optical polarization angle, suggests that both fluxes originate at the same site close to the neutron star (26). The higher rotation angle of the x-ray emission would suggest a different production site.

Our findings have clear implications for many aspects of high-energy accelerators, such as the production of the very high-energy (VHE) emission observed by ground-based Cerenkov detectors. A number of these tera-electron volt-emitting sources are associated with young, energetic, soft gamma-ray-emitting pulsars (27), including the Crab (28). If we assume that the VHE photons are produced by inverse Compton scattering by high-energy electrons from the pulsar on the cosmic microwave background and local starlight, there is a need for a constant supply of these electrons to be channeled from the pulsar to the extended site of the VHE emission. We have dem-

onstrated that in the Crab, there is high-energy acceleration of electrons to at least 10^{14} to 10^{15} eV, which are then capable of producing tera-electron volt emission via inverse Compton scattering on the cosmic microwave background or some other locally produced photons.

References and Notes

1. M. C. Weiskopf et al., *Astrophys. J.* **536**, L81 (2000).
2. J. J. Hester et al., *Astrophys. J.* **448**, 240 (1995).
3. E. V. Gotthelf, Q. D. Wang, *Astrophys. J.* **532**, L17 (2000).
4. M. L. Gaensler, M. J. Pringle, G. P. Garrone, *Astrophys. J.* **556**, 1107 (2001).
5. D. J. Helland, E. V. Gotthelf, J. P. Halpern, *Astrophys. J.* **556**, 380 (2001).
6. G. G. Pavlov, D. Y. Kargaltsev, D. Samal, G. P. Garrone, *Astrophys. J.* **554**, L189 (2001).
7. M. L. Gaensler et al., *Astrophys. J.* **569**, 878 (2002).
8. M. S. E. Roberts et al., *Astrophys. J.* **588**, 992 (2003).
9. G. G. Pavlov, M. A. Trier, D. Y. Kargaltsev, D. Samal, *Astrophys. J.* **592**, 1157 (2003).
10. J. J. Hester et al., *Astrophys. J.* **577**, L49 (2002).
11. R. Willinga et al., *Astron. Astrophys.* **365**, L212 (2001).
12. H. Mori et al., *Astrophys. J.* **609**, 186 (2004).
13. M. G. F. Kirsch et al., *Astron. Astrophys.* **453**, L73 (2006).
14. L. Kaper et al., *Astron. Astrophys.* **378**, 918 (2001).
15. C. Winkler et al., *Astron. Astrophys.* **413**, L1 (2003).
16. J. Bird et al., *Astrophys. J.* **370** (suppl.), 175 (2007).
17. E. Masaro, R. Campana, G. Cusumano, T. Mero, *Astron. Astrophys.* **459**, 859 (2006).
18. S. Agostinelli et al., *Nucl. Instrum. Methods Phys. Res. A* **506**, 250 (2003).

19. T. Minato et al., *Nucl. Instrum. Methods Phys. Res. A* **540**, 158 (2005).
20. C. Y. Ng, R. W. Romani, *Astrophys. J.* **601**, 479 (2004).
21. M. C. Weiskopf, E. H. Silver, H. J. Kestevenbaum, K. S. Long, R. Novak, *Astrophys. J.* **220**, L117 (1978).
22. G. Karbach, A. Stawikowska, S. Kellner, H. Stierle, *Mon. Not. Phys. Conf. Proc.* **B01**, 306K (2005).
23. F. Lu, A. J. Dean, G. L. Hill, *Space Sci. Rev.* **82**, 399 (1997).
24. R. A. Laing, A. H. Bridle, *Mon. Not. R. Astron. Soc.* **336**, 328 (2002).
25. E. S. Perlman et al., *Astrophys. J.* **651**, 735 (2006).
26. J. Takata, H. K. Chang, K. S. Cheng, *Astrophys. J.* **656**, 1044 (2007).
27. F. Aharonian et al., *Science* **307**, 1938 (2005).
28. F. Aharonian et al., *Astron. Astrophys.* **457**, 899 (2006).
29. The authors thank C. Jordan and P. Dubath for supplying Crab ephemeris data and the University of Southampton for the use of their Indis 2 Beowulf Cluster. This paper is based on observations with INTEGRAL, an ESA project with instruments and science data centers funded by ESA member states (especially the principal investigator countries: Denmark, France, Germany, Italy, Switzerland, and Spain), the Czech Republic, and Poland, and with the participation of Russia and the United States. This work was supported by the Italian Space Agency with contract I/00080770 and in the United Kingdom by Science and Technology Funding Council grant PP/C000714/1.

Supporting Online Material

www.sciencemag.org/cgi/content/full/321/5893/1183/DC1

SOM Text

Figs. S1 to S5

Tables S1 and S2

References

10 August 2007; accepted 17 July 2008

DOI: 10.1126/science.1149056

The Metamorphosis of Supernova SN 2008D/XRF 080109: A Link Between Supernovae and GRBs/Hypernovae

Paolo A. Mazzali,^{1,2,3,4,*} Stefano Valentini,^{5,6} Massimo Della Valle,^{7,8,9} Guido Chincarini,^{10,11} Daniel N. Sauer,¹² Stefano Benetti,¹³ Elena Pian,¹⁴ Tsvi Piran,¹⁵ Valerio D'Elia,¹⁶ Nancy Elias-Rosa,¹⁷ Raffaella Margutti,¹⁸ Francesco Pasotti,¹⁹ L. Angelo Antonelli,²⁴ Filomena Bufano,² Sergio Campana,²¹ Enrico Cappellari,²² Stefano Covino,²³ Paolo D'Avanzo,²⁴ Fabrizio Fiore,²⁴ Dino Fugazza,²⁵ Roberto Gilmozzi,²⁶ Deborah Hunter,²⁷ Kate Maguire,²⁸ Elisabetta Maiorano,²⁵ Paola Marziani,²⁹ Nicola Masetti,³⁰ Felix Mirabel,³¹ Hripsime Navasardyan,³² Ken'ichi Nomoto,^{3,4,32} Eliana Palazzi,³³ Andrea Pastorello,³ Nino Panagia,^{34,35} L. J. Pellizzari,³⁶ Re'em Sari,³⁷ Stephen Smartt,³⁸ Gianpiero Tagliaferri,³¹ Masamichi Tanaka,³⁹ Stefan Taubenberger,⁴⁰ Nozomu Tominaga,⁴¹ Carrie Trundle,⁴² Massimo Turatto⁴³

The only supernovae (SNe) to show gamma-ray bursts (GRBs) or early x-ray emission thus far are overenergetic, broad-lined type Ic SNe (hypernovae, HNe). Recently, SN 2008D has shown several unusual features: (i) weak x-ray flash (XRF), (ii) an early, narrow optical peak, (iii) disappearance of the broad lines typical of SN Ic HNe, and (iv) development of helium lines as in SNe Ib. Detailed analysis shows that SN 2008D was not a normal supernova: Its explosion energy ($E = 6 \times 10^{51}$ erg) and ejected mass [~ 7 times the mass of the Sun (M_{\odot})] are intermediate between normal SNe Ib and HNe. We conclude that SN 2008D was originally a $\sim 30 M_{\odot}$ star. When it collapsed, a black hole formed and a weak, mildly relativistic jet was produced, which caused the XRF. SN 2008D is probably among the weakest explosions that produce relativistic jets. Inner engine activity appears to be present whenever massive stars collapse to black holes.

On 9.57 January 2008 Universal Time (UT), the x-ray telescope (XRT) on board the Swift spacecraft detected a weak x-ray flash (XRF 080109) in the galaxy NGC2770 (1)

Optical follow-up revealed the presence of a supernova (SN) coincident with the XRF [SN 2008D, RA (2000) = 09 09 30.625, Dec (2000) = +33 08 20.16] (2). We detected SN 2008D pho-

tomically from Asago Observatory on 10.01 January 2008 UT, only 10.5 hours after the Swift detection. Early spectra showed broad absorption lines superposed on a blue continuum and lacked hydrogen or helium lines (3). Accordingly, SN 2008D was classified as a broad-lined SN Ic (4) SNe of this type are sometimes associated with gamma-ray bursts (GRBs) (5, 6) or XRFs (7, 8). The spectra resembled those of the XRF SN 2006aj (8) or the non-GRB hypernova (HN) SN 2002ap (9) (Fig. 1, top), but a comparison suggests that SN 2008D was highly reddened. We estimate that $E(B-V)_{\text{H}0} = 0.65$ mag [see supporting online material (SOM)]

The host galaxy of XRF 080109/SN 2008D, NGC 2770 (redshift $z = 0.006494$, distance 31 Mpc), is a spiral galaxy similar to the Milky Way, M31, or ESO 184-G82, the host of SN 1998bw/GRB 980425. NGC 2770 has roughly solar metallicity and a moderate star-formation rate, $\sim 0.5 M_{\odot} \text{ year}^{-1}$ (see SOM). In contrast, typical host galaxies of GRBs are small, compact, somewhat metal-poor, and highly star-forming (10).

In addition to the weak XRF, SN 2008D shows a number of peculiar features, most of which are new. The optical light curve had two peaks (Fig. 2): A first, dim maximum ($V \approx 18.4$) was reached less than 2 days after the XRF. After a brief decline, the luminosity increased again, reaching principal maximum ($V = 17.37$)—19 days after the XRF. An 18- to 20-day rsetime is typical of GRB-HNe. Normal SNe Ic reach maximum in 10 to 12 days. Few stripped-envelope SNe have very early data, and in GRB-HNe a first peak may be masked by

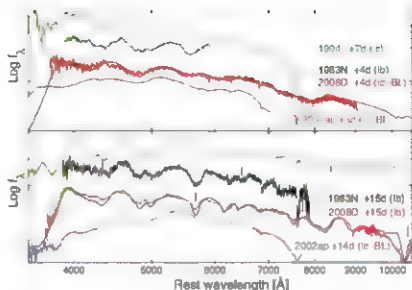


Fig. 1. The spectra of SN 2008D compared with those of other Type Ib/c SNe and to simulations. Near the first peak (top), SN 2008D has a broad-lined spectrum similar to that of SN 2002ap, a broad-lined SN without a GRB (9), but different from both the normal SN Ic 1994, and the SN Ib 1983N. At the time of the main light curve peak (bottom), the spectrum of SN 2008D has narrow lines like SNe 1994 and 1983N, whereas SN 2002ap and other HNe retain broad features throughout their evolution. Also, SN 2008D developed He lines (vertical ticks). At this epoch, the spectra of SNe 2008D, 1983N, and 1999ex are similar. Synthetic spectra are overlaid on the two SN 2008D spectra (see SOM).

the afterglow light. A first narrow optical peak was only seen in the type Ib SN 1999ex (SNe Ib are similar to SNe Ic but show strong helium lines (4)), the type Ib SN 1993j (SNe Ib are similar to SNe Ic but still have some hydrogen), and the type Ic XRF SN 2006aj. When it was discovered, SN 1999ex was dropping from a phase of high luminosity (11). It reached principal maximum ~20 days later, as did SN 2008D.

Another unusual feature is the spectral metamorphosis (Fig. 3). Unlike SNe 2006aj and 2002ap, the broad absorptions did not persist. As they disappeared, He I lines developed (12). By principal maximum, SN 2008D had a narrow-lined, type Ib spectrum (Fig. 1, bottom).

Broad lines require material moving with velocity $v > 0.1c$, where c is the speed of light (13). Their disappearance implies that the mass moving at high velocities was small.

Late development of He I lines, previously seen only in SN 2005bf (14), is predicted by theory (15). Helium levels have high excitation potentials, exceeding the energy of thermal photons and electrons. Excitation can be provided by the fast particles produced as the γ rays emitted in the decay chain of ^{56}Ni thermalize (16). This is the process that makes SNe shine. In the first few days after explosion, thermalization is efficient because of the high densities and because not enough particles are available to excite helium. Only when density drops sufficiently can more particles escape the ^{56}Ni zone and excite helium.

We reproduced the spectral evolution and the light curve of SN 2008D after the first narrow peak, using a model with $M_{\text{env}} \sim 7 M_{\odot}$ and spherically symmetric $E \sim 6 \times 10^{51}$ erg, of which $\sim 0.03 M_{\odot}$ with energy $\sim 5 \times 10^{50}$ erg, are at $v > 0.1c$ (Figs. 1 and 2 and SOM). Our light curve fits indicate that SN 2008D synthesized $\sim 0.09 M_{\odot}$ of ^{56}Ni , like the non-GRB HN SN Ic 2002ap (9) and the normal SN Ic 1994 (17) but much less than the luminous GRB HN SN 1998bw (6). The rapid rise in luminosity after the first peak re-

quires that some ^{56}Ni (0.02 M_{\odot}) was mixed uniformly at all velocities $> 9000 \text{ km s}^{-1}$. This is a typical feature of HNe and indicates an aspherical explosion (18). Asphericity may affect our estimate of the energy, but not the ^{56}Ni mass (19).

Comparing the mass of the exploding He star that we derived with evolutionary models of massive stars, we find that the progenitor had main sequence mass $\sim 30 M_{\odot}$. A star of this mass is likely to collapse to a black hole, as do GRB/SNe (20). So, SN 2008D shared several features of GRB/HNe. However, all SNe with GRBs or strong XRFs initially had velocities higher than SN 2008D or SN 2002ap (Fig. 3) and never showed helium. Had the He layer not been present in SN 2008D, the explosion energy would have accelerated the inner core to higher velocities, and broad lines may have survived.

The characteristic features of SN 2008D (weak XRF, first narrow optical peak, initially broad-lined SN Ic spectrum that later transformed into a narrow-lined SN Ib spectrum) may be common to all SNe Ib, or at least a substantial fraction of them, and perhaps some SNe Ic (which, however, contain little or no helium). The light curves of various SNe Ib are rather similar (21). The first peak was observed only for SN 1999ex, but lack of x-ray monitoring probably prevented the detection of more weak XRFs and the early discovery of the associated SNe. On the other hand, SN 2008D (and possibly most SNe Ib) was more energetic than normal core-collapse SNe, including most SNe Ic.

Type II SNe in late spiral/irregular galaxies (the typical Hubble type of GRB hosts) are about 6 times as frequent as SNe Ib (22). Although the serendipitous discovery of an SN Ib by XRT may be a statistical fluctuation, it may also suggest that the soft x-ray emission accompanying SN 2008D is typical of overenergetic SNe Ib and absent (or very weak) in normal core-collapse SNe.

The x-ray spectrum of SN 2008D (in total ~ 500 photons) can be fitted with either a simple

¹Max-Planck-Institut für Astrophysik, Karl-Schwarzschild-Strasse 1, 85748 Garching, Germany. ²Istituto Nazionale di Astrofisica-OAR, vicolo dell'Osservatorio, 2, I-35122 Padova, Italy. ³Department of Astronomy, School of Science, University of Tokyo, Bunkyo-ku, Tokyo 113-0033, Japan. ⁴Research Center for the Early Universe, School of Science, University of Tokyo, Bunkyo-ku, Tokyo 113-0033, Japan. ⁵Astrophysics Research Centre, School of Mathematics and Physics, Queen's University, Belfast, BT7 1NN, Northern Ireland, UK. ⁶Dipartimento di Fisica, Università di Ferrara, Via Giuseppe Saragat 1, 44100 Ferrara, Italy. ⁷Istituto Nazionale di Astrofisica, Capodimonte Astronomical Observatory, S. Maria delle Grazie 16, I-80131 Napoli, Italy. ⁸European Southern Observatory, Karl-Schwarzschild-Strasse 2, D-85748 Garching, Germany. ⁹International Center for Radioastronomical Physics Network, Piazzale della Repubblica 10, I-55122 Pescara, Italy. ¹⁰Department of Physics, Università di Milano Bicocca, Piazza della Scienza 3, I-20126 Milano, Italy. ¹¹Istituto Nazionale di Astrofisica, Brera Astronomical Observatory, Via Eritrea 48, I-22070 Merate (LC), Italy. ¹²Istituto Nazionale di Astrofisica-OAR, Via Tiepolo 11, I-34131 Trieste, Italy. ¹³The Racah Institute of Physics, Hebrew University, Jerusalem 91904, Israel. ¹⁴Istituto Nazionale di Astrofisica, Rome Astronomical Observatory, Via di Frascati 33, I-00040 Rome, Italy. ¹⁵Istituto Nazionale di Astrofisica, Istituto di Astrofisica Spaziale e Fisica Cosmica, Via Piero Gobetti 101, I-40129 Bologna, Italy. ¹⁶European Southern Observatory, Alonso de Cordoba 3107, Santiago, Chile. ¹⁷Institute for the Physics and Mathematics of the Universe, University of Tokyo, Kashiwa, Chiba 277-8582, Japan. ¹⁸Space Telescope Science Institute, 3700 San Martin Drive, Baltimore, MD 21218, USA. ¹⁹Istituto Nazionale di Astrofisica, Catania Astronomical Observatory, Via Santa Sofia 78, I-95123 Catania, Italy. ²⁰Instituto de Astronomía y Física del Espacio, Casilla de Correos 67, Buenos Aires, Argentina.

*To whom correspondence should be addressed. E-mail: mazzali@mpa-garching.mpg.de

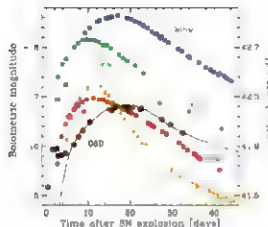
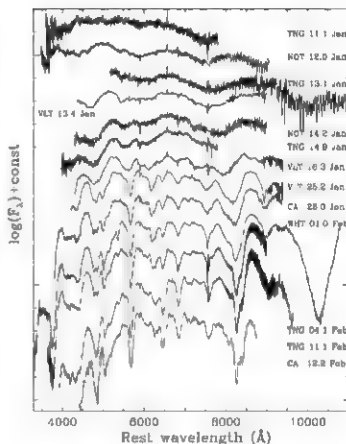


Fig. 2. The light curves of SN 2008D and of other type Ibc SNe. The shape of the light curve of SN 2008D is similar to that of SN 1998bw and other GRB/HNe, and comparable to the non-GRB HN SN 1997ef, but much broader than the XRF SN 2006aj or the normal SN Ic 1994i. This similarity suggests a comparable value of the quantity M_{ej}/E , where M_{ej} is the mass ejected and E the explosion kinetic energy (23). All known SNe Ic with a broad light curve ejected a large mass of material (29). Large values of M_{ej} and E are also suggested by the presence of He moving at $v \sim 10,000 \text{ km s}^{-1}$. The velocity of He in SN 2005bf was lower (14). The light curve of SN 1999ex, which is similar to that of SN 2008D, was fitted reasonably well by a He-star explosion model with $M_{\text{ej}} \sim 5 M_{\odot}$ and $E \sim 3 \times 10^{51} \text{ erg}$ (12). Such a model would also match the light curve of SN 2008D, but it probably would not reproduce the broad lines that characterize the early spectra. This would require a model containing some high-velocity material, leading to a larger E without noticeably affecting the value of M_{ej} or the light curve shape. The line shows a synthetic bolometric light curve computed with a Monte Carlo code (30) for a model with $M_{\text{ej}} \sim 7 M_{\odot}$ and $E \sim 6 \times 10^{51} \text{ erg}$. The model does not address the physics that may be responsible for the first narrow light curve peak, but only the main peak, which is due to diffusion of radiation in the SN envelope following the deposition of γ -rays and positrons emitted in the decay chain ^{56}Ni to ^{56}Co and ^{56}Fe .

power law indicating a nonthermal emission mechanism or a combination of a hot black body ($T \sim 3.8 \times 10^5 \text{ K}$) and a power law. In the latter case, the unabsorbed luminosity of the black-body component is a small fraction of the total x-ray luminosity. The high temperature and low luminosity ($L \approx 1 \times 10^{43} \text{ erg s}^{-1}$) of the black-body component at first peak ($\sim 100 \text{ s}$ after the onset of the XRF) imply an emitting radius $R_{\text{ph}} \sim 10^{10} \text{ cm}$ (see SOM, Section 4). This is at least one order of magnitude smaller than the size of Wolf-Rayet stars, the likely progenitors of SNe Ibc.

The x-ray flare and the first optical peak are most likely associated (23). The time scale of the first optical peak may suggest that it was related to shock breakout. A signature of shock breakout is a hot black-body x-ray spectrum immediately after the explosion. Thermal x-ray emission was suggested for SN 2006aj (24), whereas no x-ray data are available for SN 1999ex. The model of (23) uses a spherical configuration and a black-

Fig. 3. Spectral evolution of SN 2008D. In the early phase, the strongest features are broad Fe complexes in the blue (~ 4000 to 5000 \AA), the Si II-dominated feature near 6000 \AA , and Ca II lines, both in the near ultraviolet (H and I) and in the near infrared (the infrared triplet near 8500 \AA). On the other hand, O I 7774 \AA , which is strong in all HNe as well as in all SNe Ibc, is conspicuously missing. Starting 15 January, lines begin to become narrow. In the later spectra, taken near maximum, He I lines have developed. The strongest isolated lines are $\lambda 6678 \text{ \AA}$, seen near 6500 \AA , and $\lambda 7065 \text{ \AA}$, seen near 6900 \AA . Both lines indicate a helium velocity of $\sim 10,000 \text{ km s}^{-1}$. The other strong optical lines of He I are detected: $\lambda 5876 \text{ \AA}$ is blended with Na I D, near 5600 \AA , and $\lambda 4471 \text{ \AA}$ is blended with the broad Fe II trough near 4200 \AA .



9. P. A. Mazzali et al., *Astrophys. J.* **572**, 161 (2002).
 10. A. S. Fruchter et al., *Nature* **443**, 463 (2006).
 11. M. Stringer et al., *Astron. J.* **124**, 2100 (2002).
 12. M. Modjaz, R. Chernock, R. J. Foley, A. V. Filippenko, W. J. G. Stringfellow, *GCN 7212* (2006); <http://gcnc.gsfc.nasa.gov/gcn3/7212.gcn3>.
 13. P. A. Mazzali, K. Nomoto, K. Nomoto, *Astrophys. J.* **545**, 407 (2000).
 14. M. Tomimaga et al., *Astrophys. J.* **633**, 197 (2005).
 15. P. A. Mazzali, L. B. Lucy, *Mon. Not. R. Astron. Soc.* **295**, 426 (1998).
 16. J. B. Lucy, *Astrophys. J.* **383**, 308 (1991).
 17. D. Sauer et al., *Mon. Not. R. Astron. Soc.* **349**, 1939 (2006).
 18. K. Maeda et al., *Astrophys. J.* **593**, 931 (2003).
 19. K. Maeda, P. A. Mazzali, K. Nomoto, *Astrophys. J.* **645**, 1331 (2006).
 20. A. E. Macfadyen, S. E. Woosley, *Astrophys. J.* **524**, 262 (1999).
 21. A. Clodt, J. C. Wheeler, *Astrophys. J.* **491**, 375 (1997).
 22. E. Cappellaro, R. Evans, M. Turatto, *Astron. Astrophys.* **351**, 459 (1999).
 23. A. M. Soderberg et al., *Nature* **453**, 469 (2008).
 24. S. Campana et al., *Nature* **442**, 1008 (2006).
 25. P. A. Mazzali et al., *Science* **308**, 1784 (2005).
 26. K. Maeda et al., *Science* **319**, 1270 (2008).
 27. H. Bouchannan et al., *Mon. Not. R. Astron. Soc.* **383**, 12 (2008).
 28. W. D. Arnett, *Astrophys. J.* **253**, 785 (1982).
 29. P. A. Mazzali et al., *Astrophys. J.* **645**, 1323 (2006).
 30. E. Cappellaro et al., *Astron. Astrophys.* **328**, 203 (1997).

Supporting Online Material
www.sciencemag.org/cgi/content/full/1158088/DC1
 Methods
 SOM Text
 Figs. S1 to S4
 Tables S1 and S2
 References

20 March 2008; accepted 10 July 2008
 Published online 24 July 2008
 DOI: 10.1126/science.1158088
 include this information when citing this paper

Hydrodefluorination of Perfluoroalkyl Groups Using Silylium-Carborane Catalysts

Christos Douvris and Oleg V. Ozerov*

Carbon-fluorine bonds are among the most unreactive functionalities in chemistry. Interest in their activation arises in part from the high global warming potentials of anthropogenic polyfluoroorganic compounds. Conversion to carbon-hydrogen bonds (hydrodefluorination) is the simplest modification of carbon-fluorine bonds, but efficient catalytic hydrodefluorination of perfluoroalkyl groups has been an unmet challenge. We report a class of carborane-supported, highly electrophilic silylium compounds that act as long-lived catalysts for hydrodefluorination of trifluoromethyl and nonfluorinated alkyl groups by widely accessible silanes under mild conditions. The reactions are completely selective for aliphatic carbon-fluorine bonds in preference to aromatic carbon-fluorine bonds.

Carbon fluorine bonds are among the most passive functionalities in chemistry (1), and their selective activation and trans formation under mild conditions remains a poorly realized challenge (2–5). The thermodynamic issues are considerable: C–F is the strongest single bond to carbon (1–3). The thermodynamic obstacles are compounded by the kinetic issues: Organic fluorides are poor ligands or Lewis bases, and poor substrates for nucleophilic substitution or oxidative addition to metals (1–4). In all of these regards, compounds containing fully fluorinated perfluoroalkyl groups prove even more inert than compounds containing a single C–F bond. With the increasing degree of fluorination at carbon, the strength of the C–F bond increases, and the C–F bond distances decrease, resulting in substantial steric shielding of the carbon site (5).

Perfluoroalkyl-containing organic compounds have beneficial uses in technology. Some applications include blood substitutes fostered by high O₂ solubility and inertness, (1, 6) as well as solvent media for biphasic syntheses and purification (fostered by low miscibility with water and hydrocarbons) (6). On the other hand,

perfluorooctanesulfonic acid derivatives (PFOS), used in surfactants and in fluorinated polymer production, have been recently shown to be toxic, widely spread in the biota, and highly persistent (7). Perfluoroalkyl-containing chlorofluorocarbons (freons or CFCs), hydrofluorocarbons (partially fluorinated alkanes, HFCs) and perfluorocarbons (perfluoroalkanes, PFCs) are of increasing concern as anthropogenic “super greenhouse gases” (8) of high global warming potential and exceedingly high atmospheric lifetimes. Development of efficient and economical chemical strategies for their disposal is thus of vital importance.

Transition metal mediated C–F activation has received substantial attention (2–5). The approach typically employs highly reducing,

electron-rich metal reagents or catalysts. The critical cleavage of the C–F bond in this case is by definition of reductive nature, either through an oxidative addition or a single-electron transfer step. The simplest modification of the C–F bond is its conversion to the simplest functional group, a C–H bond (hydrodefluorination or HDF). The scope of the transition metal catalyzed HDF has been largely limited to fluorobenzenes (2–5). HDF of poly(tetrafluoroethylene) by stoichiometric Li metal in ammonia has been reported (9). Conversion of a C–F to a C–C bond is also of interest, but the progress so far has been limited (10). Recently, a Nb mediated activation of trifluoromethyl arene substrates with concomitant conversion of C–F bonds to C–H and C–C bonds was reported (11).

We were attracted to a conceptually different approach to C–F activation, in which the key C–F cleavage proceeds by a Lewis acid abstraction of fluoride rather than a redox event (Fig. 1A). Conventional acids, such as SiO₂ or concentrated H₂SO₄, require very high temperatures for cleavage of C–F bonds in perfluoroalkyl groups (12, 13). In 2005, we reported an implementation of the nonredox approach under ambient conditions by using a silylium (R₃Si⁺) Lewis acid (14). The proposed mechanism is depicted in Fig. 1A. Abstraction of fluoride by silylium from a C–F bond is complemented by the abstraction of hydride by the resultant carborane from an Si–H bond. The overall process can be viewed as a Si–H/C–F metathesis (with conversion to Si–F/C–H). Given that Si–F is a stronger bond than C–F, and C–H is a stronger bond than Si–H, this metathesis is a very

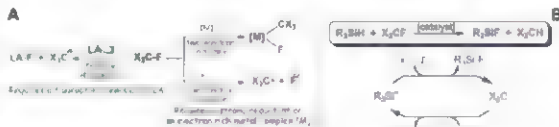


Fig. 1. (A) Representation of different approaches to C–F bond cleavage. X stands for an organic substituent, and the X₂ notation does not imply that the three substituents must be identical. **(B)** The stoichiometry of Si-mediated HDF and the proposed mechanism.

Department of Chemistry, Brandeis University, MS D15, 415 South Street, Waltham, MA 02454, USA.

*To whom correspondence should be addressed. E-mail: ozerov@brandeis.edu

thermodynamically favorable reaction (by ~ 190 kJ/mol) (15). The most relevant precedent for this chemistry is the work of Krause and Lampe, who observed Si/HCF redistribution by mass spectrometry (MS) in the gas phase upon collision of SiH_3^+ with CF_4 (16, 17).

The catalytic process as depicted in Fig. 1B requires generation of carbo- and silyl cations; these are species of exceptionally high Lewis acidity. In addition, they may also possess or give rise to species of high Brønsted acidity. The key to harnessing this chemistry in solution is the choice of the counterion. A successful anion must not only be weakly coordinating (i.e., a very weak Lewis base) but also resist decomposition via transfer of an anionic group to a Lewis or Brønsted acid. We originally employed $[\text{B}(\text{C}_6\text{F}_5)_4]^-$ as a weakly coordinating anion because it was known to support a silyl cation (18). Two other groups have since reported related chemistry (19, 20). However, the reactivity in all three cases was by and large limited to simple alkyl fluorides and trifluoromethylbenzene, and the turnover numbers were limited (<100).

The use of halogenated monocarboranes (Fig. 2) as supporting anions substantially improves the longevity of the catalyst, promoting facile activation of perfluoroalkyl groups. Our study benefits from the sophistication in the chemistry of carboranes (recently reviewed by Korbé *et al.*) (21) brought to the fore by others, studies by the Reed group are particularly relevant (22, 23). Carborane anions have been shown to be compatible with the highest levels of Brønsted and Lewis (e.g., silyl cation and carbocation) acidity in the condensed phase even under harsh conditions (22–24). For instance, $[\text{HCB}_2\text{H}_4\text{Cl}_4]^-$, the strongest known Brønsted acid, can be sublimed at 200°C without decomposition (22). We selected three carborane anions for investigation: $[\text{HCB}_2\text{H}_4\text{Cl}_4]^-$, $[\text{HCB}_2\text{H}_4\text{Cl}_3]^-$, and $[\text{HCB}_2\text{H}_4\text{Br}_2]^-$ (22–25). We used either triethyl or *trans*-*n*-hexylsulfate as the Si-H reagent and the Ph_3C^+ salt of the corresponding anion as the precatalyst. The Ph_3C^+ salt is convenient to store and is readily converted to the correspond-

ing trialkylsilylium by reaction with excess R_3SiH in the reaction mixture (20).

We chose three representative substrates (Fig. 3A and Table 1): $\text{C}_6\text{F}_5\text{CF}_3$ (a perfluorocarbon that highlights the $\text{C}(\text{sp}^2)\text{-F}$ versus $\text{C}(\text{sp}^3)\text{-F}$ selectivity), $\text{PhCH}_2\text{CH}_2\text{CF}_3$, and $^n\text{C}_6\text{F}_5\text{C}_2\text{H}_5$ (both containing nonbenzylic perfluoroalkyl groups) (26). In particular, $^n\text{C}_6\text{F}_5\text{C}_2\text{H}_5$ is a reasonable and convenient (liquid) approximation of commercially used HFC coolants, such as tetrafluoroethane (R 134a). Our approach relies on the abstraction of fluoride and generation of a carbocation. Increased fluorination should make the generation of carbocations through fluoride abstraction ever more challenging. Because of the even greater instability of aryl cations, the process targets $\text{C}(\text{sp}^3)\text{-F}$ bonds in preference to the aromatic $\text{C}(\text{sp}^2)\text{-F}$ bonds. Thus, haloarenes are acceptable solvents and, although C_6F_6 is one of the most compliant substrates in transition metal mediated C-F activation (27), here it is sufficiently inert that we use it (or $\text{C}_6\text{F}_5\text{Br}$) as a ^{19}F nuclear magnetic resonance (NMR) integration standard. In the process of the HDF reactions, fluorine is transferred from the C-F bonds of the substrate to Si, with the formation of R_3SiF and R_2SiF_2 . R_2SiF_2 is formed presumably by redistribution of Si-F substituents (R_4Si is also formed) in the Lewis acidic medium. Discrepancies in the C-F/Si-F mass balance may be due to the leaching of F into the borosilicate glassware (14).

At first, we compared the activity of the three chosen carborane supported catalysts to that of $[\text{B}(\text{C}_6\text{F}_5)_4]^-$ in the HDF reaction (all at 0.4 mol % catalyst) of Et_3SiH (~ 9 equivalents) and $\text{C}_6\text{F}_5\text{CF}_3$ in *o*- $\text{C}_6\text{H}_4\text{Cl}_2$ solvent (table S1) (26). The reaction with the $[\text{B}(\text{C}_6\text{F}_5)_4]^-$ catalyst stopped after only ~ 15 turnovers, whereas the reactions with all three carborane catalysts proceeded to $>97\%$ completion (240 turnovers). In a separate pair of similar reactions ($\text{Et}_3\text{SiH}/\text{C}_6\text{F}_5\text{CF}_3$ molar ratio of ~ 3) using higher catalyst loading for convenience of monitoring by NMR spectroscopy, we observed that the $[\text{B}(\text{C}_6\text{F}_5)_4]^-$ anion was degraded after 19 turnovers (^{19}F NMR evidence), whereas $>95\%$ (^{11}B NMR evidence) of the $[\text{HCB}_2\text{H}_4\text{Cl}_4]^-$ anion was intact after $>97\%$ conversion at 140 turnovers (figs. S1 and S2) (26).

In all likelihood, in our solution chemistry the silylium or carbocation are stabilized by weak interactions with the solvent, anion, substrates, or products (18–20). Nonetheless, these are highly electrophilic species that approximate the reactivity of true free cations. Although $[\text{B}(\text{C}_6\text{F}_5)_4]^-$ is experimentally compatible with triethylsilylium under ambient conditions (18), it is ostensibly not resistant to carbocations and high levels of Brønsted acidity (28). Thus, the advantage of the carboranes is in their incomparable robustness.

We next scrutinized the relative activity of the three carborane catalysts using the same HDF

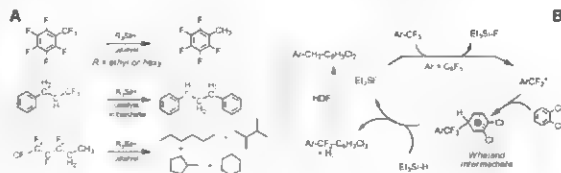


Fig. 3. (A) HDF reaction under study. (B) Proposed mechanism of formation of the Friedel-Crafts products.

Table 1. HDF reactions with $[\text{HCB}_2\text{H}_4\text{Cl}_4]^-$ as catalyst; catalyst loading is given per number of $\text{C}(\text{sp}^3)\text{-F}$ bonds. Si-F conversion is calculated as fraction of F from the original aliphatic C-F bonds, found in the Si-F bonds of R_3SiF and R_2SiF_2 (by ^{19}F NMR spectroscopy). Turnover numbers (TON) are calculated based on the C-F conversion (disappearance of the starting material by ^{19}F NMR spectroscopy) and represent the number of consumed C-F bonds per molecule of catalyst. $>97\%$ C-F conversion corresponds to the absence of discernible ^{19}F NMR resonances of the starting material. The amount of Et_3SiH used corresponded to ~ 1.1 Si-H bond per 1 $\text{C}(\text{sp}^3)\text{-F}$ bond in the substrate.

No.	Substrate	Silane	T ($^\circ\text{C}$)	Time (h)	Cat. mol (%)	Solvent	Si-F conv. (%)	C-F conv. (%)	TON
1	$\text{C}_6\text{F}_5\text{CF}_3$	Et_3SiH	25	24	0.080	<i>o</i> - $\text{C}_6\text{H}_4\text{Cl}_2$	84	>97	1250
2	$\text{C}_6\text{F}_5\text{CF}_3$	Et_3SiH	25	6	0.080	Neat	82	>97	1250
3	$\text{C}_6\text{F}_5\text{CF}_3$	Et_3SiH	25	72	0.036	<i>o</i> - $\text{C}_6\text{H}_4\text{Cl}_2$	76	>97	2700
4	$\text{PhCH}_2\text{CH}_2\text{CF}_3$	Et_3SiH	25	24	0.13	Neat	79	>97	780
5	$\text{PhCH}_2\text{CH}_2\text{CF}_3$	Et_3SiH	25	48	0.13	C_6H_6	75	>97	780
6	$^n\text{C}_6\text{F}_5\text{C}_2\text{H}_5$	HexSiH	50	120	0.50	Neat	92	>97	200

Fig. 2. Representation of the kosahedral carborane-dodecaborate(−) $[\text{HCB}_2\text{H}_4\text{Cl}_4]^-$ anion, or carborane (dots at vertices represent boron atoms; each vertex is capped with a hydrogen atom). Hexahalo substitution to give $[\text{HCB}_2\text{H}_4\text{Br}_2]^-$ and $[\text{HCB}_2\text{H}_4\text{Cl}_3]^-$ occurs in positions 7 to 12; undecachlorination to give $[\text{HCB}_2\text{H}_4\text{Cl}_4]^-$ occurs in positions 2 to 12.

Inverse Velocity Dependence of Vibrationally Promoted Electron Emission from a Metal Surface

N. H. Nahler,^{1,*} J. D. White,¹ J. LaRue,¹ D. J. Auerbach,² A. M. Wodtke^{1†}

All previous experimental and theoretical studies of molecular interactions at metal surfaces show that electronically nonadiabatic influences increase with molecular velocity. We report the observation of a nonadiabatic electronic effect that follows the opposite trend: The probability of electron emission from a low-work function surface—Au(111) capped by half a monolayer of Cs—increases as the velocity of the incident NO molecule decreases during collisions with highly vibrationally excited NO($\tilde{X}^2\Pi_{g-}$, $V = 18$, V is the vibrational quantum number of NO), reaching 0.1 at the slowest velocity studied. We show that these results are consistent with a vibrational autodetachment mechanism, whereby electron emission is possible only beyond a certain critical distance from the surface. This outcome implies that important energy-dissipation pathways involving nonadiabatic electronic excitations and, furthermore, not captured by present theoretical methods may influence reaction rates at surfaces.

Chemical processes are generally described in terms of the Born-Oppenheimer (BO) approximation whereby electrons move sufficiently rapidly to adjust adiabatically as the system evolves and nuclear motion is governed by an effective electronic ground-state potential energy surface (7). This approach, particularly in combination with density functional theory (2), has contributed appreciably to our understanding of surface chemistry and heterogeneous catalysis (3, 4). Use of the BO approximation, however, neglects electronic excitation induced by nuclear motion, which might be expected for interactions on metal surfaces where there is a continuum of low-lying electronic states. If, for example, chemical reactions at metal surfaces were accompanied by ubiquitous electronic excitations, important energy-dissipation pathways would be neglected by present theoretical approaches. This could have important consequences for predicting reaction rates—for example, overemphasizing recrossing of transition states or underestimating the importance of rapid irreversible relaxation into product wells.

There are many well documented examples of the breakdown of the BO approximation in molecular processes at metal surfaces (5–17). These include electron emission during strongly exothermic chemisorption, a process referred to as “excited electron emission” (5, 6), vibrational energy transfer at metal surfaces (7–11), the observation of currents (termed “chemicurrents”) associated with adsorption and reactions in Schottky diode and metal-insulator-metal structures (12–14), and the emission of electrons when highly vi-

brationally excited NO molecules impinge on a low-work function Cs-decorated Au(111) surface (16–18). This last phenomenon, dubbed “vibrationally promoted electron emission,” is a particularly direct observation of BO approximation breakdown.

Despite evidence of BO approximation breakdown, its effect on chemical reactions at surfaces remains unclear. On one hand, the rate of energy loss to the solid is crucial to accurately characterizing reaction conditions; however, some of the clearest examples of BO approximation breakdown occur so improbably—for example, exoelectron emission exhibits a per collision probability of 10^{-7} to 10^{-8} (19)—that it is hard to know if the electronically nonadiabatic events they reveal are minor side channels or if they have an important influence on reactivity.

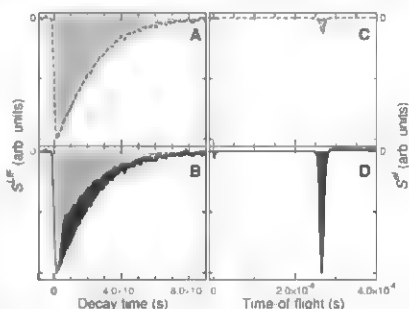
Even for processes with significant probabilities, there are reasons to question their influence

on surface chemical reactions. All observations and theories of the nonadiabatic processes cited above show a decrease in excitation probability as the velocity of the molecules relative to the surface decreases. This trend toward decreasing nonadiabatic transition probability with decreasing velocity is also seen in the gas phase—for example, in the well-known Landau-Zener, Stueckelberg theory and numerous experimental results on nonadiabatic transitions at curve crossings (20). Furthermore, the trend is expected because breakdown of the BO approximation depends on the nuclear motion being too rapid for the electrons to independently adjust. For adsorbed molecules, where the velocity relative to the surface is zero, it is thus reasonable to question the relevance of nonadiabatic processes altogether.

We report a surprising and seemingly paradoxical observation: The probability of electron emission observed when highly vibrationally excited NO($\tilde{X}^2\Pi_{g-}$, $V = 18$) molecules strike a low-work function surface increases strongly as the velocity of the incident molecules decreases. Such electron emission self-evidently involves nonadiabatic electronic excitation. Yet, as we have just discussed, the probability of nonadiabatic excitation should decrease with decreasing velocity. We also present a simple model to resolve this apparent paradox. The model is based on an extension of the vibrational autodetachment mechanism previously proposed (17). The model suggests that it is not the motion of the NO molecule relative to the surface but rather the relative motion of the N and O that drives the nonadiabatic electronic excitation observed.

The experimental setup has been described in detail elsewhere (17). Briefly, seeded supersonic pulsed molecular beams of NO in a variety of carrier gases are used to control the velocity (v) of the NO molecules. The NO molecules are prepared in vibrationally excited states of the ground $X^2\Pi_{g-}$ electronic state by stimulated emission

Fig. 1. Observed LIF and electron emission signals. (A) The LIF signal induced by the \tilde{A} ($V = 3$) \rightarrow \tilde{X} ($V = 0$) excitation laser is shown as a dashed line. (B) A second \tilde{A} ($V = 3$) \rightarrow \tilde{X} ($V = 18$) de-excitation laser induces population transfer out of the fluorescing \tilde{A} ($V = 3$) state (solid line). The difference in the signals (dark shaded area) is proportional to the number of laser-prepared vibrationally excited molecules. (C) The electron signal observed with only the \tilde{A} ($V = 3$) \rightarrow \tilde{X} ($V = 0$) excitation laser on (dashed curve). This signal arises from Franck-Condon pumping of the NO beam to a variety of excited vibrational states predominantly below $V = 13$ (17). (D) The electron signal induced by the use of both lasers (solid line). The increase in signal results from the preparation of NO $\tilde{X}^2\Pi_{g-}$, $V = 18$.



¹Department of Chemistry and Biochemistry, University of California Santa Barbara, Santa Barbara, CA 93106-9510, USA. ²GRT Inc., 861 Ward Drive, Santa Barbara, CA 93113-2920, USA.

*Present address: Department of Chemistry, Durham University, South Road, Durham DH1 1TA, UK.
†To whom correspondence should be addressed. E-mail: wodtke@chem.ucsb.edu

pumping (8, 16) and then scattered, in ultrahigh vacuum, from a low-work function surface prepared by adsorbing a fraction of a monolayer (ML) of Cs on Au(111). The surface prepared in this way has a work function of 1.61 ± 0.08 eV (27). Individual measurements of emitted electrons are carried out over only a few seconds, always within 20 min after surface preparation by means of a microchannel plate assembly (22)—conditions that ensure the cleanliness and stability of the low-work function surface. The electron currents are measured with a digital oscilloscope, which avoids saturation problems that we had with the counting electronics used in our earlier measurements.

The basic methodology for obtaining absolute quantum yields for vibrationally promoted electron emission has been previously reported (16, 17). We used a new method to determine the flux of vibrationally excited molecules. Briefly, we used a laser induced fluorescence signal, measured just after the molecular beam skimmer to derive the number density of $\text{NO}(V=0)$ and $\text{NO}(V=18)$ molecules and converted the density to beam flux using the beam velocity determined by time of flight methods. Finally, we used knowledge of the excitation geometry and the velocity-dependent divergence of seeded beams (23) to determine the subsequent transmission of the NO molecules through the apparatus to the surface. We also determined the absolute flux of $\text{NO}(V=0)$ from measurements of the NO partial pressure increase in the scattering chamber and the pumping speed of the vacuum system. These $\text{NO}(V=0)$ measurements were also used to validate the LIF transmission function method used here. The transmission function was also verified by comparison with the measurement of transmission by White *et al.* (16, 17).

In the experiment, a nanosecond-pulsed laser excites NO to a single rotational level of the $A^2\Sigma^+$ state, inducing fluorescence on a ~ 200 -ns time scale as the molecule radiatively relaxes back to the ground electronic state (Fig. 1A). This LIF signal can be used to derive the flux of NO in $V=0$. A second nanosecond-pulsed laser, spatially overlapped with the first and slightly delayed, transfers population back to the ground electronic state in $\text{NO}(V=18)$ (Fig. 1B), depicting the LIF signal (dark shaded region). The depletion signal can be used to derive the flux of $\text{NO}(V=18)$ molecules. Figure 1, C and D, shows the electron signal—detected on the 100-ns time scale—corresponding to conditions of Fig. 1, A and B, respectively. The time dependence of the electron signal is a result of flight time from excitation to impact on the surface and thus provides precise information on the velocity distribution of the molecular beam. The electron signal of Fig. 1C is due to the impact on the surface of vibrationally excited NO resulting from Franck-Condon pumping (FCP), i.e., spontaneous emission from $A^2\Sigma^+$ into a Franck-Condon distribution of vibrationally excited levels. The larger electron signal of Fig. 1D results primarily from $\text{NO}(V=18)$ mol-

ecules populated by stimulated emission. The signal of Fig. 1D also contains a small contribution from FCP. By comparison of Fig. 1, A and B, the residual FCP signal can be accounted for in the analysis.

Figure 2 shows the per-collision probability for electron emission (quantum yield) for $\text{NO}(V=0)$ (lower panel) and $\text{NO}(V=18)$ (upper panel) plotted against the inverse velocity of the molecular beam. The dashed line is a fit to the Brato-News model, in which the positive velocity dependence of the yield is given by $e^{-v_0/v}$ (24). The Brato-News model's positive velocity dependence arises from the following physical scenario. As the NO molecule approaches the surface, its lowest unoccupied molecular orbital (LUMO) is stabilized by an image charge interaction. The velocity at which the LUMO of the NO molecule passes through the Fermi level governs the energy of the LUMO at the instant it is filled by electron transfer from the surface. At high velocity, the LUMO moves far below the Fermi level before being filled, creating an electronically excited state, i.e., an unoccupied hole below the Fermi level. At low velocity, the LUMO is filled by an electron close to the Fermi level, and the system remains in the ground electronic state. The dashed-line fit to the data of Fig. 2 for $\text{NO}(V=0)$ shows that our results for the ground vibrational state conform to the velocity dependence previously reported for other systems and so provides a validation of our experimental method (24–26).

The results for $\text{NO}(V=18)$ (upper panel) clearly follow a different mechanism. The quantum yield of electron emission for $\text{NO}(V=18)$ is many orders of magnitude larger (27) than that for $\text{NO}(V=0)$ and shows the opposite trend for velocity. Over the same velocity range where the $V=0$ results increase by a factor of ~ 10 , the $V=18$ results decrease by a similar amount. The solid line results from fitting the data to a function of the form $c + \frac{a}{v}$, where the best fit was found when the fitting parameters c and a were set to zero. Thus, the quantum yield for vibrationally promoted electron emission for $\text{NO}(V=18)$ appears to follow a $1/v$ or inverse velocity dependence. How does this behavior arise?

Katz *et al.* have treated the problem of vibrationally promoted electron emission (26) by NO on Cs/Ru. Though some aspects of the experimental observations are captured in that work—for example, the positive dependence on initial vibrational excitation—like other theories of non adiabatic interactions at surfaces, their theory predicts an increase of electron emission with increasing velocity. Their model thus does not explain the results reported here.

We have previously suggested a vibrational autodetachment mechanism for vibrationally promoted electron emission (17) involving formation of a transient negative ion and autodetachment of an electron from this transient species, resulting in the transfer of vibrational energy to electronic excitation. The mechanism, illustrated in Fig. 3A, is based on the fact that the vertical electron bond

ing energy (VEBE) for NO varies strongly with intermolecular distance, at the outer turning point (r_1) of vibrational motion for $\text{NO}(V=18)$, the VEBE is about ~ 2.2 eV (i.e., the extra electron is strongly bound), whereas at the inner turning point (r_2), it is about ~ 2.6 eV (the extra electron is strongly repelled).

Figure 3A shows two electronic potential curves: one for NO with an electron at the Fermi level of the Cs/Au surface and one for the case in which a Fermi level electron has been transferred, forming NO^- . The two curves are shifted in energy relative to their gas phase spacing by the work function, Φ , to reflect the energetics of electron transfer from the metal to the molecule when the molecule is far from the surface (28). For NO bond lengths, $R_{\text{NO}} > 1.38$ Å, VEBE exceeds Φ . Thus, as the NO molecule approaches the surface, at a distance of about $z \sim 10$ Å (29), there is sufficient overlap of the surface electron density and the LUMO of NO that it becomes possible for an electron to be transferred to the “stretched” $\text{NO}(V=18)$ molecule. For simplicity, we consider only the case in which this initial electron transfer occurs precisely when $R_{\text{NO}} = 1.38$ Å, as indicated by the arrow shown in Fig. 3A (30). As

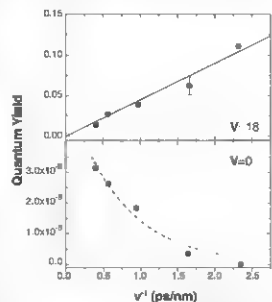


Fig. 2. The velocity dependence of electron emission from $\text{NO}(V)$ collisions with Cs/Au surfaces. (Upper panel) Results for $V=18$; (lower panel) results for $V=0$. The quantum yield is plotted against inverse velocity (v^{-1}). The dashed line is a fit to the $V=0$ results with a function of the form $e^{-v_0/v}$, based on the Brato-News model (24) for chemical hole diving, $v_0 = 1375$ m/s. The solid line is a fit to the $V=18$ data with a function of the form v_0/v with $v_0 = 44.9$ m/s. The goodness of fit is reflected in a reduced χ^2 value of 10^{-7} . The error bars reflect random errors and are 95% confidence limits based on the Student's t test with four independent measurements at 1.65 ps/nm and five independent measurements at 0.403 ps/nm. Although the shape of the $V=18$ quantum yield is well determined (indicated by the error bars), its absolute scaling is subject to larger systematic errors. We estimate these systematic errors to be less than about a factor of 3, e.g., $0.02 < 0.0232 \text{ ps/nm} < 0.03$.

NO bond compression in the anion progresses, electron release from the NO may occur near the inner turning point of vibration, r_2 , where the molecule's interaction with the electron is strongly repulsive—i.e., $VEBE < 0$. In principle, the electron may be transferred back to the surface, or it may possess sufficient kinetic energy, ΔE_2 , to be ejected in the proper direction so that it entirely escapes the surface and can be detected in our experiment.

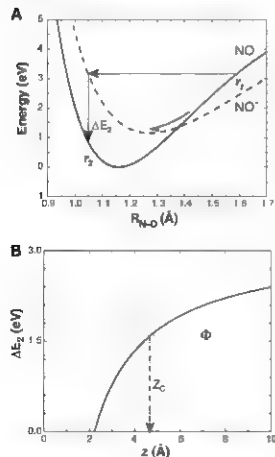


Fig. 3. The vibrational autodetachment mechanism and the existence of a critical distance. (A) The potential energy curves for the NO and an electron at the Fermi level (solid curve) and NO⁻ (dashed curve) at infinite separation from the Cs/Au surface. The relative energies are adjusted by the work function to reflect charge transfer from the surface to the molecule and back. A highly vibrationally excited molecule may capture an electron from the surface near the outer turning point, r_1 , of vibration. The horizontal line indicates the energy of NO(V = 18). After NO bond compression to a bond length near 1.38 Å, an energetically adiabatic transition to the anion potential may take place, indicated by the curved arrow. The electron may then be lost from the NO molecule near the inner turning point, r_2 , releasing ΔE_2 . If ΔE_2 exceeds the work function, the electron may be ejected from the molecule surface system and be detected at a macroscopic distance from the surface. (B) The dependence of ΔE_2 on the molecule's distance from the surface, z . The downward-pointing arrow shows the critical distance, z_c , below which ΔE_2 is less than the work function, Φ . A detailed derivation of the potentials in Fig. 3 is presented in the supporting online material. A more detailed description of this mechanism has been presented in (27) (see, especially, figure 10A and the related discussion).

Nothing in the description of the vibrational autodetachment mechanism given so far would give rise to the $1/v$ velocity dependence that we observe. However, a $1/v$ dependence could arise if three additional conditions are met: (i) There must be a defined region above the surface where the electron capture step can take place, the extent of which is not dependent on the velocity of the incident NO(V = 18); (ii) the NO molecule must move with approximately constant velocity in this region; and (iii) the probability of the non-adiabatic event resulting in emission of an electron must not depend on the velocity of the incident NO(V = 18). We next discuss how these conditions can be satisfied in the autodetachment mechanism in connection with Fig. 3.

As the NO molecule approaches the surface, the NO curve (dashed line in Fig. 3A) shows a reduction in energy due to an image potential in interaction and, as a result, ΔE_2 decreases. Figure 3B shows this reduction in ΔE_2 as a function of z . Below a critical value, $z_c \sim 4.8$ Å, electron emission is no longer possible because ΔE_2 becomes smaller than the work function, Φ . This establishes the first condition. Because z_c is large, the neutral NO molecule will interact only weakly with the surface, justifying the constant velocity approximation. We take the third condition as an assumption and use it to calculate the vibrationally promoted electron emission probability, P_{vib} .

To do so, we first model the probability of the initial electron transfer to NO. The electronic coupling will depend on the overlap of the orbital of the incident NO molecule, $|n\rangle$, with the metal electronic states, $|k\rangle$, and has the form $V \sim e^{-\kappa R}$ (37). By Fermi's golden rule, the rate of electron transfer will depend on the square of V . To calculate P_{vib} , we integrate the electron transfer rate over the trajectory of the NO molecule and multiply the result by the probability for a nonadiabatic transition P_{non} back to neutral NO. The trajectory includes three parts: (i) the incoming trajectory up to the critical distance z_c ; (ii) the trajectory proceeding inward and reflecting from the surface; and (iii) the outgoing trajectory from z_c outward. In principle, electron emission can have contributions from regions (i) and (iii), but because the probability of NO(V = 18) surviving reflections is small (8), we ignore the contribution from (iii). Using the constant velocity condition, $z = -vt$, on the incoming trajectory

$$P_{\text{vib}} = P_{\text{non}} \int_{-\infty}^{z_c} dt |e^{i\pi/\hbar}|^2 = \frac{\hbar}{2\pi} P_{\text{non}} e^{-2\kappa z_c/\hbar} \quad (1)$$

Equation (1) shows that the simple model just described does indeed reproduce the $1/v$ dependence observed experimentally (32). The $1/v$ dependence arises because the time available for electron transfer scales as $1/v$ and the probability for a non-adiabatic transition P_{non} back to the neutral NO curve is independent of v . A more complete calculation would have to take into account many details that are omitted from this description. For example, the electron capture might involve an electron originating at an energy, ϵ , below the Fermi level. For

all values of ϵ that are energetically allowed, z_c exists and hardly changes from its value for $\epsilon = 0$. Thus, summing over the contributions from different values of ϵ will retain the $1/v$ dependence. Similar arguments can be made for generalizing the model to include loss of some vibrational energy in the inner region or transfer of the available energy to more than one electron.

Our conclusions suggest that electronically nonadiabatic effects can play a role in bond dissociation of surface adsorbates. First, the vibrational autodetachment mechanism described can be important whenever the LUMO is either bonding or antibonding. In such cases, a notable structural change between the neutral molecule and its anion implies an electronic-vibrational energy exchange similar to that shown in Fig. 3A. Only in the case where the LUMO is a non-bonding orbital is this mechanism expected to be unimportant. Furthermore, the $1/v$ dependence of P_{non} in Eq. 1 requires that the nonadiabatic transition probability, P_{non} , be independent of v . This suggests rather directly that the motion of the center of mass of the NO molecule relative to the surface cannot be the driver of the observed non-adiabatic electronic excitation. Rather, it is the rapid stretching and compression of the N-O bond that drives the nonadiabatic dynamics. Thus, the nonadiabatic couplings that we observed via electron emission and attributed to dynamics at $z > 5$ Å and at finite velocities are expected to persist to small values of z and in the limit of zero velocity, conditions describing surface adsorbates. Indeed, nonadiabatic electronic coupling will only increase with decreasing values of z . More concretely, the underlying nonadiabatic excitation of electron hole pairs represents a substantial energy-dissipation mechanism not accounted for by theories based on the BO approximation. As atoms or molecular fragments react on a surface and excited electron-hole pairs are produced, the energy loss would help to rapidly stabilize the products. For example, as two recombining surface adatoms form an adsorbed diatomic molecule, the neglect of electron-hole pair excitation may result in an underestimate of energy dissipation to the surface and lead to artificial redissociation of the diatomic in a calculation without the BO approximation. Likewise, branching between two reactions with similar activation barriers might be influenced by more efficient energy dissipation in one channel preferentially trapping a particular transition state into one product channel versus another. Hence, both reaction rate and competitive reactive branching might depend strongly on BO approximation breakdown.

Our results necessitate further work, both experimental and theoretical. The critical distance model has important experimentally testable consequences: it constrains the energy distribution of emitted electrons and predicts that vibrational relaxation would not decrease as electron emission does. A more rigorous theory of the kinetic energy dependence of vibrationally promoted electron emission is also required. For example, for simplicity, the present model neglects the possibly

important role of molecular orientation. Though beyond the scope of the qualitative analysis presented here, changing the charge state of a molecule can markedly alter the orientational forces it experiences in its interaction with the metal surface. Thus, bond reorientation of the NO molecule may play a crucial role in the vibrational autodetachment mechanism. Such work should help to elucidate the nonadiabatic dynamics involved in dissociation, recombination, and reactions of molecules on metal surfaces.

References and Notes

- M. Binn, J. R. Oppenheimer, *Ann. Phys.* **84**, 457 (1977).
- W. Kohn, L. J. Sham, *Phys. Rev.* **140**, A1133 (1965).
- J. Greeley, J. K. Nørskov, M. Mavrikakis, *Annu. Rev. Phys. Chem.* **53**, 319 (2002).
- K. M. Neyman, F. Illak, *Catal. Today* **105**, 2 (2005).
- T. Greber, *Surf. Sci. Rep.* **28**, 1 (1997).
- H. Wenzhaus, *Surf. Sci. Rep.* **45**, 1 (2002).
- C. T. Rettner, F. Fabre, J. Korman, D. J. Auerbach, *Phys. Rev. Lett.* **55**, 1904 (1985).
- Y. Huang, C. T. Rettner, D. J. Auerbach, A. M. Wodtke, *Science* **290**, 113 (2000).
- Y. Huang, A. M. Wodtke, A. Hsu, C. T. Rettner, D. J. Auerbach, *Phys. Rev. Lett.* **84**, 2985 (2000).
- A. M. Wodtke, J. C. Tully, D. J. Auerbach, *Int. Rev. Phys. Chem.* **23**, 513 (2004).
- Q. Ran, D. Matsiev, D. J. Auerbach, A. M. Wodtke, *Phys. Rev. Lett.* **98**, 237601 (2007).
- B. Gerson, H. Wenzhaus, W. K. Wenzhaus, E. W. McFarland, *Science* **294**, 2521 (2001).
- X. J. A. Zuppo, J. M. Gidman, G. A. Somorjai, *J. Am. Chem. Soc.* **127**, 5792 (2005).
- E. Hasegawa, *Cond. Opin. Solid State Mater. Sci.* **10**, 192 (2004).
- D. J. Auerbach, *Science* **294**, 2488 (2001).
- J. D. White, J. Chen, D. Matsiev, D. J. Auerbach, *A. M. Wodtke, Nature* **433**, 503 (2005).
- J. D. White, J. Chen, D. Matsiev, D. J. Auerbach, A. M. Wodtke, *J. Chem. Phys.* **124**, 064702 (2006).
- Here one Å is defined as one-to-one stoichiometric equivalence of Cs to surface Au atoms.
- T. Greber, *Adv. Phys. Rev.* **8**, 80, 8755 (1994).
- E. E. Wilson, *Annu. Rev. Phys. Chem.* **50**, 1 (1999).
- J. L. Lathau, *J. Chem. Phys.* **129**, 024709 (2008).
- Under our conditions, the work function does not change over this time scale.
- R. T. Jongma, T. Rasing, G. Meyer, *J. Chem. Phys.* **102**, 1925 (1995).
- R. Beato, D. M. Mewes, *Rep. Prog. Phys.* **52**, 655 (1989).
- L. Hellberg, J. Strömquist, B. Kavenon, S. I. Lundqvist, *Phys. Rev. Lett.* **74**, 4742 (1995).
- G. Katz, Y. Zevi, R. Kordak, *J. Phys. Chem. B* **109**, 18876 (2005).
- The quantum yield reported here is larger than previously reported in (16) and (17) due to detector saturation problems in the previous experiment.
- The energetics for electron transfer to the surface become more favorable as the molecule approaches the surface.
- One may estimate tunneling distances based on principles set forth in (33).
- Energetically, the electron can originate from as much as 0.6 eV below the Fermi level, but this does not necessarily alter the analysis presented here.
- M. Shown, S. Roy, P. Parandekar, J. Tully, *J. Chem. Phys.* **125**, 154703 (2006).
- Equation 1 is valid only in the limit of negligible depletion of the initial $\text{NOV} = 10$ population and thus small quantum yield. In the more general case we must solve the differential equation for the population of $\text{NOV} = 10$. Equation 1 is then the first term of a Taylor series expansion of the solution.
- We gratefully acknowledge financial support from the NSF grant (CHE-0454806) and the Partnership for International Research and Education—for Electron Chemistry and Catalysis at Interfaces (NSF grant CHE-0530268). M.H.W. acknowledges finance support through a Feodor Lynen fellowship provided by the Alexander von Humboldt foundation. We thank D. Matsiev for many useful discussions and suggestions and a critical reading of this manuscript.

Supporting Online Material

www.sciencemag.org/cgi/content/full/321/5893/1191/DC1

SDM Text

References

5 May 2008; accepted 15 July 2008

10.1126/science.1160040

Weak Interplate Coupling by Seamounts and Repeating $M \sim 7$ Earthquakes

Kimihiro Mochizuki,¹ Tomoaki Yamada,¹ Masanao Shinohara,¹ Yoshihiro Yamanaka,² Toshihiko Kanazawa¹

Subducting seamounts are thought to increase the normal stress between subducting and overriding plates. However, recent seismic surveys and laboratory experiments suggest that interplate coupling is weak. A seismic survey in the Japan Trench shows that a large seamount is being subducted near a region of repeating earthquakes of magnitude $M \sim 7$. Both observed seismicity and the pattern of rupture propagation during the 1982 $M 7.0$ event imply that interplate coupling was weak over the seamount. A large rupture area with small slip occurred in front of the seamount. Its northern bound could be determined by a trace of multiple subducted seamounts. Whereas a subducted seamount itself may not define the rupture area, its width may be influenced by that of the seamount.

Bathymetric relief on the ocean floor has been presumed to lead to variations in mechanical coupling along the plate interface between the overriding and subducting plates in the subduction zones, which in turn yield an uneven distribution of large earthquakes (1, 2). Seamounts, an obvious feature of topographic highs on subducting crust, having relative heights of more than 1000 m are not

common (3). Such large seamounts may increase the normal stress between subducting and overriding plates by as much as 100 MPa when subducted (4), and it has been proposed that the raised interplate coupling could generate $M > 7$ earthquakes (2). Strong coupling over subducted seamounts has been proposed to explain rupture regions of large earthquakes in the Costa Rica subduction zone (5, 6) and a seismic barrier during the 1946 $M 8.1$ Nankaido earthquake (7).

Recent seismic surveys (8, 9) have shown that the base of the overriding plate is eroded while the decollement is shifted upward along with the subduction of a seamount, which would entrain fluid-rich sediment. Such effects, also seen in laboratory sandbox experiments (10), are ex-

pected to induce local weak interplate coupling, the damage caused by erosion may prevent the accumulation of elastic strain energy (11), and elevated pore pressure may reduce the effective normal stress (12). Local weak coupling at the plate interface is in accord with seismic surveys showing that some subducted seamounts have retained their shapes to depths of at least ~ 8 km (8, 9). Here, we examine a long-term record of seismicity in the Japan Trench to clarify the relation between seamounts and large earthquakes.

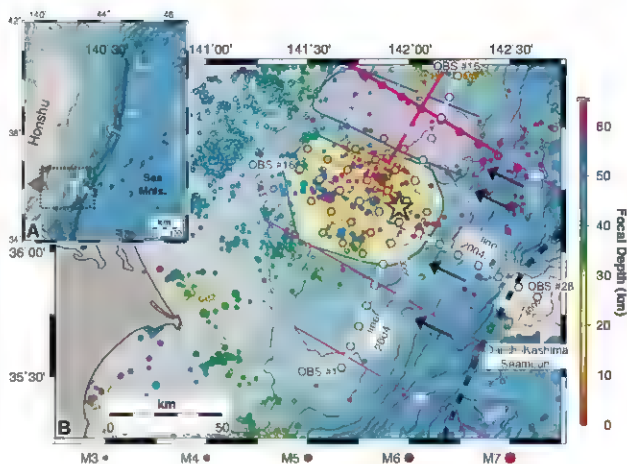
The Pacific Plate subducts beneath the North American Plate at ~ 8.3 cm/year along an azimuth of 295° along the Japan Trench (13) and contains a group of seamounts of various dimensions (Fig. 1), including Daichi Kishima Seamount, which entered the trench 150,000 to 250,000 years ago (14). Volcanic rock samples collected from the seamount yield an age of 100 to 120 million years, ~ 20 million years younger than the surrounding oceanic crust (14). Several furrows on the landward slope of the seafloor correlate with the distribution of seamounts on the offshore Pacific Plate (Fig. 1). Sandbox experiments reproduce such furrows oriented in the subduction direction behind subducting seamounts (10, 15). Similar furrows are seen along the Middle America Trench off Costa Rica (5, 8, 15). Repeating large earthquakes with a fairly constant size ($M \sim 7$) and a recurrence interval (~ 20 years) have occurred in a confined region down-dip from the Daichi Kishima Seamount since the 1920s (Fig. 2). Such occurrences suggest the existence of a stationary area of repeating rupture along the plate interface.

The most recent large event occurred in 1982 (another $M \sim 7$ earthquake likely along the series

¹Earthquake Research Institute, University of Tokyo, 1-1-1, Yayoi, Bunkyo-ku, Tokyo 113-0032, Japan. ²Graduate School of Environmental Studies, Nagoya University, Furo-cho, Chikusa-ku, Nagoya 464-8601, Japan.

*To whom correspondence should be addressed. E-mail: kim@eri.u-tokyo.ac.jp

Fig. 1. (A) Bathymetry along the Japan Trench. The depth contour interval is 1000 m. An arrow indicates the plate convergence direction. A number of seamounts occur on the Pacific Plate offshore from the Ibaraki Prefecture (indicated as I). The dotted rectangle depicts the area shown in (B). **(B)** Seismic activity off Ibaraki, seismic profiles, and OBS stations (hexagons) of the surveys in 2004 (white), in 2005 (orange), and in 1998 and 2001 (magenta) (thin, reflection; thick, refraction). Circles show epicenters of $M > 3$ earthquakes in the Japan Meteorological Agency catalog (1996–2005), with focal depth scale at right and magnitude scale at bottom. A broken black line depicts the trench axis. A seismically quiet band (blue-shaded area) exists to the north of the source region of the 1982 M 7.0 event (green-shaded area, Fig. 2). A large yellow star marks its epicenter. Several furrows of different sizes are oriented in the direction of plate convergence (black arrows).



occurred on 7 May 2008 UTC). We modeled its rupture process by means of long-period teleseismic body waves (fig. S2). Its focal mechanism was a thrust type with the P axis in the subduction direction. The amount of slip appears to have been relatively small, averaging ~ 50 cm centered at ~ 25 km downslip from the hypocenter. However, an anomalously large rupture area raised its magnitude to 7.0. The local topographic bulge around its epicenter has been considered as evidence that an underlying subducted seamount defined the rupture area. The northern limit of the source region coincides with the edge of a ~ 25 -km-wide band of low seismic activity along the subduction direction (Fig. 1). Previous refraction (lines F and I) and reflection (lines C and I) sections through the seismically quiet band revealed low velocity underthrust sediment layers with P -wave velocities (V_p) of ~ 4 km/s along the plate interface (16, 17). A trench parallel reflection section (line C) beneath the seafloor furrows shows that the sediment layers are convex upward and have dimensions similar to those of the surrounding seamounts (fig. S6). Thus, the layer was interpreted as having formed in the wake of multiple subducted seamounts (16).

In 2004, we conducted an active-source seismic survey using ocean bottom seismometers (OBSs) across the source region of the 1982 M 7.0 event along the trench normal, and trench parallel profiles (Fig. 1). We derived two-dimensional V_p structures by P -wave first-arrival travel time inversion (Fig. 3). In contrast to the horizontally stratified structure to the north (fig. S4), the structure in and around the source region

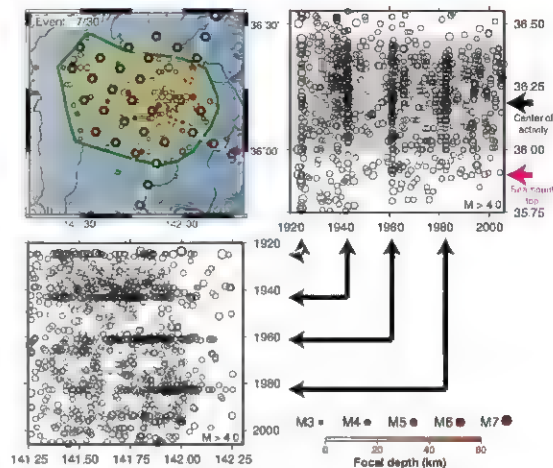


Fig. 2. Upper left: Aftershock activities of the 1982 M 7.0 earthquake. An estimated source region is indicated by the green-shaded area. Seismic profiles of the 2004 (white) and 2005 (orange) surveys and respective OBS stations are shown. Upper right and lower left: Chronological tables of earthquake activities in the region along the latitudinal and longitudinal axes. High earthquake activity associated with $M \sim 7$ earthquakes has occurred every ~ 20 years within a latitudinal band between 36.0°N and 36.4°N , centered at $\sim 36.2^\circ\text{N}$, substantially offset to the north from the subducted seamount (Fig. 4A).

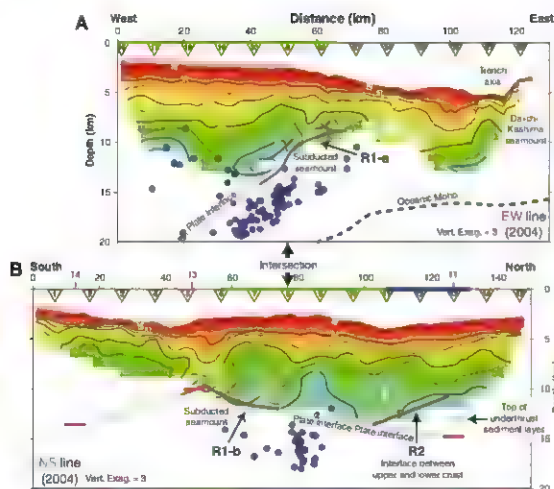


Fig. 3. (A) V_p structure along the trench-normal 2004 east-west (EW) line, and projected hypocenters observed during the 2005 seismic observation (within a 10-km-wide box on both sides along the profile for hypocenter projection). The OBS locations are shown by the yellow inverted triangles with their station numbers. A green bar along the top axis indicates the source region of the 1982 M 7.0 event. Geometry of the plate interface determined from strong reflections on the OBS record sections (hyperbolic black curves) outlines the convex upward structure (R1-a) interpreted as a subducting seamount. Earthquakes are concentrated beneath the subduction front of the seamount. (B) Same as (A) for the trench-parallel 2004 north-south (NS) line (hypocenters within a 7-km-wide box on both sides along the profile are projected). Depths to the plate interface (magenta bars) are determined on the trench-normal reflection sections (Fig. S6). Corresponding line numbers of the sections are shown in magenta at the top axis. The depth to the top of the underthrust sediment is also shown (orange bar). The reflection interface in the north (R2) corresponds to the boundary between the upper and lower crust. A blue bar along the top axis indicates the seismically quiet band.

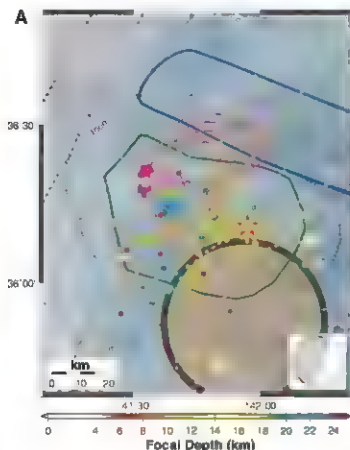


Fig. 4. (A) Geometry of the plate interface compiled from all available sections (dotted colored contours) and hypocenters of earthquakes observed during the 2005 seismic observation (depth scale at bottom). A red star indicates the epicenter of the 1982 event (its focal mechanism is shown at lower right). A thick black circle outlines the subducting seamount, a green curve denotes the source region of the 1982 event, and a blue curve shows a

seismically quiet band. Red contours indicate amounts of coseismic slip (outermost contour, 40 cm; interval, 10 cm). The dotted black curve surrounding the source region depicts an earthquake-search range by the OBS network. (B) Three-dimensional perspective view of the plate interface geometry. The hypocenter of the 1982 M7.0 event is located at the base of the subducting seamount. It ruptured a region down dip.

moisture) pine dowels would burn at 12% O_2 (6). No previous study has assessed the limits of combustion on natural (that is, not unnaturally dry) material, nor has any study been conducted in a realistic atmospheric environment.

We tested the hypothesis that prolonged low O_2 intervals occurred in the Mesozoic by using a series of combustion experiments and a compilation of geologic evidence for wildfires. These experimental burns have been undertaken in a $>8\text{ m}^3$ walk-in plant growth room equipped with a thermal imaging system and full atmosphere, temperature, and humidity control (9). The occurrence of paleowildfires (based on the occurrence of charcoal, inclusions, and geochemical evidence) in the Mesozoic is documented and compared with the predicted atmospheric O_2 levels for this time, which are in turn reassessed on the basis of results from the combustion experiments.

Combustion is defined as a sequence of exothermic chemical reactions, between fuel and oxidant, accompanied by the production of heat or both heat and light in the form of either a glow or flames. These criteria were used to judge when

combustion was occurring in a state of rigorously controlled experimental atmospheres. Charring is not a measure of combustion, because charcoal can be made without the presence of O_2 by using a heat source greater than 200°C (no heat is given off; the material is simply "cooked"). Combustion in different atmospheric O_2 concentrations was measured either as production and duration of flaming and smoldering of matches, paper, candles, and *Pinus caribaea* (Ocotillo pine) wood, or as temperature change captured using continuous thermal imaging of sphagnum moss burns on a hot plate set at $\sim 450^\circ\text{C}$.

Atmospheric CO_2 concentration had little effect on ignition or combustibility of the material (Fig. 1, A to D). A struck match produced a brief flame at 14% O_2 (Fig. 1A), which was long enough to produce a flame and short-lived smoldering in paper (Fig. 1C). A candle and *P. caribaea* sticks sustained a flame briefly at 16% O_2 (Fig. 1, B and D) but not at lower O_2 . A candle continually burned at 17% O_2 , whereas a match and paper burned to ash at 18% O_2 . *P. caribaea* wood burned with a sustained flame at 18% O_2 . The

moss charred at all ranges of O_2 concentration, however, no temperature change or flames were generated by the moss below 15% O_2 (Fig. 1, E and G). The mean maximum temperature reached by the moss was found to increase with O_2 concentration (Fig. 1E) [an r^2 (coefficient of determination) value of 0.832 reveals a reliable correlation]. The moss did not show a temperature change at O_2 concentrations below 15% (with no smoldering or flaming observed), indicating that combustion cannot occur at such low concentrations of atmospheric O_2 . The moss exceeded the temperature of the hot plate on average by 332°C (reaching a maximum value of 882°C) and flamed readily.

Figure 1E shows that combustion does not occur below 15% O_2 , that there is limited combustion between 15 and 17% O_2 , and that com-

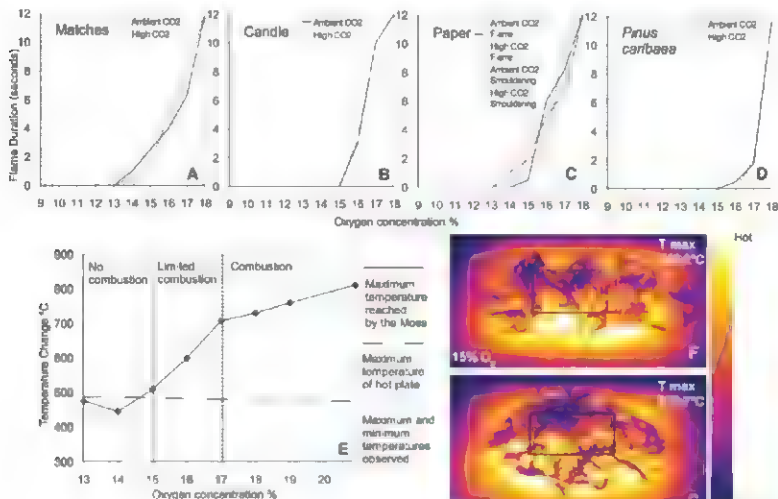


Fig. 1. Effects of O_2 on combustion. (A to D) Ignition and flame duration for various O_2 concentrations and in ambient and high CO_2 (2000 parts per million) for (A) matches, (B) a candle, (C) paper, and (D) *P. caribaea* sticks (ignition source for all was matches). (E) Temperature changes observed in sphagnum moss heated on a hot plate set at 450°C for various O_2 concentrations. All data are based on 15 repeated burns for each setting. A temperature change is first seen in the moss at 15% O_2 (shown by a positive deviation in temperature of the moss from the temperature of the hot plate).

(F) Thermal image of sphagnum moss heated in 15% O_2 , showing that the temperature of the moss is hotter than that of the hotplate at this concentration of atmospheric O_2 and above, indicating that 15% O_2 is the lower limit needed for combustion of plant material (that is, maximum temperature of some areas of moss are greater than that of the hot plate). (G) Thermal image of sphagnum moss heated in 14% O_2 , showing that no temperature change is observed (that is, maximum temperature of the moss is less than that of the hot plate).

bustion occurs readily at 17% O_2 and above, in agreement with Watson (7), who showed that dry paper cannot be ignited by a spark below 17% O_2 . Thus, our results strongly suggest that the minimum O_2 limits for combustion should be increased from 12% to 15% O_2 .

Our results contradict recently published evidence that pine wood dowels burn in 12% atmospheric O_2 (8). These experiments were performed under conditions in which the ignition source was external to the low- O_2 atmospheric environment, hence, material was ignited through a small door at the side of the apparatus. This probably affected the ignitability of the material, because the immediate area may have been flushed with present atmospheric levels (PAL) of O_2 . In addition, the moisture content of the wood dowels was between 0 and 2%, which we consider unrealistic for a natural system. The fuel moisture content above which a fire will not spread ranges between 15 and 30% for temperate ecosystems (10) and has been suggested to be similar for tropical ecosystems (11). Foliar moisture contents of 1-year-old conifers (Douglas fir, grand fir, and ponderosa pine) during summer (North America), when the atmosphere has a relative humidity of 18 to 35% (dry), are 128 to 147% (12). In addition, pine needles in the same combustion experiments of the same moisture content did not burn until 16% O_2 , and pine dowels of 12% moisture failed to ignite at 12% O_2 . The average moisture contents of the *P. caribaea* wood, the matches, and the moss in our combustion experiments were 7.31%, 24.8%, and 48.3%, respectively, revealing that even at relatively low moisture contents, natural material cannot be ignited in a fully sealed atmospheric O_2 environment below 15% O_2 . Furthermore, although the major cause of prehuman wildfires was lightning (13), the majority of lightning strikes do not initiate burning because they tend to be accompanied or followed closely by rain (14). During such circumstances, fuel moisture may be expected to rise beyond the fiber-saturation point (30%), making ignition, even under PAL of O_2 , virtually impossible (14). On the basis of our data, together with litter and vegetation moisture contents in a natural system (11), we argue that 17% O_2 is likely to be a more realistic lower limit for the occurrence of natural wildfires, confirming the suggestions of Lenton and Watson (15); however, we have set the lower limit for combustion at 15%, which allows for wildfires to occur under exceptional circumstances.

Published records of wildfire-derived charcoal, inertinite, and geochemical proxies (polycyclic aromatic hydrocarbons) were collected from the literature on the Mesozoic to test whether atmospheric O_2 could have dropped below 15% for prolonged intervals. We only include records in which the geological age of the stratigraphic units containing the wildfire evidence is known (for example, the Aptian stage) and in which the remains were considered not to have been substantially reworked (table S1). The occurrences of wildfire events throughout the Mesozoic were

plotted against the predicted atmospheric O_2 curves of Berner (2), Falkowski *et al.* (3), and Bergman *et al.* (16) (Fig. 2 and table S1). This analysis revealed that wildfires were prevalent throughout the Mesozoic and, coupled with data from our combustion experiments, did not support model-based predictions of low O_2 (<15% O_2) for the Triassic (3) or Jurassic (2) (Fig. 2). Limited occurrence of fire proxy data for the intervals 250 to 238 Ma and 236 to 222 Ma could potentially indicate a period of <15% O_2 . However, a detailed analysis of rock abundance and the availability of suitable strata to preserve charcoal (fig. S1, A and B) indicates that this apparent wildfire gap probably represents a preservational artifact rather than an indication of extremely low O_2 levels.

The various atmospheric O_2 models use different input parameters that result in differing O_2 records for the Mesozoic. The GEOCARBSULF (2) atmospheric O_2 model is calculated using the difference in O_2 input from organic carbon and pyrite sulfur burial and O_2 removal by the weathering of organic carbon and pyrite sulfur in rocks,

plus the oxidation of reduced carbon and sulfur gases emitted by volcanism and metamorphism. The Falkowski *et al.* (3) model is based on isotopic records for organic carbon, carbonates, and sulfates and on an earlier version of GEOCARBSULF [GEOCARB III (17)]. Both the Falkowski *et al.* (3) and GEOCARBSULF (2) models use $\delta^{13}C$ data as a strong input forcing. The COPSE model for O_2 (16) includes C, O, P, and S cycles, partial cycles for N and Ca, and also biological and geological processes (tectonic uplift, weathering, volcanic and metamorphic degassing, terrestrial and marine productivity; burial of marine and terrestrial organic matter, and marine inorganic burial). On the basis of our newly proposed low limit for combustion, both the Falkowski *et al.* (3) and GEOCARBSULF (2) models are currently incompatible with the record of fires in the Mesozoic, because they predict extensive periods of low (10 to 12%) atmospheric O_2 throughout the Triassic (3) and Jurassic (2). Our experimental burn data (Fig. 1), coupled with the newly compiled Mesozoic wildfire record (Fig. 2) are consistent with the Mesozoic O_2 record

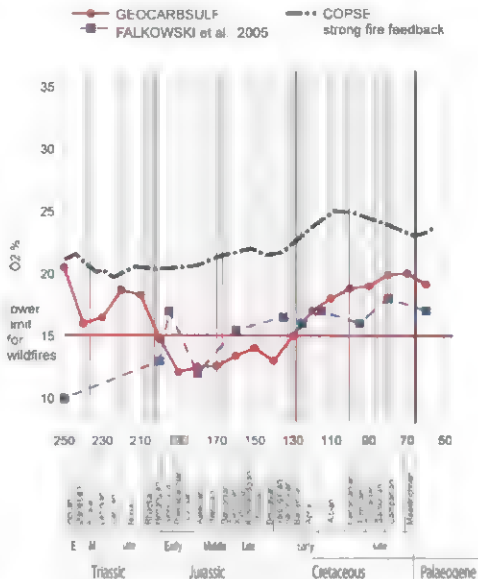


Fig. 2. Modeled O_2 curves for the Mesozoic compared with the record of paleowildfires. Vertical black lines represent known occurrences of fires in the fossil record (table S1). O_2 curves are replotted using data from the models of Berner (GEOCARBSULF (2)), Falkowski *et al.* (3), and Bergman *et al.* (COPSE) (16).

predicted by the COPSE model (16). This model, unlike GEOCARBSULF (2) and the model by Falkowski *et al.* (3), includes fire feedbacks and nutrient cycling and accounts for their controls on terrestrial productivity. These are known to affect weathering and organic carbon burial rates (18), which in turn play a role in regulating O_2 . Future models of paleoatmospheric O_2 should strongly consider the effects of changing terrestrial and marine productivity, including fire feedbacks.

We have shown that extensive periods of low O_2 (<15%) cannot have occurred in the Mesozoic, according to our revised lower limit for combustion coupled with the record of paleowildfires. This also suggests that the predicted low O_2 (<13%) levels for the Frasnian (385 to 374 Ma) in the Paleozoic (19, 20) needs reevaluation. The paleowildfire record provides a key means for testing low- O_2 events in the geological record and highlights the need for high resolution studies of paleowildfire across major mass extinction events in order to test current hypotheses that advocate a primary role of short term low-atmospheric- O_2 events in catastrophic faunal diversity loss in the Permian Triassic

(4) and Triassic Jurassic (21) mass-extinction events.

References and Notes

1. T. M. Lenton, in *Evolution of Planet Earth: The Impact of the Physical Environment*, L. Rothchild, A. Lister, Eds. (Academic Press, London, 2003), pp. 33–51.
2. R. A. Berner, *Geochim. Cosmochim. Acta* 70, 5653 (2006).
3. P. G. Falkowski *et al.*, *Science* 309, 2202 (2005).
4. R. B. Hays, P. D. Ward, *Science* 308, 398 (2005).
5. M. J. Cope, W. G. Chaloner, *Nature* 283, 647 (1980).
6. D. J. Ratbath, B. Langford, *Combust. Flame* 32, 133 (1968).
7. A. J. Watson, thesis, University of Reading (1978).
8. R. A. Wildman *et al.*, *Geology* 32, 457 (2004).
9. Materials and methods are available as supporting material on Science Online.
10. P. A. Allen, *USDA For. Serv. Gen. Tech. Rep.* N-370 (1976).
11. C. Uhl, J. B. Knappmann, *Ecology* 71, 437 (1990).
12. J. K. Agre, C. S. Wright, M. Williamson, M. H. Huff, *For. Ecol. Manage.* 167, 57 (2002).
13. A. C. Scott, *Paleogeogr. Paleoclimatol. Paleobiol.* 364, 281 (2000).
14. A. J. Watson, J. E. Lovelock, L. Margulis, *Biosystems* 10, 293 (1978).
15. T. M. Lenton, A. J. Watson, *Global Biogeochem. Cycles* 14, 243 (2000).
16. M. M. Bergman, T. M. Lenton, A. J. Watson, *Am. J. Sci.* 304, 397 (2004).

17. R. A. Berner, Z. Kothavala, *Am. J. Sci.* 301, 182 (2001).
18. T. M. Lenton, *Geoch. Change Biol.* 7, 613 (2003).
19. A. C. Scott, G. G. Gasspoil, *Proc. Natl. Acad. Sci. U.S.A.* 103, 10861 (2006).
20. R. A. Berner, D. J. Beerling, R. Outley, J. M. Robinson, R. A. Wildman, *Annu. Rev. Earth Planet. Sci.* 31, 105 (2003).
21. R. A. Berner, J. M. VandenBrooks, P. D. Ward, *Science* 316, 557 (2007).
22. We acknowledge funding through a European Union Marie Curie Excellence Grant (MECT-CT 2004-042531). We thank T. Gallagher for the use of the thermal imaging camera, M. Harwood, R. O'Hara, and D. Martin for much help and assistance in setting up the JCD Peac facility; J. Hunt and C. Hunt for supplying the moss; T. Lenton and two anonymous reviewers for improving the manuscript; L. Mander for insightful comments throughout; and M. Harwood, L. Mander, and M. Stenhardt for safety supervision while working in subambient O_2 conditions.

Supporting Online Material

www.sciencemag.org/cgi/content/full/321/5893/1197/DC1

Materials and Methods

Fig. S1

Table S1

References

27 May 2008; accepted 18 July 2008

10.1126/science.1160978

Field Experiments with Transformed Plants Reveal the Sense of Floral Scents

Danny Kessler, Klaus Gase, Ian T. Baldwin*

Plants use many means to attract pollinators, including visual cues and odor. We investigated how nonpigment floral chemistry influences nectar removal, floral visitation, florivory, rates of outcrossing, and fitness through both male and female functions. We blocked expression of biosynthetic genes of the dominant floral attractant (benzyl acetone [*Nachal1*]) and nectar repellent (nicotine [*Napmt1/2*]) in *N. attenuata* combinations in the native tobacco *Nicotiana glauca* and measured their effects on plants in their native habitat. Both repellent and attractant were required to maximize capsule production and seed siring in emasculated flowers and flower visitation by native pollinators, whereas nicotine reduced florivory and nectar robbing.

Flowers produce bouquets of scents that are believed to help reproduction by attracting pollinators. However, experimental proof that floral scents facilitate outcrossing is lacking. In contrast, the effects of visual traits on pollination have been well studied (1), and floral pigments clearly influence pollination (2, 3). The ability to manipulate nonpigment floral chemistry—to evaluate its importance in attracting floral visitors, nectaring times, and thus, mediate outcrossing—has been lacking. Floral scents are generally believed to function by tuning the largely visual process of attracting pollinators (1). Moreover, attracting pollinators may increase the probability that a plant will draw herbivores (4, 5), and thus, fragrance bouquets may also be defensive (6).

Flowers face a multidimensional challenge because they need to attract visitors, compel them to vector pollen with the least investment in rewards, and repel nectar thieves, robbers, and florivores (7, 8). Previous work with native floral visitors of the white-flowered wild tobacco plant *Nicotiana glauca* demonstrated that nicotine (N) and benzyl acetone (BA) are the most abundant repellent and attractant, respectively, of 16 floral secondary metabolites (9). Experiments with artificial flowers demonstrated that hummingbirds and hawk moths removed less nectar but increased their visits if the nectar contained N BA, which is released from the outer lips of the corolla at night (10), was consistently attractive to all flower visitors, increasing their time spent removing nectar (9). The BA synthesis pathway in flowers is generally unknown but may involve a polyketide synthase functioning as a chalcone synthase (11). We identified two plasmids (pFLO10 and pFLO70) in a cDNA library of corolla tissues (12) carrying overlapping inserts (CF920188 and FE192200)

with 99% identity to each other and 86% identity to the 5' end of the *Nicotiana tabacum* chalcone synthase mRNA (AF311783). These sequences were used to clone fragments of *Nachal1* (EU503226), which is expressed in both leaves and flowers, and *Nachal2* (EU503227), which is expressed only in the leaves (12). *Nachal1* transcripts in corollas varied diurnally, attaining maximum levels 4 hours before the crepuscular peak of BA emission (Fig. S1D) (12). Transgenic plants with RNA interference (RNAi) constructs harboring fragments of endogenous biosynthetic genes in an inverted repeat orientation were used to block BA (*Nachal1*), N [putrescine N-methyltransferase (*Napmt1/2*)], and both BA and N (*Nachal1:Napmt1/2*). Silencing the expression of *N. attenuata*'s *Napmt1/2* genes dramatically reduces N accumulation throughout the plant (13), including its nectar (9).

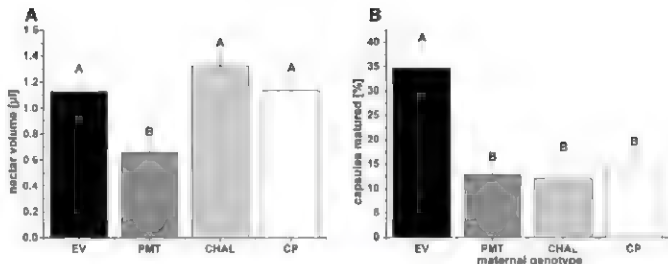
The RNAi constructs only blocked the targeted biosynthetic pathways, and the transformed plants were morphologically indistinguishable from empty vector transformed and wild type (WT) plants of the same inbred generation that was used for the transformations. Nectar volume, sugar concentration, and floral and vegetative volatiles (control and herbivore-induced) were also unchanged (Fig. S4, B and C, and table S2). T₃ generation lines, each homozygous for a single transgene insertion with diminished levels of BA, N, or both BA and N accumulations, were used for all experiments (Fig. S1B) (12). We arrayed transformed and WT individuals in an irrigated field plot (Fig. S1D) at the Lytle Ranch Preserve (12).

To protect native populations of *N. attenuata* from unwanted escape of the transgenes, all plants were monitored daily, and all flowers of each

Department of Molecular Ecology, Max-Planck Institute for Chemical Ecology, Hans-Knoll Strasse 8, D-07745 Jena, Germany

*To whom correspondence should be addressed. E-mail: baldwin@ice.mpg.de

Fig. 1. Nectar removal by floral visitors and capsule production resulting from outcrossing mediated by pollinators in EV *N. attenuata* plants and plants transformed to block BA, N, or both in the plant's native habitat. (A) Mean (\pm SE) standing nectar volume between 6:00 and 7:30 a.m. in flowers that had opened for the first time the previous night (see fig. S4D for the individual day mean (\pm SE) values). (B) Mean (\pm SE) percentage of capsules matured from 601 antherectomized flowers from each genotype (see fig. S8A for values from each day). Different letters (A and B) designate significantly different means as determined by a Fisher's protected least significant differences (PLSD) test ($P < 0.05$) of an ANOVA.

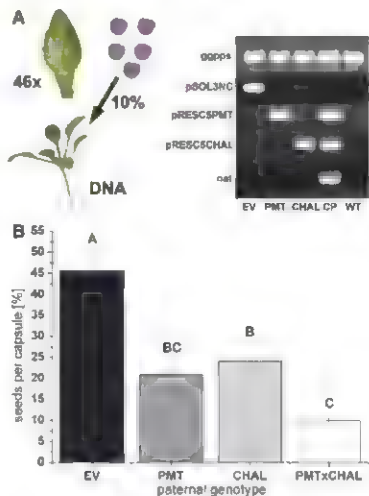


transformed plant not explicitly part of an experiment were removed before they released any pollen. Experimental flowers were labeled and emasculated (fig. S6) (12) or used as pollen donors. Each mature capsule growing in the field plot was collected before any seeds were released, and all material was destroyed upon completion of the experiment.

To determine whether the genotypes differed in nectar accumulation and whether native floral visitors preferred a particular genotype's nectar, nectar volume was measured between 5 and 7 a.m., when most nectar accumulates (fig. S4, A and B) (12). Nectar was measured from flowers of field-grown plants exposed to floral visitors, field-grown plants enclosed in mesh bags that excluded floral visitors but allowed for evapotranspiration, and greenhouse-grown plants not exposed to floral visitors (fig. S4C). No differences in nectar volume were found among the genotypes in greenhouse- and field-grown plants not exposed to floral visitors [analysis of variance (ANOVA) $F_{3,58} = 1.44$, $P = 0.242$; $F_{3,33} = 0.15$, $P = 0.930$] (fig. S4, B and C) (12). However, field-grown plants lacking N that were exposed to flower visitors had significantly less nectar volume than flowers producing N (Fig. 1A), confirming that N functions as a deterrent and that its absence increases consumption of nectar (9). In exposed plants, nectar volumes in plants lacking both N and BA did not differ from those transformed with an empty vector, suggesting that blocking BA emissions reduced pollinator visitation (Fig. 1A).

We video monitored the activity of floral visitors (fig. S11B) (12) and saw that plants lacking BA (both with or without N) received fewer visits from hawkmoths and hummingbirds (fig. S12, A and B) than those with BA-producing flowers. Hummingbirds and hawkmoths spent the least time nectaring (estimated from beak- and proboscis insertion times) flowers that lacked N [carrying transferred DNA (T DNA)] of PRESCSPMT (PMT) or PRESCCHAL and RESCSPMT (CP) as compared with flowers containing N [carrying

Fig. 2. Paternity of seeds sired by cross-pollination of antherectomized WT flowers. (A) From each of the 46 capsules that matured seeds (fig. S8A), 10 or 10% of all seeds were germinated (13). DNA was extracted from the 2-week-old seedlings and analyzed for paternity by polymerase chain reaction to determine seed paternity. *gyp6s*, *N. attenuata* geranylgeranyl diphosphate synthase gene (EF382626); *pSOL3NC*, empty vector control; *pRESCSPMT*, *Napmt 1/2* RNAi construct; *pRESCCHAL*, *Nachal 1* RNAi construct; *nat*, nourseothricin resistance gene *Sat-1* (X15995). (B) Mean (\pm SE) percentage of seeds per capsule sired by one of the four genotypes. Different letters (A, B, and C) designate significantly different means as determined by a Fisher's PLSD test ($P < 0.05$) of an ANOVA.



T DNA of *pSOL3NC*(EV) or *pRESCCHAL*], both with and without BA. This was particularly true of hummingbirds (figs. S12A and S11C). These results highlight the influence of BA emissions and nectar N on flower visitors, but whether these secondary metabolites increased plant fitness by increasing outcrossing rates was not clear.

Because *N. attenuata* is a fully self-compatible but opportunistic outcrossing species (14), we removed the anthers to measure outcrossing rates (12). Antherectomies were performed typically 12 hours before floral anthesis (fig. S6) (12). To determine the efficiency of the antherectomy in

preventing self-pollination and to measure the rate of cross-pollination in natural populations of *N. attenuata*, we antherectomized two flowers on each of 44 WT *N. attenuata* plants from a native population, 19 km away from our experiment, and removed all other flowers and buds. Half of these plants were then covered with a mesh wrapped wire cone (fig. S7A) that excluded all flower visitors, and the other half was covered after 36 hours. None of the covered plants matured capsules from antherectomized flowers, whereas plants exposed to flower visitors had 90% (28/31) of the antherectomized flowers mature

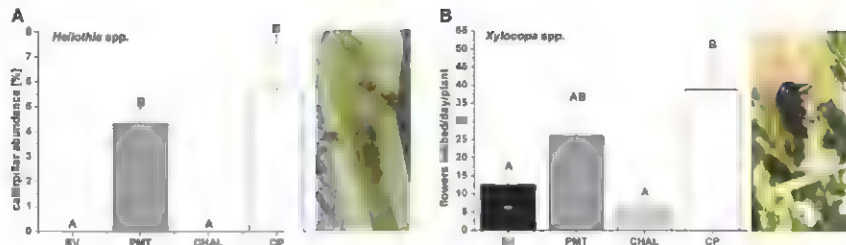


Fig. 3. (A) Mean (\pm SE) percentage of flowers damaged by tobacco budworm (*Heliothis* spp.) larvae. (B) Mean (\pm SE) flowers robbed by carpenter bees (*Xylocopa* spp.) per day and plant. Different letters (A and B) designate significantly different means as determined by a Fisher's PLSD test ($P < 0.05$) of an ANOVA.

We found no differences in pollen number, fertility, or ability to competitively sire seeds among the transgenic genotypes and WT plants (12). Therefore, differences in the maternal and paternal fitness among the genotypes in the field plantation could be attributed to the ability of flowers to attract pollinators, remove pollen, and transport pollen to receptive stigmas. To measure the effects of floral BA and N on female fitness, we emasculated three flowers on 41 to 60 plants of the transgenic genotypes on five days during the growing season; all other flowers were removed from these plants on these days. Flowering WT plants growing around the perimeter of the field plot (fig. S1D) were the only available pollen donors on these dates. In total, 601 flowers were emasculated. During one particularly windy day, no pollinators were active and no capsules were produced from the 127 emasculated flowers. A total of 87 mature capsules were produced from the 474 antherectomized flowers on the remaining 4 experimental days (fig. S8A); 45 of these were lost at an early stage of development as a result of herbivore feeding or plant death. Capsule production averaged across the 4 experimental days (12 to 14%) was significantly lower in PMT, CHAL, and CP plants as compared with EV plants (35%) (Fig. 1B and fig. S8A), demonstrating that plants' ability to attract pollinators and cross pollinate with WT flowers was lower if their flowers lacked BA, N, or both. The number of seeds produced per capsule did not significantly differ among genotypes [ANOVA $F_{3,61} = 0.170$, $P = 0.92$; CHAL, 115 ± 21 (mean \pm SE); PMT, 117 ± 43 ; CP, 96 ± 19 ; EV, 108 ± 17], showing that pollinator visits to individual flowers were the limiting factor in an individual's fitness.

To measure the effects of floral BA and N on male fitness, we antherectomized and labeled between one and eight flowers on 19 to 24 WT plants on 5 days during the growing season, totaling 502 flowers. All other WT flowers were removed. To ensure that each of the EV, PMT, CHAL, and CP genotypes had the same opportunity to function as pollen donors for the emas-

culated WT flowers, we manipulated the plants to result in the same number of open flowers for all genotypes (fig. S9B). Matured capsules were collected before opening, seeds were counted, and paternity was determined (Fig. 2A) (22). Across all 5 experimental days, EV plants sired 1.9 times more seeds in emasculated WT flowers than did CHAL plants, 2.2 times more seeds than PMT plants, and 4.7 times more seeds than CP plants (Fig. 2B and table S4). Although EV pollen was uniformly better than genotypes lacking N or BA, over the season the success of CHAL pollen tended to decrease (Student's t test, $t_{23} = 2.15$, $P = 0.043$), whereas PMT pollen success tended to increase (Student's t test, $t_{23} = -2.16$, $P = 0.042$) (fig. S9A), suggesting that the effects on male fitness wane for N and increase for BA over time.

These changes in male and female function as a result of changes in N and/or BA levels correlated with the relative frequency of visits from the main floral visitors as observed on video. Hummingbirds were more frequent floral visitors early in the growing season, and hawkmoths were more frequent later (fig. S11A). This correlation between plants' fitness through the male function and the activity of the floral visitors is consistent with earlier observations that hummingbirds respond strongly to the presence of N in nectar (9), which increases outcrossing rates. In short, the lower fitness of N- and BA-blocked flowers reflected the distinct functions of these secondary metabolites: BA is correlated with increased pollinator visits, whereas N appears to enforce mod est drinking behavior.

The daily manual inspection and video monitoring also provided quantitative data on florivory and nectar robbing. *Heliothis* spp. larvae were found feeding within the closed flowers at the stage in which flowers were emasculated (Fig. 3A) in 4.3% of PMT and 5.2% of CP flowers but in no WT flowers (of 638 emasculated flowers). Nectar-robbing carpenter bees (*Xylocopa* spp.) showed the same preference for N-deficient flowers, although attacks were higher on CP plants than PMT plants (Fig. 3B), suggesting that BA

synergizes the defensive effects of N in mediating resistance to this nectar robber. On the basis of these data, we conclude that combinations of repellents and attractants help flowers avoid predators while attracting mates. Unlike animals, plants are sessile, but through chemistry, flowers can optimize visitors' behavior.

References and Notes

1. R. A. Raguso, *Entomol. Exp. Appl.* **128**, 196 (2008).
2. M. E. Hobbah et al., *Plant Cell* **19**, 779 (2007).
3. H. D. Bradshaw, D. W. Schemske, *Nature* **426**, 176 (2003).
4. A. Kerner von Marilaun, *Die Schutzmittel der Blüten gegen unehrliche Gäste* (Wagner, Innsbruck, Austria, 1879).
5. T. Hoarman, *Proc. Natl. Acad. Sci. U.S.A.* **105**, 4541 (2008).
6. S. Y. Strauss, J. B. Whithall, in *Ecology and Evolution of Flowers*, L. D. Harder, S. C. H. Barrett, Eds. (Oxford Univ. Press, Oxford, UK, 2007), pp. 120–138.
7. H. E. M. Dobson, in *Biology of Floral Scent*, N. Dudareva, E. Pichersky, Eds. (CRC Press, Boca Raton, FL, 2006), pp. 147–198.
8. A. C. McCall, R. E. Irwin, *Ecol. Lett.* **9**, 1351 (2006).
9. D. Kessler, L. T. Baldwin, *Plant J.* **49**, 840 (2007).
10. M. Feller, T. Baldwin, *Oecologia* **107**, 102 (1996).
11. A. Abe, Y. Takahashi, M. Morita, H. Nagakura, *Eur. J. Biochem.* **268**, 1334 (2001).
12. Materials and methods are available as supporting material on Science Online.
13. A. Steppuhn, K. Giese, R. Krosch, R. Hahshtschke, T. Baldwin, *Proc. Biol. Sci.* **272**, 2217 (2005).
14. K. Sime, L. T. Baldwin, *BMC Evol. Biol.* **3**, 6 (2003).
15. Supported by the Max Planck-Gesellschaft. We thank M. Baldwin, A. Kessler, and E. Wheeler for critically reading the manuscript, Brigham Young University for the use of the Lytle Ranch Preserve field station, and U.S. Department of Agriculture–Animal and Plant Health Inspection Service for constructive regulatory oversight of the genetically modified organism releases. Gene sequences have been deposited in GenBank with accession numbers U0503276 and U0503277.

Supporting Online Material

www.sciencemag.org/cgi/content/full/321/5893/1200/DC1

Materials and Methods

Figs. S1 to S12

Tables S1 to S5

References

6 May 2008; accepted 1 July 2008
10.1126/science.1160072

Redox-Active Antibiotics Control Gene Expression and Community Behavior in Divergent Bacteria

Lars E. P. Dietrich,^{3,2} Tracy K. Teal,⁴ Alexa Price-Whelan,^{3,4} Dianne K. Newman^{1,2,3*}

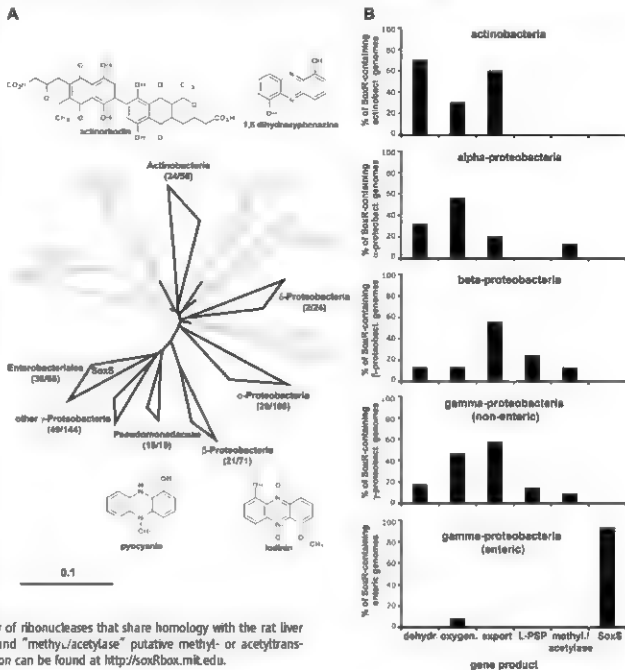
It is thought that bacteria excrete redox-active pigments as antibiotics to inhibit competitors. In *Pseudomonas aeruginosa*, the endogenous antibiotic pyocyanin activates SoxR, a transcription factor conserved in Proteo- and Actinobacteria. In *Escherichia coli*, SoxR regulates the superoxide stress response. Bioinformatic analysis coupled with gene expression studies in *P. aeruginosa* and *Streptomyces coelicolor* revealed that the majority of SoxR regulons in bacteria lack the genes required for stress responses, despite the fact that many of these organisms still produce redox-active small molecules, which indicates that redox-active pigments play a role independent of oxidative stress. These compounds had profound effects on the structural organization of colony biofilms in both *P. aeruginosa* and *S. coelicolor*, which shows that "secondary metabolites" play important conserved roles in gene expression and development.

The opportunistic pathogen *Pseudomonas aeruginosa* releases phenazines, redox-active antibiotics (1, 2). Historically, attention has focused on their toxicity in bacteria

and eukaryotes, which arises from the production of superoxide (3, 4). More recently, however, it has been recognized that these compounds have diverse physiological functions, particularly in

der oxygen-limited conditions (2, 5–7). We found that the blue phenazine pyocyanin is an intercellular signal that triggers a specific response in *P. aeruginosa*, with only 22 genes up-regulated, including the complete SoxR regulon (8). The transcription factor SoxR is well characterized in the enteric bacteria *Escherichia coli* and *Salmonella enterica* serovar Typhimurium as a stress response regulator. In these bacteria, SoxR activates the transcription factor SoxS, which controls genes involved in the removal of superoxide and nitric oxide and protection from organic solvents and antibiotics. That SoxR regulated genes were triggered by pyocyanin was, therefore, un-

Fig. 1. (A) Distribution of SoxR and SoxS among phyla of the domain Bacteria. A BLAST search for *E. coli* SoxR and SoxS was performed, and SoxS was found only in enterics. SoxR homologs were identified in 176 α -, β -, δ -, and γ -Proteobacteria and Actinobacteria. All of these homologs contain the SoxR-specific cysteine motif C(G)GCG(L)M(S/L)DXXX required for binding of the [2Fe-2S] cluster (32). The number of hits within respective phyla are indicated, followed by the total number of genomes surveyed. Members of these phyla (in black) are noted for their ability to produce and excrete redox-active small molecules, such as phenazines (28) and actinorhodin (20). Representative structures are shown. The tree was constructed using the ARB neighbor joining method from 16S ribosomal RNAs of 604 bacterial species. The bar represents 0.1 base substitutions per nucleotide. (B) Gene categories regulated by SoxR. Only in enterics are soxR boxes located upstream of soxS, which confirms the uniqueness of this network. In all other soxR-containing Proteo- and Actinobacteria, soxR boxes are mainly found upstream of five gene types as indicated; 100% correspond to 16 α -Proteobacteria, 18 β -Proteobacteria, 27 enteric, 38 non-enteric γ -Proteobacteria, or 22 Actinobacteria. "Dehydr" stands for putative dehydrogenases; "oxygen" for putative mono- or dioxygenases; "L-PSP" putative L-PSP endonucleases, a family of ribonucleases that share homology with the rat liver perchloric acid-soluble protein, L-PSP; and "methyl/acetylase" putative methyl- or acetyltransferases. Additional annotation information can be found at <http://soxRbox.mil.edu>.



ually not surprising, as this would be consistent with the conventional view of phenazines as toxic compounds (9–11).

However, recent studies of the SoxR regulons in pseudomonads indicate an alternative role to the *E. coli* SoxR–SoxS paradigm. First, superoxide is not the sole activator of SoxR, as *P. aeruginosa* pyocyanin also induces the expression of its regulon under anoxic conditions (8). Second, SoxRs from *Pseudomonas putida* (12) and *P. aeruginosa* (8, 13, 14) do not control any of the genes typically involved in superoxide resistance and detoxification, rather, SoxR from *P. aeruginosa* up-regulates expression of two transporters and a putative monooxygenase (fig. S1A). Third, *P. aeruginosa* *soxR* mutants show no decrease in resistance to superoxide, unlike *E. coli* *soxR* mutants (14). These observations led us to hypothesize that redox active signaling molecules, such as phenazines, might control other aspects of microbial behavior.

In this study, we investigated the distribution of the *E. coli*–type oxidative stress response by performing a BLAST search for SoxR and SoxS in the bacterial domain (15). SoxR was found in sequences from 176 strains in the phyla Proteobacteria and Actinobacteria (Fig. 1A), 123 of which come from completed genomes. The occurrence of SoxS was restricted to the family Enterobacteriaceae. To identify alternative SoxR targets in non-enterics, we

searched all available complete bacterial genomes (616) for the presence of *soxR* boxes (i.e., SoxR binding sites in the promoter regions of target genes) using a position weight matrix (PWM) derived from the *soxR* box sequences of 12 diverse SoxR-containing bacteria (fig. S1B). This PWM permits statistically robust predictions of SoxR binding to a *soxR* box. Of the 123 *soxR* containing genomes, 121 contain *soxR* boxes. SoxR boxes were also found in 27 genomes (19 were Firmicutes) that do not contain a *soxR* homolog. The results of our analysis (table S1 and <http://soxRbox.mut.edu>) were consistent with gene expression studies made in the Gram-negative bacteria *E. coli*, *S. enterica* (10), *P. aeruginosa* (8, 13, 14), and *Agrobacterium tumefaciens* (16), which validates our search algorithm.

The organization found in *E. coli* (fig. S1), with one *soxR* box upstream of *soxS* and no other *soxR* boxes in the genome, occurred only in enterics (27 genomes) (Fig. 1B). Two enterics contained an additional *soxR* box upstream of putative dioxygenases. The remaining organisms contained one or more *soxR* boxes upstream of genes other than *soxS*. These SoxR target genes fell into five main categories, including transporters, oxygenases, dehydrogenases, putative

acetyl- or methyltransferases, and L-PSP endonucleases (L-PSP is defined in the legend to Fig. 1B), all of which are potentially involved in the transformation or transport of small molecules, such as antibiotics (17). The occurrence of *soxR* upstream of *soxS* in enterics thus appears to be an evolutionary exception confirmed by the unique branching of the enteric orthologs on a SoxR phylogenetic tree (fig. S2).

Given that many of the bacteria that contain *soxR* boxes are producers of redox active antibiotics (18) (Fig. 1A), it seems reasonable that SoxR may have evolved to regulate their transport and/or turnover. We chose to work with the Gram-positive actinomycete *Streptomyces coelicolor* A3(2) to test whether the SoxR regulon is up-regulated in response to endogenous small molecules, because members of this phylum are widely recognized as important sources of antibiotics (19). *S. coelicolor* A3(2) produces the blue pigment actinorhodin and the red undecylprodigiosin (fig. S3) (20). On the basis of our analysis, we predicted a SoxR regulon comprising two genes for *S. coelicolor* A3(2), encoding putative redox enzymes (Fig. 2A). Expression of these genes in the wild type (strain M145) was compared with that in a mu-

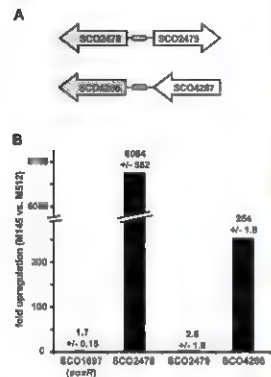


Fig. 2. The putative *S. coelicolor* A3(2) SoxR regulon is specifically up-regulated by pigments. (A) Genes predicted to be regulated by SoxR are shown in gray. (B) RNA extracted from plate-grown *S. coelicolor* A3(2) M145 and the pigment-null mutant M512 was used to generate cDNA for quantitative RT-PCR (25). Signals were standardized to SOX458 (32). The experiment was done in triplicate, and data reported represent the mean \pm SD. SoxR itself (SOX457) was also tested for changes in gene expression.

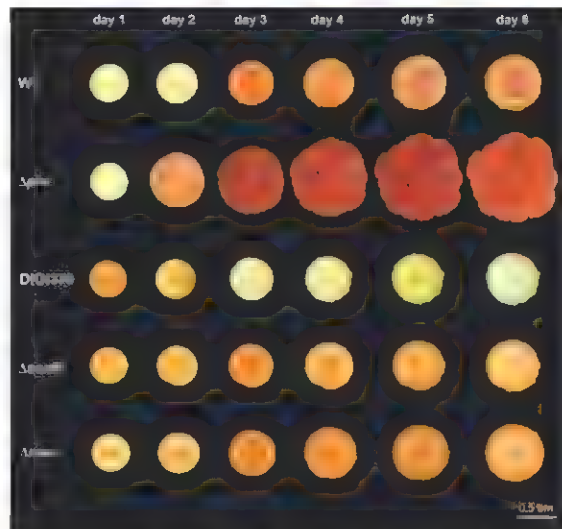


Fig. 3. Phenazine production modulates colony morphology in *P. aeruginosa* PA14. *P. aeruginosa* cultures were spotted onto agar plates containing Congo Red and Coomassie Blue, and incubated at 20°C for 6 days. The phenazine null strain (Δ phz) started to wrinkle on day 2, the wild type (wt) wrinkled on day 3, and the *soxR* and *mexGH1-opmD* deletion strains wrinkled on day 5, whereas a pyocyanin overproducer (DKN370) remained smooth and white after 6 days.

that does not produce the two pigments (strain M512) (21). Both predicted SoxR regulated genes were significantly up-regulated in the wild type relative to the pigment null mutant (~250 to 6000-fold), as determined by quantitative reverse transcription polymerase chain reaction (RT-PCR) (Fig. 2B), which confirmed that pigment production stimulated gene expression via SoxR. Hence, the primary function of SoxR in *S. coelicolor*, as in *P. aeruginosa*, is not to activate a response to superoxide but to mediate a response to endogenous pigments.

Recently, we showed that phenazines are terminal signals in *P. aeruginosa*'s quorum sensing cascade (8). The importance of quorum sensing for the coordination of many bacterial communities is well established (22). Moreover, a phenazine-dependent effect on biofilm formation has been reported in *P. aeruginosa* (23). Together with our bioinformatic SoxR results, these observations led us to hypothesize that redox active pigments might act as signals to modulate the structural organization of cellular communities.

To investigate the effect of extracellular pigments on community development, we began by focusing on *P. aeruginosa* PA14. We spotted 10- μ l aliquots of late exponential-phase cultures onto agar plates and incubated them at room temperature for 8 days. Under these conditions, wild-type cells initially formed smooth colonies (Fig. 3). After 4 days of incubation, the colonies began to wrinkle and reached a maximum area of ~2.5 cm² (Figs. 3 and 4A). However, the phenazine null mutant formed severely wrinkled colonies within 2 days of incubation (Fig. 3), which subsequently flattened and spread to ~3.5 cm² (Fig. 4A). In contrast, a mutant that overproduced pyocyanin (DKN370) remained smooth and compact (Figs. 3 and 4A). These results

demonstrated a role for phenazines in controlling bacterial colony size and structure.

Phenazines are diffusible molecules that may influence phenotype over distance. Indeed, we found that adding pyocyanin to the growth medium (Fig. 3AA) or spotting the phenazine overproducer next to the phenazine deletion mutant (Fig. 3AB) resulted in the formation of smooth compact colonies. We tested the role of SoxR in mediating the effect of phenazines on colony morphology by making a SoxR deletion mutant. However, the mutant behaved similarly to the pyocyanin overproducer, and colonies remained smooth for 4 days (Fig. 3). As for the overproducer, Δ soxR released more pyocyanin into the agar than the wild type (Fig. 4B). There thus appears to be a direct correlation between pyocyanin release and colony smoothness.

To further analyze the Δ soxR phenotype, we tested *P. aeruginosa* mutants disrupted in the SoxR target genes PA14_35160 (encoding a putative monooxygenase), *mexGH-opmD* [encoding a resistance/nodulation-cell division (RND) efflux pump], and PA14_16310 [encoding a major facilitator superfamily (MFS) transporter]. Deletions of PA14_35160 and PA14_16310 did not affect colony morphology, however, the loss of *mexGH-opmD* produced a phenotype that looked like the Δ soxR mutant, i.e., wrinkling was slow (Fig. 3), and was accompanied by a slightly elevated pyocyanin release (Fig. 4B). By contrast, the release of the yellow phenazine 1-carboxylate (PCA) and an unidentified red phenazine (possibly 5-methyl PCA), decreased by 10 and 60%, respectively, in the *mexGH-opmD* mutant relative to the wild type, which indicates that *mexGH-opmD* is a general phenazine transporter. Antibiotic biosynthetic genes are often found adjacent to their cognate trans-

porter (24), so it is interesting to note that the *mexGH-opmD* operon is clustered with the phenazine biosynthetic genes *phzM*, *phzA1-G1*, and *phzS* (Fig. S5A).

PhzA1-G1 synthesizes the yellow phenazine PCA, and *PhzM* methylates PCA to yield the red phenazine 5-methyl PCA, which is then hydroxylated by *PhzS* to form pyocyanin. Transposon insertion mutants in *mexD* and *opmD* of *P. aeruginosa* PAO1 are known to accumulate an unidentified toxic compound that causes an elongated lag phase in planktonic cultures (25). We found a similar phenotype in *P. aeruginosa* PA14 (Fig. S5B), which is probably caused by an intracellular accumulation of phenazines. Our experiments showed that SoxR target genes do not directly influence colony development; instead, SoxR regulates the efflux of phenazines via the RND transporter *MexGH-OpmD*. Although yellow PCA and red phenazine are retained in the *mexGH-opmD* mutant, the release of pyocyanin indicates an alternative efflux mechanism favoring pyocyanin. Compensatory changes in expression of RND efflux pumps are well known to occur in *P. aeruginosa* (26).

To determine whether the phenotypic effects of pigment production observed for *P. aeruginosa* were unique to this organism or more generalizable, we performed analogous experiments with *S. coelicolor* A3(2). As for *P. aeruginosa*, a pigment-defective mutant of *S. coelicolor* adopted a more wrinkled morphology than the respective wild type (Fig. 4C). The mechanisms whereby pigments control colony morphology are not understood, but are likely to be complex. For *P. aeruginosa* PA14, we know that pyocyanin affects the expression of at least 35 genes other than those in the SoxR regulon (8) and has profound effects on the cell's physiology, in-

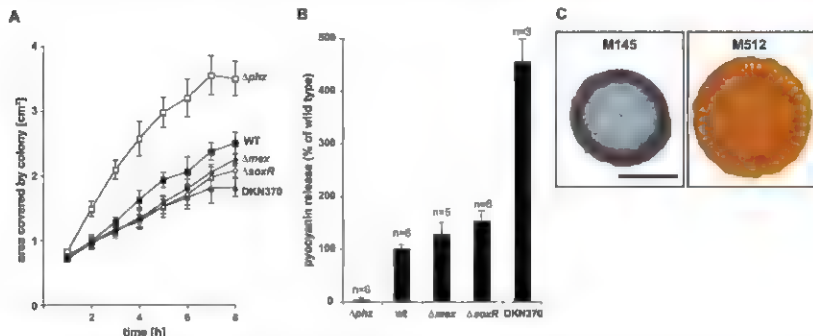


Fig. 4. (A) Surface coverage of 35 colonies per strain monitored over 8 days (\pm SD). **(B)** Concentration of pyocyanin release from three colonies into 10 ml agar supplemented with Congo Red and Coomassie Blue. After 5 days of growth at room temperature, the cells were scraped off, pyocyanin was extracted from the agar using chloroform, and extracts were analyzed by high-

performance liquid chromatography. The data reported represent the mean \pm SD. **(C)** Spore suspensions of *S. coelicolor* A3(2) M145 and the pigment mutant M512 were spotted and incubated for 5 days on R5⁺ medium at room temperature. The pigment mutant exhibits a wrinkled morphology, whereas the wild type takes on a smoother phenotype. Scale bar is 0.5 cm.

cluding the redox state of the intracellular nicotinamide adenine dinucleotide [NAD(H)] pool (27). Any number of these effects may contribute, both directly and indirectly, to the ultimate architectures observed. One component that is likely involved is extracellular polysaccharide (EPS). Congo Red, a constituent of the agar used in the experiments shown in Fig. 3, is known to bind the glucose rich exopolysaccharide PEL (28). Because the phenazine-null mutant is bright red, whereas the pyocyanin overproducer is pale, we infer there is an inverse relationship between phenazine and PEL production (Fig. 3). How phenazines affect the *pel* genes and how such changes in EPS composition contribute to colony morphogenesis remain to be determined.

Pigments excreted by bacteria have long been assumed to be "secondary" metabolites or even waste products, owing to the sporadic strain- and condition-dependent nature of their production (29). Many of these redox active compounds are known to have antibiotic activities toward competing cells (1, 20), but until recently, their potential to directly participate in the physiology of the producing organism has been largely neglected (7). We now know that small molecules initially characterized as antibiotics allow intercellular communication within bacterial populations (30), and this now implies a conserved function for redox-active pigment antibiotics of the Gram-negative bacterium *P. aeruginosa* and the Gram-positive bacterium *S. coelicolor* A3(2). These pigments influence transcriptional regulation and modulate the phys-

ical characteristics of communities of their producers at later stages in their development. Rather than being "secondary," diverse redox-active antibiotics may share similar functions of primary importance throughout the bacterial domain.

References and Notes

1. D. V. Khavard, W. Blankenfeldt, L. S. Thompson *Annu. Rev. Phytopathol.* **44**, 417 (2006).
2. A. Price Whelan, L. E. Dring, D. K. Newman *Mol. Chem. Biol.* **2**, 71 (2006).
3. S. Mahajan-Miklos, M. W. Tan, L. G. Rahner *E. M. Ausubel*, *Cell* **96**, 47 (1999).
4. M. Marzola, R. J. Cook, L. S. Thompson, D. M. Weiler *L. S. Pierson 3rd, Appl. Environ. Microbiol.* **58**, 2616 (1992).
5. M. E. Hernandez, A. Kappes, D. K. Newman *Appl. Environ. Microbiol.* **70**, 921 (2004).
6. Y. Wang, D. K. Newman *Environ. Sci. Technol.* **42**, 2390 (2008).
7. M. E. Hernandez, D. K. Newman *Cell. Mol. Life Sci.* **58**, 1562 (2002).
8. L. E. Dring, A. Price Whelan, A. Peterson, M. Whitley *D. K. Newman Mol. Microbiol.* **61**, 308 (2006).
9. S. I. Louchie, I. Benze, D. Tsouli, I. Fridman, J. Biol. Chem. **274**, 9479 (1999).
10. P. J. Ponsoppasella, B. Dimple, *J. Bacteriol.* **182**, 73 (2000).
11. P. J. Ponsoppasella, B. Dimple, *J. Bacteriol.* **192**, 4797 (1990).
12. W. Park, S. Penna, J. Yang, Y. Lee, B. Dimple *Biochem. Biophys. Res. Commun.* **341**, 51 (2006).
13. K. Kobayashi, S. Tagawa, *J. Biochem.* **136**, 607 (2004).
14. M. Palma, et al., *Infect. Immun.* **73**, 2598 (2005).
15. Materials and methods are available as supporting material on Science Online.
16. W. Fieringhsmann, M. Chatterjee, P. Vattanasorn, S. Kundlich, *J. Bacteriol.* **188**, 8669 (2006).
17. E. Lundkvist *Annu. Rev. Microbiol.* **43**, 207 (1989).
18. J. M. Turner, A. J. Messenger *Adv. Microbiol. Physiol.* **27**, 211 (1986).

29. A. K. Heywood, *Streptomyces in Nature and Medicine: The Antibiotic Makers* (Oxford Univ. Press, Oxford, 2007).
 30. K. F. Chater, *Philos. Trans. R. Soc. Lond. B Biol. Sci.* **362**, 761 (2006).
 31. B. Floriano, M. Bibb, *Mol. Microbiol.* **23**, 1395 (1996).
 32. D. G. Davies et al., *Science* **280**, 295 (1998).
 33. V. S. Madhala, Z. Zhang, F. A. Pierson, I. S. Pierson 3rd, *Microb. Ecol.* **78**, 289 (2006).
 34. K. Tashken et al., *Mol. Microbiol.* **36**, 951 (2007).
 35. A. Amdenk et al., *Microbiology* **152**, 1113 (2005).
 36. A. Z. Li, B. R. K. Barre, K. Poole, *J. Antimicrob. Chemother.* **46**, 101 (2000).
 37. A. Price Whelan, E. D. Diehl, D. K. Newman, *J. Bacteriol.* **189**, 6372 (2007).
 38. J. Friedman, R. Kolter, *Mol. Microbiol.* **52**, 675 (2004).
 39. R. P. Williams, *Bacteriol. Rev.* **20**, 182 (1956).
 40. G. Yim, H. H. Wang, J. Davies, *Philos. Trans. R. Soc. Lond. B Biol. Sci.* **362**, 1195 (2007).
- Single letter abbreviations for the amino acid residues are as follows: A: Ala; C: Cys; D: Asp; E: Glu; F: Phe; G: Gly; H: His; I: Ile; K: Lys; L: Leu; M: Met; N: Asn; P: Pro; Q: Gln; R: Arg; S: Ser; T: Thr; V: Val; W: Trp; Y: Tyr; and X, any amino acid.
35. Mueha et al., *J. Mol. Microbiol. Biotechnol.* **33**, 159 (2006).
36. I. Hsieh (Ph.D. thesis Harvard University), M. Bibb and A. Wankhoff (Sloan Institute, Harvard Univ. JGI) for providing the sequencing AB21 strains M45 and M52 and M. S. Calafate, C. T. Bui, and B. Wolf for helpful discussions. This work was supported by an EMBO young team fellowship (C.F.D.) and grants from the Packard Foundation and Howard Hughes Medical Institute (D.K.N.).

Supporting Online Material

www.sciencemag.org/cgi/content/full/321/5893/1203/DC1

Materials and Methods

Figures S1

Table 51

References

19 May 2009; accepted 24 July 2009

10.1126/science.1160619

Solution Structure of the Integral Human Membrane Protein VDAC-1 in Detergent Micelles

Sebastian Hiller,¹ Robert G. Garces,^{1*} Thomas J. Malia,^{1,†} Vladislav Y. Orekhov,^{1,3}
Marco Colombini,² Gerhard Wagner^{1‡}

The voltage-dependent anion channel (VDAC) mediates trafficking of small molecules and ions across the eukaryotic outer mitochondrial membrane. VDAC also interacts with antiapoptotic proteins from the Bcl-2 family, and this interaction inhibits release of apoptogenic proteins from the mitochondrion. We present the nuclear magnetic resonance (NMR) solution structure of recombinant human VDAC-1 reconstituted in detergent micelles. It forms a 19-stranded β barrel with the first and last strand parallel. The hydrophobic outside perimeter of the barrel is covered by detergent molecules in a beltlike fashion. In the presence of cholesterol, recombinant VDAC-1 can form voltage-gated channels in phospholipid bilayers similar to those of the native protein. NMR measurements revealed the binding sites of VDAC-1 for the Bcl-2 protein Bcl-x_L, for reduced β -nicotinamide adenine dinucleotide, and for cholesterol. Bcl-x_L interacts with the VDAC barrel laterally at strands 17 and 18.

The integral membrane protein VDAC forms the primary path for diffusion of metabolites between the mitochondrial intermembrane space and the cytosol (1, 2). VDAC is conserved across eukaryotes, with about 30% sequence identity between yeast and human. The three isoforms, VDAC-1, VDAC-2, and VDAC-3,

found in humans are 68% to 75% pairwise identical. All three isoforms allow the exchange of metabolites through the membrane but have distinct physiological roles and expression profiles (3, 4).

Numerous reports have suggested that VDAC 1 is involved in mitochondrial apoptosis (5-7)

Apoptotic signals lead to the formation of a mitochondrial exit channel that allows the release of apoptogenic proteins, which in turn cause cell death by activating executioner caspase or through other mechanisms (8-10). Functional studies indicate that VDAC 1 closure leads to the opening of the mitochondrial exit channel (11). The anti-apoptotic protein Bcl-x_L opens the VDAC 1 channel for trafficking of metabolites and thus inhibits the release of apoptogenic proteins (12). Direct interaction between VDAC 1 and Bcl-x_L has been demonstrated (11, 13).

Insights into VDAC organization have come from biochemical and biophysical studies (14, 15) and low-resolution electron microscopy (EM) data showing that VDAC-1 is a cylindrical channel with a diameter of 20 to 30 Å (16, 17). Electrophysiological experiments revealed that, at low membrane potentials of 10 mV, VDAC is in the open state, but it switches to the closed state at

²Department of Biological Chemistry and Molecular Pharmacology, Harvard Medical School, Boston, MA 02115, USA

²Department of Biology, University of Maryland, College Park, MD 20742 USA. ³Swedish NMR Centre, University of Goth.

enborg, Box 465, 40530 Gøteborg, Sweden

*These authors contributed equally to this work

†Present address: Centronics Incorporated, Radnor, PA 19087.

Presented by: Cengage, Incorporated, Raleigh, NC 27607, USA

†To whom correspondence should be addressed. E-mail

gerhard.wagner@hms.harvard.edu

increased membrane potentials of about 30 mV (18). Thus, Donnan or diffusion potentials across the outer mitochondrial membrane may regulate small molecule passage (19). In a lipid bilayer, recombinant VDAC can form stable open states and feature voltage-dependent transitions (20).

We present the three-dimensional (3D) solution structure of human VDAC-1 reconstituted in detergent micelles as determined by high-resolution nuclear magnetic resonance (NMR). We have assayed the binding of VDAC-1 with two natural ligands, reduced β -nicotinamide adenine dinucleotide (β -NADH) and cholesterol, and with the protein BeL_{24} by NMR and identified the location of these interaction sites on the structure of VDAC-1.

For the structure determination of VDAC-1 with NMR spectroscopy, we refolded bacterially expressed human VDAC-1 into lauryldimethylamine oxide (LDAO) detergent micelles (21). The channel exhibits a well-dispersed 2D [^1H , ^1H] TROSY (transverse relaxation optimized spectroscopy) spectrum indicating the presence of extensive β sheet secondary structure (fig. S1). High field triple

resonance TROSY-type experiments and selective labeling enabled sequence-specific resonance assignment of 80% of the protein backbone, including the C^{α} resonances (Fig. 1 and figs. S2 and S3). Nineteen β strands are formed within residues 25 to 283, and a short α helix is located at the N terminus containing residues 6 to 10, as indicated by C^{α} and C^{β} secondary chemical shifts (fig. S4). To complement the backbone assignments, we prepared specifically isotope-labeled samples to assign methyl groups of Ile, Leu, and Val residues (22) (fig. S5). These side-chain assignments were essential for defining the overall structure of the protein and the location of the N-terminal helix with respect to the channel.

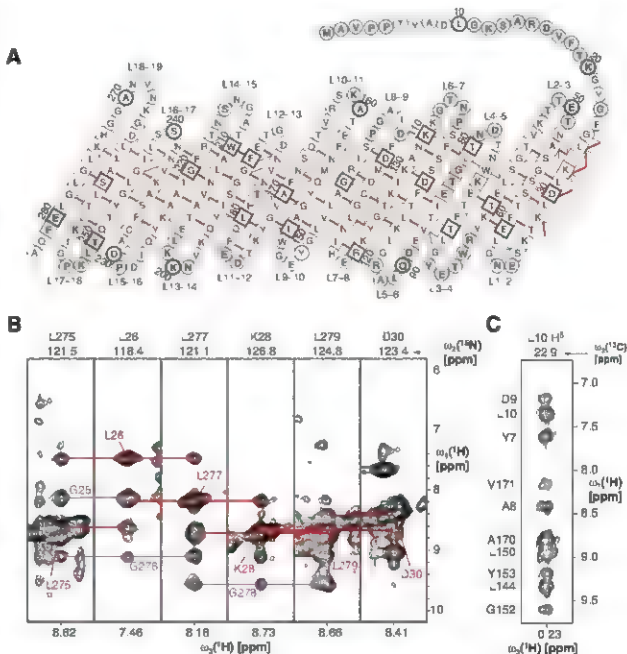
For the acquisition of long-range structural information, we used nuclear Overhauser effect spectroscopy (NOESY) to establish spatial correlations between nuclei spins (23). To obtain adequate signal, we needed to record these NOESY experiments on a fully deuterated background, including the use of perdeuterated LDAO molecules. From the cross peaks observed in 3D and

4D NOESY experiments, we identified a network of more than 600 NOE contacts that confirmed the 19-stranded β sheet topology for VDAC-1 in LDAO micelles and established the relative orientation of the strands (Fig. 1, figs. S6 and S7, and table S1). Strands 1 to 19 form an antiparallel β sheet, which is closed to a β barrel by parallel pairing of strands 19 and 1.

Thirty two discrete β -barrel membrane protein structures have so far been solved, all from prokaryotic organisms and all consisting of even numbers of β strands with antiparallel orientation (24) (fig. S8). The eukaryotic VDAC-1 thus represents a new class of a β -barrel membrane protein fold. Whereas N- and C-termini ends are aligned next to each other in even-stranded barrels, they protrude from opposite sides of the VDAC-1 barrel. However, the N terminus of VDAC reaches through the channel to return to the same side of the barrel as the C terminus. In previous predictions of the VDAC topology, the number of β strands ranged from 12 to 19, with one corresponding to the topology determined here (25).

Fig. 1. Architecture of VDAC-1. (A)

The amino acid sequence of VDAC-1 in one-letter code (36) is arranged according to the secondary and tertiary structure. Amino acids in squares denote β sheet secondary structure as identified by secondary chemical shifts; all other amino acids are in circles. Red and blue lines denote experimentally observed NOE contacts between two amide protons and NOE contacts involving side chain atoms, respectively. Bold lines indicate strong NOEs typically observed between hydrogen-bonded residues in β sheets. For clarity of the presentation, not all observed NOEs are shown. The 19th strand is duplicated at the right, next to strand 1, to allow for indicating the barrel-closure NOEs. The side chains of white and orange residues point toward the inside and the outside of the barrel, respectively. Dashed lines show probable contacts between protons with degenerate ^1H chemical shifts. Gray residues could not be assigned so far. Every 10th amino acid is marked with a heavy outline, and corresponding residue numbers are indicated. (B) Strips from a 3D [^1H , ^1H] NOESY- ^1H -TROSY defining the barrel closure between parallel strands 1 and 19. Red lines show the interstrand contacts for the depicted residues, whereas the violet lines indicate the NOE contacts for the respective opposite residues. ppm, parts per million. (C) Strip from a 3D [^1H , ^1H] NOESY- ^{13}C -HMQC heteronuclear multiple-quantum coherence) taken at the position of a methyl group of Leu¹⁰. The assignments of the individual NOE signals are indicated on the left and exemplify the NOEs defining the location of the N-terminal helix in the barrel. The frequency axes ω_1 , ω_2 , and ω_3 are indicated.



On the basis of the experimental constraints, we calculated the 3D structure for VDAC 1 in LDAO micelles (Fig. 2 and table S1). The 19 β strands form the wall of an open barrel with the strands being tilted by about 45° with respect to the barrel main axis. Alternating between the two ends of the barrel, adjacent strands are connected by loops with lengths of 2 to 10 residues. The height of the barrel including the loops is about 30 Å, and a circular conformer of VDAC-1 has an open diameter of about 25 Å, corresponding nicely to EM data (16, 17).

Consistent with the function of VDAC 1 as a wide diffusion pore, no tertiary contacts were observed between residues across the barrel diameter. This is reflected within the calculated bundle of 20 structural conformers, among which the β barrel adopts differently circular and oval shapes (fig. S9). It is unclear whether this variation of the barrel shape represents actual molecular motions. The relative orientations of the β strands with respect to each other are well defined by the observed NOEs and thus identical in all members of the conformational ensemble.

The N-terminal tail of VDAC 1, consisting of residues 1 to 23, is not part of the barrel wall but is located inside the channel. NOE contacts connect residues 7, 8, 9, and 10 with several residues around a small hydrophobic patch formed by residues Val¹⁴³ (V143) and Leu¹⁵⁰ (L150) on the inside of the barrel wall (Figs. 1 and 2). The observation that the N-terminal 23 residues are structurally not involved in the main barrel architecture is consistent with experiments showing that a deletion mutant with the N-terminal part missing properly targets to the mitochondrial outer membrane (26). Because the N-terminal region is involved in voltage gating (27), this segment might adopt different conformations depending on the external conditions.

The overall theoretical charge of VDAC 1 at neutral pH is +3, because 29 negative charges from Asp and Glu residues oppose 32 positive charges from Arg and Lys residues. These charges are located predominantly in the loops and in the anterior, water-accessible wall of the channel, where they cluster to form one negative and two positive patches (Fig. 2). The VDAC channel is known to be open to both anions and cations, with a 2:1 preference for anions (28, 29); thus, these two features of the channel could be correlated.

The surface of VDAC 1 that is in contact with the detergent micelle was determined with the help of the detergent 16-doxyl stearic acid (16-DSA), which has a paramagnetic spin label at the end of its hydrophobic tail, quenching all NMR resonances of residues in close contact with the micelle interior (30). The data show that the detergent micelle covers the entire periphery of the VDAC 1 barrel like a belt, corresponding to the position of hydrophobic residues on the outside of the barrel (Fig. 3 and fig. S10). On the inner wall, only two hydrophobic residues are located, the above-mentioned L150 and V143 (Fig. 3C). Thus, the protein-micelle complex in aqueous

solution has a topology that would be consistent with the assumption that the protein adopts a similar fold in a lipid bilayer as in the LDAO micelle. The data obtained in the micellar state cannot address which opening of the channel faces into the mitochondria and which faces into the cytosol. Previous studies attempting to determine this orientation have reached different conclusions (15, 31). Experiments on *Neurospora crassa* VDAC suggested a different barrel topology and proposed a membrane-inserted N-terminal helix (32), which is inconsistent with the structure presented here. The VDAC 1 solution structure will stimulate revisiting the large body of previous biochemical data and the design of new experiments to resolve this issue.

The possibility of a multimeric state of VDAC is a matter of ongoing debate. There is evidence to support the formation of dimers, trimers, and tetramers, possibly in dynamic equilibrium with monomers (13). Because the entire perimeter of VDAC-1 is in contact with the micelle-immersed spin labels (Fig. 3A), our data exclude formation of stable oligomers in the LDAO micelle; however, a dynamic interchannel interaction cannot be excluded. A possible interaction site is located on strands 4 and 5, where the resonances of several residues are unresolved presumably because of exchange broadening (Fig. 1). This potential contact may be due to the high protein/detergent

ratio used here and may not exist in mitochondrial membranes.

In its native environment in the outer mitochondrial membrane, VDAC has several post-translational modifications such as phosphorylation and acetylation (33). In an attempt to determine whether these affect function, we compared the gating parameters of our unmodified recombinant protein with those of native VDAC carrying post-translational modifications. To achieve functional properties similar to wild-type, recombinant VDAC-1 had to be reconstituted into planar membranes in the presence of cholesterol and the detergent triton X100, which were both also present in the reference measurements with native VDAC (34, 35). Under these conditions, the refolded VDAC 1 exhibited functional behavior similar to that of native VDAC from eukaryotic sources as measured by the single-channel conductance, the effective valence of the voltage sensor, the energy difference between open and closed states ($\Delta E_{\text{open/closed}}$), and ion selectivity (fig. S11 and Table 1). Although the present data do not directly address the structure of VDAC-1 in lipid bilayers, it is clear that our recombinantly produced VDAC 1 polypeptide can be induced to adopt a structure with functional properties very similar to those of native wild-type VDAC and that the gating properties of VDAC are thus not substantially affected by the posttranslational mod-

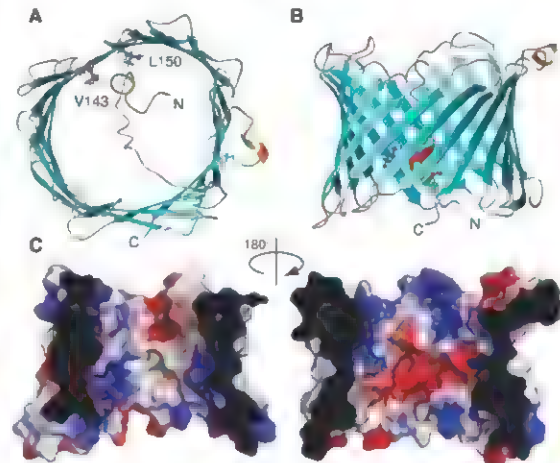


Fig. 2. NMR solution structure of VDAC-1 in LDAO micelles. (A and B) Top and side views, respectively, of the conformer closest to the mean of the conformational ensemble in ribbon representation. β sheets are shown blue, and α helical secondary structures in red and yellow. N- and C-terminal and residues L150 and V143 are indicated. (C) Van der Waals surface of VDAC-1. The surface is colored according to the surface potential, calculated by using vacuum electrostatics in the program PyMOL (38). Blue indicates positive charge, and red, negative charge.

ifications in native VDAC or by the C-terminal His tag present in our preparations.

Because cholesterol was necessary to obtain wild type-like function of recombinant VDAC 1 and because mammalian VDAC has tightly bound cholesterol (35), we used chemical shift mapping to examine the effect of cholesterol on

recombinant VDAC-1 in LDAO micelles (fig S12). The overall structure of VDAC 1 in LDAO micelles is unchanged by cholesterol concentrations up to 1.5:400 for VDAC-1:cholesterol:LDAO. The chemical shift changes induced by cholesterol revealed two distinct interaction sites located at β strands 7 and 8 and β strand 11 (Fig. 4A).

Cholesterol is dissolved in the hydrophobic phase of the micelle and thus approaches the residues at these interaction sites from the outside of the barrel.

Weak interactions with VDAC have also been reported for some of its water soluble natural ligands, such as adenosine triphosphate (ATP) (13). NMR chemical shift mapping indicates that neither ATP nor β -NAD interacts with a specific site of VDAC-1 (fig S13). However, for the interaction with β -NADH, a distinct interaction surface was observed at strands 17 and 18 involving residues G242, L243, I244, A261, L263, and D264 (36) (fig. S13 and Fig. 4B). Our results are consistent with a study of native VDAC, which showed that β -NADH but not β -NAD favors the closure of VDAC and predicted that the β -NADH binding site would comprise the partial Walker B motif SALLD (36) at residues 260 to 264 (37).

We have mapped the binding site of the native binding partner Bcl-x_L onto reconstituted VDAC 1 (Fig. 4C and fig. S14). Bcl-x_L binds to VDAC-1 at strands 17 and 18. Interestingly, the loops adjacent to the Bcl-x_L binding site contain several basic residues (Lys 266, 252, 200, and 201), so that this face of the molecule has a positive electrostatic surface. Bcl-x_L, with an estimated pI of 4.9, is negatively charged at neutral pH, and the interaction between VDAC 1 and Bcl-x_L may thus contain a substantial electrostatic component. Some residues affected by Bcl-x_L binding are not located closely to this binding site. These effects could originate from allosteric changes or from a second Bcl-x_L binding site at the lumen opening.

References and Notes

1. T. Hodge, M. Colombini, *J. Membr. Biol.* **157**, 271 (1997).
2. G. Nostrovski, M. Colombini, *Biophys. J.* **72**, 1954 (1997).
3. M. J. Sampson et al., *J. Biol. Chem.* **276**, 39206 (2001).
4. K. D. Hinsch et al., *J. Biol. Chem.* **279**, 15281 (2004).
5. M. G. Vander Velden, C. B. Thompson, *Nat. Cell Biol.* **1**, E209 (1999).
6. M. Brutsaers, J. M. Dubinsky, B. Antonsson, R. Jermerson, *J. Neurochem.* **84**, 196 (2003).
7. T. K. Nostrovski et al., *J. Biol. Chem.* **279**, 13575 (2004).
8. S. Deshaies, J. C. Martinou, *Trends Cell Biol.* **10**, 349 (2000).
9. M. H. Daniel, S. J. Korsmeyer, *Cell* **116**, 205 (2002).
10. G. Nostrovski, I. Galluzzi, C. Brenner, *Immunity Rev.* **87**, 99 (2002).
11. S. Shimizu, M. Marita, Y. Tsujimoto, *Nature* **399**, 483 (1999).
12. M. G. Vander Velden et al., *J. Biol. Chem.* **276**, 19424 (2001).
13. J. J. Mulla, G. Wagner, *Biochemistry* **46**, 514 (2007).
14. L. Thomas, E. Blachy-Dyson, M. Colombini, M. Forte, *Proc. Natl. Acad. Sci. U.S.A.* **90**, 5446 (1993).
15. S. Stanley, J. A. Dias, D. Darcangelo, C. A. Mannella, *J. Biol. Chem.* **270**, 26694 (1995).
16. C. A. Mannella, *J. Cell Biol.* **94**, 680 (1992).
17. X. W. Guo, P. R. Smith, C. A. Mannella, *J. Struct. Biol.* **114**, 41 (1995).
18. M. Colombini, *Nature* **279**, 643 (1979).
19. M. Colombini, *Mol. Cell. Biochem.* **256**, 107 (2004).
20. D. A. Koppel et al., *J. Biol. Chem.* **273**, 13794 (1998).
21. Information on materials and methods is available on Science Online.

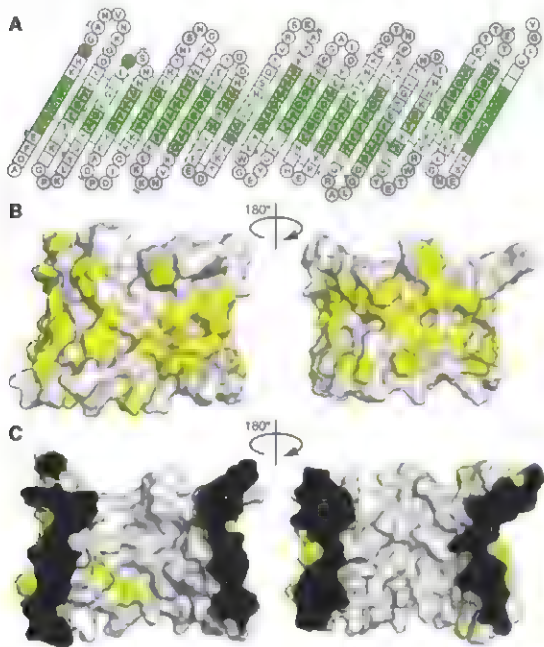


Fig. 3. Hydrophobic surface of VDAC-1. (A) Result of a titration with the spin-labeled detergent 16-D5A. Residues with a relaxation enhancement $\epsilon > 20 \text{ s}^{-1} \text{ mM}^{-1}$ are green (30). These residues are in close contact to the hydrophobic interior of the micelle. Residues with $\epsilon < 20 \text{ s}^{-1} \text{ mM}^{-1}$ are white. Gray residues are unassigned. Residues 1 to 21 have been omitted; no interaction with the spin label was observed for these. (B and C) Surface plot of outer and inner surfaces of VDAC-1, respectively, with the side chains of the hydrophobic residues Leu, Val, Ile, Met, Phe, and Trp shown in yellow and all other residues in white.

Table 1. Functional properties of VDAC voltage gating in lipid bilayers. Human VDAC-1 properties obtained from this study (see also fig. S11); rat VDAC properties are from (34).

	Recombinant human VDAC-1	VDAC isolated from rat liver mitochondria
Single conductance (nS)	3.9 ± 3.4	4.0–4.5
Voltage sensor valence	2.5–4.0	3.5–4.5
$\Delta E_{\text{apparent}} (\text{kJ mole}^{-1})$	9 ± 2	10 ± 3
Ion selectivity $P_{\text{Cl}^-}/P_{\text{K}^+}$	1.4–1.6	1.7–1.8

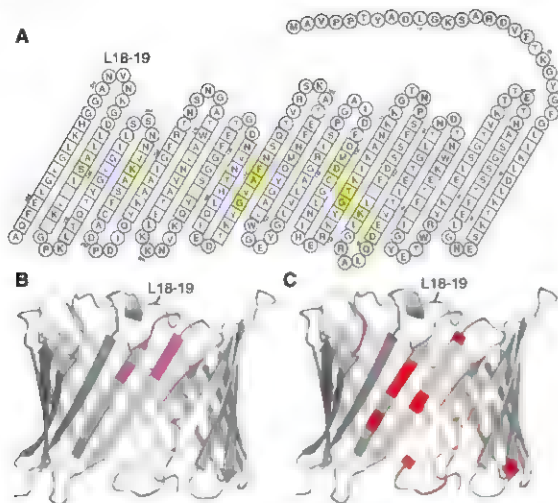


Fig. 4. Interactions of VDAC 1. In all three panels, the loop connecting strands 18 and 19 is indicated for orientation. (A) Residues with substantial chemical shift changes ($\Delta\delta(\text{HN}) > 0.05$ ppm) caused by cholesterol binding are shown in yellow (fig. S12). The amino acids of VDAC 1 are shown as in Fig. 1A. (B) Amide resonances of VDAC 1 with β -NADH, chemical shift changes (fig. S13) caused by β -NADH are labeled magenta in this ribbon representation; all other residues are gray. (C) Residues involved in Bckx binding (13) are marked red in this ribbon representation; all other residues are gray.

22. M. K. Rosen et al., *J. Mol. Biol.* **263**, 627 (1996).
23. K. Wüthrich, *NMR of Proteins and Nucleic Acids* (Wiley, New York, 1986).

24. S. H. Wüthrich, *Membrane Proteins of Known 3D Structure*, http://blanco.biomol.ucla.edu/Membrane_Proteins_atlas, version 20080801.

25. M. Forte, H. R. Guy, C. A. Mannella, *J. Bioenerg. Biomembr.* **19**, 343 (1987).
26. V. De Pinto et al., *ChemBioChem* **8**, 744 (2007).
27. J. Song, C. Midson, E. Blachly-Dyson, M. Forte, M. Colombini, *Biophys. J.* **74**, 2926 (1998).
28. S. J. Schein, M. Colombini, A. Finkelstein, *J. Membr. Biol.* **30**, 99 (1976).
29. A. G. Kossanyi, B. H. Graham, W. J. Craigen, M. Colombini, *Biophys. J.* **86**, 152 (2004).
30. C. Hilly, G. Widler, C. Fernández, K. Wüthrich, *ChemBioChem* **5**, 467 (2004).
31. V. De Pinto, G. Prossino, F. Thirumangalakudi, T. A. Link, F. Palmieri, *Biochemistry* **30**, 10191 (1991).
32. J. Song, C. Midson, E. Blachly-Dyson, M. Forte, M. Colombini, *J. Biol. Chem.* **273**, 24406 (1998).
33. J. V. Olsen et al., *Cell* **127**, 635 (2006).
34. M. Colombini, *J. Membr. Biol.* **211**, 103 (1998).
35. V. De Pinto, R. Benz, F. Palmieri, *Eur. J. Biochem.* **183**, 179 (1989).
36. Single letter abbreviations for the amino acid residues are as follows: A, Ala; C, Cys; D, Asp; E, Glu; F, Phe; G, Gly; H, His; I, Ile; K, Lys; L, Leu; M, Met; N, Asn; P, Pro; Q, Gln; R, Arg; S, Ser; T, Thr; V, Val; W, Trp; and Y, Tyr.
37. M. Zuri, M. Forte, E. Blachly-Dyson, M. Colombini, *J. Biochem.* **269**, 1614 (1994).
38. PyMOL, <http://pymol.sourceforge.net>.
39. This work was supported by NIH roadmap grant GM075079. Purchase, operation, and maintenance of instruments used were supported by NIH grants GM066360, GM47467, and EB002026. S.H. was supported by the Swiss National Science Foundation. V.V.D. was supported by the Wenner-Gren Foundation, Stockholm. Initial research on this project was supported by the Ludwig Foundation for Cancer Research. We thank V. Gelles from TDR.org for providing the β -NADH, Massachusetts, for custom synthesis of the ^{15}N -L-DAG, S. Santambrogio for help with the electrophysiological measurements, and D. Frank, A. Koylik, Z.-Y. J. Sun, K. Orsted, and S. Jerni for technical help and valuable discussions. The atomic coordinates of VDAC 1 in L-DAG micelles have been deposited at the Protein Data Bank with code 2Z0C.

Supporting Online Material

www.sciencemag.org/cgi/content/full/321/5893/1206/DC1

Materials and Methods

Figs. S1 to S14

Table S1

References

3 June 2008; accepted 24 July 2008

10.1126/science.1161302

A Structural Mechanism for MscS Gating in Lipid Bilayers

Valeria Vázquez,^{1,2} Marcos Sotomayor,³ Julio Cordero-Morales,^{3,2} Klaus Schulten,¹ Eduardo Perozo^{1,2}

The mechanosensitive channel of small conductance (MscS) is a key determinant in the prokaryotic response to osmotic challenges. We determined the structural rearrangements associated with MscS activation in membranes, using functional measurements, electron paramagnetic resonance spectroscopy, and computational analyses. MscS was trapped in its open conformation after the transbilayer pressure profile was modified through the asymmetric incorporation of lysophospholipids. The transition from the closed to the open state is accompanied by the downward tilting of the transmembrane TM1-TM2 hairpin and by the expansion, tilt, and rotation of the TM3 helices. These movements expand the permeation pathway, leading to an increase in accessibility to water around TM3. Our open MscS model is compatible with single-channel conductance measurements and supports the notion that helix tilting is associated with efficient pore widening in mechanosensitive channels.

Mechanosensation is involved in many physiological roles, including osmotic balance, touch, and hearing (1, 2). At the molecular level, mechanosensitivity relies on

the activity of ion channels that transduce a variety of mechanical stimuli to open a conductive pore. Mechanosensitive (MS) channels are grouped by function rather than sequence sim-

ilarity (3, 4). In prokaryotic systems, MS channels respond directly to bilayer deformations, with a transduction mechanism defined at the protein/lipid interface (5, 6). Although this is also true for some eukaryotic MS channels (7), many also respond to mechanical deformations through their association with the cytoskeletal network (8).

Although the molecular identification of eukaryotic MS channels remains challenging (2, 9, 10), the biophysical and structural properties of prokaryotic MS channels have proved far more tractable at the molecular level. The crystal structures for the MS channels of large (MscL) and small (MscS) conductance (11–13) have provided a molecular framework to interpret functional and biophysical data and have helped establish the basic mechanistic principles by which these two distinct channels sense the physical state of the bilayer (14–17). Nevertheless, given the critical role that lipid protein interactions play in prokaryotic function (15), two questions arise. First, what is the correspondence between these crystal structures and mech-

anistically defined functional states? Second, what are the conformational rearrangements underlying the transitions along the gating pathway?

Functional, spectroscopic, and computational studies have shown that in the pentameric MscL, activation gating proceeds as a result of a large tilt of both transmembrane (TM) segments (14, 17, 18). Concerted helical rotation and tilting generate a large aqueous pore, much as in the iris of a camera lens. However, an equivalent gating mechanism is not as obvious in the case of MscS. With three TM segments arranged as a homotrimer (12), the structural design of MscS is very different from that of MscL. Furthermore, although the MscL crystal structure appears to be a good representation of the closed conformation in its native environment (19, 20), the functional state represented by the MscS crystal structure (12, 13) has yet to be determined (21–26). Finally, in the presence of a sustained mechanical stimulus, MscS undergoes a desensitization/inactivation transition (22, 27, 28) that is not fully understood at the molecular level. Thus, although MscL and MscS respond to similar bilayer perturbations, the mechanism of transducing these forces might be different.

Electron paramagnetic resonance (EPR) measurements on a lipid reconstituted closed state of MscS have provided direct evidence for a more compact TM domain arrangement than that seen in the crystal structure (21). In the closed conformation, the TM1 and TM2 segments realign 9° toward the normal of the membrane, allowing TM3 to further narrow the permeation path. We investigated how bilayer deformations trigger MscS opening. To this end, we used site-directed spin-labeling and EPR spectroscopy to monitor the structural rearrangements in all three MscS TM segments, relative to the MscS crystal structure (12, 13) and in comparison with our spectroscopic data on the closed state.

We used cone-shaped amphiphiles that modify the bilayer tension profile (7, 15, 29) to stabilize the open conformation of MscS (Fig. 1). As expected (22, 28, 30), application of a sustained negative pressure elicits the activation and subsequent inactivation of MscS (Fig. 1A). Even in the absence of an applied external pressure, perfusion with lysophosphatidylcholine (LPC) micelles elicited spontaneous MscS openings (Fig. 1B) that displayed single-channel properties identical to those activated by transbilayer pressure differences. Under these conditions, MscS channels can be continuously recruited by

sequential incorporation of LPC, until the membrane seal breaks. We found no evidence of an LPC induced desensitization/inactivation. This fortuitous observation makes LPC a very useful tool for the investigation of MscS in its open conformation by spectroscopic approaches. At the same time, it suggests that LPC incorporation might be exerting bilayer perturbation forces that are different from those of the better-characterized transbilayer pressure difference (31, 32).

One hundred twenty seven cysteine mutants (Fig. 2A), covering the N terminal region and all TM segments (residues 2 to 128), were expressed, spin labeled, and reconstituted into liposomes (21, 33). Each labeled mutant was activated by incorporation of LPC (25 mole %), and EPR spectroscopic measurements were carried out on both the closed (21) and LPC-open conformations. Changes in probe mobility were evaluated from line shape differences (the ν in the width in the central resonant line, ΔH_{eff}) and the accessibility to either the membrane lipid [O_2 collision frequency (PO_2)] or the aqueous environment [NiEDda collision frequency (TiNiEDda)] from power saturation experiments (34). Figure 2B shows spectra from residues lining the permeation pathway [Lys¹⁰⁵–Cys¹⁰⁵ spin label (L105C-SL) to G113C-SL] (35). The complete EPR environmental data set for the TM domain (Fig. 2C) shows that the transition to the open state in MscS is accompanied by smaller structural changes than those seen in the pentameric MscL (14). This is not unexpected,

given the smaller single-channel conductance of MscS (in respect to MscL) and the fact that small intersubunit movements in the homotrimer could generate the radial pore changes needed to support ion conduction.

Upon opening, both the N terminus and the TM2 loop reduce their accessibility to the polar agent NiEDda. Given that the overall periodicity of TM1 and TM2 is preserved, the most parsimonious explanation for this change in accessibility is the partial tilting of the segments into the membrane (Fig. 2C, bottom). Although the central portion of TM1 (from positions 138C-SL to 144C-SL, Fig. 2C) did not show major changes in dynamics, TM2 and TM3 became more mobile, and TM2 in particular became more exposed to the lipids (Fig. 2C, middle). Residues in the TM3 helix that are fully buried and isolated from water and lipids in the closed conformation (21) show a periodic increase in NiEDda accessibility in the open state (Fig. 2C, bottom, and Fig. 3B). This suggests that TM3 moves away from the sevenfold symmetry axis and increases the diameter of the permeation pathway.

The location and extent of these conformational rearrangements can be visualized by mapping the differences between open- and closed-state data sets onto the recently refined MscS crystal structure (12, 13) or its closed-state model (21) (Fig. 3A). Mobility changes for the TM1 helix were largest at both of its ends (Fig. 3A and Fig. S2), as would be expected from the downward tilting of the most peripheral of TM

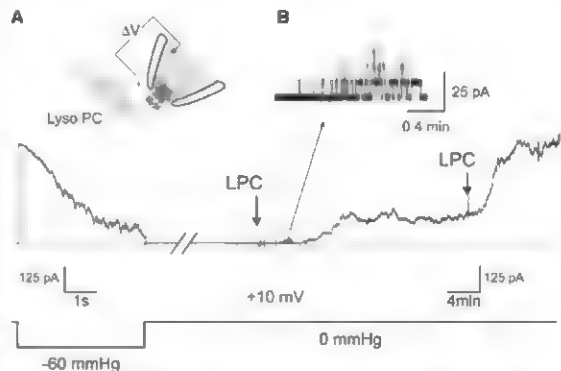


Fig. 1. LPC incorporation permanently activates MscS. (A) (Top) MscS orientation in the inside-out patch-clamp configuration and perfusion of LPC micelles. ΔV , transmembrane voltage; lyso PC, lysophosphatidylcholine. (Bottom) Representative MscS macroscopic currents (~55 channels in the patch) activated by negative pressure (at -60 mmHg and $+10$ mV) reveal the presence of a time-dependent inactivation process. (B) Sequential incorporation of LPC ($2 \mu\text{M}$) into the internal leaflet of inside-out patches from *Escherichia coli* spheroplasts and in the absence of applied tension elicits spontaneous openings (after ~ 2 min). All the channels present in the patch (as determined from tension-induced macroscopic currents) are activated by LPC. The inset shows single-channel transitions.

¹Department of Molecular Physiology and Biological Physics, University of Virginia, Charlottesville, VA 22908, USA.

²Department of Biochemistry and Molecular Biology, Institute for Biophysical Dynamics, University of Chicago, Chicago, IL 60637, USA. ³Howard Hughes Medical Institute and Department of Neurobiology, Harvard Medical School, Boston, MA 02115, USA. ⁴Department of Physics, University of Illinois at Urbana-Champaign, and Beckman Institute for Advanced Science and Technology, Urbana, IL 61801, USA.

*To whom correspondence should be addressed. E-mail: eperzo@uchicago.edu.

segments. Thus rearrangement might represent the end effect of the transducing bilayer forces in the channel perimeter and would be in agreement with the suggestion that the tension sensor in MscS is located at both ends of the membrane channel interface (6). Residues immediately preceding TM1 gained O₂ accessibility while simulta-

neously reducing NiEdda exposure (Fig. 3A). Mapping the TM1 and TM2 environmental changes onto the crystal structure revealed a better spatial correlation than when they were mapped onto the closed state model (Fig. 3A). This might suggest that the crystal structure represents an intermediate gating conformation

more reminiscent of the open than the closed state (22–26).

After LPC incorporation, most of TM3 spin-labeled residues become more mobile and display a periodic increase (α -helical) in accessibility to NiEdda (Fig. 3B and fig. S4), as protein-protein contacts presumably weaken upon

Fig. 2. Structural rearrangements underlying channel opening. (A) A single MscS monomer is represented as part of the heptamer according to the MscS closed-state model obtained from the EPR-based refinement (21). The amino acid residues subjected to cysteine-scanning mutagenesis in the present study are shown as black spheres. (B) Representative X-band EPR spectra of consecutively spin-labeled mutants along the permeation pathway (TM3). Black and red traces were obtained from channels in the closed and open conformations, respectively. All spectra were obtained from samples at the same protein-to-lipid ratio, and a dielectric resonator with the microwave power set to 2 mW was used. Channel opening was obtained in dioleoylphosphatidylcholine:palmitoylphosphatidylglycerol + 25 mole % LPC vesicles. (C) Residue-specific environmental parameter profiles obtained in the open and closed (black curve) conformations for the N-terminal and TM segments: mobility parameter ΔH_{mob} (top, green curve), O₂ accessibility parameter $\Delta \Pi_{\text{O}_2}$ (middle, red curve), and NiEdda accessibility parameter $\Delta \Pi_{\text{NiEdda}}$ (bottom, blue curve) are shown. The black horizontal bar covers the region for which EPR spectra are shown in (B). Gray areas represent the TM segment assignment derived from the MscS crystal structure (12, 13).

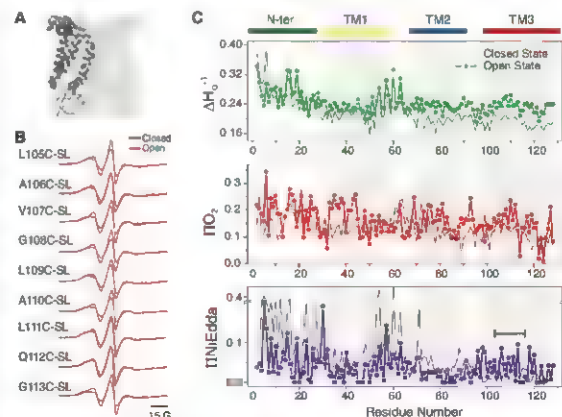
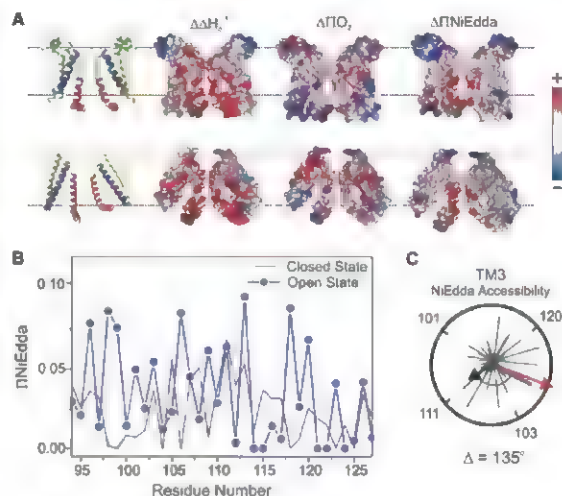


Fig. 3. Extent and direction of environmental parameter changes upon MscS opening. (A) Changes in local dynamics and solvent accessibilities mapped onto molecular surfaces of the closed-state EPR-based model (top) and the crystal structure (bottom). At left are ribbon representations of MscS (two subunits are shown for clarity), where individual TM segments are color-coded as follows: N terminus, green; TM1, yellow; TM2, blue; and TM3, red. From left to right, mobility (ΔH_{mob}), oxygen accessibility ($\Delta \Pi_{\text{O}_2}$), and NiEdda accessibility ($\Delta \Pi_{\text{NiEdda}}$) changes are shown. (B) $\Delta \Pi_{\text{NiEdda}}$ residue-specific environmental parameter profile for the TM3 helix obtained in the open (blue curve) and closed (black curve) conformations. (C) Vector analysis of TM3 environmental data in the open conformation. $\Delta \Pi_{\text{NiEdda}}$ parameters have been superimposed in a polar coordinate. Resultant moments for the closed (black arrow) and open (red arrow) conformations were calculated from the accessibilities.



opening. When mapped in nonconducting models (Fig. 3A), the NiEdda accessible face of the TM3 helix in the open state points away from the permeation pathway. This suggests that TM3 undergoes a substantial rotation about its principal axis. Moreover, the C terminal part of TM3 also appears to face into the permeation pathway. This accessibility change would have to at least some straightening of the two TM3 segment helices, because regions immediately after the G113 kink show no measurable NiEdda accessibility in the closed conformation (Fig. 3B). This experimental evidence agrees with previous molecular dynamics (MD) simulations (21, 23), as well as with an experimental study in which helical formation induced by G113A and G121A prevented inactivation and inactivation and closure, respectively (30).

The direction of the TM helices' movement can be deduced from changes in individual environmental moments between the closed and open states, as shown on a helical wheel representation (Fig. 3C and Fig. S4). Calculation of the resultant angular vector differences shows that in order to explain the changes in O₂ accessibilities (A33C SL to L39C SL, and G41C SL to H44C SL), TM1 and TM2 segments must rotate about 50° and 36°, respectively, in the counter clockwise direction (Fig. S5). Furthermore, to satisfy the changes in NiEdda accessibility data, the TM3 helices not only have to translate away from the symmetry axis but also need to rotate about 130° in the counterclockwise direction (Fig. 3C). Although the magnitude of the helix rotations reported might be biased by repacking of some of the spin labeled mutants, the overall trend and direction of helix rotations (derived from the combination of data from multiple independent mutants) should not be affected. These movements provide a mechanistically feasible way to expose the helix face highlighted by residues A98C-SL, A106C-SL, and G113C-SL to the permeation pathway in the open state (Fig. 3B), while defining intersubunit contacts in the closed state. Such rotations would break a proposed hydrophobic seal responsible for state using the seven-helix bundle in the closed state and serve as an energetic barrier to the ion flow (25, 36). Given the diameter of NiEdda (~6 Å) and the average length of the nitroxide tether (~5 Å), the diameter of the permeation path in the open conformation should be at least 11 Å to allow unimpeded diffusion of the collisional contrast agent into the open pore (22, 30).

Using a computational approach that takes advantage of EPR determined solvent accessibility restraints (37), we previously generated an EPR based model of the closed state (21) in this work, we used this as a starting conformation to model a symmetrized version of the MscS open state. First, MscS TM helices were rotated according to the changes in helical environment moments obtained from the EPR data sets. Then, pseudo-atoms representing EPR spin label probes were attached to residues 2 to 128. Finally, MD

simulations were performed in which interactions between EPR probes and pseudo-atoms representing NiEdda and O₂ were chosen to enforce the environments detected in the EPR experiments. In addition, an external cylindrical harmonic potential was applied to Ca atoms to induce channel opening [see supporting online material (SOM) for details].

The resulting MscS open model that best satisfied our experimental constraints is shown in Fig. 4A. Comparison with the closed conformation suggests three key gating mechanisms: (i) The TM1 helix tilts downward and rotates to expose TM2 to the membrane, and (ii) helices TM3a and TM3b move away from the permeation pathway, while (iii) TM3a inclines toward the plane of the bilayer, decreasing the kink angle at G113 Residue L105 (Fig. 4B), previously forming a putative hydrophobic seal, now faces away from the pore, and the narrowest part of the pore (about 11 Å in diameter) is lined by residue V99.

We have analyzed our current models of MscS closed and open conformations in light of the available experimental data. All-atom MD simulations of the open state (SOM) predict an ionic conductance that approximates the 1 nS seen experimentally (38). Furthermore, when some of the extreme mutations that cause either loss- or gain-of-function phenotypes (LOF or

GOF) are mapped on both the closed and open models, a strong spatial correlation emerges (Fig. 4B). In either conformation, LOF mutants tend to localize at the protein/membrane interface, whereas GOF mutants cluster in the middle of the TM segments. The location of the LOF mutants (6) might help explain their phenotype, because specific polar substitutions could strengthen an interaction with lipid head groups, increasing the energetic cost of the TM1 TM2 helix tilting required for channel opening. On the other hand, polar GOF substitutions in the middle of TM1 and TM2 would affect interhelix packing, perhaps favoring the interhelix rearrangement between TM1 and TM2 (Fig. 4B) that leads to opening. Strong GOF phenotypes derived from mutations in the pore (39) destabilize the hydrophobic seal required to keep the channel closed and might promote TM3 rotation.

Vertical cross sections of the permeation pathway calculated (40) for the closed and open models and the refined MscS crystal structure (13) highlight the pore's morphological changes in the different structural snapshots during gating (Fig. 4C). The MscS crystal structure shows a narrow (~6 Å) region in the intracellular side of the pore that extends 10 Å in the z axis and has been associated with the formation of a non-conductive "vapor plug" (24–26). In our closed-state model (21), this narrowing extends 25 Å

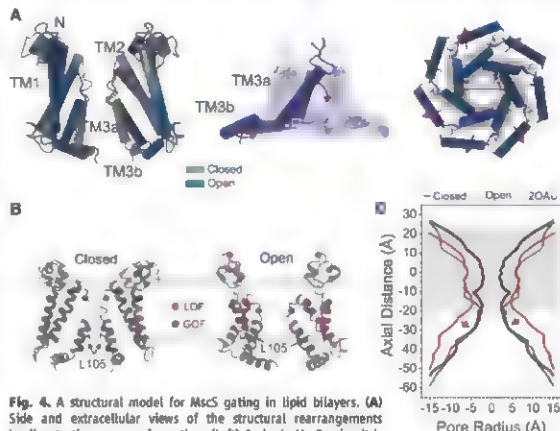


Fig. 4. A structural model for MscS gating in lipid bilayers. (A) Side and extracellular views of the structural rearrangements leading to the open conformation. (Left) A single MscS subunit is highlighted in blue and gray for the open and closed states, respectively. (Middle) TM3a and TM3b helices (residues 94 to 128 and 91 to 128 for the closed and open models, respectively). (Right) Extracellular view of the pore helical movements are illustrated by red arrows. (B) GOF (blue) and LOF (red) mutants mapped onto two subunits of MscS closed (left) and open (right) conformation models. GOF 139N and 178N (6); V40D (41); and T93R, A102P, and L109S (39). LOF V6C and A39C (21); L48D/S49P (39); and A51N, L55N, F68N, A85N, and L86N (6). Residue L105 (arrows) is shown in stick representation. (C) Cross-sectional area of the MscS pore in the closed, open, and crystal conformations. Each cross section was obtained from the calculated surface with the use of the program HOLE (40).

dispersed, multicentric pattern of plaza towns (~20 to 50 ha) and villages (<10 ha) was organized in a nested hierarchy, which gravitated toward an exemplary political ritual center. We refer to these hierarchical supralocal communities as galactic clusters, inspired by Tambiah's (12) "galactic polity" model, which draws attention to the basic similarities between small-to-large centers and the "radial mapping" of satellites in relation to an exemplary center. The galactic clusters existed within a regional peer polity composed of geographically and socially articulated but independent polities that shared basic features of techno economy, sociopolitical organization, and ideology (Fig. 1B) (13).

¹Department of Anthropology, University of Florida, Gainesville, FL 32611, USA. ²Land Use and Environmental Change Institute, University of Florida, Gainesville, FL 32611, USA. ³Museu Nacional, Universidade Federal do Rio de Janeiro, Quinta da Boa Vista, Rio de Janeiro 20940-040, Brazil. ⁴Department of Anthropology, University of Florida, Gainesville, FL 32611, USA. ⁵Department of Geography, University of Florida, Gainesville, FL 32611, USA. ⁶Coordenação de Ciências Humanas, Museu Paraense Emílio Goeldi, Belém 66077-830, Brazil. ⁷Museu Nacional, Universidade Federal do Rio de Janeiro, Quinta da Boa Vista, Rio de Janeiro 20940-040, Brazil. ⁸Associação Indígena Kulikura do Alto Xingu, Parque Indígena do Xingu (PIX), Mato Grosso, Brazil.

*To whom correspondence should be addressed. E-mail: rhecky@ufl.edu.

The Upper Xingu headwater basin is a lobe of tropical forest, transitional between the dense evergreen rainforests at the core of the Amazon and scrub forests and woody savannas of the central Brazilian highlands. It is part of the transition forest region that extends across the southern Amazon (14). Within core areas of the basin, our studies document several major episodes of prehistoric change within a cultural continuum extending from initial colonization, ~1500 to 1200 years before the present (yr B.P.) or earlier, to the present. Our survey and excavations have focused on the organization and development of the galactic clusters ~750 to 450 yr B.P. (table S1) (15, 16). After ~500 to 400 yr B.P., early European colonialism resulted in substantial depopulation and forest expansion.

We have identified 28 prehistoric residential sites, most or all of which are associated with two galactic clusters that represent small territorial polities (17). Our investigations demonstrate that clusters integrated large (>40 ha) and medium-sized (<30 ha) plaza towns and smaller (<10 ha) plaza villages as well as small (nonplaza) hamlets (Fig. 2 and figs. S1 and S2) (15). Plaza towns are distinguished by major ditches (500 to >2000 m long), defining settlement boundaries and, in some cases, occurring within settlements (fig. S1) (18). Ditches range from 1 to 3 m deep and 5 to

10 m wide. They are associated with raised interior berms (formed from ditch fill) and were augmented with a wooden palisade wall (19). Extensive residential occupations are documented across interior portions of walled settlements, including structural remains (house and trash midden areas) and ceramic cooking utensils, covering >20 ha in first-order settlements (figs. S3 and S4). Smaller nonwalled plaza villages are similar in size and form to larger contemporary villages (20).

Each cluster had an exemplary plaza center, although all permanent settlements had a central plaza (120 to 150 m in diameter), which, like today, served as the political ritual center and probably the cemetery of the local group. This underscores the importance of public ritual as a major integrating feature of the prehistoric polities (15). In addition to their larger size and structural elaboration, including gates, roads, and secondary plazas (possible ritual staging areas), walled towns are distinguished by their position in relation to the cluster center. The largest residential centers are located roughly equidistant (3 to 5 km) from the exemplary center to the northwest and southeast (21) and medium-sized centers to the northeast and southwest, roughly 8 to 10 km from the center. The area enclosed by the primary satellites represents the core area of

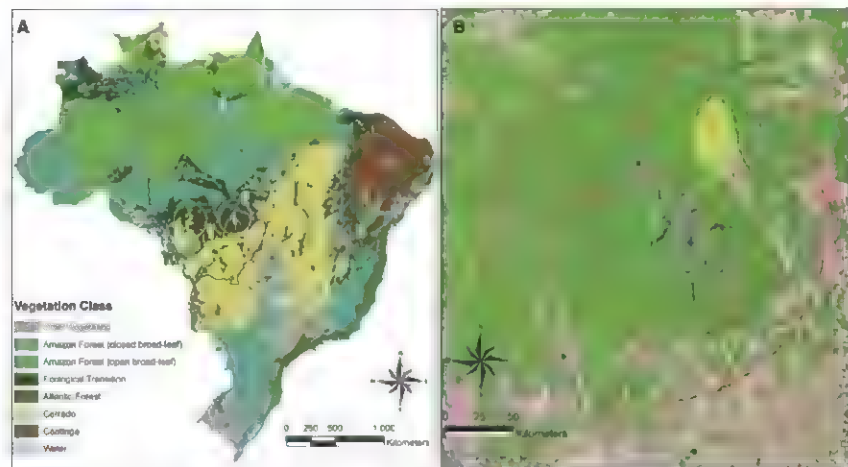


Fig. 1. (A) Map of Brazil showing major vegetative regions and areas of Amazonian complex societies, including (1) Mato Grosso state outlined, (2) blue-green forest in eastern Brazil is open broad-leaf associated with the Atlantic Forest biome. (B) Proposed cluster distributions in the Upper Xingu basin. White numbered circles are based on presence of major (>30 ha) walled centers; red unnumbered circles are hypothetical (47, 48). Area of acute anthropogenic influence is denoted by an orange circle (150 km diameter, ~17,500 km²) and

moderate to minimal anthropogenic influence by a red circle (250 km diameter, ~50,000 km²). PIX is denoted by a black line. The study area is denoted by a black box. A hatched yellow line denotes the ecological boundary between the southern Amazon forest (north) and the wooded savanna/scrub forest (south). Indigenous areas other than PIX are marked with light green. Black dots are general locations of sacred areas of Morená (north), Kamakaka (southwest), and Sagihengyu/Ahasulugu (southeast).

each polity, with smaller nonwalled settlements situated in a hinterland area.

The southern Kukikugu cluster is centered on site X11, which was the principal political ritual center and largest residential center. The better-known northern Ipatsé cluster has two major residential centers located to the north-northwest and south-southeast of the exemplary center (X13). X13 is interpreted as a primarily ceremonial center because of the paucity of domestic remains in areas outside the central plaza, the central location between X6 and X18, and the elaborated ground plan (22). The relation of X6 and X18 to X13 is similar to the orientation of high-ranking houses in the contemporary Kukikuro village, situated to the north-northwest and south-southeast of the plaza center. Secondary centers are situated to the north-northeast and south-southwest of X13.

Our survey and mapping of earthworks within and between settlements documented extensive planning based on standardized geometric and relational principles, which became durably fixed in settlement and road architecture. These relational principles are calibrated or "fitted" to basic ecological features, such as settlement position at wetland/upland interface. Four primary orientations have been recognized: (i) the formal road, roughly corresponding to the northeast-southwest solstice axis ($\sim 67^\circ/247^\circ$), present in all plaza settlements (23); (ii) the perpendicular north-south axis, which also forms a primary axis of regional distributions (in north-south road) (X13, X18, X19, and X20); (iii) intercardinal angles (X13); and (iv) the southeast-northwest solstice axis in the two largest residential centers (X6 and X11). Major roads in settlements (20 to 50 m wide) are contiguous with those between settlements (10 to 20 m wide), which extend up to 3 to 5 km. Traffic networks link satellites across a broader area and include wetland features such as raised causeways, bridges, and canoe canals. At the supra-local level, our survey revealed a grid-like pattern, created by regularly spaced settlements and road networks (Fig. 3A).

Our investigations of the two galactic clusters indicate that the territory of each polity was composed of 15 or more clusters across an area $\geq 20,000 \text{ km}^2$. Within each cluster, we estimate 100 to 150 ha or more of settlement space and a population at the mid-thousands (>2500) distributed between walled towns, which are estimated to have 800 to 1000 or more persons [as known ethnographically from adjacent areas (24)], and smaller nonwalled villages (250 ± 100 persons). The centers of the two clusters (X11 and X13) are separated by $\sim 20 \text{ km}$, which is also the distance separating X11 from X24, another putative cluster center, and other known centers across the region (15). The distribution of large centers indicates that the regional peer polity was composed of 15 or more clusters across an area $\geq 20,000 \text{ km}^2$, including sites far to the north and south of the study area. We estimate a regional population of $\geq 50,000$ (~ 2.5 persons/ km^2) (25).

The clusters of walled towns and nonwalled villages were maintained by semi-intensive resource management systems (26). Similar to villages today, these were probably focused on

manioc agriculture, with diverse lesser crops (including arboriculture), as suggested by continuity in land use and utilitarian technology, and extensive wetland management (such as fish

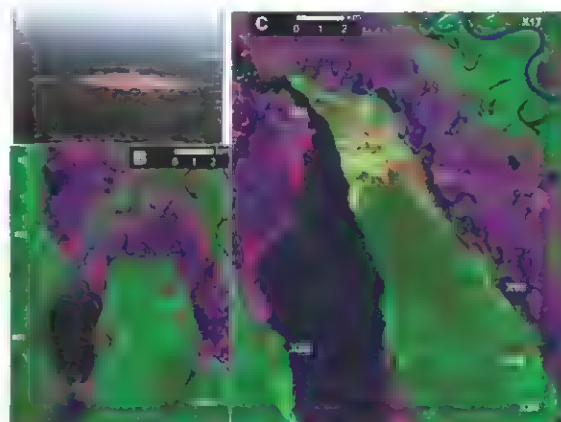


Fig. 2. (A) Contemporary Kukikuro village (2003). (B) Southern (Kukikugu) cluster (hatched lines are projected from mapped village earthworks). (C) Northern (Ipatsé) cluster sites. Global Positioning System (GPS)-mapped earthworks are denoted by red lines for road and plaza berms and black lines for ditches in (B) and (C). Pronounced anthropogenic "scarring" is found around areas of prehistoric sites. The location of Kukikuro village in (C) is just right of X6.

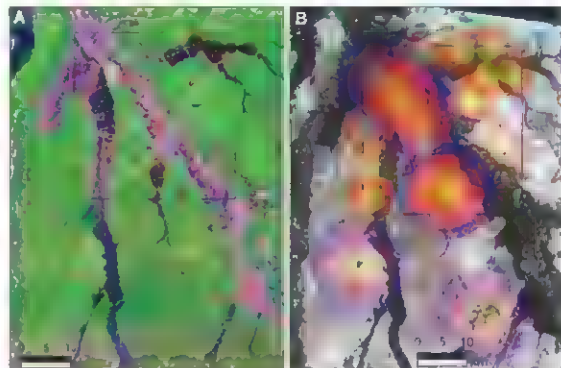


Fig. 3. (A) Regional road networks, extrapolated from GPS-mapped earthworks in and between sites (Fig. 2 and Fig. 5). (B) Northern and southern clusters are denoted by large white circles, GPS-mapped sites by small solid red circles, sites lacking GPS coordinates by open red circles, hypothetical site locations by squares, putative cluster by the dashed white circle, and extrapolated road orientations by dashed lines. (C) Overlapping concentric use areas of 2.5-km (yellow), 5.0-km (orange), and 10-km (blue) diameters positioned over pre-Columbian sites; black dots are sites that lack GPS coordinates.

farming), as indicated by the presence of earthen dikes and artificial ponds (15, 27, 29). Contemporary land use can be roughly divided into three concentric zones: village agricultural countryside (~2.5 km from settlements), a more remote but active resource use zone (~5 km), and deep forest. The density of prehistoric settlements created overlapping zones with far more extensive and intensive land use (Fig. 3B) (26). Mosaic landscapes alternated between areas or islands of acute human influence (in settlements, along roads, and in agricultural countryside) and less affected areas between settlements, between cluster cores and satellites, and particularly between clusters in the regional peer polity, characterized by large tracts of high forest. Intrasettlement production included large compost areas, characterized by anthropogenic dark earth and large open areas (devoid of domestic refuse), probably used for manioc cultivation (15, 30, 31).

Land use planning and modification of local and regional ecology were no less remarkable or sophisticated than in other areas of early urban societies worldwide. As elsewhere, urbanism resulted in a landscape "compositionally more heterogeneous, geometrically more complex, and ecologically more fragmented" (32) than those associated with small-scale societies traditionally viewed as typical of the region. Regardless of scale, such areas of semi-intensive land use have very different ecological parameters than those characteristic of small-scale indigenous groups in recent times (SOM text).

The Upper Xingu is another case that underscores the need to move beyond narrow typological approaches, which conflate early urban societies with full-blown cities or the state, and to focus instead on degrees and kinds of urbanism, including dispersed, multicentric urban settlements (7–9). In Amazonia, there is little evidence for the type of large, singular centers considered cities in other world areas. Substantial variability characterized this vast region, including cycling between more centralized and more diffuse settlement patterns in certain areas (34), but the largest settlements rarely exceed 50 ha (1–3). Our findings support claims that ancient civilizations in broadly forested regions, such as temperate Europe, eastern North America, and the Amazon basin, are generally more dispersed and less centralized than classical (oasis) civilizations in Egypt, Mesopotamia, and Indus River areas or, in the South American case, coastal desert or arid highland river valleys (35, 36).

Long ago, Howard (37) proposed a model for lower-density urban development, a "garden city," designed to promote sustainable urban growth. The model proposed networks of small and well-planned towns, a "green belt" of agricultural and forest land, and a subtle gradient between urban and rural areas. The pre-Columbian polities of the Upper Xingu developed such a system, uniquely adapted to the forested environments of the southern Amazon. The Upper Xingu is one of the largest contiguous tracts of transitional forest

in the southern Amazon [the so-called "arc of deforestation" (38)], our findings emphasize that understanding long-term change in human-natural systems has critical implications for questions of biodiversity, ecological resilience, and sustainability. Local semi-intensive land use provides "home grown" strategies of resource management that merit consideration in current models and applications of imported technologies, including restoration of tropical forest areas (39–42). This is particularly important in indigenous areas, which constitute over 20% of the Brazilian Amazon and "are currently the most important barrier to deforestation" (43). Finally, the recognition of complex social formations, such as those of the Upper Xingu, emphasizes the need to recognize the histories, cultural rights, and concerns of indigenous peoples—the original architects and contemporary stewards of these anthropogenic landscapes—in discussions of Amazonian futures.

References and Notes

1. A. Roosevelt, in *Complex Politics in the Ancient Tropical World*, E. B. Bacus, J. Lucero, Eds. (American Anthropological Association, Washington, DC, 1999), pp. 32–33.
2. C. McLean, E. Neves, C. Barreto, Eds., *The Urban Amazon* (British Museum, London, 2001).
3. W. Balke, C. Erickson, Eds., *Time and Complexity in Historical Ecology: Studies in the Neotropical Lowlands* (Columbia Univ. Press, New York, 2006).
4. Upper Xingu refers to the headwater basin of the Xingu River, one of the four principal southern tributaries of the Amazon River.
5. M. Hecdenberg et al., *Science* **301**, 1710 (2003).
6. M. Hecdenberg et al., *Science* **301**, 1710 (2003).
7. G. Campbell, *Ann. Rev. Anthropol.* **33**, 525 (2004).
8. R. McIntosh, *Ancient Middle Niger: Urbanism and the Self-Organizing Landscape* (Cambridge Univ. Press, Cambridge, 2005).
9. M. Yoffee, *Myths of the Ancient State* (Cambridge Univ. Press, Cambridge, 2005).
10. U. Hanner, in *Social Science Encyclopedia*, A. Kuper, J. Kuper, Eds. (Cambridge Univ. Press, Cambridge, 1986), pp. 84–88.
11. We use "early" to broadly refer to urban societies that existed before early modern Europe, that is, pre-1500 CE, although patterns continue beyond this date in many areas.
12. S. Tarnish, *Ann. NY Acad. Sci.* **293**, 69 (1977).
13. C. Renfrew, J. Cherry, Eds., *Peer Polity Interaction and Civilizational Change* (Cambridge Univ. Press, Cambridge, 1986).
14. D. Ackerly, W. Thomas, C. Ferreira, J. Pears, *Britannia* **41**, 113 (1989).
15. Materials and methods are available as supporting material on Science Online.
16. Of 30 radiocarbon dates, 32 were land collected from the interface of quarried peat earthwork and earthen construction deposits (overbaked) and date major site reformation at X6, X11, and X13. ~750 to 700 ± 100 yr B.P. (date 51) (15).
17. The study area conforms to the territory of the Kaluaru Amerindian community: one of eight primary subgroups of the contemporary Xinguanian nation.
18. Earlier occupations had major earthworks, but expansion and structural elaboration of settlements ~750 to 650 yr B.P. removed many earlier deposits.
19. Standing structures are suggested by funnel-shaped ditch bases (>50 cm base), interpreted as footings for tree trunk walls, and a large vertical "hoist" in ditch 10, interpreted as a oiled trunk (Fig. S4). Indigenous oral history and regional ethnography also describe palisaded settlements.
20. Recent Xinguanian villages are <5 ha (maximum of <3 ha domestic area) and range up to ~350 persons in <3 ha houses, averaging 250 m² (Fig. 2A and Fig. S6).

21. X20 is situated to the north-northeast of X11, but the larger residential core of X38 is located to the west.
22. X13 was apparently a smaller occupation site, similar in size to the early occupations of X6 (concentrated within the innermost ditch) which was reconstituted as the cluster center, ~750 yr B.P.
23. The "formal ceremonial causeway (t'angra)" in Kulkuro always points away from wetlands into forest areas.
24. C. Henebri, *The Arawak: On the Origins of the Amerindians*, C. Henebri, N. B. B. (1967).
25. We consider these conservative estimates. In particular, we expect more clusters are located in the vast areas currently uninvestigated, including far northern and southern sites (Fig. 1B).
26. W. Denevan, *Cultivated Landscapes of Native Amazonia and the Andes* (Oxford Univ. Press, Oxford, 2001).
27. R. Carneiro, in *Adaptive Responses of Native Americans*, R. M. H. Vickers, Eds. (Academic Press, New York, 1983), pp. 65–111.
28. M. Hecdenberg, *The Ecology of Power: Person, Place, and Culture in Southern Amazon*, AD 1250–2000 (Routledge, New York, 2005).
29. C. Erickson, *Nature* **408**, 190 (2000).
30. B. Glaser, W. Woods, Eds., *Amazonian Dark Earths: Explorations in Space and Time* (Springer, Berlin, 2004).
31. J. Lehmann, D. Kern, B. Glaser, W. Woods, Eds., *Amazonian Dark Earths: Origins, Management, Properties* (Wiley-VCH, Weinheim, 2003).
32. E. Erickson, *Ecol. Soc.* **12**, 34 (2006).
33. A. Makarewicz, in *Handbook of South American Archaeology*, H. Silverman, W. Isbell, Eds. (Springer, New York, 2008), pp. 633–657.
34. E. Neves, J. Peterson, in *Time and Complexity in Historical Ecology: Studies in the Neotropical Lowlands*, W. Balke, C. Erickson, Eds. (Columbia Univ. Press, New York, 2006), pp. 239–230.
35. J. Le Goff, *Le Croisé du Occident Medieval* (G. B. Roth, Paris, 1964).
36. R. Carneiro, *Science* **369**, 733 (1970).
37. H. Howard, *Garden Cities of Tomorrow* (Routledge, London, 2007 [1902]).
38. For popular discussions, see (44–46).
39. W. Lawrence et al., *Science* **293**, 348 (2001).
40. K. Willis, J. Gibson, S. Knapp, Eds., *Philos. Trans. R. Soc. London Ser. B* **362**, 169–174 (2007).
41. D. Larrin, P. Erdos, J. Paruta, *Science* **303**, 1678 (2005).
42. R. Henebri, D. Spaul, *Science* **317**, 902 (2007).
43. D. Hargrave et al., *Conserv. Biol.* **20**, 63 (2006).
44. S. Hest, C. Mann, *Fauna* **16** January 2008, p. 92–105.
45. S. Wallace, *National Geographic*, January 2007, p. 40–71.
46. M. Grunwald, *Time* **7** April 2008, p. 40–45.
47. Figures 1B and 3A are images by Landsat 7 Enhanced Thematic Mapper (ETM+), path 225, of rows 68 and 69 taken 12 August 1999; and Fig. 2 is by Landsat 4, Enhanced Thematic Mapper, of path 225, row 69 taken 21 June 1997 (bands assigned were 5, red, 4 green; and 3 blue; forest is generally green, wetlands are dark red/purple, and seasonally wet grassy areas and deforested areas are pink). Figure 3B is by Landsat 7 ETM+ (assigned gray-scale principal components analysis).
48. Maps suggested cluster locations (red circles) in Fig. 3A are supported by indigenous knowledge of major sites with ditches.
49. Research was sponsored by the Museu Nacional Universidade Federal do Rio de Janeiro, and Museu Paraense Emílio Goeldi. We acknowledge support by NSF Archaeology Program (grants BCS 0004687 and 0353129), the William T. H. Morgan Foundation and the University of Florida.

Supporting Online Material

www.sciencemag.org/content/321/5893/1214/DC1
Materials and Methods

SOM Text

Figs. S1 to S7

Table S1

References and Notes

29 August 2008; accepted 1 August 2008
DOI:10.1126/science.1159769

Induced Pluripotent Stem Cells Generated from Patients with ALS Can Be Differentiated into Motor Neurons

John Y. Dimos,^{1,2} Klt T. Rodolfa,^{1,2} Kathy K. Niakan,¹ Laurin M. Weisenthal,¹ Hiroshi Mitsuhashi,^{3,4} Wendy Chung,^{4,5} Gist F. Croft,¹ Genevieve Saphier,¹ Rudy Leibel,⁵ Robin Goland,⁶ Hynek Wichterle,^{4,6} Christopher E. Henderson,^{4,6} Kevin Eggan^{1,2}

The generation of pluripotent stem cells from an individual patient would enable the large-scale production of the cell types affected by that patient's disease. These cells could in turn be used for disease modeling, drug discovery, and eventually autologous cell replacement therapies. Although recent studies have demonstrated the reprogramming of human fibroblasts to a pluripotent state, it remains unclear whether these induced pluripotent stem (iPS) cells can be produced directly from elderly patients with chronic disease. We have generated iPS cells from an 82-year-old woman diagnosed with a familial form of amyotrophic lateral sclerosis (ALS). These patient-specific iPS cells possess properties of embryonic stem cells and were successfully directed to differentiate into motor neurons, the cell type destroyed in ALS.

Amyotrophic lateral sclerosis (ALS) is a neurodegenerative disorder in which motor neuron loss in the spinal cord and motor cortex leads to progressive paralysis and death (1). Studies aimed at understanding the root causes of motor neuron death in ALS and efforts to develop new therapeutics would be greatly advanced if a robust supply of human motor neurons carrying the genes responsible for this condition could be generated. It was recently reported that mouse (2–5) and human (6) skin fibroblasts can be reprogrammed to a pluripotent state, similar to that of an embryonic stem (ES) cell, following transduction with retroviruses encoding *KLF4*, *SOX2*, *OCT4*, and *c-MYC*. However, it remains unclear whether induced pluripotent stem (iPS) cells can be generated directly from elderly patients with chronic disease—that is, from material that has been exposed to disease-causing agents for a lifetime—and whether such patient-specific iPS cells could be differentiated into the particular cell types that would be needed to treat or study the patient's condition.

Here, we show that iPS cells can be produced using skin fibroblasts collected from an 82-year-old patient diagnosed with a familial form of ALS. These patient-specific iPS cells

possess a gene expression signature similar to that of human ES cells and can be differentiated into cell types representative of each of the three embryonic germ layers. We have used these iPS cells to produce patient-specific motor neurons and glia, the cell types implicated in ALS pathology.

Under human research subject and stem cell protocols approved by the institutional review boards and embryonic stem cell research oversight committees of both Harvard University and Columbia University, we recruited patients with ALS and healthy controls to donate skin biopsies to be used in reprogramming studies and the production of pluripotent stem cell lines. Our initial studies focused on two female Caucasian siblings, patients A29 and A30, who were 82 and 89 years old at the time of donation. These sisters are both heterozygous for the same rare L144F (*Leu*¹⁴⁴ → *Phe*) dominant allele of the superoxide dismutase (*SOD1*) gene that is associated with a slowly progressing form of ALS (7). Patient A29 had a clear clinical manifestation of motor neuron disease, including difficulty in swallowing and weakness of the arms and legs. Patient A30 was clinically asymptomatic but had signs of upper motor neuron disease upon physical examination, presenting with bilateral plantar responses and hyperreflexia. These sisters are among the oldest living patients with disease-associated *SOD1* alleles.

Primary skin cells isolated by biopsy from these patients exhibited the morphology (Fig. 1A), cell cycle profile (Fig. S2), and antigenic expression pattern (Fig. S3) of human fibroblasts. Trans genes encoding *KLF4*, *SOX2*, *OCT4*, and *c-MYC* were introduced into these fibroblasts by means of vesicular stomatitis virus glycoprotein (VSV)-pseudotyped Moloney based retroviruses. About 30,000 fibroblasts were transduced twice over 72 hours, cultured for 4 days in standard fibroblast medium, and then passaged onto a feeder layer of mouse embryonic fibroblasts in an ES cell supportive medium. As described previously,

within 1 week hundreds of colonies composed of rapidly dividing cells with a granular morphology not characteristic of ES cells had appeared (8). However, 2 weeks later, a small number of colonies with an ES cell morphology (Fig. 1, B and C) could be identified. All ES cell-like colonies, 12 from A29 and three from A30, were chosen by hand and clonally expanded. Of these colonies, seven from A29 and one from A30 gave rise to stable cell lines that could be further expanded. Because donor A29 had been diagnosed with classical ALS, we focused our initial characterization on three putative patient-specific iPS cell lines derived from her.

To verify that the patient-specific iPS cell lines were genetically matched to the donor, we performed DNA fingerprinting analysis of the three putative iPS cell lines (A29a, A29b, and A29c) and the fibroblasts from which they were derived. Allele assignments indicated that each of the putative iPS cell lines carried the genotype of the patient's fibroblasts (table S1). Additionally, we used direct sequencing (Fig. 1D) and an allele-specific restriction fragment length polymorphism (Fig. S1, A and B) to compare the *SOD1* genotype of these cell lines with that of the donated fibroblasts and genotyping results in the patient's medical history. In each of these assays, we detected the expected L144F polymorphism in both the putative A29 iPS cell lines and the fibroblasts from which they were derived, but not in fibroblasts isolated from a healthy control individual (A18). Furthermore, polymerase chain reaction (PCR) analysis of genomic DNA from these three cell lines revealed that they all carried integrated copies of the four retroviral transgenes with which they had been transduced (Fig. S1C).

To establish that reprogramming of the patient fibroblasts had occurred and that the putative iPS cells were pluripotent, we evaluated their similarity to ES cells. Like ES cells (8)—and unlike the parental A29 fibroblasts—the A29 iPS cells displayed an active cell cycle profile, with 35% of cells in S or G₂/M phases (Fig. S2). The putative iPS cell lines also maintained a normal karyotype (Fig. S1D). Additionally, all three iPS cell lines exhibited strong alkaline phosphatase activity and expressed several ES cell-associated antigens (SSEA-3, SSEA-4, TRA-1-60, TRA-1-81, and NANOG), but were not immunoreactive for a fibroblast-associated antigen (TE-7) (Fig. 1, E and F, and Fig. S3).

Quantitative reverse transcription PCR showed that genes expressed in pluripotent cells (*REX1*/*ZFP42*, *FOXD3*, *TERT*, *NANOG*, and *CRUPTO*/*TGDF*) were transcribed at levels comparable to human ES cells in each of the three putative iPS cell lines (Fig. 2A). Moreover, the stem cell marker genes *SOX2* and *OCT4* were not expressed in the patient fibroblasts, whereas the endogenous loci in the putative iPS cells had become activated to levels similar to those in ES cells (Fig. 2B). As in previous reports (8), expression levels from the endogenous *KLF4* and *c-MYC* loci were similar in ES cells, iPS cells, and the parental fibroblasts

¹Harvard Stem Cell Institute, Stem Cell Biology, Department of Stem Cell and Regenerative Biology, Harvard University, Cambridge, MA 02138, USA. ²Department of Chemistry and Chemical Biology, Harvard University, Cambridge, MA 02138, USA. ³Eleanor and Jos Gehrig MDA-ALS Research Center, Neurological Institute, Columbia University Medical Center, New York, NY 10032, USA. ⁴Center for Motor Neuron Biology and Disease, Columbia University Medical Center, New York, NY 10032, USA. ⁵Division of Molecular Genetics and Human Genetics Center, College of Physicians and Surgeons, Columbia University, New York, NY 10032, USA. ⁶Department of Pathology, Neurology and Neuroscience, Columbia University Medical Center, New York, NY 10032, USA. ⁷Department of Medicine and Naomi Berrie Diabetes Center, Columbia University Medical Center, New York, NY 10032, USA.

*These authors contributed equally to this work.
†To whom correspondence should be addressed. E-mail: eggan@mdc.harvard.edu.

(Fig. 2B). Human iPS cells have been shown in some (6), but not all (6, 9), cases to silence expression of the retroviral transgenes used to reprogram them. RT-PCR analyses performed using primers specific to the retroviral transcripts demonstrated nearly complete silencing of viral *SOX2* and *KLF4*. However, some expression of viral *OCT4* and *c-MYC* persisted, as previously reported (6).

Pluripotent cells are by definition capable of differentiating into cell types derived from each of the three embryonic germ layers (10). A property of both ES cells and previously established human iPS cells is their ability, when plated in suspension culture, to form embryoid bodies (EBs) composed of diverse cell types (fig. S4A) (6, 9, 10). When grown in these conditions, all three iPS cell lines from patient A29 readily formed EBs (Fig. 3A). Immunocytochemical analyses of EBs

after 13 to 16 days of culture showed that each line had spontaneously differentiated into cell types representative of the three embryonic germ layers (Fig. 3, B to F, and fig. S4B). Together, these data indicate that we have reprogrammed primary fibroblasts isolated from an elderly ALS patient into iPS cells.

Much of the hope invested in patient specific stem cells is based on the assumption that it will be possible to differentiate them into disease relevant cell types. ALS is characterized by the progressive degeneration of spinal cord motor neurons (1, 11), and recent studies have shown that both cell autonomous and non-cell autonomous factors contribute to disease progression (12, 13). In particular, glia from ALS animal models were shown to produce factors that are toxic to motor neurons (14–16). These studies indicate that pro-

duction of both motor neurons and glia would be essential for mechanistic studies and perhaps for eventual cell replacement therapies for ALS.

We therefore attempted to generate spinal motor neurons and glia with the use of a directed differentiation protocol developed for mouse and human ES cells (17–20). EBs formed from iPS cells were treated with two small molecules: an agonist of the sonic hedgehog (SHH) signaling pathway and retinoic acid (RA) (fig. S5A). When these differentiated EBs were allowed to adhere to a laminin-coated surface, neuron-like outgrowths were observed (Fig. 4A). Many of these processes stained positive for a neuronal form of tubulin, β -tubulin IIIb (TuJ1), confirming their neuronal nature (Fig. 4B and fig. S6).

To further characterize the cells after directed differentiation, we plated dissociated EBs onto

Fig. 1. iPS cells can be established from patient fibroblasts after biopsy. (A) Primary dermal fibroblasts (hFB, human fibroblasts) derived from an 82-year-old female ALS patient, A29. (B) iPS cells produced from patient A29. (C) iPS cells produced from a second patient, A30, sister to patient A29. (D) Direct sequencing of a PCR product from A29 iPS cells, confirming the presence of one copy of the dominant L144F *SGD1* allele. (E and F) SSEA-4 and NANOG protein expression in A29 iPS cells. Scale bars, 200 μ m.

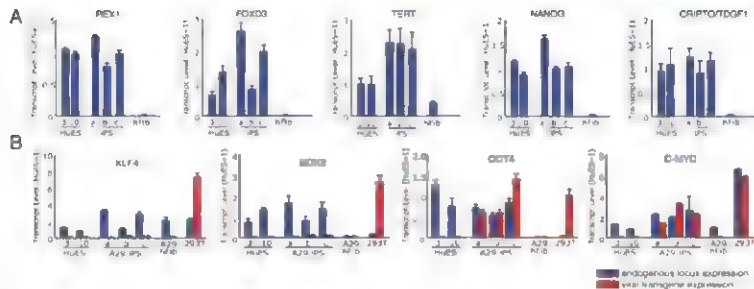
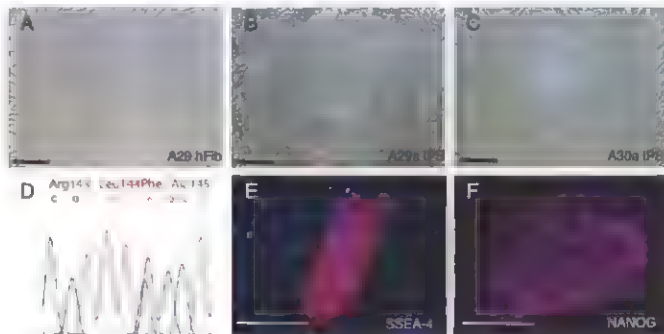


Fig. 2. A29 iPS cells are similar to human ES cells in their expression of genes associated with pluripotency. (A) The ES cell-associated transcripts *REX1/ZFP42*, *FOXD3*, *TERT*, *NANOG*, and *CRIP1/TGFI* are activated in the three putative iPS cell lines (A29a, A29b, and A29c) to levels comparable to human ES cells, as measured by quantitative RT-PCR. (B) Primers specific for either endogenously (blue) or virally (red) encoded transcripts of the four reprogramming factors

were used to measure their respective expression levels. Expression was detected from all four endogenous loci in the iPS cells at levels similar to those in the human ES cell lines HuES-3 and HuES-10. Expression from the retroviral *KLF4* and *SOX2* transgenes was not detected, although both retroviral *OCT4* and *c-MYC* were expressed. As a positive control for expression of the viral transgenes, 293T cells were transiently transfected with the four plasmids used to produce virus.

laminin-coated slides as a single-cell suspension. *TuJ1* positive neurons that coexpressed the motor neuron marker HB9 [a motor neuron-specific transcription factor (17)] could be readily identified in cultures derived from both the A29a and A29b cell lines (Fig. 4C and figs. S5B and S7). In cultures differentiated from A29b iPS cells, we examined 3262 nuclei (from three independent differentiation experiments) and found that 651 stained for HB9, indicating that 20% of all cells expressed this motor neuron marker. Moreover, more than 90% of these HB9-positive cells also expressed ISLET 1/2 [ISL, transcription factors involved in motor neuron development (17, 18)]

(Fig. 4, E to H, and figs. S5C and S8). More than half of these HB9- and ISL-positive neurons expressed choline acetyltransferase (ChAT), demonstrating an advanced degree of cholinergic motor neuron maturation (17) (figs. S5D and S9B). Cells expressing the spinal cord progenitor markers *OLIG2* and *PAX6* were also prevalent in these cultures (fig. S9A), which suggests that these patient-specific iPS-derived motor neurons arose from progenitors similar to those found in the developing spinal cord. In addition, cells expressing the glial markers GFAP [glial fibrillary acidic protein] and S100 were readily identified (Fig. 4D and fig. S10). Thus, patient-specific iPS cells—like

human ES cells—can respond appropriately to developmentally relevant patterning signals, demonstrating the feasibility of leveraging the self-renewal of iPS cells to generate a potentially limitless supply of the cells specifically affected by ALS.

Our results with patient-derived cells confirm the initial finding that the exogenous expression of only four factors—*KLF4*, *SOX2*, *OCT4*, and *c-MYC*—is sufficient to reprogram human fibroblasts to a pluripotent state (6). Previous reports using these four genes to generate human iPS cells have required the overexpression of either a murine viral receptor (6) or additional oncogenes such as *Large T Antigen* and *TERT* (21). In contrast, our results using retroviruses pseudotyped to transduce human cells dispel the suggestion by a recent study that these four genes are not sufficient to induce reprogramming (21).

We have demonstrated that it is possible to produce patient-specific pluripotent stem cells. It is particularly encouraging that neither the advanced age nor the severely disabling disease of patient A29 prevented us from reprogramming her fibroblasts. Attempts to generate similar pluripotent cell lines using somatic cell nuclear transfer and ES cell fusion have been confronted by technical, logistical, and political obstacles that have not yet been overcome (22, 23). The use of defined reprogramming factors for the generation of patient-specific iPS cells has allowed us to circumvent these obstacles. Note that the multiple integrations of retroviral DNA in the host genome, which were required for reprogramming, did not preclude our ability to terminally differentiate these cells into motor neurons. Nonetheless, long-term studies will be needed to compare the *in vitro* physiology of iPS-derived motor neurons and those derived from human ES cell lines.

Our study also demonstrates the feasibility of producing large numbers of motor neurons with a

Fig. 3. Patient-specific iPS cells are pluripotent stem cells. (A) EBs formed from A29b iPS cells, 5 days after seeding. Scale bar, 200 μ m. (B to F) These EBs contained cells representative of each of the three embryonic germ layers: endoderm ((B), α -fetoprotein (AFP)), mesoderm ((C), desmin; (D), α -smooth muscle actin (α -SMA)), and ectoderm ((E), β -tubulin 11b (TuJ1); (F), GFAP). Scale bars, 100 μ m.

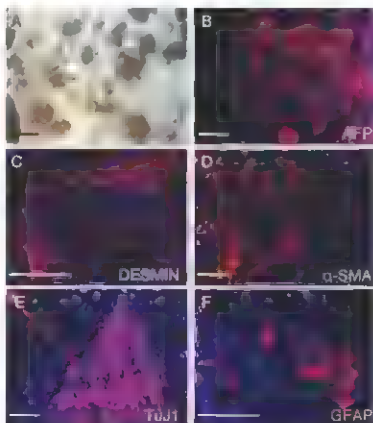
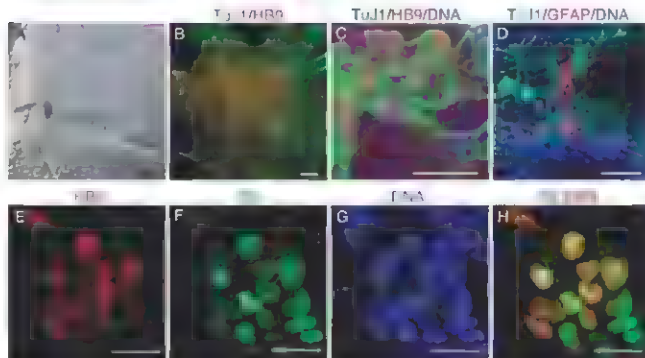


Fig. 4. iPS cells generated from ALS patients can be differentiated into motor neurons. A29b iPS cell EBs were patterned with RA and SHH, then plated on laminin, either whole (A and B) or after dissociation (C to H), and allowed to mature for 7 to 15 days. (A) Neuron-like outgrowths are visible from whole A29b patient-specific iPS cell EBs. (B) Extensive *TuJ1*-positive neuronal processes grow out from plated whole iPS EBs, which contain a high proportion of HB9-stained nuclei. (C) Neuronal identity of HB9-expressing cells is confirmed by high-magnification image of HB9 and *TuJ1* coexpression in dissociated patient-specific motor neuron cultures. (D) GFAP-expressing glial cells can be found in addition to *TuJ1*-expressing neurons in differentiated patient-specific iPS cell cultures. (E to H) The motor neuron identity of HB9- and *TuJ1*-positive cells is confirmed by the coexpression of HB9 and ISL. HB9 (E) and ISL (F) localization is nuclear (G) and highly coincident (H). Scale bars, 100 μ m [(A) to (D)], 75 μ m [(E) to (H)].



patient's exact genotype, which would be miniature-matched to that individual—a long-sought goal of regenerative medicine. However, several major challenges need to be resolved before cell replacement therapy using IPS technology can become a clinical reality. First, among several other safety issues, IPS-derived neurons will not be suitable for transplantation until the oncogenic genes and retroviruses (24, 25) used here are replaced with more controlled methods of reprogramming. Second, it likely will be necessary to understand and correct any intrinsic defects in the patient's neurons and glia before they can be rationally used as a basis for cell therapy.

Many recent insights into the pathophysiology of ALS come from the study of familial forms of this disease. The patient-specific IPS cells produced here will be important tools for further studies of mechanisms by which familial disease arises. However, more than 90% of ALS patients are afflicted by a sporadic form of disease, thought to arise from complex interactions between genetic and environmental factors (26). As a result of these complexities, it has been impossible until now to devise *in vitro* cell-based models for this most common type of ALS. Patient-specific IPS cells generated from individuals with sporadic disease would carry the precise constellation of genetic information associated with pathology in that person. This approach would allow study of

living motor neurons generated from ALS cases with unknown genetic lesions, providing insight into their intrinsic survival properties, their interactions with other cell types, and their susceptibility to the environmental conditions that are considered to play an important role in ALS pathogenesis.

References and Notes

1. P. Parashar, R. H. Brown, *Nat. Rev. Neurosci.* **7**, 710 (2006).
2. K. Takahashi, S. Yamanaka, *Cell* **126**, 663 (2006).
3. X. Ohtsuka, T. Ichikawa, S. Yamanaka, *Nature* **448**, 313 (2007).
4. N. Mahboubi et al., *Cell Stem Cell* **1**, 55 (2007).
5. A. Mueser, M. Wernig, R. Jaenisch, *Bioethics* **25**, 1177 (2007).
6. X. Takahashi et al., *Cell* **131**, 861 (2007).
7. L. Ferreira et al., *Amphiphilic Lipid Scaffolds: Other Motor Neuron Disorders*, *Cell* **126**, 1353 (2006).
8. C. A. Cowan et al., *Nat. Engl. J. Med.* **350**, 1333 (2004).
9. J. Yu et al., *Science* **318**, 1917 (2007); published online 19 November 2007 DOI:10.1126/science.11515261.
10. J. A. Thomson et al., *Science* **282**, 1145 (1998).
11. D. W. Cleveland, J. D. Rothstein, *Nat. Rev. Neurosci.* **2**, 806 (2001).
12. C. Rando et al., *Neuron* **35**, 1067 (2002).
13. S. Bolik et al., *Science* **312**, 1349 (2006).
14. F. P. Di Giorgio, M. A. Carrasco, M. C. Sloan, T. Mammitz, K. Egan, *Nat. Neurosci.* **10**, 608 (2007).
15. M. Nagai et al., *Nat. Neurosci.* **10**, 615 (2007).
16. X. Yamanaka et al., *Nat. Neurosci.* **11**, 251 (2008).
17. H. Wadiche, L. Luehrmann, J. A. Porter, T. M. Jessell, *Cell* **130**, 385 (2002).
18. X. Li et al., *Nat. Biotechnol.* **23**, 215 (2005).
19. X. Li et al., *Stem Cells* **26**, 886 (2008).
20. M. Singh Roy et al., *Exp. Neurol.* **196**, 224 (2005).
21. I. H. Park et al., *Nature* **455**, 141 (2008).

22. K. Egan, *Cloning Stem Cells* **9**, 21 (2007).
23. J. Cibelli, *Science* **318**, 1287 (2007).
24. S. Haeberling-Albani et al., *Science* **302**, 415 (2003).
25. K. Hoshino, Y. Yamada, C. Beard, R. Jaenisch, *Cell* **121**, 465 (2005).
26. T. Dondelinger et al., *N. Engl. J. Med.* **357**, 775 (2007).
27. We thank D. Melton, D. Egli, A. McMahon, K. O'Brien, K. Huh, S. Fiedler, and K. Hoshino for helpful discussions, T. Kishimoto, S. Yamanaka, and R. Weinberg for providing viral vectors through Addgene, R. Rubin for generously providing the small molecule SHH agonist, the Developmental Studies Hybridoma Bank for monoclonal antibodies, and J. Montes and M. Lee for their support in obtaining institutional review board approval and culturing biopsies. This collaboration was supported and enabled by the Project ALS/Genetics Estess Laboratory for Stem Cell Research, where much of the Columbia research was carried out. Supported by the Harvard Stem Cell Institute, Project ALS, the SMA Foundation, the Cure and Howard T. Foundation, ADA Wings Over Wall Street, the Spina and Bowen families, and the New York Stem Cell Foundation. K.T.R. is a National Science Foundation predoctoral fellow, G.F.C. is a Project ALS predoctoral fellow, and K.E. is a fellow of the John D. and Catherine T. MacArthur Foundation.

Supporting Online Material

www.sciencemag.org/content/318/5979/1221/DC1
Materials and Methods

Figs. S1 to S10
Tables S1 and S2
References

7 April 2008; accepted 2 July 2008

Published online 31 July 2008

DOI:10.1126/science.1158799

include this information when citing this paper:

Amyloid- β Dynamics Correlate with Neurological Status in the Injured Human Brain

David L. Brody,^{1,2,4*} Sandra Magnoni,^{3,4} Kate E. Schwetty,^{1,2} Michael L. Spinner,^{1,2} Thomas J. Esparza,^{1,2} Nino Stocchetti,^{3,4} Gregory J. Zipfel,⁵ David M. Holtzman^{1,2}

The amyloid- β peptide ($A\beta$) plays a central pathophysiological role in Alzheimer's disease, but little is known about the concentration and dynamics of this secreted peptide in the extracellular space of the human brain. We used intracerebral microdialysis to obtain serial brain interstitial fluid (ISF) samples in 18 patients who were undergoing invasive intracranial monitoring after acute brain injury. We found a strong positive correlation between changes in brain ISF $A\beta$ concentrations and neurological status, with $A\beta$ concentrations increasing as neurological status improved and falling when neurological status declined. Brain ISF $A\beta$ concentrations were also lower when other cerebral physiological and metabolic abnormalities reflected depressed neuronal function. Such dynamics fit well with the hypothesis that neuronal activity regulates extracellular $A\beta$ concentration.

A β is the principal constituent of the hall mark amyloid plaques found in Alzheimer's disease and is the target of many potentia treatments for the disease (1). However, little is known about the concentration and dynamics of this secreted peptide in the extracellular space of the human brain where these plaques form. *In vitro* and animal studies have shown that neuronal and synaptic activity dynamically regulate soluble extracellular $A\beta$ concentrations (2–4). Whether similar regulation of $A\beta$ levels occurs in the human brain is unknown.

We used intracerebral microdialysis (5) to obtain serial brain interstitial fluid (ISF) samples in 18 intensive care unit (ICU) patients who had sustained acute brain injury and were undergoing invasive intracranial monitoring for clinical purposes. In all patients, $A\beta_{1-42}$ was detected in hourly or bihourly intracranial microdialysis samples. None had a diagnosis of Alzheimer's disease or dementia, demonstrating that $A\beta$ is a normal constituent of human brain extracellular fluid (6). The $A\beta_{1-42}$ enzyme-linked immunosorbent assay (ELISA) used detects $A\beta$ species from amino acid 1 to amino acid 28 or greater (3, 7).

There were rising trends in brain ISF $A\beta$ concentrations over several hours to days in most patients, though the specific pattern of these trends was variable (Fig. 1, B, D, and F; Fig. 2B, and Fig. 4, A to D). Median brain ISF $A\beta_{1-42}$ at 60 to 72 hours was 59% higher than at 0 to 12 hours (Fig. 1G) ($P = 0.0002$, Wilcoxon signed rank test). Urine concentrations in the same samples, which control for the stability of the microdialysis catheter function (8), remained stable over the same time frame (Fig. 1H) (median 14% lower, $P = 0.06$, Wilcoxon signed rank test). Thus, the observed $A\beta$ dynamics are likely to be of cerebral origin and not an artifact of the measurement procedure.

$A\beta_{1-42}$ concentrations were lower in microdialysate than in concomitantly sampled ventricular cerebrospinal fluid (CSF) (Fig. 2, B and D). However, at the flow rate used (0.3 μ l/min), the microdialysis is not in complete equilibrium with the surrounding extracellular space (5). To calculate the true brain extracellular concentrations,

¹Department of Neurology, Washington University, St. Louis, MO 63110, USA; ²Biocenter for Neurological Disorders, Washington University, St. Louis, MO 63110, USA; ³Department of Anesthesia and Intensive Care, Fondazione Istituto di Ricovero e Cura a Carattere Scientifico, Ospedale Maggiore Policlinico, Mangiagalli e Regina Elena, Via Sforza 35, 20100 Milan, Italy; ⁴Allian University, Milan, Italy; ⁵Department of Neurological Surgery, Washington University, St. Louis, MO 63110, USA.

*These authors contributed equally to this work. [To whom correspondence should be addressed. E-mail: brodyd@neuro.wustl.edu.]

we used two methods to estimate the fractional recovery of $A\beta$ under these conditions (Fig. 2C). First, we performed *in vitro* recovery experiments with known concentrations of $A\beta$. Second, we used *in vivo* zero-flow extrapolation, which relies on the principle that as flow rate approaches zero, equilibration across the membrane will approach completion (9). These two methods agreed well, recovery of $A\beta$ was ~30% at 0.3 μ l/min (Fig. 2C and figs. S1 and S2). After correction for this recovery, the concentrations in ventricular CSF and brain ISF were, on average, very similar (Fig. 2D). However, the range of concentrations in brain ISF was significantly wider (Fig. 2D), and the hour-by-hour dynamics of $A\beta$ changes correlated poorly (Fig. 2, B and E).

The 42 amino acid form of $A\beta$ ($A\beta_{1-42}$) is of special interest, this form appears to have the greatest propensity to deposit into insoluble plaques, one of the pathological hallmarks of Alzheimer's disease, as well as to aggregate into oligomeric $A\beta$ species, reported to be especially neurotoxic (10–12). Current ELISA methods are not sensitive enough to measure $A\beta_{1-42}$, $A\beta_{1-40}$ and $A\beta_{1-38}$ in individual hourly or bihourly microdialysis samples, so 8-hour pools of microdialysis samples were combined for five patients. In these pooled samples, the $A\beta_{1-40}/A\beta_{1-42}$ ratio was 14 ± 5.2 . $A\beta_{1-42}$ concentrations were lower than $A\beta_{1-40}$ concentrations by a factor of 35 \pm 12, and $A\beta_{1-40}$ concentrations were lower than $A\beta_{1-38}$ concentrations by a factor of 2.5 \pm 0.9. Thus, much

of the $A\beta$ measured by the $A\beta_{1-40}$ assay does not appear to be either $A\beta_{1-40}$ or $A\beta_{1-42}$. Brain ISF $A\beta_{1-42}$ concentrations were consistently proportional to those of $A\beta_{1-40}$ (Fig. 2F). The relation was similar in ventricular CSF (Fig. 2F), though greater variability was observed. Thus, the observed trends in brain ISF $A\beta_{1-42}$ levels over time likely reflect changes in $A\beta_{1-42}$ levels as well.

To address potential mechanisms underlying these dynamics, we compared brain ISF $A\beta_{1-40}$ concentrations from single samples with various microdialysis parameters and physiological measures obtained concurrently as part of clinical care in the intensive care unit (Fig. 3 and figs. S3 and S4). A positive correlation with brain ISF glucose (Fig. 3A), as well as negative correlations with brain ISF lactate/pyruvate ratio (Fig. 3B), elevated intracranial pressure (Fig. 3C), and extremes of cerebral temperature (Fig. 3D), were the most salient.

Thus, brain ISF $A\beta$ increased as overall physiology normalized. Indeed, in several patients, brain ISF $A\beta$ concentrations tracked the patients' global neurological status, as assessed with the Glasgow Coma Score (Fig. 4, A to D); brain ISF $A\beta$ concentrations rose as patients improved, remained stable in clinically stable patients, and appeared to decline when clinical status worsened. The Glasgow Coma Score (13) is a crude but reliable measure of neurological status in severely brain-injured patients that ranges from 3 (deeply comatose) to 15 (eyes open spontaneously, following commands, and speaking appropriately).

To quantify this relation across patients, we plotted change in brain ISF $A\beta_{1-40}$ from single samples versus change in Glasgow Coma Score (Fig. 4E). The clinical importance of a one-point change in the Glasgow Coma Score is often unclear, especially in critically injured, sedated patients. So for our primary analysis, we assessed changes in brain ISF $A\beta$ only at times when Glasgow Coma Score had changed by two or more points from baseline (Fig. 4E). The correlation in this analysis was markedly strong (Spearman $r = 0.82$, $P < 0.0001$). The correlation, including one-point changes in Glasgow Coma Score, was still quite robust (Spearman $r = 0.52$, $P < 0.0001$). Such correlations were present in both traumatic brain injury patients and subarachnoid hemorrhage patients ($r = 0.72$, $P < 0.0001$ and $r = 0.39$, $P = 0.0004$, respectively; fig. S5). A much weaker correlation with neurological status was seen for ventricular CSF $A\beta$ ($r = 0.20$, fig. S6).

What underlies this seemingly surprising association between local brain ISF $A\beta$ levels and global neurological status (Fig. 4F)? Our findings in the human brain are consistent with previous results that indicate a direct causal relation between neuronal activity and extracellular $A\beta$ *in vitro* (2) or brain ISF $A\beta$ concentrations in mice (3, 4). From this perspective, the correlations between brain ISF $A\beta$ concentrations and the other measured parameters fit well, low glucose and high lactate/pyruvate ratio indicative of abnormal brain metabolism, high intracranial pressure, and

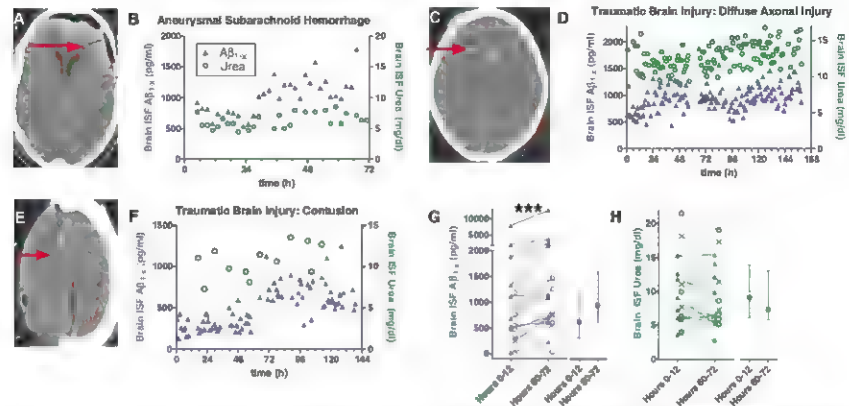


Fig. 1. $A\beta$ dynamics in human brain ISF assessed with intracerebral microdialysis after acute injury. (A, C, and E) Computerized tomography scans demonstrating location of microdialysis catheters; the radio-opaque gold tips of the catheters are indicated by red arrows. (B, D, and F) Brain ISF $A\beta$ concentrations (blue triangles) measured hourly or bihourly in individual patients. Urea (green circles) was measured in several of the same microdialysis samples. Time (x axis) reflects interval from initiation of microdialysis. (G) Trends over time in brain ISF $A\beta$ (*** $P = 0.0002$, Wilcoxon signed rank

test). (Left) Individual patient values. Closed triangles: traumatic brain injury patients with catheters placed in right frontal lobe white matter regions with no apparent focal injury ($n = 9$); x-symbols: traumatic brain injury patients with catheters placed in pericontinental brain tissue ($n = 3$); open circles: subarachnoid hemorrhage patients with catheters placed in right frontal lobe white matter ($n = 6$). (Right) Median, interquartile interval, across all 18 patients. (H) Brain ISF urea was essentially stable. (Left) Individual patient values; (right) median, interquartile interval.

extremes of brain temperature all would likely result in impaired neuronal function (5). The absence of a correlation with glutamate levels, brain oxygenation, or cerebral perfusion pressure should

not be taken as evidence against the neuronal activity hypothesis, because these parameters were rarely outside of their normal ranges in our patients (fig. S3).

Our findings complement the evidence from lesion studies in mice (14) and imaging studies in humans linking neuronal activity and A β deposition (15). However, based on prior results, the

Fig. 2. Brain ISF A β versus

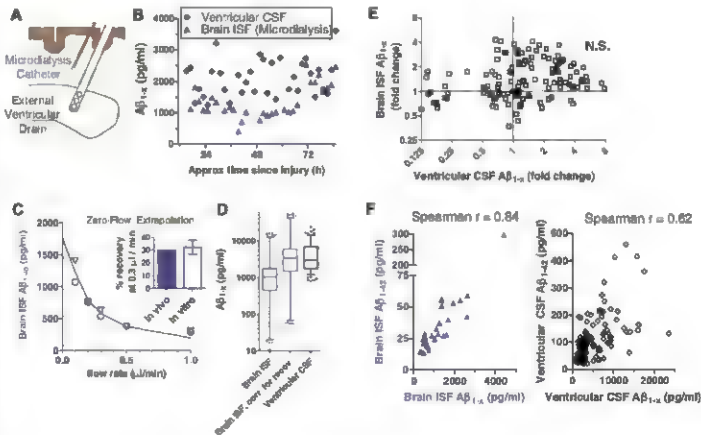
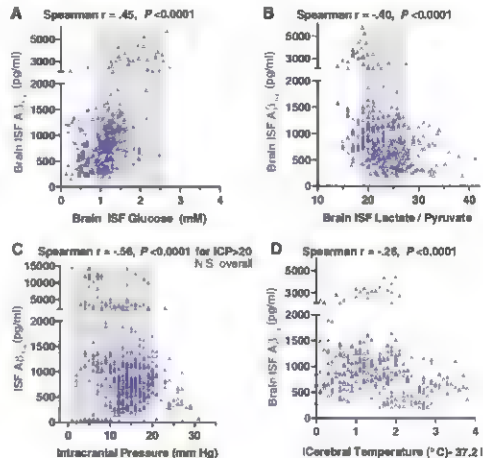


Fig. 3. Correlations of brain ISF A β concentrations with other microdialysis parameters and physiological measures. (A) Brain ISF glucose versus brain ISF A β measured in the same microdialysis samples ($n = 388$ paired measurements). (B) Brain ISF lactate/pyruvate ratio versus brain ISF A β ($n = 374$). (C) Intracranial pressure (ICP) versus brain ISF A β ($n = 565$). (D) Absolute value of the difference between measured temperature cerebral temperature and normal cortical temperature, 37.2°C (27) versus brain ISF A β ($n = 324$). Each point represents a single paired measurement. Data are from 11 to 17 patients. Not all patients had all parameters measured at all time points (see supporting online material). Shaded regions represent mean \pm 1 SD of estimated normal values (5, 27, 28).



confidence interval; circles: outliers. (E) Changes from initial values of A β over time in ventricular CSF versus changes from initial values over time in brain ISF. (F) A β_{1-42} concentrations compared with total A β_{1-42} concentrations in brain ISF (left) and ventricular CSF (right). The correlation in brain ISF was stronger than in ventricular CSF ($P = 0.029$, difference test).

speed and magnitude of the dynamics seen here were unexpected. Smaller fluctuations in A β levels over hours to days have been observed in lumbar CSF from normal subjects (16).

Global neurological status was better correlated with brain ISF A β measurements in our patients than with ventricular CSF A β . This was surprising because ISF sampled by microdialysis comes from a relatively restricted area of the brain near the catheter, whereas ventricular CSF is derived from diffuse periventricular brain regions. On the other hand, many of the processes involved in acute brain injury and subsequent ICU care (e.g., sedation, anesthesia, etc.; fig. S7) likely affect neocortical neuronal and/or synaptic activity relatively homogeneously. We hypothesize that sampling from white matter adjacent to any cortical region gives a reliable indicator of global neuronal and/or synaptic function. Changes in global neuronal and/or synaptic function are in turn likely to be directly reflected in changes in the Glasgow Coma Score. In contrast, the relatively weak relation with ventricular CSF in these patients may indicate that factors other than neuronal/synaptic activity contribute much of the variance in ventricular CSF A β concentrations.

The relation between brain ISF A β and CSF A β is clearly complex and requires further study. Lumbar CSF (16) may be derived from cortical ISF to a greater extent than ventricular CSF, and future studies will be required to address this issue because lumbar CSF was not obtained in these patients.

It is unlikely that there is a direct relation between the reported deposition of insoluble A β after traumatic brain injury (17–19) and the changes in brain ISF A β levels that we observed. A β deposits have been observed in a minority (approximately one-third) of subjects, whereas the rise in ISF A β over time was a nearly universal phenomenon (Fig. 1G). Thus, the relation between our findings and the reported epidemiological link between acute brain injury and the later development of Alzheimer's disease (20, 21) is unclear.

Similarly, it is unlikely that these dynamics are related to axonal injury. If A β were being released into the extracellular space as a consequence of immediate axonal injury, we would have expected to see initially high brain ISF A β values, which then would have been expected to fall over time. This is the opposite of what we observed. We recognize that an increase of total tissue or intracellular A β levels (22, 23) would not have

been detected, because microdialysis samples derive only from the extracellular space. Likewise, an early, transient rise in brain ISF A β concentrations would not have been detected, because catheters were implanted 12 to 48 hours after injury.

Our results provide direct information on the true extracellular fluid A β levels in the living human brain. To our knowledge, all but one of our patients had an acute brain injury, and none had dementia or Alzheimer's disease. Nonetheless, this information is useful when considering whether levels of exogenous (10, 12, 24, 25) or endogenous A β in experimental animals (26) are likely to be physiologically relevant in humans.

References and Notes

1. D. J. Selkoe, *J. Clin. Invest.* **110**, 1375 (2002).
2. F. Kammerer et al., *Neuron* **37**, 925 (2003).
3. J. R. Cirrito et al., *Neuron* **48**, 913 (2005).
4. J. R. Cirrito et al., *Neuron* **58**, 42 (2006).
5. L. Hillered, P. M. Vespe, D. A. Hovda, *J. Neurotrauma* **22**, 3 (2005).
6. F. Seubert et al., *Nature* **359**, 325 (1992).
7. K. Johnson-Wood et al., *Proc. Natl. Acad. Sci. U.S.A.* **94**, 1550 (1997).
8. E. Roemer-Gusterson et al., *J. Neurosci.* **94**, 397 (2001).
9. P. D. Hutchinson et al., *J. Neurosci.* **93**, 37 (2003).
10. D. M. Walsh et al., *Nature* **436**, 535 (2002).
11. S. Lesné et al., *Nature* **440**, 352 (2006).
12. G. M. Shankar et al., *Nat. Med.* **14**, 837 (2008).
13. G. Teasdale, B. Jennett, *Lancet* **2**, 81 (1974).
14. O. Aasov, M. Lee, D. A. Peterson, S. S. Sisodia, *J. Neurosci.* **22**, 9785 (2002).
15. R. L. Buckner et al., *J. Neurosci.* **25**, 7709 (2005).
16. R. J. Bateman, G. Wen, J. C. Morris, D. M. Holtzman, *Neurology* **68**, 666 (2007).
17. G. W. Roberts et al., *J. Neurol. Neurosurg. Psychiatry* **57**, 419 (1994).
18. D. H. Smith, X. H. Chen, A. Iwata, D. L. Graham, *J. Neurosurg.* **98**, 1072 (2003).
19. M. D. Monaghan et al., *Exp. Neurol.* **190**, 192 (2004).
20. K. A. Jellinger, *Curr. Opin. Neurol.* **17**, 719 (2004).
21. G. Tesco et al., *Neuron* **54**, 721 (2007).
22. D. H. Smith et al., *Am. J. Pathol.* **153**, 1005 (1998).
23. E. E. Abrahamson et al., *Exp. Neurol.* **197**, 437 (2006).
24. L. Klyachko et al., *Nat. Med.* **11**, 556 (2005).
25. J. P. Cleary et al., *Nat. Neurosci.* **8**, 75 (2005).
26. D. Games, M. Buttini, D. Kobayashi, D. Schenk, P. Seubert, *J. Alzheimer's Dis.* **9**, 133 (2006).
27. R. Corbett, A. Caplock, P. Weatherall, *J. Cereb. Blood Flow Metab.* **17**, 363 (1997).
28. P. Renshaw et al., *Neuroscience* **47**, 701 (2000).
29. We thank the participants and their families for their invaluable contributions. We appreciate the assistance of our neurosurgical colleagues for relieving patients, M. Hadley for placing several microdialysis catheters, and P. Bianchi, G. Brandt, M. Carbonara, J. Deidra, B. Hall, L. Magni, E. Miller, J. Segar, and T. Zorle for help collecting samples. Valuable discussions with R. Bateman, R. Bellack, J. Cirrito, R. Dacey, N. Dringler, L. Hillered, P. Hutchinson, J. Ladenson, H. Temkin, and W. Powers are acknowledged. We are grateful to Eli Lilly and Co. for providing the antibodies used in the A β ELISAs. This work was supported by NIH grant NS049237 (D.L.S.), a Burroughs Wellcome Career Award in the Biomedical Sciences (D.L.S.), NIH grant AG13994 (D.M.H.), and Cure Alzheimer's Fund (D.M.H.).

Supporting Online Material

www.sciencemag.org/cgi/content/full/323/5893/1222/DC1

Methods

SOM Text

Figs. S1 to S7

References

10 June 2008; accepted 27 July 2008
10.1126/science.1161591

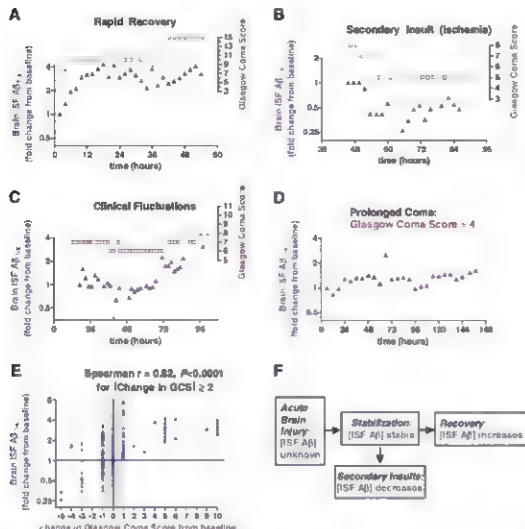


Fig. 4. Brain ISF A β and neurological status. **(A to D)** Examples of the time course of changes in brain ISF A β concentrations and changes in neurological status, as reflected by Glasgow Coma Score (GCS). A β changes appear to track (A and B), and in some cases even precede (C), neurological status changes. **(E)** Correlation of change in brain ISF A β from baseline with changes in neurological status across 13 patients in which serial GCS measurements could be reliably obtained ($n = 173$ paired measurements). **(F)** Model of brain ISF A β dynamics in the setting of acute brain injury.

Gel Documentation System

The U:Genius is an affordable gel documentation system for accurately recording DNA and protein gel images. Built to the same high standards as the G:BOX image analyzers, U:Genius provides 2 megapixel resolution. The system has a compact darkroom with a unique touch screen and can accommodate any benchtop transilluminator. The darkroom comes with internal white light for viewing and focusing and has self-stowing doors that automatically turn off the transilluminator when opened to prevent accidental ultraviolet exposure. The touch screen's icons are linked to Syngene's latest imaging methods, so users needing to rapidly resolve close band images can produce true 16-bit images using the EDR (extended dynamic range) icon. Users can reduce background noise with the neutral fielding icon. Images can be rotated, sharpened, and annotated.

Syngene
For information
800-686-4407
www.syngene.com



Bibliographic Software

EndNote Web is an upgrade to an online bibliographic tool that complements and integrates seamlessly with EndNote desktop and the ISI Web of Knowledge research platform. EndNote Web's fresh new look introduces administrative tools to customize online search connection files, import filters, and bibliographic styles. The program makes organizing and citing references a simple task so users can concentrate on content. It encourages collaboration by enabling users to group references and share these groups with colleagues. With EndNote Web, users can connect to ISI Web of Knowledge, PubMed, and hundreds of online library catalogs, import references from online sources to build a reference collection, and create bibliographies instantly in more than 3,200 publishing styles.

Thomson Reuters
For information 760-438-5526
www.thomsonreuters.com

WDXRF Spectrometer System

The Rigaku Supermini is a high-power benchtop wavelength dispersive X-ray fluorescence (WDXRF) spectrometer system. Delivering rapid, high-sensitivity, nondestructive analysis of elements from fluorine through uranium in solids, liquids, powders, and thin films, the Supermini offers performance and value in a compact package. It is offered as a cost-effective, high-precision alternative to energy dispersive X-ray fluorescence technology. The instrument features three analyzing crystals, two detectors, a 12-position sample changer, and a choice of analysis in air, vacuum, or helium. An air-cooled 50 V, 200W tube provides exceptional light element performance and does not require external cooling.

Rigaku Americas Corp.
For information 281-362-2300
www.rigaku.com

Microplate Thawing Station

The MicroStream microplate thawing station circulates ambient air around the base of a frozen microplate or tube rack to gently and evenly thaw samples without risk of damage. Because many samples are stored using the solvent DMSO, which has a freezing point of 18°C, thawing samples from microplates or sample storage tubes is often a laboratory bottleneck. Economical, quiet,

and compact, the MicroStream not only increases laboratory productivity, but also maintains sample integrity by protecting compounds during multiple freeze-thaw cycles, reducing the precipitation risk.

Porvair Sciences
For information +44-1372-824290
www.porvair.com

Sequencing Software

The NextGENe software suite was developed to efficiently analyze the vast amount of data generated by "next generation" sequencing systems. NextGENe's applications include de novo and target assembly, single nucleotide polymorphism and indel discovery, digital gene expression analysis, transcriptome with complementary DNA analysis, and microRNA discovery and quantification. The software's preprogrammed applications, easy-to-use interface, and unique algorithms quickly process the sequence and quality files on standard Windows 64-bit operating system hardware. The software's ability to run on 64-bit desktop systems eliminates the need for users to acquire costly servers.

SoftGenetics
For information 814-237-9340
www.softgenetics.com

Liquid Dispensing Pump

Ecofluidic pumps are designed for low-cost, simple liquid transfer. Innovative features include a safety switch to ensure the pump runs only when the pump head is closed; a single, multifunction control knob for simple forward and reverse control; and an easy-to-use tubing holder for trouble-free operation. These peristaltic pumps offer advantages in scientific applications; for example, they are suitable for handling sterile media because the liquid is safely contained within the tube, preventing contamination. They are especially suited to low-pressure, low-flow pumping applications in which accuracy is key. Ecofluidic pumps deliver flows up to 3.8 liters per minute at pressures up to 1.5 bar. They have a single channel, three pump rollers, and a speed range from 80 rpm to 670 rpm.

Michael Smith Engineers
For information +44-0800-316-7891
www.michael-smith-engineers.co.uk

Electronically submit your new product description or product literature information! Go to www.sciencemag.org/products/newproducts.dtl for more information. Newly offered instrumentation, apparatus, and laboratory materials of interest to researchers in all disciplines in academic, industrial, and governmental organizations are featured in this space. Emphasis is given to purpose, chief characteristics, and availability of products and materials. Endorsement by Science or AAAS of any products or materials mentioned is not implied. Additional information may be obtained from the manufacturer or supplier.

THE POSTDOC EXPERIENCE: NOT ALWAYS WHAT YOU EXPECT

"A great mentor, an encouraging lab environment, and exciting science..."

"A learning opportunity for you to grow as a scientist..."

"A period of work that allows you to finish with quality publications, having made lots of contacts in the field, formed collaborations, and started forming an independent body of research..."

These statements describe what a successful postdoctoral experience should provide, according to respondents to a recent survey by *Science Careers*. But how can you ensure you get what you want out of your postdoc? And what happens if things don't turn out as planned? By **Laura Bonetta**

“What was really important to me in choosing a postdoc was that I was really interested in the research going on in the lab and I knew I could do really good science there,” says **Renald Schaub**, a research associate at the School of Chemistry of the University of St. Andrews in Scotland. But Schaub chose the laboratory of someone who not only had strong scientific credentials but was also supportive of the people working for him. “I went to Denmark for two days to interview, and right away I could tell he was a really good guy,” he says of his former postdoctoral adviser **Flemming Besenbacher**, head of the Interdisciplinary Nanoscience Center (iNANO) at the University of Århus in Denmark.

Besenbacher's support turned out to be particularly critical when Schaub started looking for a job. “A year and a half before I decided I would end my postdoc I started to send out job applications in Europe and in the States. I had no positive responses even though I already had two *Science* papers by then,” says Schaub. That's when Schaub decided to ask Besenbacher for help. His adviser wrote reference letters and suggested colleagues Schaub could contact at various institutions. “He knew someone in the department where I eventually got my position,” says Schaub.

A Successful Postdoctoral Experience

Schaub was one of close to 4,000 current or former postdocs polled in this year's survey (see “Survey Methodology”). Almost all survey participants agreed that the research topic (88 percent), good publication prospects (78 percent), and principal investigator (PI, 78 percent) had the greatest influence in their choosing of a postdoctoral position. The institution/company came in at a lowly 57 percent.

When asked about the importance of various factors in contributing to a successful postdoctoral experience, most survey respondents considered certain attributes of the PI as key (see graph on p1230). Top of the list (63 percent of respondents rated this as very important) was the scientific standing—defined as publishing in leading journals, having strong contacts, and being a recognized leader. Many respondents thought it was also very important for the supervisor to have direction and vision for their research (57 percent); to provide opportunities to attend scientific meetings and meet other researchers (56 percent), and to provide or assist in obtaining the financial resources needed to conduct their research (56 percent).

Doing a postdoc in a lab where she was not free to set up collaborations or attend scientific meetings to talk about her work eventually steered former postdoc **Anna Webb** away from research. “You need to make connections and gain a certain level of independence during your postdoc if you are going to have a career in academic research,” she says. Webb gave up the bench for a position at BiomedCentral, a UK-based publisher of open-access scientific journals—a job that allows her to interact closely with scientists and learn about their work on a daily basis. “I don't regret doing a postdoc. I learned a lot and I always enjoyed the science,” she says. “I ended up in a job I really enjoy, which I wouldn't have a chance of doing without my scientific experience.”

What About Communication?

Last year's *Science Careers* survey polled not postdocs but their supervisors. *continued »*

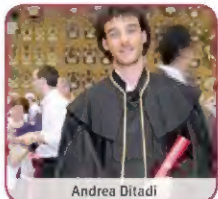


Anna Davis



Laura Colgin

“I ended up in a job I really enjoy, which I wouldn't have a chance of doing without my scientific experience.”

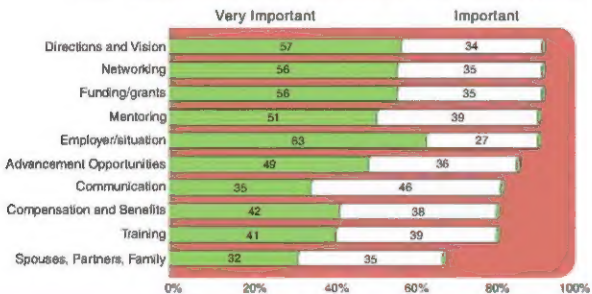


Andrea Diliti

UPCOMING FEATURES

Faculty Feature:
Enriching Your Academic Career — September 12
Focus on France — September 26
Top Employers — October 10

How Postdocs Rate Factors Contributing to a Successful Postdoc



They ranked communication and mentoring as very important in contributing to a successful postdoctoral experience (dx.doi.org/10.1126/science.opms.r0700037). Interestingly, these factors were not ranked highly by the postdocs surveyed this year—with mentoring coming in at No. 5 (51 percent of respondents ranked this as very important) and communication at No. 9 (35 percent) in a list of 10 factors.

But it is hard to argue against the value of good and open communication between a postdoc and his or her adviser. Now in the fourth year of a postdoctoral position at the University of Colorado in Boulder, **Sandi Clement** says communication was difficult when she first started out in the lab of Jens Lykke-Andersen. "When I first started I was intimidated and did not communicate as much as I do now," she says. One tool she thinks would have been helpful is the individual development plan offered by the Federation of American Societies for Experimental Biology. "It makes you ask questions like: This is where I want to be in 5 years so what do I need to accomplish? Or, this is what you wanted to accomplish this year, why didn't you?" explains Clement.

Clement says Lykke-Andersen turned out to be a "great mentor" and contributed to "an awesome experience." But she may be in the minority. Only 62 percent of survey participants had someone they would describe as a mentor during their postdoctoral years, and for only half of them that person was the PI of the lab. "A postdoc is a mentored apprenticeship into the job market. The person you are working with should be helping you along. But if the person who hired you turns out not to be a mentor, you need to seek out other people," says **Alyson Reed**, former executive director for the National Postdoctoral Association (NPA).

David Angelini, a postdoctoral fellow pursuing research into the developmental and genetic aspects of evolution (or "evo-devo") at the University of Connecticut, agrees. "I think it is important to have a mentor during your postdoctoral years. It does not necessarily have to be your PI. In graduate school I was in a large lab, so there were lots of postdocs and others who could give me advice," he says. "As a postdoc I relied more on my supervisor."

And for people looking for a postdoctoral position Angelini, who in September 2008 will be starting a faculty position at American University in Washington, D.C., has this advice: "Find an environment where you can talk to someone about how your career is going and the execution of science."

Survey Methodology

The survey was launched on March 19, 2008, with an e-mail invitation to approximately 60,000 Ph.D.s located in North America and Europe who were current or former postdocs. Of the 3,850 qualified surveys collected, 75 percent came from individuals in the United States or Canada, 20 percent from continental Europe, and 5 percent from the UK. About twice as many current postdocs participated as former postdocs. Most (79 percent) postdoctoral positions were held in academic institutions. Life or medical sciences were the most common (72 percent) disciplines for postdoctoral studies among respondents. Most respondents were 31 to 40 years of age (62 percent current and 57 percent former postdocs).

The Good and the Bad

According to verbatim responses from this year's survey respondents, some of the best things about the postdoc experience are having the independence and freedom to choose research projects and schedules, learning new techniques, and interacting with other colleagues. The worst things about it, for some, were poor relationships with their supervisors and low salary and job security, as well as the lack of independence for postdocs with controlling advisers.

Laura Colgin was one of the lucky ones. During her Ph.D. she had been studying how rhythms are involved in the function of the brain using tissue slices. For her postdoc she wanted to continue with the same line of research but with recordings in living animals—a technique she had never done. At a scientific meeting, Colgin approached **Edvard and May-Britt Moser** from the Norwegian University of Science and Technology. Although the Mosers' research did not focus on rhythms, she proposed starting that work in their lab if they were willing to train her in doing live recordings. "They were open to it and that is how the position worked out," says Colgin. "If someone is willing to put in a time investment to teach you something new they will probably be a good adviser. Many postdocs get their positions because the lab wants their existing skills instead of providing them with additional scientific training."

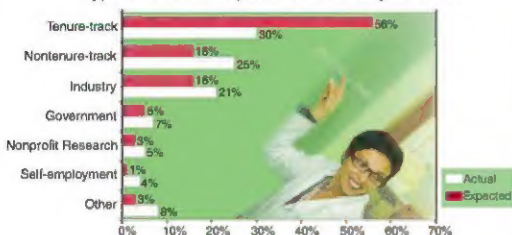
Salary Woes

Some of the biggest hardships for many postdocs are low salaries and lack of retirement benefits. According to this year's *Science Careers* survey only 15 percent of respondents received benefits—53 percent received no benefits and worried about a negative impact on their long-term retirement situation, whereas the remaining 32 percent did not receive benefits but were neutral about the impact.

Had she had some retirement funding, **Michelle Marquette** might have extended by a year or two her postdoctoral studies on the effects of microgravity on muscle at the NASA Johnson Space Center. "I went to graduate school after working for several years so I was older than most Ph.D. students. I had no retirement benefits as a student and that continued in my postdoc," she says. "It will take a long time for me to catch up."

And if the thought of not putting any money away for retirement does not aggravate some postdocs, having to live on a meager salary does. The median (50th percentile) postdoctoral salary reported by survey respondents located in the United States was **continued »**

Type of Position Expected vs. Actually Obtained



A larger percentage (56%) of former postdocs desired tenure-track academic positions than actually obtained such positions (30%). Similarly, only 16% of former postdocs initially expected to seek nontenure-track research scientist positions, compared with the 25% who ended up in such positions. The "other" types of positions that were cited included nonbench careers such as consulting, technology transfer, and administration.

\$40,000, which was an increase of just over 5 percent compared to the 2006 survey. The median salary of foreign postdocs was £27,500 in the UK and €25,200 in continental Europe.

Andrea Ditadi at the University of Padua, Italy, had to live on no salary for several months into his postdoc. "I was not paid for three months. That was a critical situation. You cannot go three months without money," he says. "I was lucky because I live close to my parents."

After working in France for three years Ditadi decided to do a postdoc in Italy "to try to stay and do something for my country," he says. But a year into his postdoc, he is frustrated by not being able to obtain the resources he needs to carry out his research. He has decided to look for postdoctoral positions abroad.

Expectations Versus Reality

Although only 2 percent of survey participants had done a postdoc in industry, many of those who did say this is a good option for anyone thinking about a career in industry and wanting to get a head start (see June 16 career feature at dx.doi.org/10.1126/science.opms.r0800055). Industry can also expose a postdoc to different aspects of doing science, according to Christopher Campion, director of the chemistry department at HF Scientific in Fort Myers, Florida. While working on his Ph.D. in physical organic chemistry at the University of Rhode Island, Campion had the opportunity to do an internship at Lithion, Inc., in Pawcatuck, Connecticut, which then turned into a postdoctoral fellowship. "My experience was different from the typical postdocs that only focus on one entity. I was working on multiple projects. I helped set up a lab, bought instruments, learned about applying for grants," says Campion. "One of the many good things about my postdoctoral adviser is that there were no taboo subjects. I came out a more diversified and well-rounded scientist."

The majority of survey respondents (79 percent) held postdoctoral positions in academic institutions—and they expected to get a job in academia. Over half (56 percent) of former postdocs wanted a tenure-track academic position after completing their postdocs, but only 30 percent got one (see graph above). Only 16 percent of former postdocs expected to seek nontenure-track research scientist positions, but 25 percent ended up in such posts. And a

Featured Participants

American Association for the Advancement of Science
www.aasas.org

American University
www.american.edu

BiomedCentral
www.biomedcentral.com

Harvard University
www.harvard.edu

HF Scientific, Inc.
www.hfscientific.com

Interdisciplinary Nanoscience Center, University of Aarhus
www.inano.dk

Lithion, Inc.
www.lithion.com

NASA Johnson Space Center
www.jsc.nasa.gov

Norwegian University of Science and Technology
www.ntnu.no/english

University of Colorado at Boulder
www.colorado.edu

University of Connecticut
www.uconn.edu

University of Padua
www.unipd.it/en

University of Texas Medical Branch, Galveston
www.utmb.edu

University of Washington
www.washington.edu

University of Wisconsin
www.wisc.edu

significant number of former postdocs (12 percent of respondents) who were expecting to obtain tenure-track positions ended up working in government or the nonprofit research sector, being self-employed, or working with other types of positions. These data should be a wake-up call to grad students and postdocs: having a backup plan is essential in today's job market.

Anna Davis knows that life can take unusual twists and turns. While doing a postdoc at the University of Washington in Seattle she started her family and wanted to explore different options for working part time. She and several colleagues wrote a grant with her postdoctoral adviser and got funding from the National Science Foundation for six years to produce educational software called NerveWorks, which is now commercially available (www.ecobeaker.com/products-college/NerveWorks).

After her Ph.D. in molecular and environmental toxicology at the University of Wisconsin Lisa Van Pay started a postdoc at Harvard University needing to "publish a lot and quickly." But she also started doing other things during her postdoctoral years, including working with the public at science and technology museums. When the needed publications did not come through, she applied for a prestigious public policy fellowship at the American Association for the Advancement of Science. In September she will be starting a one-year fellowship in Washington, D.C., with the possibility of a renewal. "I am really pleased at how things turned out, but I could not have predicted it," says Van Pay.

Former and current postdocs advise graduate students planning their postdocs to do their research on the prospective lab and PI. A literature search is a good start, but it also helps to query colleagues, current and former lab members, and of course the PI. Many survey participants also suggest having a well-laid-out timeline of accomplishments for the postdoctoral years. And while someone might start out wanting a career in academia, it pays to be open to other paths. "You have to continually assess your goals," says Van Pay. "Often people don't pay attention, and it could be several years before they realize that things are not going according to plan."

Laura Bonetta is a scientist turned freelance writer based in the Washington, D.C., area.

DOI: 10.1126/science.opms.r0800058